# Reconstruction and Simulation of Neocortical Microcircuitry

Graphical Abstract

Authors

Henry Markram, Eilif Muller,
Srikanth Ramaswamy,
Michael W. Reimann, ..., Javier DeFelipe,
Sean L. Hill, Idan Segev, Felix Schürmann

Correspondence

henry.markram@epfl.ch

In Brief

A digital reconstruction and simulation of the anatomy and physiology of neocortical microcircuitry reproduces an array of in vitro and in vivo experiments without parameter tuning and suggests that cellular and synaptic mechanisms can dynamically reconfigure the state of the network to support diverse information processing strategies.

Highlights

- The Blue Brain Project digitally reconstructs and simulates a part of neocortex

- Interdependencies allow dense in silico reconstruction from sparse experimental data

- Simulations reproduce in vitro and in vivo experiments without parameter tuning

- The neocortex reconfigures to support diverse information processing strategies

CrossMark

CellPress

Reconstruction and Simulation of Neocortical Microcircuitry

Henry Markram,[1,2,19,*] Eilif Muller,[1,19] Srikanth Ramaswamy,[1,19] Michael W. Reimann,[1,19] Marwan Abdellah,[1] Carlos Aguado Sanchez,[1] Anastasia Ailamaki,[16] Lidia Alonso-Nanclares,[6,7] Nicolas Antille,[1] Selim Arsever,[1] Guy Antoine Atenekeng Kahou,[1] Thomas K. Berger,[2] Ahmet Bilgili,[1] Nenad Buncic,[1] Athanassia Chalimourda,[1] Giuseppe Chindemi,[1] Jean-Denis Courcol,[1] Fabien Delalondre,[1] Vincent Delattre,[2] Shaul Druckmann,[4,5] Raphael Dumusc,[1] James Dynes,[1] Stefan Eilemann,[1] Eyal Gal,[4] Michael Emiel Gevaert,[1] Jean-Pierre Ghobril,[2] Albert Gidon,[3] Joe W. Graham,[1] Anirudh Gupta,[2] Valentin Haenel,[1] Etay Hay,[3,4] Thomas Heinis,[1,16,17] Juan B. Hernando,[8] Michael Hines,[12] Lida Kanari,[1] Daniel Keller,[1] John Kenyon,[1] Georges Khazen,[1] Yihwa Kim,[1] James G. King,[1] Zoltan Kisvarday,[13] Pramod Kumbhar,[1] Sébastien Lasserre,[1,15] Jean-Vincent Le Bé,[2] Bruno R.C. Magalhães,[1] Angel Merchán-Pérez,[6,7] Julie Meystre,[2] Benjamin Roy Morrice,[1] Jeffrey Muller,[1] Alberto Muñoz-Céspedes,[6,7] Shruti Muralidhar,[2] Keerthan Muthurasa,[1] Daniel Nachbaur,[1] Taylor H. Newton,[1] Max Nolte,[1] Aleksandr Ovcharenko,[1] Juan Palacios,[1] Luis Pastor,[9] Rodrigo Perin,[2] Rajnish Ranjan,[1,2] Imad Riachi,[1] José-Rodrigo Rodríguez,[6,7] Juan Luis Riquelme,[1] Christian Rössert,[1] Konstantinos Sfyrakis,[1] Ying Shi,[1,2] Julian C. Shillcock,[1] Gilad Silberberg,[18] Ricardo Silva,[1] Farhan Tauheed,[1,16] Martin Telefont,[1] Maria Toledo-Rodriguez,[14] Thomas Tränkler,[1] Werner Van Geit,[1] Jafet Villafranca Díaz,[1] Richard Walker,[1] Yun Wang,[10,11] Stefano M. Zaninetta,[1] Javier DeFelipe,[6,7,20] Sean L. Hill,[1,20] Idan Segev,[3,4,20] and Felix Schürmann[1,20]

[1]Blue Brain Project, École polytechnique fédérale de Lausanne (EPFL) Biotech Campus, 1202 Geneva, Switzerland
[2]Laboratory of Neural Microcircuitry, Brain Mind Institute, EPFL, 1015 Lausanne, Switzerland
[3]Department of Neurobiology, Alexander Silberman Institute of Life Sciences, The Hebrew University of Jerusalem, Jerusalem 91904, Israel
[4]The Edmond and Lily Safra Center for Brain Sciences, The Hebrew University of Jerusalem, Jerusalem 91904, Israel
[5]Janelia Farm Research Campus, Howard Hughes Medical Institute, Ashburn, VA 20147, USA
[6]Laboratorio Cajal de Circuitos Corticales, Centro de Tecnología Biomédica, Universidad Politécnica de Madrid, 28223 Madrid, Spain
[7]Instituto Cajal (CSIC) and CIBERNED, 28002 Madrid, Spain
[8]CeSViMa, Centro de Supercomputación y Visualización de Madrid, Universidad Politécnica de Madrid, 28223 Madrid, Spain
[9]Modeling and Virtual Reality Group, Universidad Rey Juan Carlos, 28933 Móstoles, Madrid, Spain
[10]Key Laboratory of Visual Science and National Ministry of Health, School of Optometry and Opthalmology, Wenzhou Medical College, Wenzhou 325003, China
[11]Caritas St. Elizabeth's Medical Center, Genesys Research Institute, Tufts University, Boston, MA 02111, USA
[12]Department of Neurobiology, Yale University, New Haven, CT 06510 USA
[13]MTA-Debreceni Egyetem, Neuroscience Research Group, 4032 Debrecen, Hungary
[14]School of Life Sciences, University of Nottingham, Nottingham NG7 2UH, United Kingdom
[15]Laboratoire d'informatique et de visualisation, EPFL, 1015 Lausanne, Switzerland
[16]Data-Intensive Applications and Systems Lab, EPFL, 1015 Lausanne, Switzerland
[17]Imperial College London, London SW7 2AZ, UK
[18]Department of Neuroscience, Karolinska Institutet, Stockholm 17177, Sweden
[19]Co-first author
[20]Co-senior author
*Correspondence: henry.markram@epfl.ch
http://dx.doi.org/10.1016/j.cell.2015.09.029

SUMMARY

We present a first-draft digital reconstruction of the microcircuitry of somatosensory cortex of juvenile rat. The reconstruction uses cellular and synaptic organizing principles to algorithmically reconstruct detailed anatomy and physiology from sparse experimental data. An objective anatomical method defines a neocortical volume of 0.29 ± 0.01 mm^3 containing ~31,000 neurons, and patch-clamp studies identify 55 layer-specific morphological and 207 morphoelectrical neuron subtypes. When digitally reconstructed neurons are positioned in the volume and synapse formation is restricted to biological bouton densities and numbers of synapses per connection, their overlapping arbors form ~8 million connections with ~37 million synapses. Simulations reproduce an array of in vitro and in vivo experiments without parameter tuning. Additionally, we find a spectrum of network states with a sharp transition from synchronous to asynchronous activity, modulated by physiological mechanisms. The spectrum of network states, dynamically reconfigured around this transition, supports diverse information processing strategies.

INTRODUCTION

Since Santiago Ramón y Cajal's seminal work on the neocortex (DeFelipe and Jones, 1988; Ramón y Cajal, 1909, 1911), a vast number of studies have attempted to unravel its multiple levels

of anatomical organization (types of neurons, synaptic connections, layering, afferent and efferent projections within and between neocortical regions, etc.) and functional properties (neuronal response characteristics, synaptic responses and plasticity, receptive fields, functional neocortical columns, emergent activity maps, interactions between neocortical regions, etc.). However, there are still large gaps in our knowledge, especially concerning the anatomical and physiological organization of the neocortex at the cellular and synaptic levels.
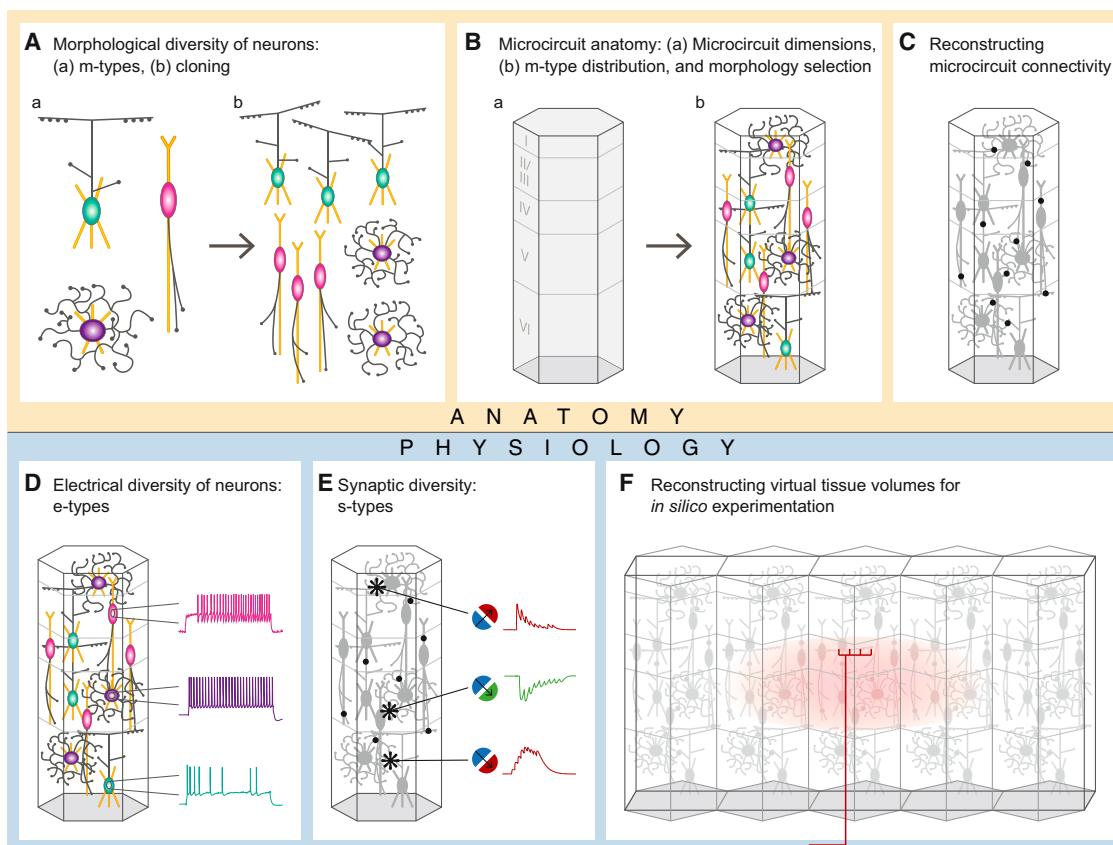
Specifically, while neurons have been classified in terms of their electrophysiological behaviors (Connors and Gutnick, 1990; Kasper et al., 1994; McCormick et al., 1985), expression of different calcium-binding proteins and neuropeptides (Celio, 1986; DeFelipe, 1993; Gonchar and Burkhalter, 1997; Kawaguchi and Kubota, 1997; Toledo-Rodriguez et al., 2005) and morphological features (Kisvárday et al., 1985; Larkman, 1991a; Tamás et al., 1998; Wang et al., 2002), there is still no consensus on an objective and comprehensive classification of neuron types. Although the distribution of protein and genetic markers for different neurons (Grange et al., 2014; Hendry et al., 1989; Kawaguchi and Kubota, 1997; Meyer et al., 2002; Toledo-Rodriguez et al., 2004) and the relative proportions of some morphologically and electrically classified neurons (Beaulieu and Colonnier, 1983; Cauli et al., 1997; Hendry et al., 1984; Meyer et al., 2010a; Rudy et al., 2011) have been described, we lack a comprehensive view of the number of each type of neuron in each layer. Since the advent of paired recording techniques, several studies have characterized the anatomical and physiological properties of synaptic connections between some types of neurons (Cobb et al., 1997; Feldmeyer et al., 1999; Frick et al., 2008; Gupta et al., 2000; Mason et al., 1991; Reyes et al., 1998; Thomson et al., 1993), but a large proportion have yet to be studied. Although labeling with retrograde and anterograde tracers and trans-synaptic viral vectors, imaging with array tomography, and saturated reconstruction with electron microscopy have made it possible to begin mapping pre- and postsynaptic neurons for individual neocortical neurons (Boyd and Matsubara, 1991; Callaway, 2008; Glenn et al., 1982; Kasthuri et al., 2015; Killackey et al., 1983; Micheva and Smith, 2007; Micheva et al., 2010; Wickersham et al., 2007), we know neither the numbers and types of the pre- and postsynaptic neurons associated with any specific neuron type nor the numbers and locations of the synapses that they form with their immediate neighbors.

At a functional level, there have been many investigations of emergent behavior in neocortical slices (Cunningham et al., 2004; Mao et al., 2001; McCormick et al., 2003; Sanchez-Vives and McCormick, 2000; Yuste et al., 1997), correlated activity (Hasenstaub et al., 2005; Livingstone, 1996; Salinas and Sejnowski, 2001; Shu et al., 2003; Silberberg et al., 2004; Singer, 1993), and the functional impact of individual neurons across cortical layers (Sakata and Harris, 2009; Schroeder and Foxe, 2002; Silva et al., 1991; Steriade et al., 1993), as well as in vivo activity in somatosensory and other cortical areas (Chen et al., 2015; Klausberger et al., 2003; Leinekugel et al., 2002; Luczak et al., 2007; Reyes-Puerta et al., 2015; Wilson et al., 2012), However, we still lack an understanding of the cellular and synaptic mechanisms and the role of the different layers in the simplest

of behaviors, such as correlated and uncorrelated single-neuron activity and, more generally, synchronous and asynchronous population activity. For example, it is known that different types of neurons are connected through synapses with different dynamics and strengths, strategically positioned at different locations on the neurons' dendrites, somata, and axons, but the functional significance of this organization remains unclear. Computational approaches that abstract away this level of biological detail have not been able to explain the functional significance of such intricate cellular and synaptic organization. Although future experimental research will undoubtedly advance our knowledge, it is debatable whether experimental mapping alone can provide enough data to answer these questions.

Here, we present a complementary algorithmic approach that reconstructs neuronal microcircuitry across all layers using available sparse data and that leverages biological principles and interdependencies between datasets to predict missing biological data. As a test case, we digitally reconstructed a small volume of tissue from layers 1 to 6 of the hind-limb somatosensory cortex of 2-week-old Wistar (Han) rat. This model system was chosen not only because it is one of the most comprehensively characterized in the neocortex, but also because experimental data on its cellular and synaptic organization are readily available and validation experiments are relatively easy to perform. In brief, we recorded and digitally reconstructed neurons from in vitro brain slices and classified the neurons in terms of well-established morphological types (m-types; Figure 1A), positioned the neurons in a digital volume of objectively defined dimensions according to experimentally based estimates of their layer specific densities (Figure 1B), and reconstructed the connectivity between the neurons (Figure 1C). Neurons were then classified into electrical types (e-types), using an extended version of the classification proposed in the Petilla convention (Ascoli et al., 2008), and models were produced that captured the characteristic electrical behavior of each type. (Figure 1D); similarly, synapses were modeled to capture the characteristic synaptic dynamics and kinetics of particular synapse types (s-types; Figure 1E). Finally, we constructed a virtual slice and reconstructed thalamic input using experimental data (Figure 1F; Meyer et al., 2010b).

This approach yielded a first-draft digital reconstruction of the microcircuitry, which was validated against a multitude of experimental datasets not used in the reconstruction. The results suggest that it is possible to obtain dense maps of neural microcircuitry without measuring every conceivable biological parameter and point to minimal datasets required, i.e., strategic data. Integrating complementary, albeit sparse, datasets also makes it possible to reconcile discrepancies in the literature, at least partially addressing the problem of data quality and reproducibility. Simulations exploring some of the emergent behaviors of the reconstructed microcircuitry reproduce a number of previous in vitro and in vivo findings and provide insights into the design and functioning of neocortical microcircuitry. The experimental data, the digital reconstruction, and the simulation results are available at the Neocortical Microcircuit Collaboration Portal (NMC Portal; https://bbp.epfl.ch/nmc-portal; see Ramaswamy et al., 2015).

Figure 1. Workflow for Data-Driven Reconstruction of Neocortical Microcircuitry

(A) Morphological diversity of neurons. (a) Identify the morphological diversity in the neocortical microcircuit (m-types). (b) Repair and then clone the various m-types with statistical variations to enrich the number of exemplars.

(B) Microcircuit anatomy. (a) Define the spatial dimensions of a unitary microcircuit. (b) Assemble individual neurons in 3D space according to the frequency of occurrence of each m-type per layer, selecting the appropriate m-type instance that satisfies laminar constraints on the axonal and dendritic distribution.

(C) Reconstructing microcircuit connectivity. Derive the number and location of synaptic contacts formed between all neurons in the microcircuit, based on a series of synaptic connectivity rules.

(D) Electrical diversity of neurons. Map and model the electrical types (e-types) of each m-type to account for the observed diversity of morpho-electrical subtypes (me-types).

(E) Synaptic diversity of neurons. Map and model the diversity of synaptic types (s-types) observed between pre-post combinations of me-types, according to rules derived from synaptic physiology.
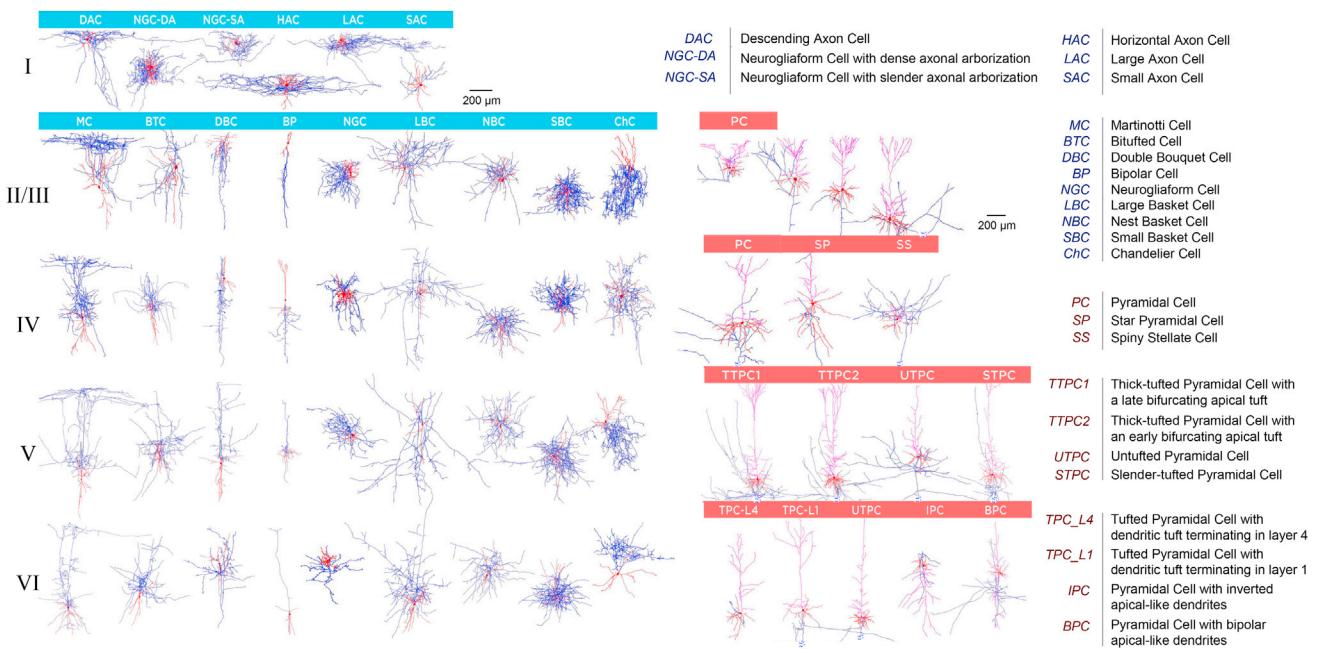
(F) Reconstructing virtual tissue volumes. Apply the above strategy to reconstruct defined circuit volumes (microcircuits, slices, mesocircuits) for in silico experiments; insert synapses formed by thalamocortical fibers for stimulation experiments.

RESULTS

Neuron-type Nomenclature

Neurons differ in terms of their location in the brain, morphology, electrical properties, projections, and the genes and proteins that they express (for reviews, see Harris and Shepherd, 2015; Markram et al., 2004). The combination of these properties implies an immense diversity of neuron types. Given the lack of sufficient data for other dimensions, the neuronal classification used for this first-draft digital reconstruction considered only layer, local morphology, and electrophysiology. Naming of morphological types was based on the most common names used over the past century (Connors and Gutnick, 1990; DeFelipe, 1993; DeFelipe et al., 2013; Douglas and Martin, 2004;

Fairén et al., 1984; Hestrin and Armstrong, 1996; Kawaguchi and Kubota, 1997; Kisvárday et al., 1985; Oberlaender et al., 2012; Somogyi et al., 1982, 1998; Svoboda et al., 1997; Szabadics et al., 2006), extended with a layer prefix (e.g., Layer_Morphology, L5_MC for layer 5 Martinotti cells). Electrical types, based on the Petilla convention (Ascoli et al., 2008), were treated as subtypes, (e.g., L5_MC_NAC for the non-accommodating subtype; see Experimental Procedures). When whole-brain axonal tracing data for a sufficient number of projecting neurons becomes available (e.g., L5_TTPC_CP and L5_TTPC_CT to represent cortico-pontine and cortico-tectal subtypes; Hallman et al., 1988; Wang and McCormick, 1993; for a review, see Ramaswamy and Markram, 2015), the proposed classification can be extended to include projection subtypes. Similarly, when there

Figure 2. Table of Neocortical Neuronal Morphologies

Exemplar 3D reconstructions of 55 m-types. Morphologies in L2 and L3 are not separated. Axon in blue, dendrites in red. Full morphologies are not always shown. See also Figure S1 for average arbor densities of each m-type and Figure S2 for objective classification of m-types and details of the morphology cloning process. See also Movie S1A.

are sufficient single-cell gene and protein expression data to systematically identify cells, it can be extended to include molecular subtypes. The abbreviations used for each m-type are provided in Figure 2. A mapping between the nomenclature used in this study and alternative names present in the literature is provided in Table 1.

Morphological Diversity of Neocortical Neurons

We recorded and labeled >14,000 neurons from all six layers in the somatosensory cortex of P14 male Wistar (Han) rats, using patch-clamp electrodes in in vitro slices. Of these neurons, 2,052 were sufficiently well stained to allow expert classification into m-types, based on well-established characteristic features of their dendritic and axonal arbors, a procedure initiated by early neuroanatomists and still in use today (Fairén et al., 1984; Karagiannis et al., 2009; Karube et al., 2004; Kawaguchi and Kubota, 1997; Kisvárday et al., 1985; Larkman, 1991a; Perrenoud et al., 2013; Peters and Kaiserman-Abramof, 1970; Ramón y Cajal, 1909, 1911; Somogyi et al., 1982, 1998; Wang et al., 2004; Yuste, 2005). We were able to digitally reconstruct a subset of 1,009 of these neurons. This allowed validation of the expert classification using an objective method (see below) based on clustering of characteristic features and provided the initial pool of digital neuron models needed to reconstruct the microcircuitry. In a few cases, we had no morphological reconstructions for rare m-types known to be present in the microcircuitry (L5_BP, L5_ChC, L6_NGC; Oláh et al., 2007; Szabadics et al., 2006). These were represented using exemplars of the same morphology from neighboring layers. Although L6 horizontal and

sub-plate pyramidal cells (L6_HPC and L6_SPC) were present in the dataset and have also been reported in the literature (Ghosh and Shatz, 1993; Hevner et al., 2001), the quality of the stains was not sufficient for reliable reconstruction. These morphologies are not represented in the first draft.
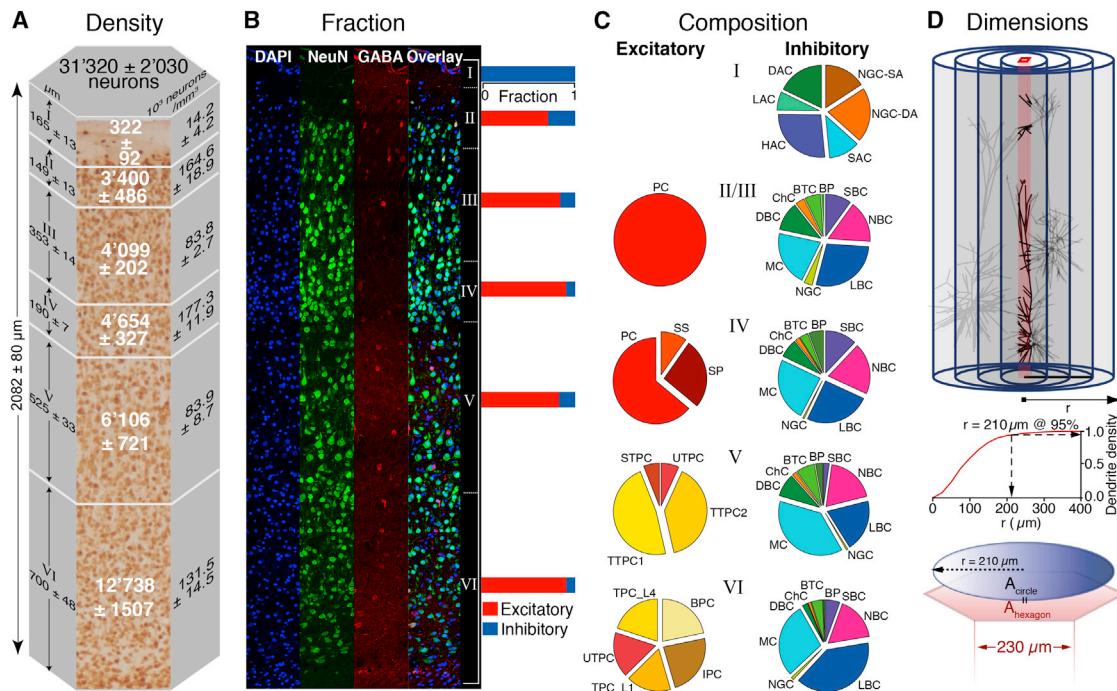
Aggregating morphological reconstructions and reports in the literature, we distinguished 55 m-types (65 if layers 2/3 are considered separately and 67 if L6_HPC and L6_SPC are also considered; Figure 2). Inhibitory types are mostly distinguished by axonal features and excitatory types by dendritic features (for reviews, see Markram et al., 2004; Ramaswamy and Markram, 2015; Spruston, 2008). Figure S1 shows overlays of multiple exemplars of each of the 55 major m-types, and Figures S2A and S2B illustrate the objective classification. While in some cases, it might have been possible to introduce a finer separation between m-types, this would have limited the size of the samples for individual types, reducing the reliability of the classification.

The same inhibitory types were present in all layers except layer 1, which contained a unique set of inhibitory neuron types. Pyramidal cell morphologies varied across layers (Figure 2, right) and also with depth within layer, as illustrated by the diversity of L23_PCs (Figure 2, upper-right). The number of pyramidal cell types, as defined by their local morphology, increased from upper to lower layers. Several types of interneuron (e.g., LBC and DBC) had axonal arbors that tended to descend to deeper layers when they were in upper layers and to ascend to upper layers when they were in deeper layers. Consistent with this trend, one type of pyramidal cell (L6_IPC) also had inverted axonal arbors.

Table 1. Relation of Interneuron Classes to Classification Schemes Found in the Literature

Morphological Type	Neurogliaform Cell (NGC)	Small Basket Cell (SBC)	Double Bouquet Cell (DBC)	Bipolar Cell (BP)	Martinotti Cell (MC)	Bitufted Cell (BTC)	Large Basket Cell (LBC)	Nest Basket Cell (NBC)	Chandelier Cell (ChC)
Other morphological classifications	Dwarf cell, button-type cell	Clutch cell	Bitufted cell/ interneuron, horse-tail cell	Bitufted cell/ interneuron	Bitufted cell/ interneuron	Bitufted interneuron	Common basket cell, typical basket cell	Willow cell, arcade cell, shaft-biased cell, atypical basket cell	Axo-axonic cell
Predominantly expressed Ca^{2+}-binding proteins and peptides	CB (−), NPY (+), PV (−), VIP (−), CR (−) SOM (−)	CB (++), NPY (+), PV (−), VIP (+++), CR (−) SOM (++)	CB (+), NPY (−), PV (−), VIP (+++), CR (+) SOM (++)	CB (−), NPY (−), PV (−), VIP (+++), CR (++) SOM (++)	CB (++), NPY (++), PV (−), VIP (−), CR (−) SOM (+++)	CB (++), NPY (+), PV (−), VIP (+), CR (++) SOM (++)	CB (++), NPY (+), PV (+++), VIP (+), CR (+) SOM (−)	CB (++), NPY (+), PV (+++), VIP (+), CR (++) SOM (−)	CB (+), NPY (−), PV (−), VIP (−), CR (−) SOM (−)
Electrical types	bNAC (7%), cNAC (79%), cSTUT (7%), cAC (7%)	bNAC (36%), cAC (36%), dNAC (29%)	bAC (9%), cAC (9%), bIR (37%), cIR (18%), bNAC (9%), cNAC (9%), bSTUT (9%)	bAC (7%), cAC (29%), bIR (14%), cNAC (14%), bNAC (29%) dSTUT (7%)	bAC (37%), cNAC (3%), bIR (11%), cSTUT (3%), bSTUT (4%), dNAC (3%), cAC (37%)	bAC (17%), cAC (67%), cNAC (17%)	bAC (6%), cNAC (17%), cAC (12%), dNAC (17%), cIR (6%) dSTUT (24%)	bAC (6%), cIR (7%), bIR (6%), cNAC (20%), bSTUT (13%), cSTUT (20%), cAC (20%) dSTUT (7%)	cAC (38%), cNAC (38%), dNAC (25%)
Other electrical classifications	Non-fast spiking, late spiking	Fast spiking, non-accommodating, non-adapting	Irregular spiking, regular spiking non-pyramidal, adapting	Late spiking, regular spiking non-pyramidal, adapting	Regular spiking non-pyramidal, burst spiking non-pyramidal, low threshold spiking	Regular spiking non-pyramidal, adapting, burst spiking non-pyramidal	Fast spiking, non-accommodating, non-adapting	Fast spiking, non-accommodating, non-adapting	Fast spiking, late spiking, non-adapting

The terms used in this paper are in the first row, followed by other common names in the literature. Interneurons can be categorized according to which primary marker they express (calcium-binding proteins: parvalbumin [PV], calbindin [CB], and calretinin [CR]; neuropeptides: somatostatin [SOM], vasoactive intestinal polypeptide [VIP], neuropeptide Y [NPY], and cholecystokinin [CCK]). The mapping to serotonergic receptors ($5HT_{3A}R$) is not included since this was not assayed in the RT-PCR. We assign several possible electrical types to each morphological type, based on the Petilla convention, and show other names frequently used in the literature. See Figure 4 for definitions of electrical types.

Figure 3. Neuron Densities and Composition and Microcircuit Dimensions.

(A) Neuron densities and numbers. Vertical thicknesses as determined by transitions in neuronal somata size and density in NeuN stained slices (six animals; mean ± SD). Neuron densities and numbers (six animals; mean ± SD).

(B) Neuron fractions. Confocal block imaging of dual immunohistochemical labeling. DAPI labels all cells (blue). NeuN labels all neurons (green), GABA labels all GABAergic cells including glia (red), dual GABA and NeuN labels only GABAergic neurons (green). Bars to the right show fractions of excitatory (red) and inhibitory (blue) neurons in each layer.

(C) m-type composition. Fractions of inhibitory (left) and excitatory (right) m-types per layer (n = 2052).

(D) Dimensions. The horizontal dimension was defined as the smallest circle required to attain maximal dendritic volume at a central minicolumn (brown, top); cut-off radius, 95% of the plateau volume (r = 210 μm, middle). To allow tiling, the circle was transformed into a hexagon, preserving the area. For m-type acronyms, see Figure 2.

See also Figure S3 for details on morphology placement and Figure S4 for validation of the composition. See also Movie S1B.

Using multiple exemplars obtained from different animals for each m-type, we developed a repair process to recover arbors cut during the slicing process, which was validated using in vivo reconstructed neurons (see Experimental Procedures; Anwar et al., 2009). To generate an even larger pool of unique morphologies, we cloned multiple exemplars of each m-type (Figures S2C–S2F), jittering branch angles, and section lengths in the clones (see Experimental Procedures). The morphometric properties of the resulting population were validated against distributions of features obtained from reconstructed neurons (see Experimental Procedures). This approach allowed us to establish a dataset of neuronal morphologies (see Movie S1A) that respects biological variability. Software applications for repairing and cloning in vitro neuron morphologies and for automated classification of neurons into the 55 m-types are available through the NMC Portal.

Reconstructing Neuron Densities, Ratios, and Composition

Reconstruction began by specifying the dimensions of the microcircuit, the fractions of excitatory and inhibitory neurons, the proportions of each m-type, and the number of neurons of each

m-type. The height of the neocortex and heights of each layer were measured experimentally in six animals, yielding an average overall height of 2,082 ± 80 microns (mean ± SD; n = 6; Figure 3A). Layer thicknesses were determined experimentally by measuring the location of transitions in cell densities and soma sizes in NeuN-stained tissue blocks (see Experimental Procedures). Fractions of excitatory and inhibitory neurons per layer (E-I fractions) were established by counting cells stained for DAPI (all cells), NeuN (all neurons), and GABA (all inhibitory neurons) in tissue blocks (Figure 3B; see Experimental Procedures). Overall, excitatory and inhibitory neurons represented 87% ± 1% and 13% ± 1% of the population, respectively, with a trend toward higher fractions of excitatory neurons in deeper layers (Figure 3B).

The m-type composition for all excitatory and all inhibitory neurons in each layer was obtained from the relative frequencies of each m-type in the experimental dataset of 2,052 classified neurons mentioned earlier (Figure 3C; see Experimental Procedures). It is not possible to exclude sampling bias in this dataset. However, since E-I fractions were obtained in an unbiased manner, any bias is restricted to the proportions of m-types within the excitatory and inhibitory neurons and does not affect the overall E-I balance.

The E-I fractions and m-type composition determined in this way are broadly consistent with previous reports (DeFelipe et al., 2002; Lefort et al., 2009). For example, it is well established that ~50% of inhibitory interneurons are basket cells (i.e., LBCs and NBCs—predominantly parvalbumin-positive cells; SBCs—predominantly vasoactive intestinal peptide (VIP)-positive cells; we found ~53%, see below), that Martinotti cells (i.e., predominantly somatostatin-positive cells; we found ~22%, see below) are frequent in all layers except L1, and that bitufted and bipolar cells (i.e., many of the calbindin and calretinin-positive cells) and double bouquet cells (i.e., many of the VIP-positive cells) are both found in layers 2–6. Other inhibitory interneuron types are also found in L2–L6 but less frequently (Kawaguchi and Kubota, 1997; Krimer et al., 2005; Meyer et al., 2011; Oláh et al., 2007; Sancesario et al., 1998; Somogyi et al., 1998; for a review, see Markram et al., 2004). Previously published neuron densities could not be used because they varied by a factor of two (40,000–80,000 neurons/mm^3; Beaulieu, 1993; Cragg, 1967; DeFelipe et al., 2002; Keller and Carlson, 1999; Peters, 1987) and are too low to account for the number of synapses in the microcircuit (see below, "Digital Reconstruction of Connectivity"). We therefore performed new experiments, counting cells in NeuN-stained tissue blocks. The experiments yielded a mean cell density of 108,662 ± 2,754 neurons/mm^3 (mean ± SEM, n = 6; see Experimental Procedures), comparable to observations in rat barrel cortex (Meyer et al., 2010a). Neuron densities were highest in L4 (Figure 3A), consistent with previous studies (Meyer et al., 2010a).

Since hind-limb somatosensory cortex, unlike barrel cortex, has no anatomically defined horizontal columnar organization (Horton and Adams, 2005; Markram, 2008), we chose to define the radius of the microcircuit by placing reconstructed neurons in a cylindrical volume and determining the minimal radius where the density of dendrites saturates at the center (Figure 3D; 95% of the plateau value obtained at a radius of 210 μm; see Experimental Procedures). We chose dendrites, as opposed to axons, because they only arborize locally. This convention, which yields a minimal radius that reflects saturated dendritic density along the central axis, could allow comparisons between microcircuits in different brain regions. It yields a radius similar to the horizontal extent of the dendrites of the largest neuron in the microcircuit (i.e., the L5_TTPC; for a review, see Ramaswamy and Markram, 2015) and is comparable with the dimensions of the barrels in the rodent barrel cortex (Meyer et al., 2010b; Wimmer et al., 2010). To allow tiling of multiple microcircuits while minimizing edge effects, the volume of the microcircuit was defined as a hexagonal prism (Figure 3D, bottom) with a cross-sectional area equal to that of the circle with the radius defined above and a height determined by the combined height of the layers.

With these densities, m-type composition, and circuit dimensions, we calculated the number of each m-type in each layer and in the whole microcircuit. To approximate inter-individual variation in layer dimensions and neuronal densities, we digitally reconstructed separate microcircuits corresponding to layer heights and densities measured in five animals (Bio1–Bio5). The five reconstructions had an average of 31,375 ± 2,251 neurons (mean ± SD, n = 5), with the number of neurons increasing in each layer from L1 to L6. We then constructed an additional microcircuit using the averaged data (BioM). To assess the variation introduced by the digital reconstruction process (stochastic variations in m-type composition, selection and positioning of model neurons, and synaptic connectivity [see below]), we reconstructed seven instances of each microcircuit (i.e., seven reconstructions each from Bio1–Bio5 and seven from BioM; 42 in total).
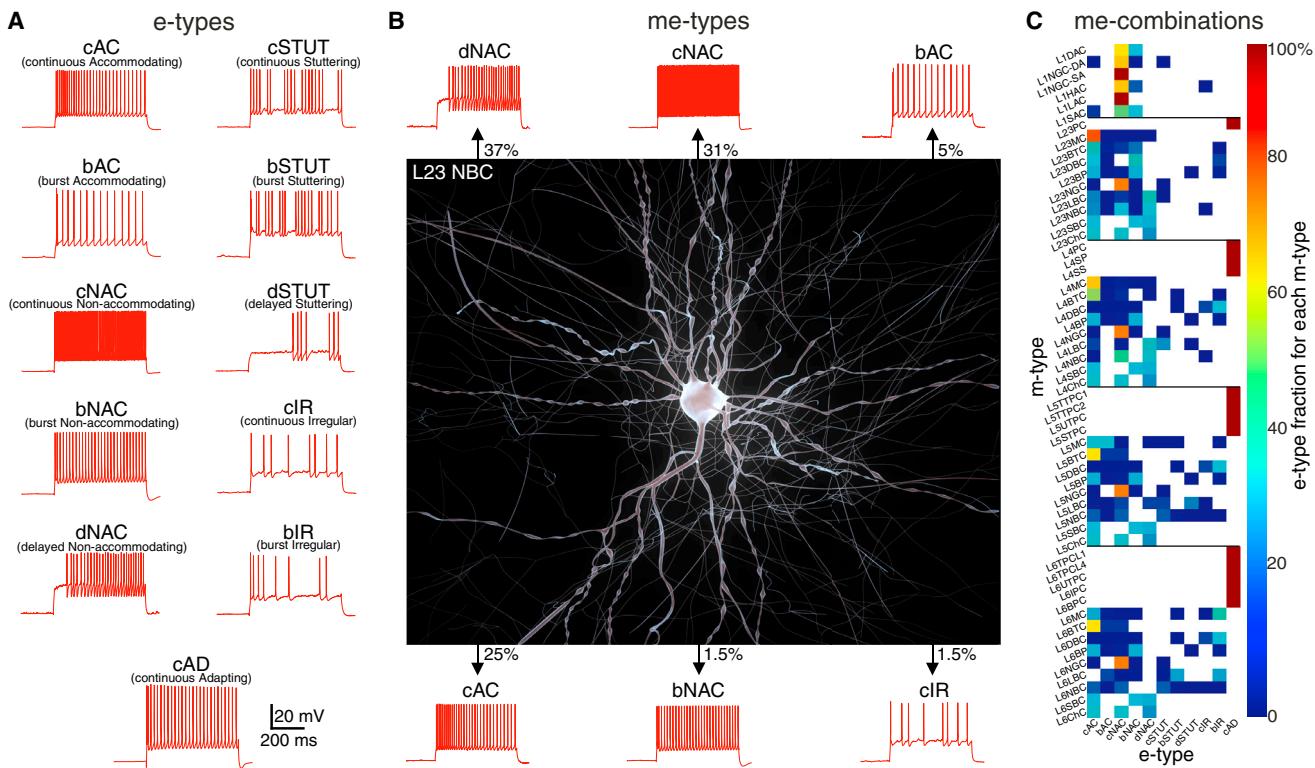
Positioning Morphologically Reconstructed Neurons

After establishing the dimensions of the microcircuit and the number of neurons belonging to each m-type in each layer, it was necessary to position each neuron in the digital reconstruction. Consistent with reports of weak minicolumnar organization in rodents, (Mountcastle, 1998), neurons were arranged in 310 minicolumns at horizontal positions drawn from 2D Gaussians around the center of each minicolumn, thus relaxing the strictness of the minicolumnar organization (see Experimental Procedures). The positions of the neurons along the vertical axis of the minicolumn were randomly chosen within each layer, using a space-filling algorithm to ensure that somata did not overlap (see Experimental Procedures).

Once the positions of the neurons were established, a second algorithm randomly selected a suitable morphology for each position from the top 8% of morphologies, scored by their match to typical patterns of arborization within and across layers (Figure S3; see Experimental Procedures). These patterns were manually annotated on each reconstructed neuron, based on the depth of the recorded neuron within each layer and cross-layer arborization patterns described in the literature (see Experimental Procedures and NMC Portal). Figure S4A illustrates the microcircuit at this stage of reconstruction (see also Movie S1B). The total lengths of axons and dendrites in the average microcircuit were 350 ± 4 m and 215 ± 3 m (mean ± SD, n = 7), respectively.

Biological accuracy at this stage of the reconstruction was validated against two experimental datasets that had not been used thus far. The first tissue-level dataset provides in vitro immunohistochemical staining of 30 μm sections for seven markers (calcium-binding proteins and neuropeptides) commonly used to label inhibitory interneurons (Figure S4B). The second cellular-level dataset provides estimated probabilities that the genes for these markers are expressed in specific m-types (Toledo-Rodriguez et al., 2005; Wang et al., 2002, 2004). We used the second dataset to add the markers to the model neurons. We then performed in silico immunohistochemical staining of the whole reconstructed tissue for each marker separately and compared the in silico stains against immunohistochemical stains from the first dataset. Although gene expression data are noisy and genes do not translate equally to protein levels, we found a reasonable correspondence between the numbers of neurons at different depths stained for specific markers in the in silico and the in vitro stains (regression, r = 0.65; Figure S4C). Furthermore, the layer-dependent pattern of in silico stained cells was consistent with previous staining experiments in this brain region (Ascoli et al., 2008; Condé et al., 1994; DeFelipe, 1993; Dumitriu et al., 2007; Gentet et al., 2010, 2012; Gonchar and Burkhalter, 1997; Gonchar et al., 2007; Kawaguchi and Kondo, 2002; Kawaguchi and Kubota, 1993,

Figure 4. Table of Morpho-Electrical Neuron Types

(A) e-types. Diverse firing patterns in response to depolarizing step current injections in neocortical neurons. c, continuous; d, delayed; b, bursting. AC, accommodating; NAC, non-accommodating; STUT, stuttering, IR, irregular; AD, adapting.

(B) An exemplar neuron (L23NBC) with a diversity of e-types. Percentages indicate the relative frequency of e-type occurrence.

(C) Fractions of e-types (11 e-types) recorded experimentally in each of the 55 m-types, making up 207 me-types. Solid lines indicate layer boundaries. See Table 1 for relation of e-types to other classifications in the literature.
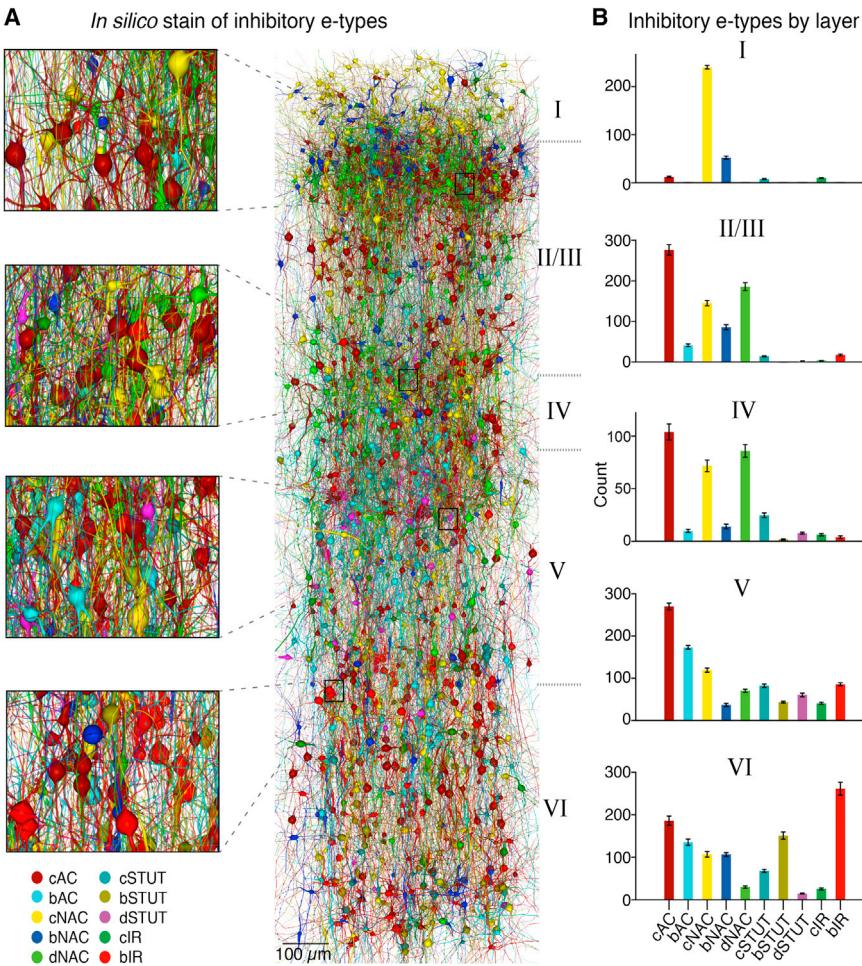
1997; McGarry et al., 2010; O'Connor et al., 2009; Packer and Yuste, 2011; Santana et al., 2013; see also NMC portal). The observed correspondence would be unlikely in the presence of major errors in neuron densities, m-type composition, or positioning of reconstructed neurons. However, the biological data are highly variable, and the validation of the inhibitory m-type composition used only a small proportion of markers reported in the literature. The reconstruction should thus be considered as a first draft, to be refined as it is challenged with additional markers.

Morpho-Electrical Composition

We applied a standardized battery of stimulation protocols (Le Bé et al., 2007; Wang et al., 2002, 2004) to >3,900 neurons from all layers, recording and analyzing their responses. The neurons were classified using quantified features of the neuronal response to step current pulses, according to the criteria established by the Petilla convention (Ascoli et al., 2008; Figure 4A, top), with the exception of stuttering cells, which were considered as a separate class (see Druckmann et al., 2013). Since no significant bursting behavior was observed in excitatory m-types from animals of the age used in this study, all excitatory m-types were classified as continuous adapting (cAD) neurons (Figure 4A, bottom). Using this feature-based classification scheme, we identified 11 e-types (10 inhibitory e-types and 1 excitatory e-type) (Figure 4A; see Experimental Procedures). Objective clustering of the same features produced a similar classification, validating the original classification scheme (Druckmann et al., 2013). The fact that the e-types identified in this way have characteristic ion channel profiles provides further evidence for their distinctive identity (Khazen et al., 2012; Toledo-Rodriguez et al., 2004).

Most inhibitory m-types expressed multiple e-types (Figure 4B), consistent with previous observations (Ascoli et al., 2008; Cauli et al., 2000; Nelson, 2002; Toledo-Rodriguez et al., 2005). Combining m- and e-types yielded 207 morpho-electrical types (me-types), providing an integrated view of the morpho-electrical diversity of the microcircuit (Figure 4C). A dataset of 511 morphologically and electrically classified inhibitory neurons was used to determine the relative proportion of e-types for each inhibitory m-type (in a layer-dependent manner for m-types with sufficient samples and otherwise in a layer-independent manner; Figure 4C, color map; see Experimental Procedures). The relative proportions were combined with neuron densities to calculate the number of neurons for each me-type in each layer. The resulting diversity and spatial distribution of inhibitory e-types is illustrated in Figure 5A. This integrated view of the microcircuitry reveals that, at this age, the most common inhibitory

A *In silico* stain of inhibitory e-types

cAC   cSTUT
bAC   bSTUT
cNAC   dSTUT
bNAC   cIR
dNAC   bIR

100 μm

B   Inhibitory e-types by layer

Figure 5. Layer-Dependent Distribution of Inhibitory e-Types

(A) In silico "brainbow" staining of a random selection of inhibitory morphologies, colored by e-type.

(B) Layer-wise distribution of inhibitory e-types (n = 35 reconstructions; mean ± SD). See Figure 4 for definitions of e-types.

other connection types (synapse locations; Hill et al., 2012). We now show that they reproduce the connectivity (numbers and locations) of all connection types that have been studied experimentally (see NMC Portal). For example, the anatomy of in silico synaptic connections between L5 Martinotti cells and L5 thick-tufted PCs (Figure S5) compares well with available experimental data (Silberberg and Markram, 2007). The algorithm provides detailed anatomical predictions for connection properties, which it has not yet been possible to measure experimentally (e.g., numbers of source and target cells and synapses) (Figure S5). The reconstruction also allows studies of neurons involved in polysynaptic pathways (see NMC Portal) forming known motifs (Honey et al., 2007; Perin et al., 2011; Silberberg, 2008; Sporns and Kötter, 2004).

The algorithm yields 1,941 biologically plausible multi-synapse connection types (out of a theoretical 3,025) that are consistent with the connectivity principles described above. Figure 7 shows the predicted average number of synapses formed by each potentially viable connection type (Figure 7A) as well as their predicted average connection probabilities (Figure 7B). The predicted number of synapses/connection is 4.5 ± 0.1 (3.6 for excitatory connections, 13.9 for inhibitory connections; n = 35). We also predict 27,625 types of connection between neurons of different me-types (see NMC Portal).
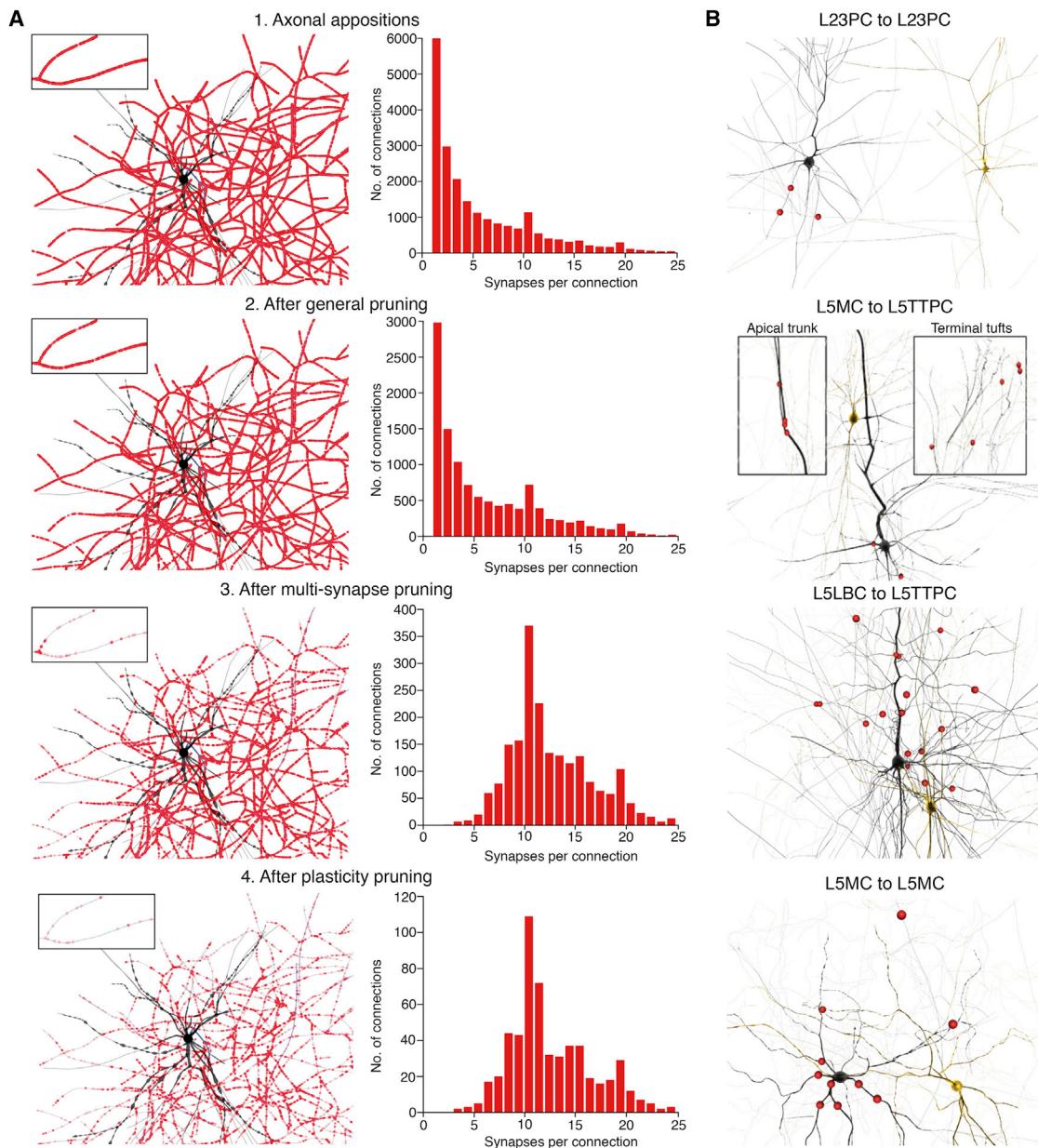
On average, each neuron innervates 255 ± 13 other neurons belonging to 32% ± 1% of m-types, forming an average of 1,145 ± 75 synapses per neuron present in the microcircuit (Figure S6A; mean ± SD, across the 35 Bio1-5 reconstructions; all neurons sampled). As a population, the neurons belonging to a given m-type innervate 63% ± 6% of the m-types in the microcircuit. The individual reconstructions (Bio1-5) yield an average of 638 ± 74 million appositions and 36.7 ± 4.2 million synapses (27.0 ± 2.9 million excitatory and 9.7 ± 1.5 million inhibitory). Taken together, the neurons of the microcircuit form 8.1 ± 0.9 million connections. Figure 7C and Table S1 provide a first view of the connectivity between neurons of the neocortical microcircuit. Analyzing these data, we find that, at this age, the fraction of excitatory synapses (red) increases from L1 to L6 (Figure S6B). At later ages, this trend may change as axons

e-type is cAC, followed by cNAC and dNAC, and that stuttering and irregular e-types (cSTUT, bSTUT, dSTUT, cIR, and bIR) are relatively rare (Figure 5B). Inhibitory e-types with regular firing patterns (cAC, bAC, cNAC, bNAC, and dNAC) occur more frequently in superficial layers, whereas e-types with irregular firing patterns (cSTUT, bSTUT, dSTUT, cIR, bIR) are more common in deep layers (Figure 5B).

Digital Reconstruction of Connectivity

We developed an algorithmic approach to reconstruct synaptic connectivity between neurons in a companion study (Reimann et al., 2015). The approach is based on five rules of connectivity described in the Experimental Procedures and validated in Reimann et al. (2015). We implemented these rules in four stages that yield plausible multi-synapse connections, consistent with the rules and constrained by experimental bouton densities (Figure 6A).

The algorithm predicts the characteristics of multi-synapse connections between pairs of neurons that belong to specific m-types (Figure 6B). We have previously shown that these predictions faithfully reproduce detailed anatomical data on connectivity between L5 thick-tufted PCs (number of synapses and locations; Ramaswamy et al., 2012) and for a number of

Figure 6. Reconstructing Connectivity
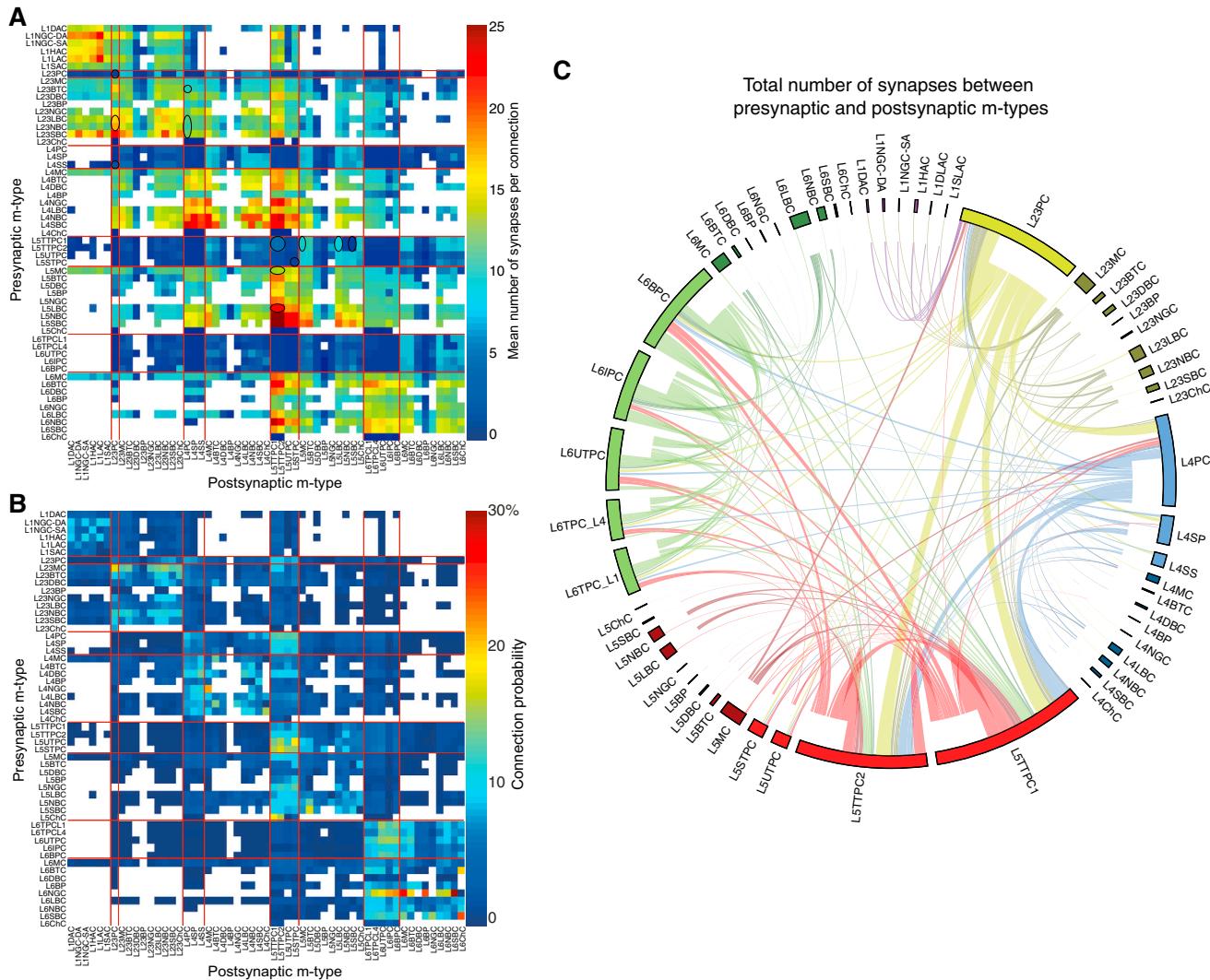
(A) Four-step algorithm to convert putative axo-dendritic appositions into functional synapses. (1) Axonal appositions. For an exemplar L23SBC (left, soma and dendrites in black, axon in blue), connectivity based on all axo-dendritic appositions (in red) is characterized by an extremely wide distribution of synapses per connection and almost 100% connection probability (right, pooled data from efferent connections to L23PCs of n = 100 L23SBCs). (Inset) A selected axon collateral with all appositions. (2) After general pruning. For the same exemplar, L23SBC, randomly removing a fraction of appositions removes the right side of the distribution of synapses per connection (right). (3) After multi-synapse pruning. Removing connections formed by too few appositions prunes the left side of the distribution of synapses (right) but leaves short inter-bouton intervals. (4) After plasticity pruning. The last step randomly removes more connections (right), leading to correct inter-bouton-intervals and connection probabilities.

(B) Examples of in silico multi-synapse connections resulting after the four-step apposition to synapse conversion algorithm. The pre- and postsynaptic m-types forming the synaptic connection are indicated. The presynaptic neuron is shown in yellow, postsynaptic neuron in black, and synaptic contacts as red circles.

mature and reach higher layers. Pooling all excitatory and inhibitory cells in each layer reveals that recurrent excitation increases with cortical depth while recurrent inhibition is weak in all layers, that descending interlaminar projections are stronger than ascending projections, and that intralaminar inhibition is weakest in layer 4 (Figure S6C).

The seven statistical instantiations of the mean microcircuit (BioM) yield 636 ± 10 million appositions and 36.5 ± 0.5 million

Figure 7. Predicted Synapse Numbers and Connection Probabilities

(A) Synapses per connection. A matrix of the average synapses per connection for multi-synapse connections formed between the 55 m-types (1,941 biologically viable connection types).

(B) Connection probabilities. A matrix of average connection probabilities within 100 μm.

(C) The connectome of the reconstructed microcircuit grouped by m-type (i.e., 1,941 m-type pathways). Colors group m-types by layer. Thickness of ribbon proportional to the number of synapses; inner ring segments, outputs (axons); outer ring segments, inputs (dendrites).

See also Figure S5 for anatomical details of an exemplary pathway; Figure S6 and Table S1 for more details of synaptic innervation strength; and Figure S20 for a comparison of the predicted connectome to a recent EM study. See also Movie S1C.

synapses (25.8 ± 0.4 million excitatory and 10.6 ± 0.2 million inhibitory; n = 7; Table S1 and Movie S1C). The lower variability of the statistical instantiations compared to the individual reconstructions (Bio1–Bio5; Table S1) indicates that the variation across digital reconstructions falls well within the bounds of biological variability.

From the space remaining on dendrites after accounting for predicted intrinsic connectivity (assuming 1.1 synapses/μm; Datwani et al., 2002; Kawaguchi et al., 2006; Larkman, 1991b), we predict that afferent fibers from beyond the microcircuit (extrinsic synapses) form a further 147 ± 4 million synapses (mean ± SD; n = 35) (Figures S6D and S6E). The total

predicted number of synapses in the microcircuit is thus 184 ± 6 million (mean ± SD; n = 35), of which only 20% ± 2% of synapses are formed by neurons belonging to the microcircuit (i.e., intrinsic synapses), consistent with previous estimates in neocortex (Stepanyants et al., 2009). In a parallel electron microscopy study in which we determined average synapse density (0.63 ± 0.1/μm³; mean ± SD; n = 25) and calculated the number of synapses in a comparable volume of the neocortex, we obtained 182 ± 6 million synapses. On the assumption that the average number of synapses/connection is the same for afferent fibers as for excitatory connections within the microcircuit (3.6 ± 0.04 synapses/connection; n = 35), we predict that

the microcircuit contains ~41 million mostly en passant afferent fibers.

The reconstructed microcircuitry reproduces numerous other experimental findings that were not used in the reconstruction process, described in a companion paper (Reimann et al., 2015). Nevertheless, it is clear that the predicted connectivity is a first draft that will be challenged and refined as experimental studies discover exceptions to the connectivity rules used here.

Reconstructing Neuronal Physiology

A series of algorithms and an automated workflow were developed to configure NEURON models to reproduce the electrophysiology of each me-type, (Druckmann et al., 2007, 2011; Hay et al., 2011) (see Experimental Procedures). In brief, we selected a morphologically reconstructed neuron and distributed Hodgkin-Huxley (HH)-type models of 13 known classes of ion channels (Figure S7) along the neuronal arbors (Figure 8A). Salient features were extracted from electrophysiological traces of e-type responses to step current pulses and data on back-propagating action potentials (Figure 8B; Larkum et al., 2001; Nevian et al., 2007). A multi-objective optimization algorithm (Druckmann et al., 2007) computed the vector of ion channel conductance densities that best reproduced features such as spike amplitudes and widths, spike frequency, and changes in frequency, and the resulting vector was transplanted into all neurons belonging to the m-type. Neurons in the resulting pool of models were challenged with a separate battery of stimuli not used to fit the vector of ion channel conductances. We then selected those that fell within observed distributions of features (~40% of models accepted; Figure 8C). This workflow provided a generic high-throughput method for modeling the electrical behavior of a potentially unlimited number of neurons of any e-type (Figure 8D). We automated the workflow to model all 207 me-types (Figure 8E), generating a pool of 121,231 unique neuron models. Exemplars can be downloaded from the NMC portal together with NEURON models of each m-type with all of their intrinsic synapses (see Movie S2). Morpho-electrical variation in the ensemble of model neurons was comparable to the biological variation observed experimentally. The quality of the final selection was quantified by comparing model and biological neurons in terms of their median z-scores for all electrical features (Figure 8E; see Experimental Procedures).

The generalization power of these models has been demonstrated previously (Druckmann et al., 2011). As a further test, we compared dendritic attenuation of synaptic potentials in the models against past experiments (Berger et al., 2001; Nevian et al., 2007). While attenuation along basal dendrites (Figure S8; space constant, 40.0 ± 0.1 μm) was consistent with these results (Nevian et al., 2007), the reconstruction displayed stronger attenuation along apical dendrites (Figure S8; 174.3 ± 0.4 μm) than previously reported (273 μm; Berger et al., 2001). However, the data in the literature were obtained from adult animals whose apical dendrites have larger diameters (Zhu, 2000) than those of the animals used in this study. In a subset of model neurons whose apical dendrites had similar diameters to those of adult animals (Zhu, 2000), attenuation was similar (Figure S8, B2, dark blue).
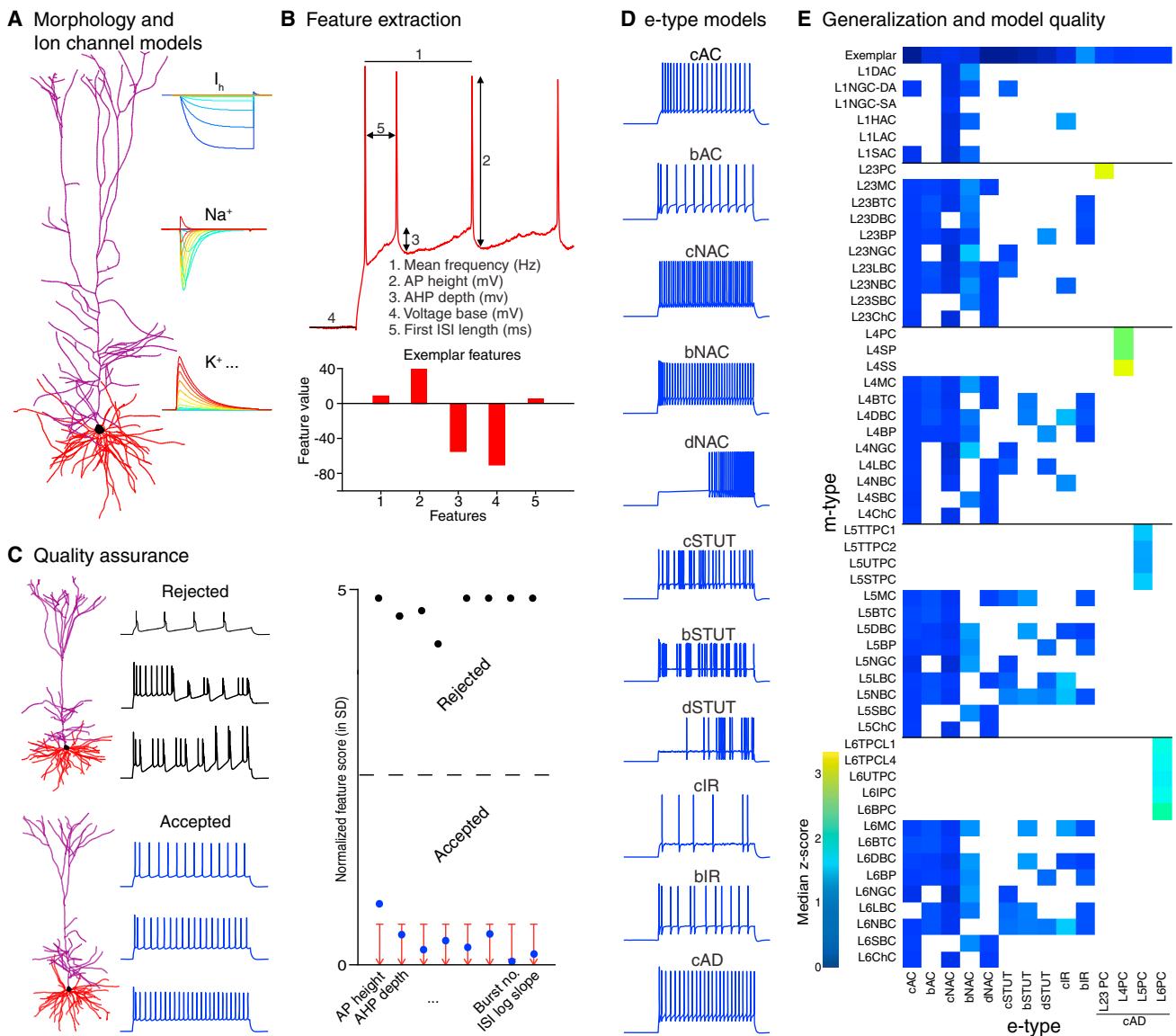
In most cases, transplantation of the vector of conductances to variants within the same inhibitory m-type preserved target physiology (~80% of models accepted), which was often maintained, even when conductances were transplanted to other inhibitory m-types (~60% of models accepted). This suggests that, in animals of the age used in the experiments, electrical behavior is relatively independent of the specific neuron morphologies.

Reconstructing Synaptic Physiology

To predict the physiology of the ~36 million synapses in the reconstruction, we integrated published paired-recording data and reported synaptic properties (conductances, postsynaptic potentials [EPSPs/IPSPs], latencies, rise and decay times, failures, release probabilities, etc.; see Experimental Procedures and NMC portal).

Neocortical synapses display known forms of short-term dynamics, which we used to classify synaptic connections as facilitating (E1 and I1), depressing (E2 and I2), or pseudo-linear (E3 and I3) s-types (Figures 9A and 9B) (Beierlein et al., 2003; Reyes and Sakmann, 1999; Reyes et al., 1998; Thomson and Lamy, 2007; Thomson et al., 1996; Wang et al., 2006). The s-types of specific connections were determined from the combination of their pre- and postsynaptic me-types (Ali et al., 2007; Bannister and Thomson, 2007; Beierlein and Connors, 2002; Feldmeyer et al., 2002; Frick et al., 2007; Gupta et al., 2000; Markram et al., 1998; Reyes et al., 1998; Somogyi et al., 1998; Thomson et al., 1993). Based on the available experimental data, we identified five rules to predict s-types for broad classes of connections: (1) pyramidal-to-pyramidal connections are always depressing (E2) (Feldmeyer et al., 1999; Frick et al., 2007, 2008; Gupta et al., 2000; Maffei et al., 2004; Markram et al., 1998; Mason et al., 1991; Mercer et al., 2005; Reyes et al., 1998; Thomson and Bannister, 1998; Thomson et al., 1993), (2) pyramidal-to-interneuron connections are also depressing (E2) (Angulo et al., 1999; Blatow et al., 2003; Holmgren et al., 2003; Markram et al., 1998; Reyes et al., 1998; Silberberg and Markram, 2007; Thomson and Deuchars, 1997; Wang et al., 2002), except for connections onto Martinotti, bitufted and other interneuron types displaying spike frequency accommodation, which are facilitating (E1) (Kapfer et al., 2007; Markram et al., 1998; Reyes et al., 1998; Rozov et al., 2001; Silberberg and Markram, 2007), (3) facilitation from inhibitory neurons is around two times stronger than from excitatory neurons (Gupta et al., 2000; Silberberg and Markram, 2007), (4) synaptic dynamics are preserved across layers for all me-type-specific connections, and (5) any remaining connections belong to the most common s-type (type 2; E2 or I2).

Since physiological characterization of all 27,625 unique me-type-to-me-type connections is not feasible, s-types in which experimental data were missing were specified using the rules above. Parameters for the synaptic dynamics of individual synapses were drawn from experimental distributions. In this manner, we generated a complete, albeit sparsely characterized, map of synaptic dynamics (Figure 9C). Stochasticity of synaptic transmission was modeled by extending a previously reported model (Fuhrmann et al., 2002). As an independent validation of the modeled synaptic dynamics, we compared the

Figure 8. Workflow for High-Throughput Reconstruction of Morpho-Electrical Behaviors

(A) Morphology and ion channel models. Selection of exemplar morphology, ion channel models, and their distribution on soma, dendrites, and axon.

(B) Feature extraction. Selection of experimental traces from a population of recorded cells as targets for fitting. Extraction of voltage and spiking features from experiments.

(C) Quality assurance. Multi-objective optimization of the vector of ion channel conductance densities to match the statistics of the extracted biological features in the model. Screen out models with electrical features that do not match the statistics for equivalent features in biological recordings.
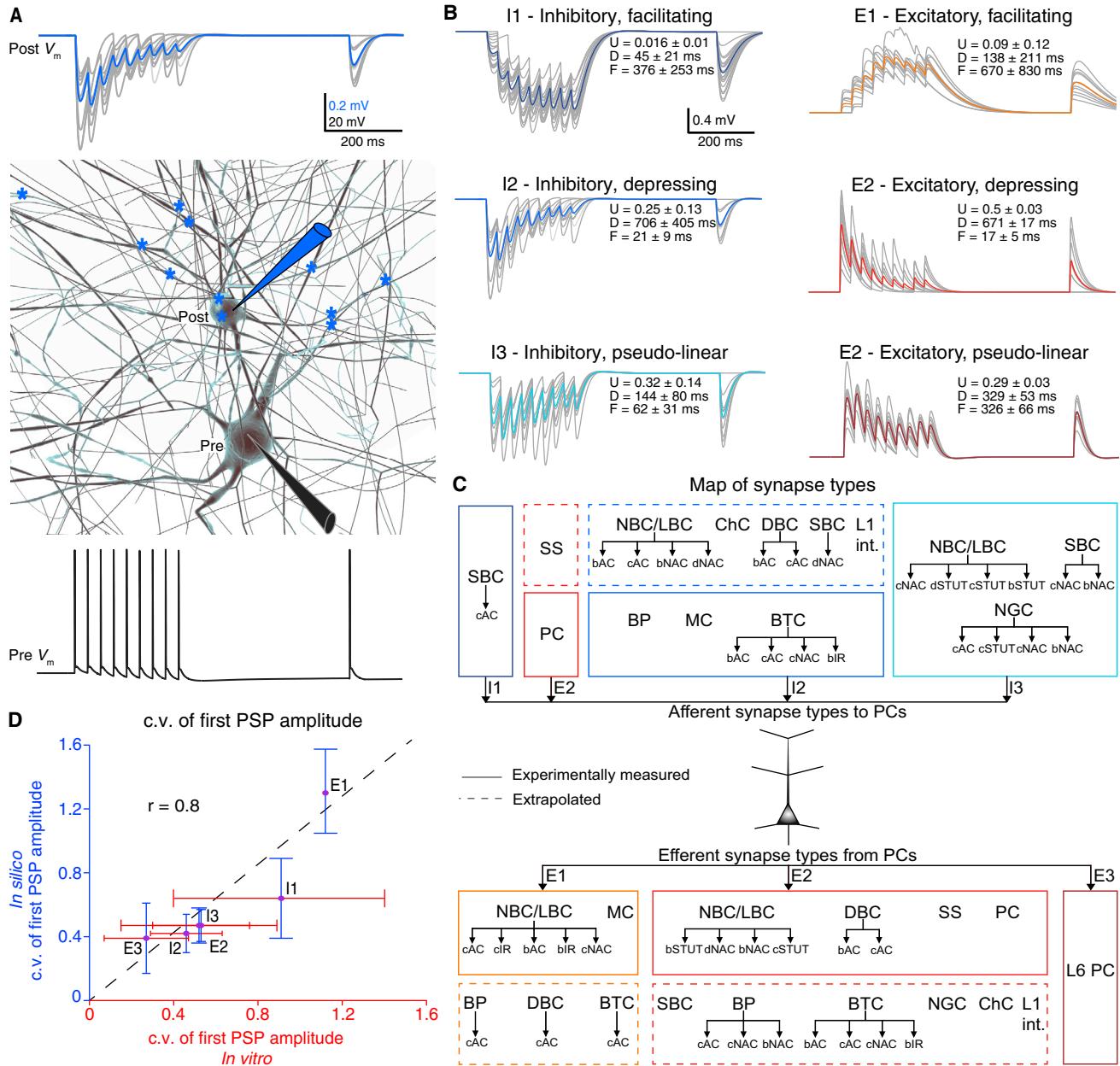
(D) Models of e-types. Shows the 11 e-types modeled.

(E) Generalization and model quality. Generalization of the vector of ion channel conductance densities to other exemplars of the same m-type; application of a standardized set of measurement protocols to each model neuron to determine generalization; quality scores for accepted models (median z-score).

See also Figure S7 for properties of modeled ion channels and Figure S8 for dendritic properties.

coefficient of variation (c.v.) of first PSPs against reported experimental data (r = 0.8; Figure 9D; Gupta et al., 2000; Markram et al., 1998; Wang et al., 2006).

We then applied unitary synaptic conductances obtained in previous experiments that also measured somatic postsynaptic potentials (PSP) between specific pairs of m-types and compared the resulting in silico PSPs with the corresponding in vitro PSPs (Figure 10A). The in silico PSPs were systematically lower. Since the neuron models and the numbers and locations of synapses between pairs of m-types had been validated, we hypothesized that the reported synaptic conductances had been underestimated, because of inadequate compensation for space-clamp errors (Feldmeyer et al., 2002; Gupta et al., 2000; Rinaldi et al., 2008). To quantify the underestimate,

Figure 9. Reconstructing Dynamic Synaptic Transmission.

(A) In silico synaptic connection. Experimental protocol recreated in silico to obtain the frequency dependence of synaptic transmission between pairs of neurons. A presynaptic L4NBC (black pipette) was stimulated with a 30 Hz pulse train to evoke eight APs + 1 "recovery" AP (bottom trace), resulting in inhibitory depressing responses (top traces) in the postsynaptic L4SS (blue pipette); 30 individual trials in gray, average in blue. The connection was mediated by 12 synaptic contacts (blue stars).
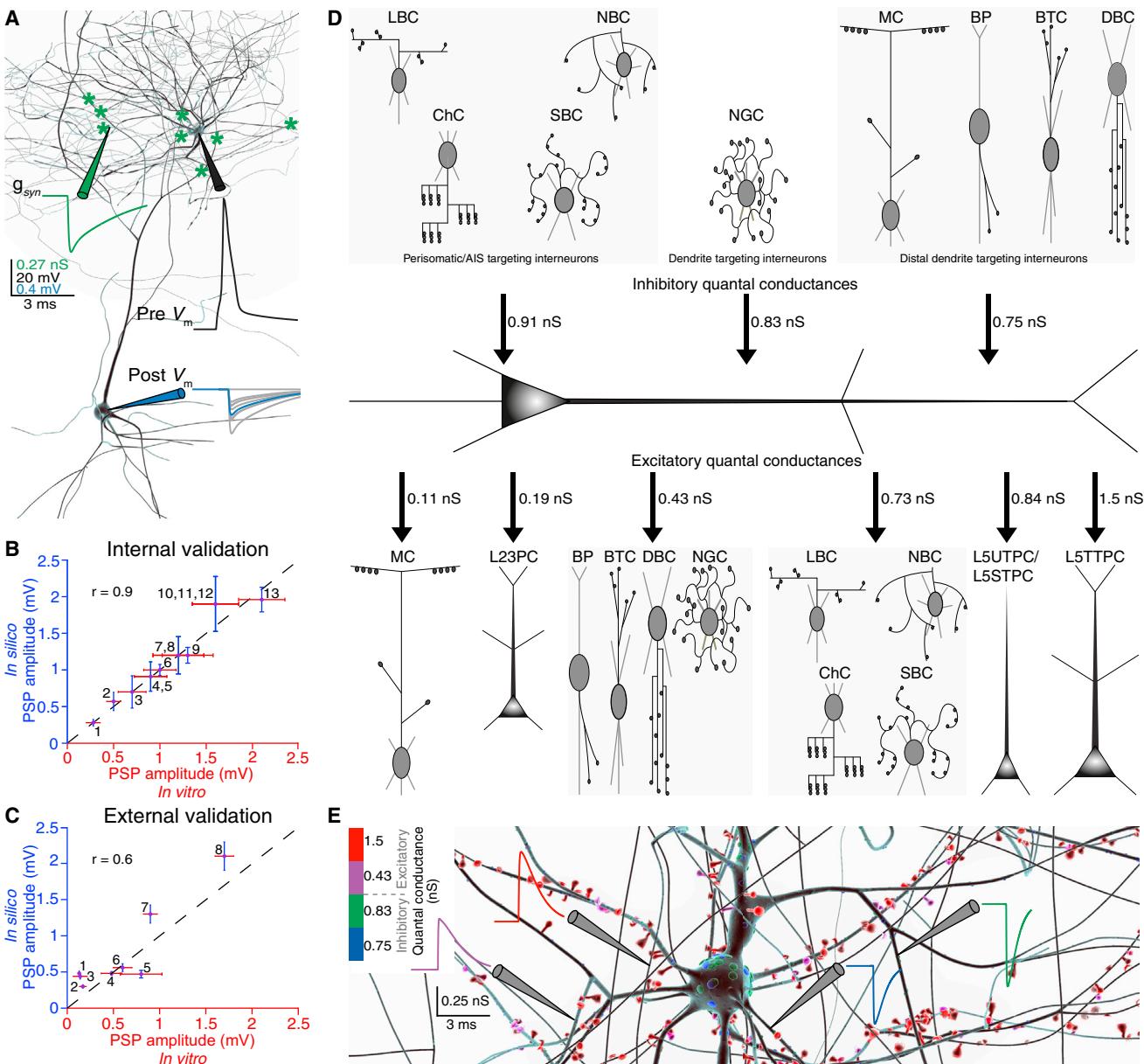
(B) Synapse types (s-types). Parameters describing six s-types in the Tsodyks-Markram phenomenological synapse model (see Experimental Procedures).

(C) Map of predicted synaptic dynamics. Previously established mapping rules were used to constrain s-types for connections that have not yet been characterized experimentally (see Figure S8), yielding a complete map for all 1,941 m-type-to-m-type connections in the reconstructed microcircuit.

(D) Validation. Trial-to-trial variability for different s-types in silico compared to in vitro data. Dots and error bars show mean ± SD of the data; dashed line shows regression fit.

synaptic conductances were adjusted until in silico PSPs matched experimental levels (Figure 10B and Table S2; Angulo et al., 1999; Le Bé et al., 2007; Feldmeyer et al., 2006; Feldmeyer et al., 1999, 2002; Markram et al., 1997; Silberberg and Markram, 2007). The results suggested that reported conductances are about 3-fold too low for excitatory connections, and 2-fold too low for inhibitory connections (Table S2; Gupta et al., 2000; Rinaldi et al., 2008). Other recent studies also suggest that

Figure 10. Reconstructing Quantal Synaptic Conductances.

(A) Unitary synaptic responses. A single AP was evoked in a presynaptic L1HAC (black pipette and trace). The postsynaptic potential was recorded at the soma of a L23PC (blue pipette; 30 individual trials in gray, average in blue); synaptic conductance was recorded simultaneously in the dendrite (green pipette and trace).

(B) Validation. Comparison of in silico PSP amplitudes to in vitro characterized connections (n = 9; mean ± SD; Table S2), explicitly correcting reported conductances for space-clamp errors (see Experimental Procedures). Dots and error bars show mean ± SD of the data; dashed line shows regression fit.

(C) Validation. As B for connections that lack conductance estimates (n = 10; mean ± SD; Table S4). Conductances were generalized from B for broad classes of excitatory and inhibitory connections (see Experimental Procedures).

(D) Quantal synaptic conductances. In the absence of experimental data for postsynaptic potentials, synaptic conductances were generalized from data for similar connections, allowing the prediction of quantal synaptic conductances for all synapses on a neuron. Simultaneous recording of quantal synaptic conductances in a L5TTPC are shown in colored traces (excitatory, red to pink; inhibitory, green to blue).

(E) Predicted map of quantal conductances. Circles indicate connections used in B (black) and C (white) above. Black lines separate excitatory m-types.

See also Figure S9 for examples of in silico synaptic patch and staining experiments and Table S2 for corrected conductances. See also Movie S2.

previously reported values are underestimated to a similar degree (Sarid et al., 2007; Williams and Mitchell, 2008).

For the vast majority of connection types, no experimental data for synaptic conductances were available. Therefore, we computed the average corrected synaptic conductances for broader classes of synaptic connections (e.g., E-E, E-I, I-I, I-E; see Experimental Procedures) and applied these conductances to all specific connections where data were missing. The resulting amplitudes of in silico PSPs were validated against experimental data for ten connection types not used in determining the conductances (regression, r = 0.6; Figure 10C and Table S2). The derived synaptic dynamics and quantal conductances compared well with previous reports (Feldmeyer et al., 2002; Ramaswamy et al., 2012; Silberberg and Markram, 2007; Thomson and Deuchars, 1997) (see NMC Portal). Using the same method, we generated a first prediction of mean synaptic conductances for all 1,941 m-type-to-m-type connections (Figure 10D). Unique quantal synaptic conductances for individual synapses were drawn from truncated normal distributions around these means (Figure 10E; see Experimental Procedures).

We performed in silico paired recordings of all 1,941 m-type-to-m-type connections in the average microcircuit (BioM) and found results comparable to previously published paired recordings in vitro (see Figures S9A–S9J for an example; see NMC Portal). Obtaining the anatomical and physiological properties of all the intrinsic synapses formed onto and by any neuron has long been an experimental challenge (Crick, 1979). The reconstruction now allows in silico retrograde staining experiments for any neuron in the microcircuit, providing a detailed view of its presynaptic neurons and their synapses (Figure S9K). In silico anterograde staining for postsynaptic neurons is also possible. Figure S9L illustrates predicted locations of afferent synapses formed onto a L23_PC. Figure S9M shows the mean number of presynaptic (red) and postsynaptic (blue) neurons for excitatory (top) and inhibitory (bottom) m-types. Predicted input-output synapses for all 31,346 neurons in the BioM microcircuit and summary statistics for each of the 55 m-types, 11 e-types, and 207 me-types can be downloaded from the NMC Portal. The portal also provides NEURON models of each m-type, allowing simulation experiments exploring dendritic integration of m-type-specific synaptic inputs.

We found that the m-, e-, and s-types of inputs to any particular neuron were always strikingly different from those of its outputs (i.e., inputs and outputs were highly asymmetrical; see NMC Portal). The predicted average total synaptic conductance for single neurons was ∼1000 nS (∼750 nS excitatory and ∼250 nS inhibitory conductance; based on all synapses in BioM). Predicted average quantal conductance was 0.85 ± 0.44 nS for excitatory synapses (corresponding to ∼150 AMPA and ∼20 NMDA receptors; Yoshimura et al., 1999) and 0.84 ± 0.29 nS for inhibitory synapses (corresponding to ∼40 $GABA_A$ receptors; Ling and Benardo, 1999). The average failure rate across all 1,941 m-type-to-m-type connections was 11.1% ± 14.1%.

Simulating Spontaneous Activity

To simulate reconstructed microcircuits at the level of detail described above, the NEURON simulator was extended to run on supercomputers (Figure S10; Carnevale and Hines, 2006;
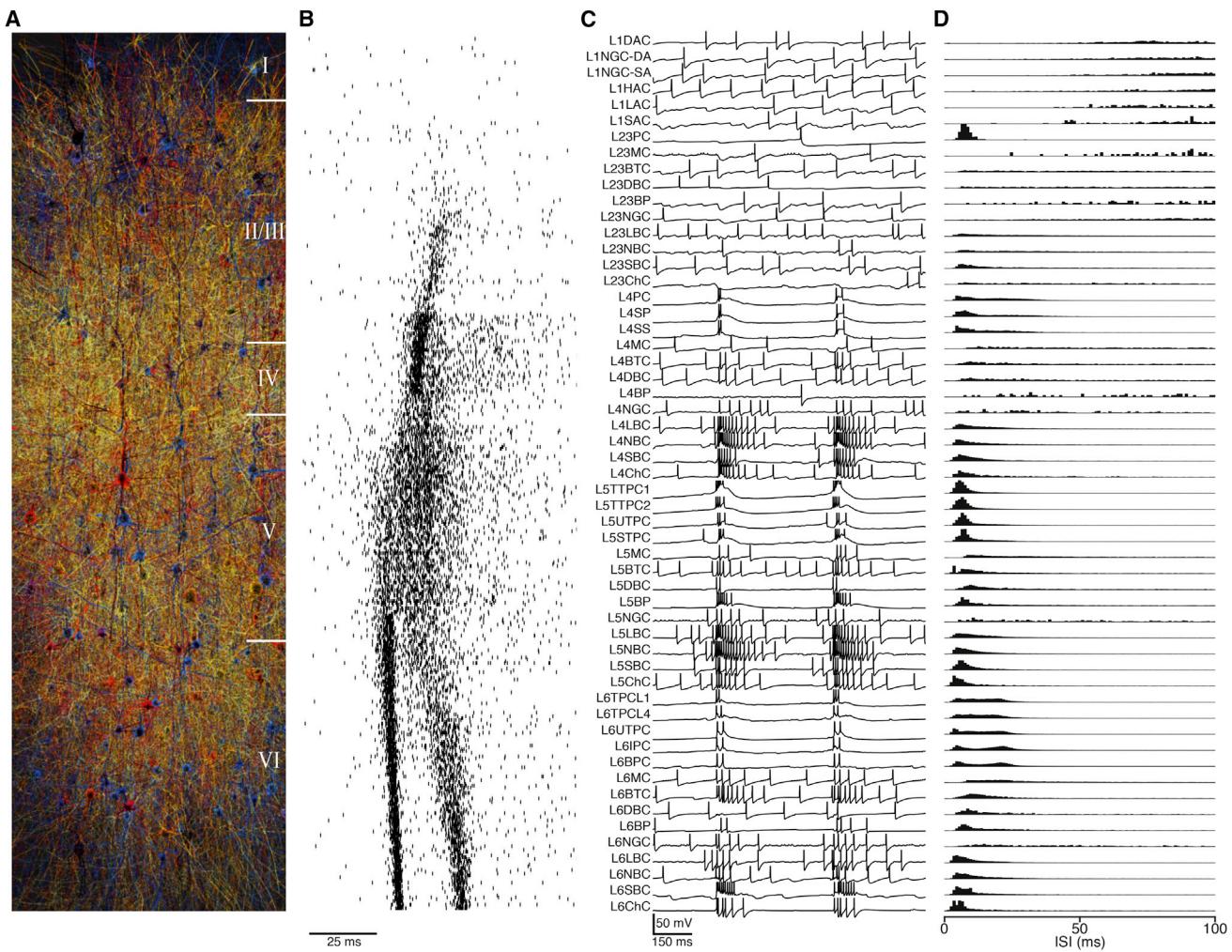
Hines and Carnevale, 1997; Hines et al., 2008a, 2011, 2011; Migliore et al., 2006), and additional functionality was developed to support in silico experimentation (see Experimental Procedures). We then used simulations to investigate the neuronal activity of the reconstructed microcircuitry (Figure 11A) under different conditions. We began by simulating spontaneous activity during tonic depolarization (see Movie S3A), attempting to mimic previous in vitro experiments (see Experimental Procedures). Under these conditions, neurons belonging to all m-types were active and the network exhibited spontaneous slow oscillatory population bursts, initiated in L5, spreading down to L6, and then up to L4 and L2/3 with secondary bursts spreading back to L6 (Figure 11B). Despite apparent global synchrony, the 55 m-types generated diverse patterns of spiking (Figures 11C and 11D).

To allow comparison with the in vitro experiments, from which the physiological data were obtained, we reconstructed a virtual brain slice (a mesocircuit) that was 230 μm thick and whose width was equivalent to that of seven microcircuits (containing a total of 139,834 neurons) (Figure 12A; see Movie S3B and Experimental Procedures). The virtual slice reproduced the oscillatory bursts (∼1 Hz) found in the previous microcircuit simulations (Figure 12B), which are comparable to those found in in vitro experiments (Lőrincz et al., 2015; Sanchez-Vives and McCormick, 2000).

In vitro experiments are typically performed at 2 mM $[Ca^{2+}]_o$, while the level of $[Ca^{2+}]_o$ in vivo is reported to lie in the range 0.9–1.1 mM (Amzica et al., 2002; Jones and Keep, 1988; Massimini and Amzica, 2001; also see Borst, 2010), increasing in oscillatory cycles to 1.2–1.3 mM during the transition from wakefulness to sleep (Amzica et al., 2002; Heinemann et al., 1977). Although it is not possible to fully mimic in-vivo-like conditions, we nonetheless explored the behavior of the circuit at these lower Ca^{2+} levels as an approximation of the in vivo condition.

It is well known that the $[Ca^{2+}]_o$ in the extracellular space modulates the probability of neurotransmitter release (Borst, 2010; Ohana and Sakmann, 1998; Rozov et al., 2001). We therefore modified the probability of release, consistent with experimental data for the specific sensitivities of different s-types to changes in $[Ca^{2+}]_o$ (Gupta et al., 2000; Rozov et al., 2001; Silver et al., 2003; Tsodyks and Markram, 1997) (Figure S11; see Experimental Procedures). We found that, in the low Ca^{2+} condition, slow oscillatory bursting disappeared and the neuronal activity became asynchronous and irregular (Figure 12C). To validate this in silico finding, we performed multi-electrode array recordings in vitro (Figure 12D) in high and low Ca^{2+} conditions (see Experimental Procedures). As predicted by the simulations, we found that the slow oscillatory bursts present in high Ca^{2+} (Figure 12E) were replaced by asynchronous and irregular activity under low Ca^{2+} conditions (Figure 12F).

We then used the virtual slice to explore the behavior of the microcircuitry for a wide range of tonic depolarization and Ca^{2+} levels. We found a spectrum of network states ranging from one extreme, where neuronal activity was largely synchronous, to another, where it was largely asynchronous (the synchronous-asynchronous [SA] spectrum; Figure S12). The spectrum was observed in virtual slices, constructed from all 35 individual instantiations of the microcircuit (seven for each of Bio1–Bio5) and all seven instantiations of the average microcircuit (BioM).

Figure 11. Simulation of the Reconstructed Microcircuit

(A) Simulation of spontaneous activity. Individual neurons at different levels of depolarization in the microcircuit are colored according to a heatmap (blue, hyperpolarized; red, depolarized; white, spike).

(B) Rastergrams of randomly selected neurons for each m-type during synchronous bursting.

(C) Exemplar voltage traces for each of the 55 m-types during spontaneous activity in the microcircuit (traces truncated at −30 mV).

(D) Inter-spike interval (ISI) distributions of each of the 55 m-types for the activity shown in C.

See also Figure S10 for an overview of the software ecosystem surrounding the simulation of the microcircuit. See also Movie S3A.

This implies that it is a highly reproducible phenomenon, robust to biological and statistical variations in parameters such as layer thickness, cell density, and composition; specific synaptic connectivity; and the specific dimensions of the microcircuit (see Movie S3C).
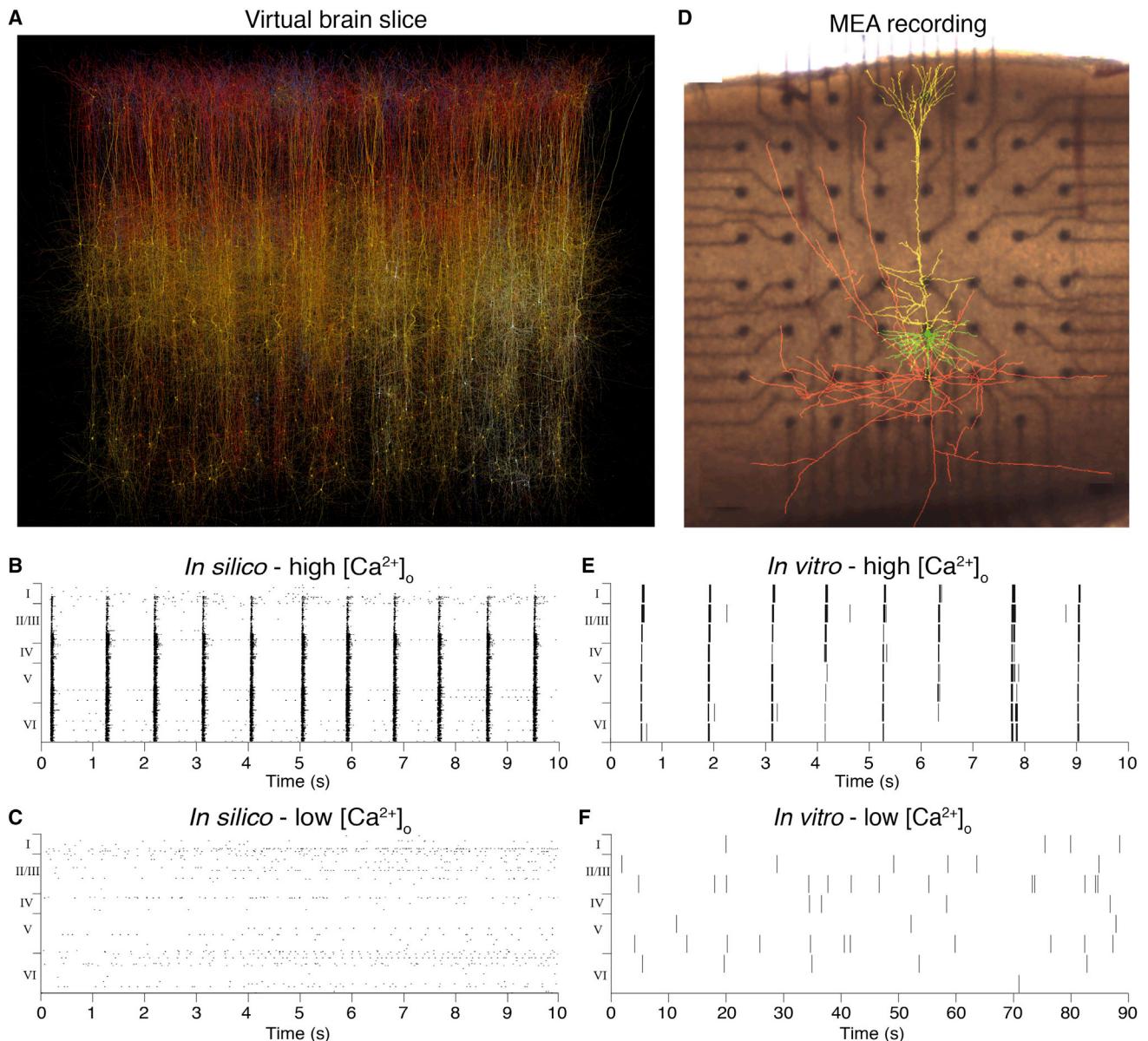
We observed that a change in $[Ca^{2+}]_o$ of < 1 mM can lead to a transition from the synchronous to the asynchronous state, revealing two distinct activity regimes (Figure S12). The level of $[Ca^{2+}]_o$ at the transition varied slightly across the different instantiations of the microcircuit (Bio1–Bio5; Figure S13).

Since the reconstructed microcircuitry displays synaptically coupled assemblies comparable to those found experimentally (Perin et al., 2011; Reimann et al., 2015), we also analyzed correlations in neuronal activity within these assemblies. Neuronal activity was found to be slightly more correlated within assem-blies compared to randomly sampled neurons (Figure S14). Near the transition, a fall in $[Ca^{2+}]_o$ of just ~0.15 mM (Figure S14) led to a sharp decrease in correlated spiking, clearly demar-cating a transition in the SA spectrum.

The mechanism underlying this sharp transition is likely to involve the differential Ca^{2+} sensitivities of inhibitory and excit-atory synapse types. Indeed, we found that changing $[Ca^{2+}]_o$ from 2 mM to 1.3 mM alters the ratio between excitatory and inhibitory synaptic PSPs by a factor of ~3.5, in favor of inhibition (Figure S11). This suggests the existence of a threshold level of Ca^{2+} beyond which inhibition is insufficient to prevent a super-critical state (see below).

The finding that differential sensitivity of s-types to Ca^{2+} levels determines the position of the network along the SA spectrum suggests that other mechanisms that change the

Figure 12. Predicting and Validating Synchronous and Asynchronous States in Spontaneous Activity

(A) A spontaneously active virtual slice formed from seven unitary microcircuits ($230.9 \times 2800 \times 2082$ μm).

(B) Rastergram of a random selection of neurons during in silico spontaneous activity under in-vitro-like conditions (somatic depolarization to ~90% threshold, ($[Ca^{2+}]_o = 2.0$ mM). Number of neurons displayed per layer is proportional to the total number of neurons per layer.

(C) Rastergram of a random selection of neurons during in silico spontaneous activity under in-vivo-like conditions (somatic depolarization to ~90% threshold, ($[Ca^{2+}]_o = 1.0$ mM).

(D) To assess network activity, 300-μm-thick cortical slices were mounted on a 3D multi-electrode array (MEA) (reconstruction of a layer 5 pyramidal cell overlaid).

(E) Experimentally observed spontaneous multi-unit activity under in vitro $[Ca^{2+}]_o$.

(F) Experimentally observed spontaneous multi-unit activity under in vivo-like $[Ca^{2+}]_o$.

See also Figure S11 for $[Ca^{2+}]_o$ sensitivity of synapse types; Figures S12 and S13 for activity along the full spectrum of $[Ca^{2+}]_o$ concentrations and its biological variability; Figure S14 for synchrony in synaptically clustered neurons along the spectrum; Figure S15 for the effect of selective knockouts on microcircuit activity. See Movie S3B for a visualization of B and Movie S3C for C.

excitatory-inhibitory balance may have similar effects. We therefore performed in silico knockout experiments to understand the roles of the different layers, neurons, and connections in control-

ling the position of the microcircuit on the spectrum (Figure S15). We found that blocking activity in the upper layers tended to shift the network toward the synchronous state, while blocking the

deeper layers had the opposite effect (Figure S15A). Similarly, blocking soma-targeting basket cells produced a stronger shift toward the synchronous state than blocking other interneurons, while blocking pyramidal cells caused a shift toward the asynchronous state (Figure S15B). Corresponding differential effects were found when blocking associated inhibitory and excitatory connections (Figure S15C). These effects were observed both at high and low $[Ca^{2+}]_o$. It follows that differential regulation of layers, neurons, and connections plays an important role in controlling the position of the microcircuit along the SA spectrum, independently of $[Ca^{2+}]_o$.

Simulating Thalamic Activation of the Microcircuit

To examine spatio-temporal patterns of evoked activity, we constructed a mesocircuit consisting of a central microcircuit surrounded by six additional microcircuits. Connectivity was established for the mesocircuit as a whole, with no anatomical borders between microcircuits. An algorithm was developed to approximate input from the thalamus to the central microcircuit in such a way as to satisfy experimental constraints. We used data for the number of incoming fibers, bouton density profiles, and the numbers of synapses per connection (to layer 4) for the ventral posteromedial (VPM) thalamic input to the barrel region of somatosensory cortex (Constantinople and Bruno, 2013; Gil et al., 1999; Meyer et al., 2010b). To represent the number of fibers, we instantiated one fiber centered in each minicolumn with a horizontal spread (Meyer et al., 2010b). We then used the layer-by-layer bouton density profiles (Meyer et al., 2010b) (Figure 13A, left), experimental measurements of the mean number of synapses per thalamic connection in layer 4 (Amitai, 2001; Gil et al., 1999), and the multi-synapse principle (see above and Experimental Procedures) to predict the synapses that each thalamic fiber forms onto different m-types (Figure 13A, right). The reconstruction reproduced the number of synapses formed on L4PCs (Figure 13B) (Amitai, 2001; Gil et al., 1999) and predicted, for example, an average of ~12 synapses on L5 pyramidal neurons (Figure 13B), more than for L4PCs. Overall, we predicted that each thalamic fiber innervates 903 ± 66 neurons (mean ± SD; n = 100 fibers; Figure 13C; 775 ± 57 excitatory and 83 ± 11 inhibitory neurons) with an average of 8.1 ± 4.2 synapses/connection. In total, we found that thalamic fibers form ~2 million synapses in the central microcircuit (~1% of synapses across all layers; see Meyer et al., 2010b).

Thalamocortical synaptic transmission was modeled using in vitro data on synaptic dynamics (Figure 13D, left; Amitai, 2001; Gil et al., 1999) and the generalized excitatory-to-excitatory conductances derived above (i.e., similar to L4_EXC, E2 s-type; see Experimental Procedures). Ca^{2+} dependency was modeled as for other excitatory connections. The resulting synaptic transmission was validated by comparing in silico PSPs in L4 and L5 PCs in low-Ca^{2+} conditions against previous in vivo reports (Bruno and Sakmann, 2006; Constantinople and Bruno, 2013; Figure 13E). Distributions of PSPs in L4 and L5 PCs in high-Ca^{2+} conditions were also predicted (Figure 13D, right).
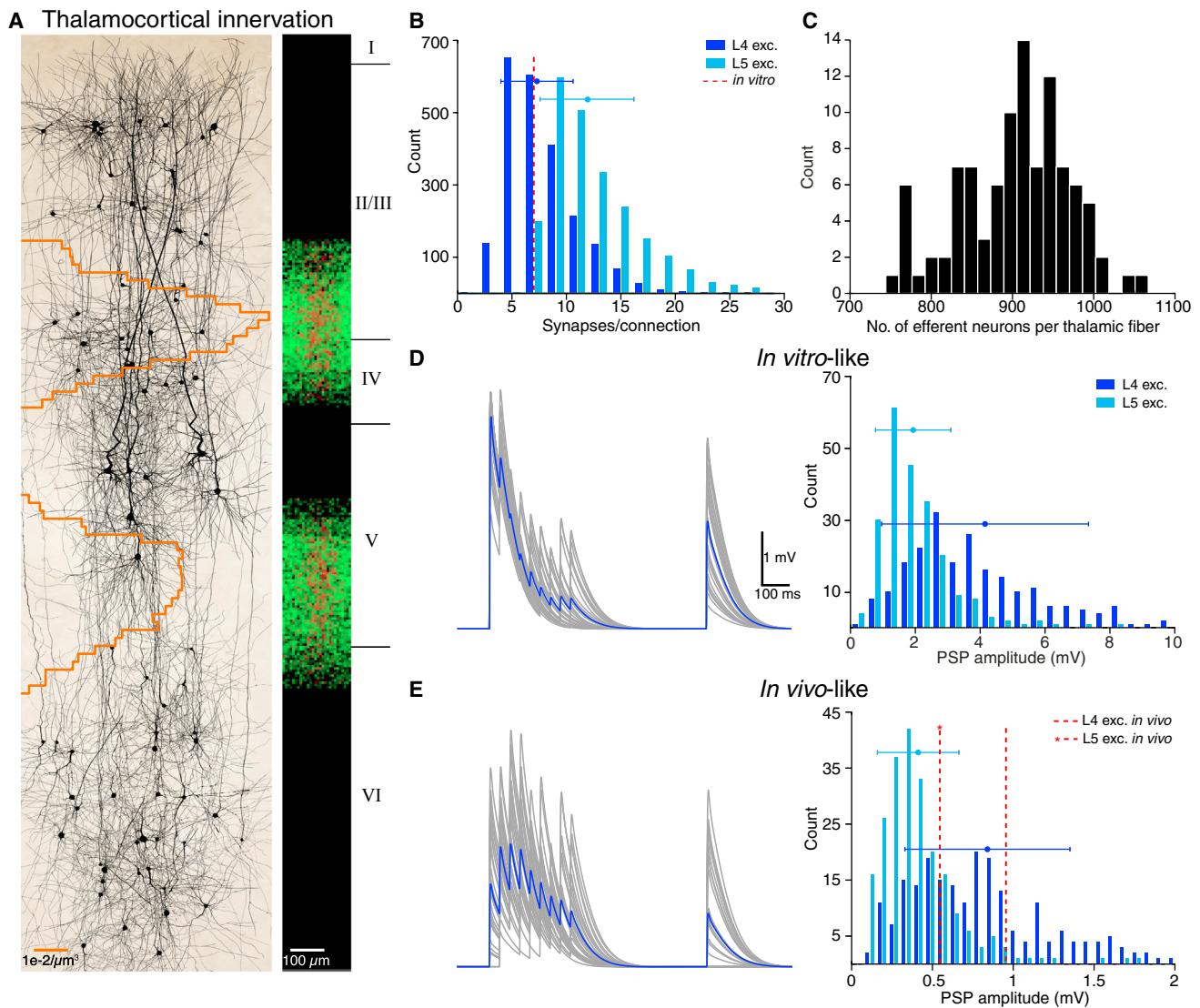
With $[Ca^{2+}]_o$ at 1.25 mM and moderate depolarization (in-vivo-like conditions), the main response to stimulation of thalamic fibers was in L4 to L6 (Figure S16A). Examination of the spiking activity of a random selection of neurons, covering all 55 m-types, showed that most m-types in these layers re-

sponded to the stimulus (Figure S16B). To investigate the effects of a graded stimulus, we used a single synchronous spike to activate a progressively increasing number of fibers innervating the center of the mesocircuit. With $[Ca^{2+}]_o$ at 2.0 mM and zero depolarization (in-vitro-like conditions), activating four or more fibers evoked a stereotypical high-amplitude PSTH response (>80 Hz, Figure 14A), similar to previous in vitro observations (Beierlein et al., 2002). In contrast, stimulation under in-vivo-like conditions produced graded responses, with 20–30 Hz oscillations emerging in the lower layers, particularly in L6, when higher numbers of fibers were stimulated (Figure 14B). While under in-vitro-like conditions, stimulating as few as four thalamic fibers produced all-or-none behavior, indicative of a regenerative state that spread across the whole mesocircuit (Figure 14C), under in-vivo-like conditions, the activity remained localized (Figure 14D).

With increasing Ca^{2+} levels, the stimulus response curves measured during the first 10 ms of thalamic stimulation shifted from a linear to a sharp sigmoidal shape (Figure 14E). Analysis of the velocity of spread revealed a qualitative difference between the synchronous and asynchronous regimes. In the synchronous regime, the spread of activity accelerated over time, while in the asynchronous regime, it was constant until the amplitude of the activity fell to zero (Figure 14F). This suggests that, in the synchronous regime, inhibition cannot act fast enough to curb the excitation and prevent uncontrolled spreading activity. Correlated activity is maximal in the regenerative regime and minimal in the non-regenerative regime (Figure S14), suggesting a dynamic range for correlations to emerge during information processing under in-vivo-like conditions. Taken together, the simulations predict that, at the average $[Ca^{2+}]_o$ reported in the awake state (Jones and Keep, 1988; Massimini and Amzica, 2001; Westerink et al., 1988), the neocortex will exhibit graded and spatially restricted activation, a prerequisite for the emergence of functional maps with high spatial resolution.

At a level of tonic depolarization where the network is spontaneously active in both the regenerative and non-regenerative regimes, we observed a spectrum of oscillations with lower frequencies (~1 Hz) in the regenerative regime and higher frequencies in the non-regenerative regime (~10–20 Hz; data not shown). Maximum power was observed in layers 5–6 in the regenerative regime and in layers 2–3 in the non-regenerative regime (data not shown). This suggests that shifts along the SA spectrum contribute to the spectra of oscillatory frequencies observed in spontaneously active neocortex (see also Tan et al., 2014).

To establish a more complete demarcation between different activity regimes, we performed a series of simulations systematically exploring network state at varying levels of $[Ca^{2+}]_o$ and depolarization. An analysis of average firing rates demarcated the boundary between evoked and spontaneous activity (Figure 15A). The boundary between spontaneous regenerative and non-regenerative regimes was demarcated by the presence or absence of spontaneous bursting activity (Figure 15B). The transition between the evoked regenerative and non-regenerative regimes was determined by an analysis of the amplitude of the response to stimuli at the edge of the mesocircuit (Figure 15C). The combination of these activity maps demarcates four distinct activity regimes: evoked regenerative

Figure 13. Reconstructing Thalamocortical Input

(A) Bouton and synapse profiles. (Left) The distribution of boutons across the depth of the microcircuit (orange line, Meyer et al., 2010b) assuming one afferent fiber from ventral posteromedial (VPM) thalamic nucleus per minicolumn, overlaid on randomly chosen neurons. (Right) The resulting synapses formed (green) with synapses formed by a single fiber (red).

(B) Distribution of the number of synapses per connection formed by the population of thalamic fibers onto L4 and L5 excitatory neurons. L4 distribution is compared against in vitro data (dashed red line; Gil et al., 1999). Horizontal bar: mean ± SD.

(C) Postsynaptic neurons. Distribution of the number of postsynaptic neurons innervated by individual thalamic fibers.

(D) In-vitro-like conditions. (Left) Synaptic dynamics of thalamocortical connections to L4 excitatory cells (gray, 30 trials; blue, average; $[Ca^{2+}]_o = 2.0$ mM). (Right) Distribution of PSP amplitudes of thalamocortical connections to L4 and L5 excitatory cells ($[Ca^{2+}]_o = 2.0$ mM, horizontal bar, mean ± SD).

(E) In vivo-like conditions. (Left) Synaptic dynamics of thalamocortical connections to L4 excitatory cells (gray, 30 trials; blue, average; $[Ca^{2+}]_o = 1.3$ mM). (Right) Distribution of PSP amplitudes of thalamocortical connections to L4 and L5 excitatory cells ($[Ca^{2+}]_o = 1.3$ mM, horizontal bar, mean ± SD). L4 and L5 distributions are compared against in vivo data (L4, dashed red line, left; Bruno and Sakmann, 2006; L5, star dashed red line; Constantinople and Bruno, 2011).
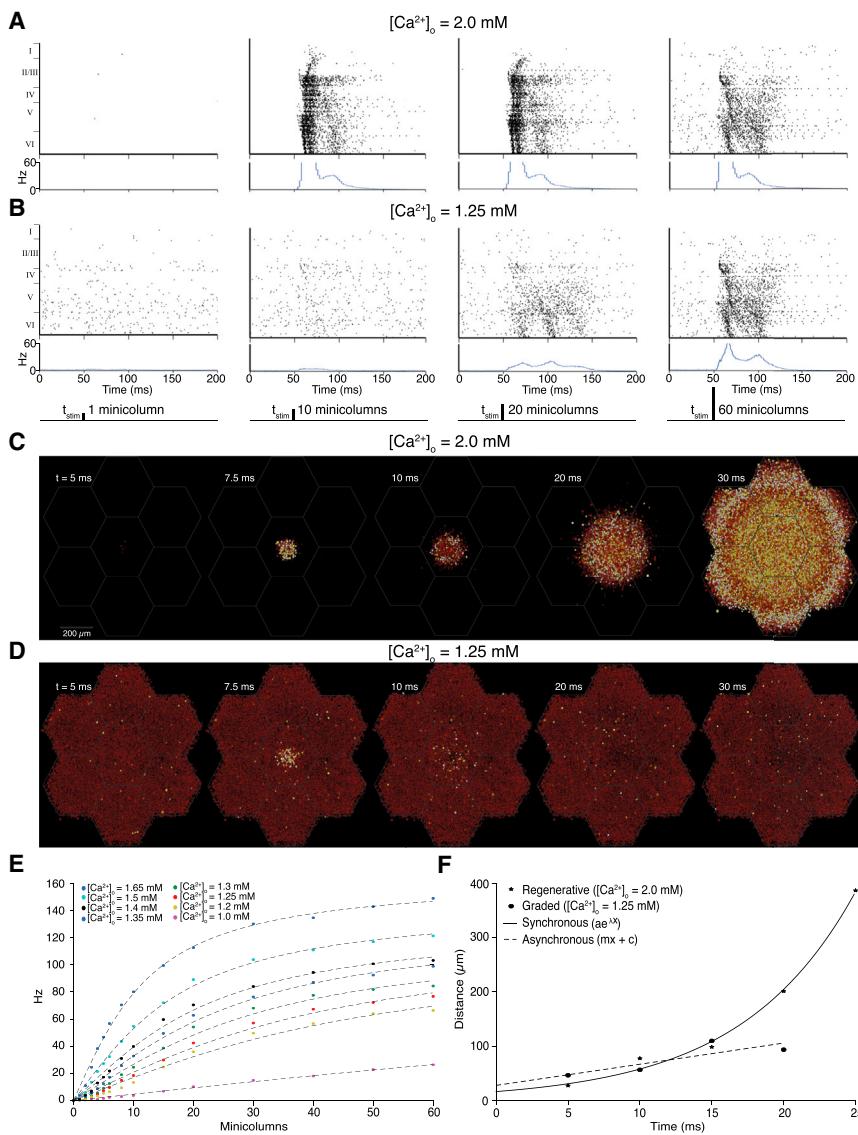
See also Figure S11 for $[Ca^{2+}]_o$ sensitivity of synapse types.

(ER), spontaneous regenerative (SR), evoked non-regenerative (EN), and spontaneous non-regenerative (SN) (Figure 15D).

Reproducibility of Emergent Properties

The reconstructed microcircuitry is based on biological data from a large number of different animals and, in some cases, from different neocortical regions that together provide statistical distributions for layer heights, neuron densities, cellular composition, and morphological and electrophysiological diversity within and across types of neuron and reflect the diversity of synaptic anatomy and physiology observed in biological experiments. The reconstruction process stochastically creates

Figure 14. Activity Evoked by Thalamic Input

(A) In-vitro-like stimulus-dependent evoked activity. Raster plots (top) and PSTHs (bottom) of the response to stimulation of varying number of thalamic fibers under in vitro-like conditions (somatic depolarization to ~60% threshold, $[Ca^{2+}]_o$ = 2.0 mM).

(B) In-vivo-like stimulus-dependent evoked activity. Same as in A for in-vivo-like conditions (somatic depolarization to ~100% threshold, $[Ca^{2+}]_o$ = 1.25 mM). Stimulation times and number of fibers stimulated are shown below.

(C) In-vitro-like activity propagation. A mesocircuit under in vitro-like conditions (no somatic depolarization, $[Ca^{2+}]_o$ = 2.0 mM) stimulated with single synchronous spikes to each of 16 thalamic fibers at the center of the central microcircuit. The mesocircuit at L4 is depicted from above at different times after stimulation. Neuronal somata are rendered with a heat color map indicating level of depolarization.

(D) In-vivo-like activity propagation. Same as in D but under in vivo-like conditions (somatic depolarization to ~100% threshold, $[Ca^{2+}]_o$ = 1.25 mM).

(E) Stimulus response curves for various levels of Ca^{2+} and somatic depolarization to ~85% threshold. Response amplitude determined as the peak response for the central ten minicolumns in the first 10 ms of the response.
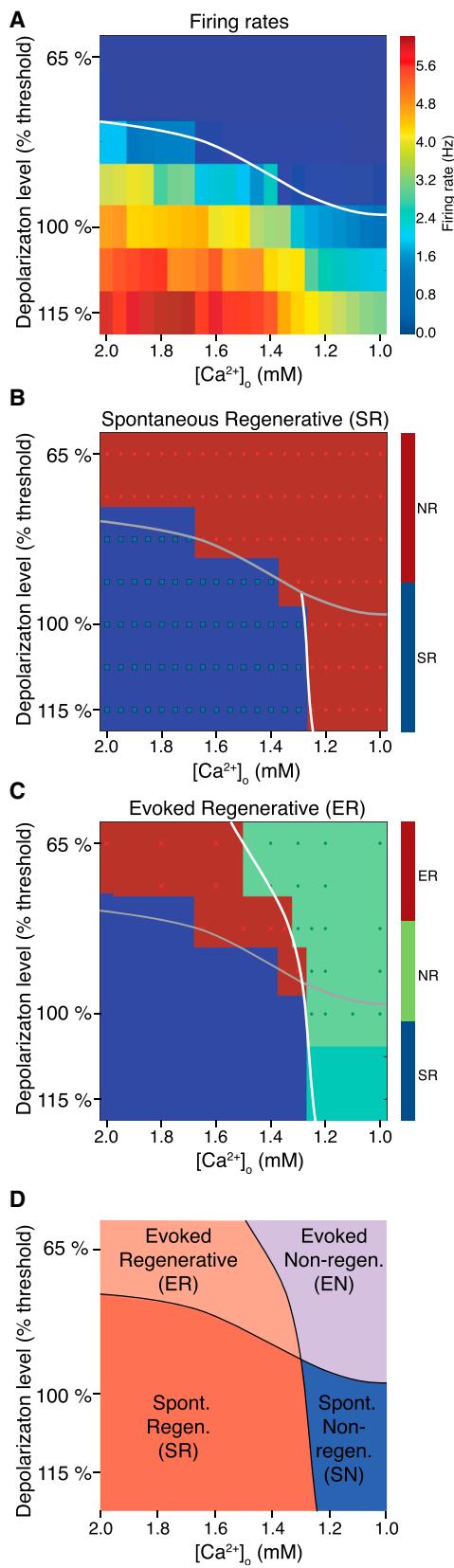
(F) Propagation of the wave front with time in response to thalamic stimulation (at t = 0), measured as the half-maximum of a one-sided Gaussian fit to the wave front. Exponential fit for the regenerative activity and linear fit for non-regenerative activity (conditions as in C and D, respectively). In the non-regenerative regime, the amplitude of the wave front was zero at 25 ms. See also Figure S16 for stimulus responses of individual m-types.

instantiations of the digital microcircuit that respect these distributions. We have previously shown that detailed synaptic physiology is largely invariant across different instantiations of the digital microcircuit (Ramaswamy et al., 2012) and that emergent parameters such as the distributions of the locations of synapses formed by different presynaptic neurons are also largely invariant (Hill et al., 2012).

To further assess the reproducibility of the reconstruction as a whole, we measured the variance of a range of its emergent anatomical and physiological properties (i.e., properties not directly specified by the data). The anatomical properties measured from seven instantiations of each microcircuit (seven instantiations of BioM and seven each for Bio1–Bio5) included total number of appositions and synapses, convergence and divergence of connectivity for each m-type, numbers of excitatory and inhibitory synapses and connections, mean numbers and types of presynaptic neurons innervating neurons belonging

to different m-types, and numbers of intra-and inter-laminar synapses and connections. In each case, we found low variance compared to the mean (see Figure S17 for a sample; see Table S1 for selected values; see also NMC Portal).

To gain a deeper understanding of the physiological variability of the digital reconstruction, we examined trial-to-trial variability in the spiking activity of individual neurons and variability across neurons of the same type, as well as variability across layers and across digital reconstructions individualized with data from five different animals (Bio1–Bio5). Cell responses to a single thalamic stimulation, roughly comparable to a single whisker deflection (stimulation of a cluster of 60 minicolumns), displayed varying degrees of trial-to-trial variability (Figure 16A). Since the digital reconstruction implements biologically grounded stochastic mechanisms for synaptic transmission, spontaneous release, and some ion channels, this was expected. However, each cell-type also displayed a characteristic delay to first spike response. In some cases, the distribution of single-neuron responses was similar to that of the population (Figure 16B, left),

Figure 15. The Regime Map

Characterization of spontaneous and evoked activity under different levels of depolarization and $[Ca^{2+}]_o$.

(A) Average spontaneous firing rates. White line indicates interpolated transition between evoked and spontaneous regimes.

(B) Presence of spontaneous bursting activity. White line indicates transition between spontaneous regenerative (SR) and non-regenerative (NR) activity.

(C) Map of evoked regenerative (ER) and non-regenerative activity determined by the amplitude of the response to stimuli at the edge of the mesocircuit in relation to the initial response at the center. White line indicates the transition between the ER and NR regimes. Blue-green region is extrapolated to be NR.

(D) Schematic map of showing the four activity regimes. Evoked regenerative, ER; spontaneous regenerative, SR; evoked non-regenerative, EN; spontaneous non-regenerative, SN.
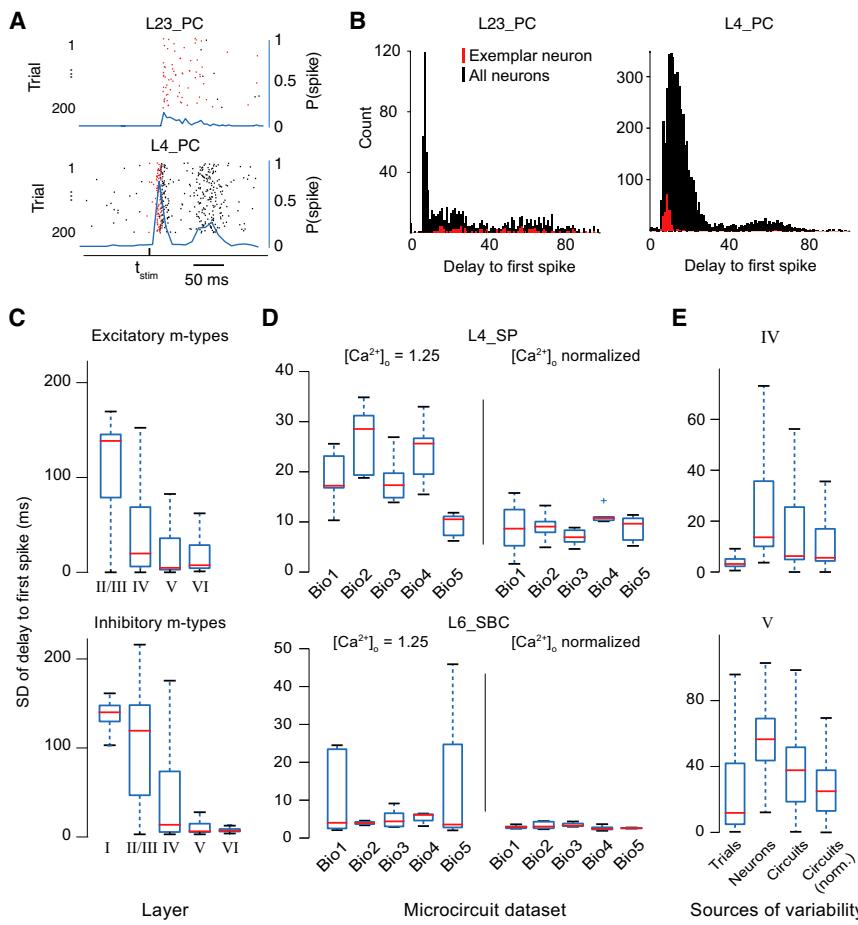
while in others it was markedly different (Figure 16B, right). For both excitatory and inhibitory neurons, variance in response times decreased with cortical depth (Figure 16C). In all layers, trial-to-trial variability was lower than the variability between individual neurons of the same type in single trials.

Responses from neurons of the same m-type, in digital reconstructions based on data from individual animals (Bio1–Bio5), displayed higher variability across reconstructions than in different instantiations of the average microcircuit (BioM) (for an example, see Figure 16D, left). To isolate the source of this inter-individual variability, we began by re-examining the SA spectra for the reconstructions at different levels of Ca^{2+}. We found that they all displayed the spectrum but that the precise level of Ca^{2+} at the transition between the synchronous and asynchronous state was slightly different for each reconstruction, ranging from 1.23 to 1.31 mM $[Ca^{2+}]_o$ (Figure S13). We therefore repeated the simulations, setting the Ca^{2+} level such that each reconstruction was shifted to the same point along the spectrum relative to the transition. Under these normalized conditions, the variance in the responses of specific m-types across reconstructions decreased strikingly (Figure 16D, right). Figure 16E summarizes the different sources of variability for all neurons in L4 and L5.

Taken together, these results demonstrate the ability of the digital reconstruction to accommodate physiological variability while maintaining reproducibility and are evidence of its potential to generate useful biological insights. To further test this potential, we attempted to replicate results from an array of recent in vivo studies.

Reproducing In Vivo Findings

The digital reconstructions described above aimed to recreate the anatomy and physiology of an isolated slice of neocortical tissue, but not specifically to replicate any particular in vivo experiment. Nonetheless, we tested the ability of the digital reconstruction to replicate such experiments. We selected a set of recent in vivo studies in which a reasonable replication of the stimulation and analysis protocols was technically feasible. We then selected an arbitrary instantiation of BioM and used this model for all tests. In each case, we maintained the model's original parameters, without introducing modifications to fit previously reported results—a "zero tweak" strategy. All simulations were performed near the transition from the synchronous to the asynchronous state.

Figure 16. Reliability of Microcircuit Responses

(A) Raster plot of the spiking activity of an exemplary L23PC (top) and an exemplary L4PC (bottom) in response to simulated thalamocortical stimulation with 60 fibers. The first spike after the stimulus in each of 200 trials is indicated in red, other spikes in black. The blue line indicates the probability that the neuron fires a spike in a 5 ms bin.

(B) Histograms of the response delay (delay of the first spike after stimulus presentation) for L23PCs (left) and L4PCs (right). (Black) For 200 trials of 25 randomly chosen neurons of the indicated type. (Red) For 200 trials of the neurons indicated in A.

(C) Standard deviation of the response delay of neurons in different layers across trials. Red line indicates the median of neurons, blue boxes the 25th and 75th percentiles, and whiskers the full data spread. (Top) Excitatory neurons; (bottom) inhibitory neurons.

(D) Standard deviation of the response delay across trials of neurons when placed in microcircuits constructed from different biological datasets (Bio1–Bio5). (Top) Of five L4SPs. (Bottom) Of five L6SBCs. (Left) Under simulated extracellular Ca^{2+} concentration of 1.25 mM. (Right) When the calcium concentration was set to a value on the border between regenerative and non-regenerative activity for that particular microcircuit. Boxes and whiskers as in C.

(E) Comparison of the different sources of variability. (Left to right) Inter-trial variability (same neuron in same microcircuit across trials); neuronal variability (same trial in same microcircuit across neurons of a given m-type); inter-circuit variability (same neuron in different microcircuit); inter-circuit variability under normalized Ca^{2+} concentrations. (Top) In layer IV; (bottom) in layer V. Boxes and whiskers as in C.

See also Figure S17 for the anatomical variability of microcircuits.
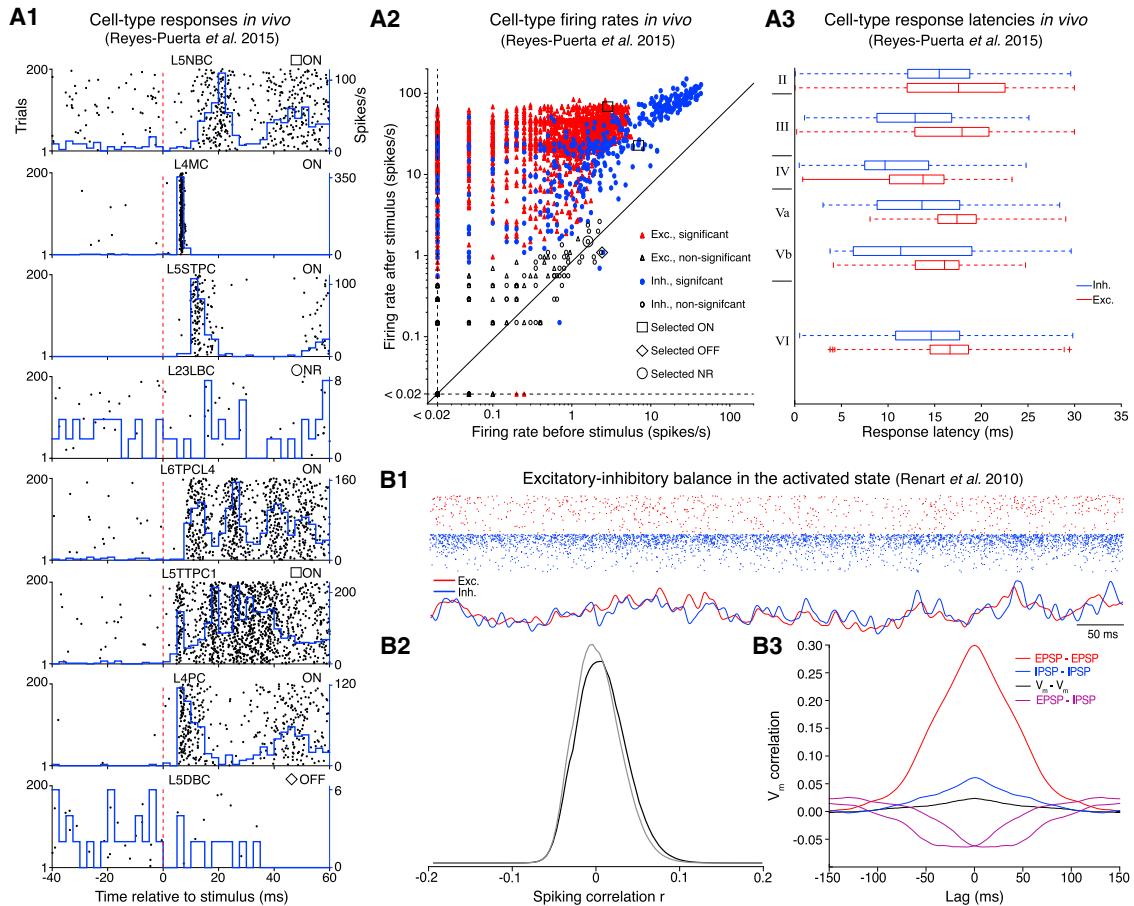
Neuronal Responses to Single-Whisker Deflection

Many in vivo studies of evoked neuronal activity have reported that basal activity is sparse in all cell types, that the response characteristics of individually recorded neurons display cell-type-specific diversity, and that response latencies are cell type and layer specific (Constantinople and Bruno, 2013; Reyes-Puerta et al., 2015). To test the ability of the reconstruction to reproduce these findings, we attempted to replicate some of the experiments reported in a recent study by Reyes-Puerta et al. (2015), in which the authors recorded and analyzed neuronal responses to a single-whisker deflection in the barrel cortex of anaesthetized adult rats. We approximated the stimulus as a single pulse in 60 reconstructed thalamic fibers projecting to the center of the digital microcircuit. As shown in Figure 17A1, the response to the stimulation displays cell-type-specific diversity that compares reasonably well with the results reported in Figure 3A of the Reyes-Puerta et al. study (Reyes-Puerta et al., 2015), with the exception of the OFF response, which is not as prominent. The general distribution of responses for excitatory and inhibitory cells is also comparable (Figure 17A2 in silico versus Figure 3B in vivo), though again with fewer OFF

responses. As in Reyes-Puerta et al. (Reyes-Puerta et al., 2015), most responses occurred within 10–20 ms of the stimulus and were generally led by inhibitory cells and, more specifically, by inhibitory cells in L4 and L5 (Figure 17A3 in silico versus Figure 4B1 in vivo).

Anti-correlated Inhibitory Activity Cancels Out Highly Correlated Excitatory Activity

Many previous studies have struggled to explain the uncorrelated neuronal spiking activity that is often observed in vivo (Celikel et al., 2004; Mazurek and Shadlen, 2002), with some suggesting that it is the result of poorly correlated excitatory activity (as expected if excitatory neurons generate a rate code), while others argue that correlations in excitatory activity are cancelled out by anti-correlated inhibition (Beierlein et al., 2000; Okun and Lampl, 2008). A model developed to address this issue by Renart et al. (2010) shows that it is indeed theoretically feasible for anti-correlated inhibitory activity to cancel out highly correlated excitatory activity (see their Figure 3). To test this hypothesis, we therefore analyzed whether this phenomenon was evident during spontaneous activity in the digital reconstruction. Although the digital reconstruction was not specifically

Figure 17. Cell-Type Responses In Vivo and E-I Balance

(A1) Cellular response types to simulated single-whisker deflection. Each subplot represents the activity of an individual cell, containing the raster plot aligned to simulated whisker deflection and the PSTH. Upon simulated whisker deflection, neurons increased their firing rate (ON cells), showed no change in firing rate (NR cells), or decreased their firing rate (OFF cells). (A2) Comparison of mean firing rates before and after whisker deflection plotted in logarithmic scale (2630 excitatory and 550 inhibitory neurons). Empty symbols represent neurons showing no significantly different activity in both periods (NR cells), and filled symbols represent neurons showing significantly different ($p < 0.05$) activity (ON and OFF cells). (A3) Mean first-spike latencies of inhibitory (INH) and excitatory (EXC) neurons to simulated whisker deflection, defined by first spike occurrence within 30 ms after stimulation, mean over 200 trials, for all 31,346 neurons in the stimulated column. Each box plot represents median, interquartile, and range of latencies; crosses represent outliers (2.5 times interquartile range).

(B1) Raster (top) of the spontaneous spiking activity of 500 excitatory (red) and inhibitory (blue) neurons under in-vivo-like conditions (100% depolarization and $[Ca^{2+}]_o = 1.25$ mM). Bottom curves show tracking of instantaneous population-averaged activities (transformed to z-scores, bin size 3 ms). Average firing rates of E and I cells were 1.09 ± 1.0 Hz and 6.00 ± 8.95 Hz, respectively (n = 1,000; mean ± SD). (B2) Histogram of spike-spike correlations (black, count window 50 ms) and of jittered spike trains (gray, jitter ± 500 ms). (B3) Population-averaged cross-correlograms of the somatic membrane current, when cells are held at the reversal potential of inhibition (blue) or of excitation (red) in both cells, or at one potential for one cell and at the other potential for the other cell (magenta). The black curve is for pairs at resting potential.

See also Figure S18 for details of E-I balance.
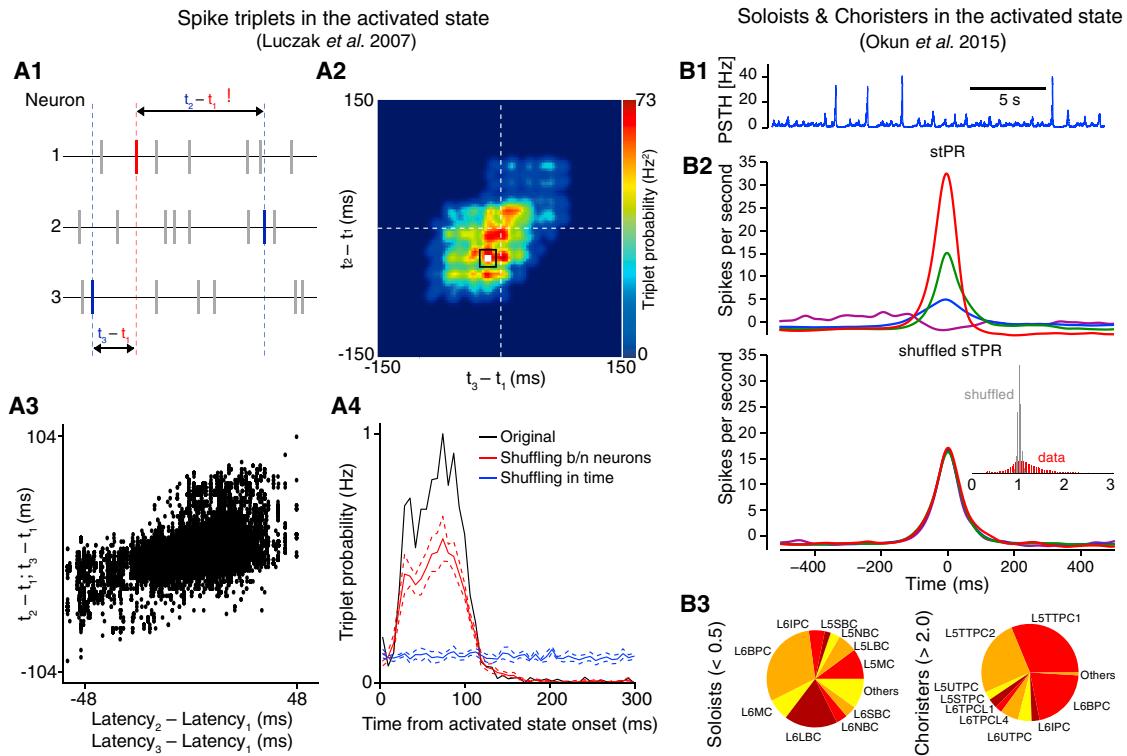
designed to produce this phenomenon, it nonetheless generated excitatory conductances in single neurons that were highly correlated but effectively cancelled out by anti-correlated inhibitory conductances (Figure 17B).

Deeper investigation revealed that spiking is correlated with momentary imbalances between excitatory and inhibitory conductances lasting <10 ms and that the timing of spikes can be predicted from the difference in the E and I conductances (Figure 17B). We also found that the precision with which these imbalances drive spiking falls dramatically as the network state shifts away from the transition in either direction. When it shifts toward the synchronous state, the correlation is strong but broad, resulting in a temporally imprecise increase in spiking more suitable for a rate code. When it shifts toward the asynchronous regime, the correlation is sharp but too weak to effectively drive spiking, a regime more suitable for a population code based on a high degree of correlated activity (Figure S18).

Temporally Sequential Structure during Spontaneous Activity of L5 Neurons

The search for precise temporal structures in brain activity, such as synfire chains, motifs, repeated spike patterns, etc., has a

Spike triplets in the activated state
(Luczak *et al.* 2007)

A1

A2

A3

A4

Soloists & Choristers in the activated state
(Okun *et al.* 2015)

B1

B2

B3

Figure 18. Triplet Structure and Diverse Population Coupling

Precisely repeating triplet structures can be predicted from individual neural latencies under synchronous stimulation (20 thalamic fibers, $[Ca^{2+}]_o = 1.25$ mM; cf. Luczak et al., 2007, Figure 5).

(A1) Schematic depicting the structure of a spike triplet for a triad of neurons. (A2) Count matrix for a representative neuron triad. Black box indicates region containing precisely repeating triplets. White square signifies mode. (A3) Correlation between neural latency differences and triplet structures. (A4) Precisely repeating triplet probability peaks shortly after onset of activated state. This peak is significant when compared with two null hypotheses (independent Poisson model, blue curve; common excitability model, red curve). Dashed lines show standard deviation.

(B1) Time course of population firing rate just below the transition to the synchronous regime (microcircuit "Bio5," $[Ca^{2+}]_o = 1.27$ mM). (B2) (Top) Spike-triggered average of population activity (stPR) for four representative neurons in layers V and VI. (Bottom) Same as above but after shuffling (see Okun et al., 2015; cf. Figures 1E and 1G). (Inset) Distribution of the population-coupling coefficient before and after shuffling (see Okun et al., 2015). (B3) Relative fractions of m-types of soloists (population coupling < 0.5) and choristers (> 2.0).

See also Figure S19 for results under lower $[Ca^{2+}]_o$.

long history. These patterns are thought to reflect "stereotypical organized sequential spread of activation through local cortical networks," as demonstrated recently (Luczak et al., 2007). Luczak et al. (2007) found a temporally sequential structure during spontaneous activity of L5 neurons in vivo in the somatosensory cortex (Luczak et al., 2007). In particular, they found that, after the onset of an UP state, trios of neurons generated spike motifs (triplets) with a precisely defined temporal relationship between spikes that could not be explained by random correlations during high-frequency spiking (see their Figure 5). A similar analysis of the evoked response to thalamic stimulation of L5 neurons in the digital reconstruction found the same repeating triplet structures as observed in vivo (Figure 18A). A second in silico experiment further into the asynchronous regime (i.e., at lower Ca²⁺ levels; 1.0 mM) showed no evidence of triplet structures (Figures S19A–S19C), supporting our prediction that, in the highly asynchronous regime, it is difficult for single neurons to track fine temporal structure in network activity unless the population of

presynaptic neurons becomes highly synchronized, for example, by external input.

Soloists versus Choristers

A recent study showed that some neurons in a network display spiking activity that is tightly correlated with the average activity of the population of neurons in the network (choristers), while others display a diversity of spiking patterns whose correlation with that of the population is smaller than expected by chance (soloists), suggesting that they actively avoid correlating with the rest of the population (Okun et al., 2015). We simulated the spontaneous activity of a single microcircuit in the asynchronous state but close to the transition to synchronous state for 800 s (Figure 18B1; see also Figure S19D) and analyzed the spiking activity of every individual neuron in L5 and L6 with respect to the spiking of all others. Replication of the analysis in Okun et al. (2015) yielded comparable results, although the proportion of choristers appears to be somewhat higher in the digital reconstruction (Figure 18B2 in silico versus Figures 1E and 1G in vivo).

We found that soloists are predominantly interneurons, while choristers are mainly pyramidal neurons (Figure 18B3). Pyramidal cells can be found on both extremes; they tend to be soloists when their spontaneous firing rate is high, the ratio of excitatory to inhibitory synaptic innervation is high, and most of the innervating synapses are close to their somata (data not shown).

Shifting the network further into the synchronous regime leads to an increase in the number of choristers, consistent with general recruitment of all neurons and a rate-based response. On the other hand, shifting the network further into the asynchronous regime results in a loss of both choristers and soloists during spontaneous activity (data not shown). This finding supports our prediction that, when the network is far into the asynchronous regime, single neurons cannot easily sense and respond to fine temporal structure in network activity.

Functional Implications

These replications of in vivo studies suggest that the digital reconstruction can yield physiologically relevant insights. We therefore went on to address two issues that it has not been possible to address experimentally, either in vitro or in vivo.

In a first experiment, we investigated the ability of single L5 pyramidal neurons to discriminate between spatially segregated inputs. As previously, we used stimuli that approximated a whisker deflection (Figure 19A). To measure how far apart the stimuli needed to be for single neurons of the microcircuit to discriminate between them, we progressively increased the spatial separation between the stimuli and measured the response of L5 pyramidal cells in terms of rate (represented by the number of spikes emitted) and timing (represented by the latency to first response). Analysis of the difference between responses yielded a measure of latency- and rate-based discrimination. Figure 19B1 shows the responses of a single, arbitrarily selected neuron to stimuli applied at locations separated by 150 μm. In this case, latency- and rate-based discrimination are both significant (Figures 19B2 and 19B3). Exploration of the discriminatory power of L5 pyramidal neurons with different separations between the stimuli and at different levels of Ca^{2+} (Figures 19C1 and 19D1) showed that many neurons discriminate between inputs separated by 150 μm or more and that a few can discriminate between stimuli with separations as small as 50 μm (i.e., approximately two minicolumns apart). In general, timing-based discrimination is much stronger than rate-based discrimination (Figures 19C2 and 19D2). Interestingly, at all separations, discrimination is strongest at Ca^{2+} levels close to the transition between the synchronous and asynchronous regimes (Figure 19D).
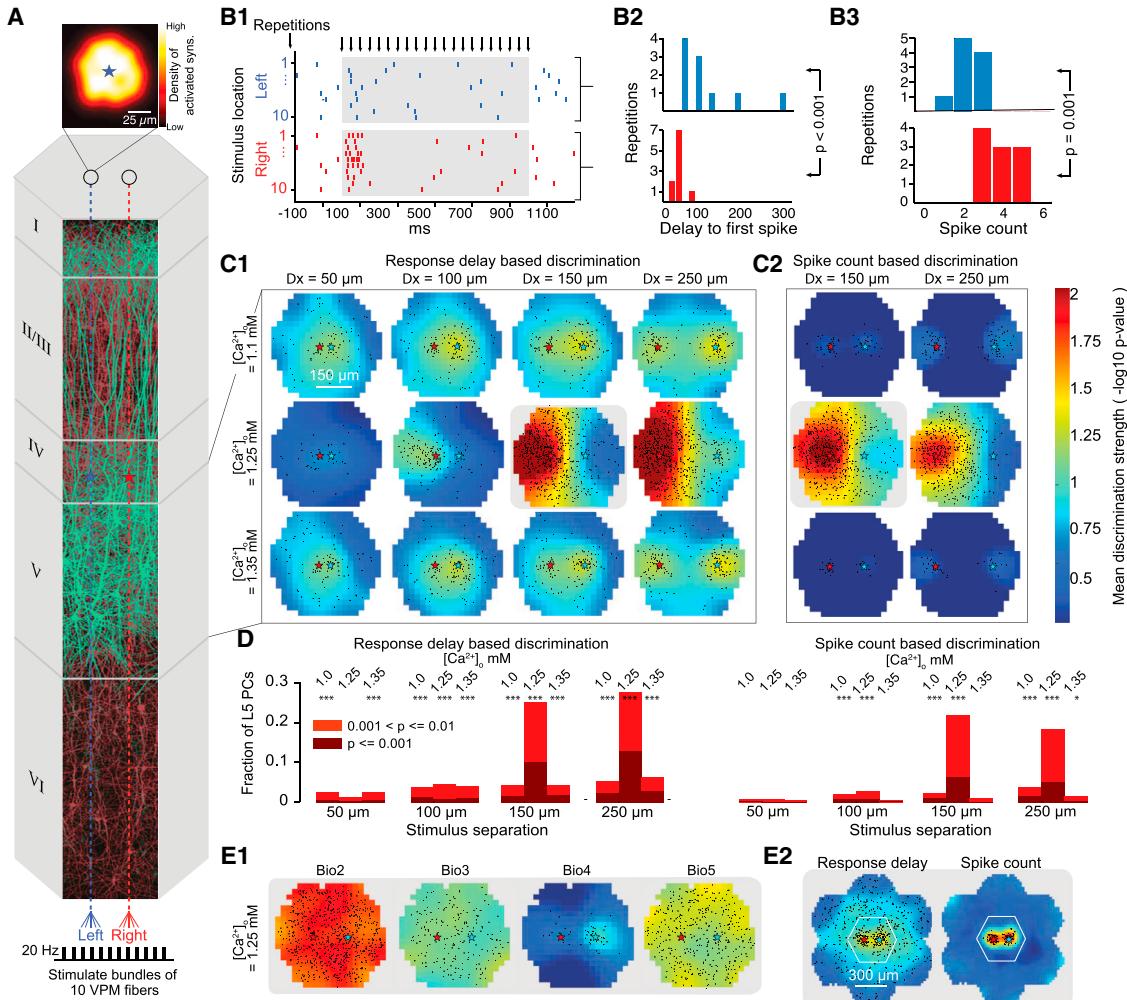
Unexpectedly, we noticed a spatial asymmetry in the discriminatory power of the neurons (Figures 19C1 and 19C2, shaded background). To test the reproducibility of the phenomenon, we repeated the simulation using instantiations of Bio1–Bio5 that we already knew to be highly variable (see Figure S17 and Table S1). All reconstructions showed asymmetry, but the specific degree and pattern of asymmetry was different in each case (Figure 19E1, four instantiations shown). We therefore hypothesized that the asymmetry reflects local variations in connectivity arising from the statistical instantiation of the digital microcircuit, amplified by edge effects. To test this hypothesis,

we repeated the discrimination experiment with a mesocircuit constructed as previously described ([Ca^{2+}]$_o$ 1.25 mM, separation 150 μm, see shaded background in Figures 19C1 and 19C2), taking the same microcircuit used in the previous experiment (Figures 19C1 and 19C2) as its central microcircuit (Figure 19E2, white hexagon). Under these conditions, the asymmetry was markedly reduced. We also found strong variation in overall discrimination power across the different instantiations (Figure 19E1).

In the final series of simulations, we explored the relationship between the size of the network and its emergent properties, the emergence of the transition between the synchronous and asynchronous states, and the emergence of spontaneous spatio-temporal patterns for different sized networks (10–1,000 minicolumns). In reconstructions smaller than the anatomically defined microcircuit, the transition occurred at high levels of Ca^{2+} and fell sharply with increasing size of the reconstruction, reaching a plateau in reconstructions larger than ~300 minicolumns (i.e., the size of the anatomically defined microcircuit; Figures 20A and 20B). Even in reconstructions as large as 1,000 minicolumns, the spectrum of states did not exhibit any further qualitative change (Figure 20B). Figures 20C and 20D show the emergence of spontaneous clustered activity as the network increases in size. We found that, in smaller reconstructions, the time course of spontaneous firing rates in different clusters of ~10 minicolumns was very similar and became progressively dissimilar as the reconstructions increased in size (Figure 20D). The between-cluster correlation coefficient decreased exponentially with increasing distance between clusters, also plateauing at distances comparable to the diameter of the anatomically defined microcircuit (~202 μm; Figure 20E). As a related measure, we also examined the trend in correlated activity within a central set of ~50 minicolumns as the surrounding network increased in size. We found that, in larger networks, the correlation fell exponentially, bottoming out in microcircuits of ~300 minicolumns and larger (r = ~0.4; Figure 20F).

DISCUSSION

This paper presents a first-draft digital reconstruction of neocortical microcircuitry that integrates experimental measurements of neuronal morphologies, layer heights, neuronal densities, ratios of excitatory to inhibitory neurons, morphological and electro-morphological composition, and electrophysiology, as well as synaptic anatomy and physiology (see "Reconstruction Data" and Table S3). It has been validated against a spectrum of separate anatomical and physiological measurements not used in the reconstruction (see "Validation Data" and Table S3). The reconstruction provides predictions of a wide range of anatomical and physiological properties of the neocortical microcircuitry (Box 1). Simulation of the reconstruction shows a spectrum of emergent network activity states with a sharp transition from synchronous to asynchronous states. At this particular point along the spectrum, digital reconstructions reproduce a number of findings from in vivo studies, allowing deeper investigation of their underlying cellular and synaptic mechanisms. They also enable experiments that have not so far been possible either in vitro or in vivo. Investigation of the

Figure 19. Spatial Resolution

(A) The ability of L5PCs in the microcircuit to discriminate between inputs given by bundles of ten thalamic fibers was examined. The stimuli were centered on locations offset from the center of the circuit to the left or right. (Top) Spatial extent of the synapses activated by ten thalamic fibers in the microcircuit.

(B1) Raster plot of spiking activity of a neuron in response to ten repetitions of spatially constrained stimuli at different locations (1 s of pulses at 20 Hz). Black arrows on top indicate individual pulses. (B2) Histogram of the delay to the first spike after the start of stimulus presentation of the neurons in B1. The difference in delay is statistically significant ($p < 0.001$, Wilcoxon rank sum test). (B3) Histogram of the number of spikes during stimulus presentation (gray window in B1). Differences in spike counts were statistically significant.

(C1) Mean discrimination strength. $-\log10$ of the p value as in B2 of L5PCs at different locations is indicated as color coded. Red and blue stars indicate the centers of the two stimuli to discriminate. Black dots indicate locations of individual L5PCs with a discrimination strength >2 ($p < 0.01$). Each row indicates a different extracellular Ca^{2+} concentration. (C2) Same, for the discrimination power based on spike count as in B3.

(D) Fraction of L5PCs with a discrimination power >2 (light red) and >3 (dark red) for different conditions shown in C. Asterisks indicate instances in which the number of neurons with separation strength >2 is larger than can be explained as false positives (*p < 0.05; ***p < 0.001).
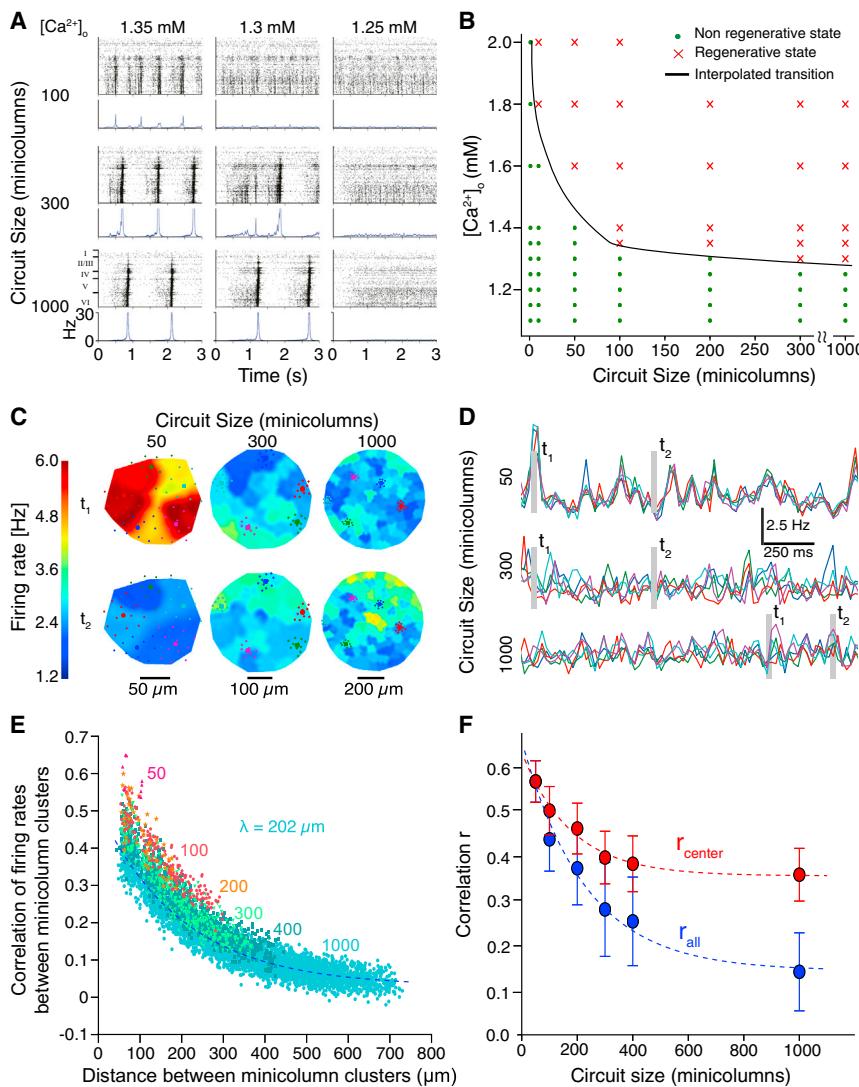
(E1) Discrimination power for a stimulus separation of 150 μm at 1.25 mM $[Ca^{2+}]_o$ for four microcircuits based on biological datasets Bio2–Bio5. (E2) Discrimination based on response delay and spike count when the same microcircuit was embedded in six surrounding microcircuits.

size of network required to reproduce key functional properties of the microcircuit shows that it is roughly equivalent to the volume of neocortical tissue used as the basis for the reconstruction. This is evidence that a network of this size is the minimum functional unit required for neocortical information processing.

Validity of the Digital Reconstruction

The reconstruction certainly includes errors due to mistakes and gaps in experimental datasets and incomplete understanding of biological principles. For instance, additional cell type markers would improve the accuracy of the morphological composition, saturated EM reconstructions could be used to further validate the derived connectivity, more experiments reporting combined voltage and current measurements for synaptic responses will strengthen conclusions on quantal conductances and connection-specific synaptic dynamics, and further characterization of the sensitivity of different synapses to $[Ca^{2+}]_o$ may allow more accurate demarcation of the transitions between different

(A) Transition between regenerative and non-regenerative regimes as a function of circuit size and calcium concentration. Panels of raster plots (top) and PSTHs (bottom) of spontaneous activity are shown for a selection of circuit sizes and calcium concentrations (100% depolarization).

(B) Overview of a broad range of circuit sizes and calcium concentrations as in A. Red crosses and green dots indicate regenerative and non-regenerative circuit behavior, respectively, as assessed by visual inspection. Black curve depicts interpolated transition between regenerative and non-regenerative regimes.

(C) Spatial profile of instantaneous firing rates for circuits of increasing size. Mean instantaneous firing rates were estimated for contiguous groupings (clusters) of approximately ten minicolumns using a K-means algorithm. Six spatial firing rate profiles are shown, generated by interpolating these rate estimates (see Experimental Procedures) at two selected times for three circuit sizes. Colored circles show five exemplary cluster centers.

(D) Time traces of firing rates for selected clusters. Firing rate time courses are shown for the clusters in C in corresponding color for all three circuit sizes. Dashed boxes indicate the times, t_1 and t_2, at which spatial profiles are compared in C.

(E) Pairwise cross-correlation coefficients of cluster firing rate time courses for all cluster combinations versus inter-cluster separation for varying circuit sizes (50 to 1,000 minicolumns). Pair-wise correlation decays exponentially with distance (blue dashed line shows exponential fit to 1,000 minicolumn circuit dataset, space constant $\lambda = 202\ \mu m$).

(F) Mean pairwise cluster correlation coefficients versus circuit size for each circuit's centermost five clusters (red circles) and for all clusters (blue circles). Error bars indicate SD. Dashed curves indicate exponential fits to respective data.

activity states and may allow a more precise determination of the role played by each neuron and synapse type in maintaining and shifting regimes. For example, a recent EM study found evidence for a higher number of synapses per connection than predicted by a naive interpretation of Peters' rule (Kasthuri et al., 2015). Applying the same analysis to the digital reconstruction produced comparable findings (Figure S20 in silico versus Figures 7D, 7F, and S6B in Kasthuri et al., 2015). These properties emerge in the digital reconstruction as a consequence of preferential pruning of connections with low numbers of synapses (Reimann et al., 2015).

The validation tests conducted at multiple stages of the reconstruction process reduce the risk that errors could lead to major inaccuracies in the reconstruction or in simulations of its emergent behavior. For example, validation of electrical neuron models against independent data insulates the emergent behavior of the network from the impact of our limited knowledge of ion channel kinetics and distributions. More generally, the reconstruction passed multiple tests broadly validating

its underlying anatomy and physiology. For instance, major errors in cell morphology, densities, composition, and connectivity would make it difficult to reproduce the types of neuronal assemblies discovered in 12-patch experiments, the numbers of GABAergic synapses on pyramidal somata, protein staining patterns, layer-wise synapse densities, connection probabilities, bouton densities, and distributions, etc. (see Table S3). These properties lie well within experimentally reported ranges. The reproducibility of observations and predictions in multiple reconstructions using data from different animals and incorporating statistical variations provide evidence that they are robust.

Although the reconstruction is, to our knowledge, the most detailed to date, it omits many important details of microcircuit structure and function, such as gap junctions, receptors, glia, vasculature, neuromodulation, plasticity, and homeostasis. Furthermore, it represents a snapshot of just one brain region, in one strain of male rat, at a young age. This limits the generality of the conclusions that can be drawn. For instance, in

---

Box 1. Microcircuit Predictions

1. The cellular composition of the microcircuit
2. Total lengths of dendrites and local axons
3. Increase in neuronal diversity with cortical depth
4. Total number of appositions and synapses
5. Total number of connections and connection types
6. Number of connections and synapses per connection between different neuron types
7. Number of connections and synapses formed by incoming fibers
8. Increase in the E-I neuronal fraction with cortical depth
9. All input and output synapses for all neuron types
10. Quantal synaptic conductances for all intrinsic synapses
11. Total excitatory and inhibitory conductances for all neuron types
12. Number and combination of pre- and postsynaptic neurons for all neuron types
13. Detailed synaptic physiology for connections between all neuron pairs
14. E-I ratios within and across layers
15. A spectrum of network states ranging from synchronous to asynchronous activity
16. Extracellular calcium regulates the network state through differential effects on synaptic dynamics
17. Role of layers, neuron, and connection types in modulating network states
18. The in vivo phenomena examined only emerge near the transition between synchronous and asynchronous states

---

animals of the age used for the study, dendritic morphologies have already matured to adult levels (Larkman, 1991a; Romand et al., 2011), but the ascending axons may not be fully represented and are certainly not completely mature (Romand et al., 2011). However, studies at a greater level of biological detail (e.g., including glia, receptors, and signaling pathways) and investigations of different brain regions in animals of different ages, gender, and species, as well as in disease models can use the reconstruction as a reference point. Findings consistent with the reconstruction would indicate the sufficiency of the principles of organization used in the reconstruction process; discrepancies may point to new principles. For example, if application of the connectivity algorithm to another brain region or to animals at a different age or belonging to a different species failed to yield results consistent with experimental findings, this would point to specific variations in the connectivity rules.

Failure in validation could also indicate errors in experimental data. For instance, the reconstruction indicated that cell densities from a dozen previous studies were all too low to account for spine and synapse densities, suggesting new experiments, which verified this prediction. The reconstruction also revealed that many experiments underestimate synaptic conductances and suggests that in vitro experiments that do not account for calcium level in the bath may misinterpret the relevance of their findings for in vivo conditions. These examples illustrate how the reconstruction process does not take experimental data at face value but uses complementary, related datasets to constrain the use as parameters, wherever possible.

Functional Implications

Simulations of the spontaneous and evoked activity that accounted for the differential sensitivity to Ca^{2+} of different types of synapses and that explored changes in Ca^{2+} levels revealed a spectrum of activity states ranging from synchronous to asynchronous behavior. Varying the Ca^{2+} level profoundly changes the overall E-I balance and hence the position of the network along the spectrum, leading to a sharp transition between activity regimes. These in silico predictions were verified by new in vitro experiments.

Further simulations showed that the level of Ca^{2+}, where the transition occurred, varies across digital reconstructions that use data from different animals and that this accounts for a significant proportion of the variance in neuronal spiking and the spatial resolution of the network. We also found that a small adjustment in Ca^{2+} levels ($\sim$0.05 mM) in individual reconstructions significantly reduces their physiological variability. These simulations provide an example of how variations in individual neuroanatomy may lead to functional differences.

Inspired by this finding, we performed further simulations, which demonstrated that activating or inhibiting specific layers, neurons, and synaptic connections also shifts the network along the spectrum. While it is well known from previous theoretical findings that changing E-I balance changes the state of the network (Brunel, 2000; van Vreeswijk and Sompolinsky, 1996), the simulations further suggest that any mechanism that differentially changes the synaptic dynamics of different types of synapses (e.g., through neuromodulation; for reviews, see Lee and Dan, 2012; Zagha and McCormick, 2014) could alter the boundaries between activity regimes in complex ways. We speculate that other emergent properties, such as UP and DOWN states with two meta-stable fixed points, as observed in vivo (Steriade et al., 1993), which are not reproduced by the digital reconstruction, may require thalamo-cortical interactions (Hughes et al., 2002), cortico-cortical interactions (Timofeev et al., 2000), intrinsic oscillators (Lőrincz et al., 2015; Sanchez-Vives and McCormick, 2000), or neuro-modulation (Constantinople and Bruno, 2011; Lőrincz et al., 2015; Sigalas et al., 2015). Modulation of cellular or synaptic

physiology may therefore serve as mechanisms to dynamically reconfigure the network to satisfy different computational requirements.

Reproducing In Vivo Findings

Although the digital reconstruction was largely based on in vitro data and was not designed to reproduce any particular experiment or to capture complex in vivo conditions, it yielded results that were qualitatively comparable to a number of major in vivo findings and made predictions beyond what was possible in these experiments, without tweaking any of the model parameters.

For example, the digital reconstruction made it possible to address a long-standing question concerning the mechanisms underlying the uncorrelated activity frequently observed in in vivo experiments (Haider et al., 2006). Previous theoretical work has shown that uncorrelated activity could be the result of tightly correlated excitatory conductances that are effectively cancelled out by anti-correlated inhibitory conductances (Renart et al., 2010; van Vreeswijk and Sompolinsky, 1996). Our simulations, using a model not specifically designed to address this question, confirm this effect as an emergent property of the network. The simulations further suggest that cortical activity in vivo approaches a critical transition along the synchronous asynchronous spectrum, beyond which regenerative activity leads to neuronal avalanches (see also Beggs and Plenz, 2003). Around this transition, spiking activity is highly correlated with fine temporal structure in synaptic input, reflected in brief moments of imbalance between excitatory and inhibitory conductances. Maximal discrimination between spatially segregated inputs, the generation of fine temporal structures such as triplets, and soloist-like and chorister-like behavior all emerge close to the transition. A recent study has experimentally characterized the plasticity mechanisms for maintaining the network close to this transition (Delattre et al., 2015).

Reproducing these in vivo findings was surprising because the digital reconstruction was based on data and architectural principles obtained from the immature rat somatosensory cortex, while many of the in vivo findings came from different neocortical regions in adult animals, sometimes belonging to other species. The fact that the reconstruction reproduces these phenomena suggests that they arise from fundamental properties of the neocortical microcircuit.

Concluding Remarks

This study demonstrates that it is possible, in principle, to reconstruct an integrated view of the structure and function of neocortical microcircuitry, using sparse, complementary datasets to predict biological parameters that have not been measured experimentally. Although the current digital reconstruction can already be used to gain insights into the way the microcircuitry operates, it is only a first step. To facilitate integration of new experimental data and challenges to the principles on which it is based, we have created a public web resource, which provides access to experimental data, models, and tools used in the reconstruction (The Neocortical Microcircuit Collaboration [NMC] Portal, https://bbp.epfl.ch/nmc-portal; Ramaswamy et al., 2015). This will allow the community to integrate their own data, perform their own analyses, and test their own hypotheses.

EXPERIMENTAL PROCEDURES

A detailed description is available in the Supplemental Experimental Procedures.

Data Acquisition
Neuron Morphology
Neuron morphologies were obtained from digital 3D reconstructions of biocytin-stained neurons from juvenile rat hind-limb somatosensory cortex, following whole-cell patch-clamp recordings in 300-μm-thick brain slices (Markram et al., 1997). In some of the reconstructed neurons, bouton locations were annotated on the axon (Wang et al., 2002). Reconstruction used the Neurolucida system (MicroBrightField).
Neuron Electrophysiology
Neurons were stimulated with a set of previously described protocols (Le Bé et al., 2007; Wang et al., 2002, 2004). A subset of these stimuli was used to generate neuron models; a different subset was used to validate the models.
Synaptic Anatomy
Data on the anatomy of synaptic connections were collected from previous studies in which synaptically coupled neurons were digitally reconstructed, and putative synapses were identified using criteria identifiable in light microscopy and validated using EM. In brief, putative synapses were identified at appositions between arbors, where a bouton was also present on the axon of the presynaptic neuron (Markram et al., 1997).
Synaptic Physiology
Presynaptic neurons were stimulated with a set of previously described protocols (Gupta et al., 2000; Markram et al., 1998; Tsodyks and Markram, 1997; Wang et al., 2002, 2006). The synaptic parameters required to model the synapses were obtained by fitting the responses against the Tsodyks-Markram model for dynamic synaptic transmission (Fuhrmann et al., 2002; Tsodyks and Markram, 1997).
Tissue Immunohistochemistry
Standard immunohistochemical methods were used to label markers of cell types (Lefort et al., 2009). Stained cells were counted under light microscopy. Layer boundaries and densities per layer were computed on slices using optical dissectors on NeuN-stained tissue (West and Gundersen, 1990; Williams and Rakic, 1988) and Stereo Investigator software (StereoInvestigator 7.0, MicroBright Field). Data for each cortical layer (I, II, III, IV, Va, Vb, VI) were collected from different animals (n = 5). Final values for neuronal densities and layer thicknesses were corrected for shrinkage. E/I ratios were determined by soma counting in confocal microscopy imaging of dual NeuN- and GABA-stained tissue.
Electron Microscopy
Serial EM stacks were obtained for blocks of neocortical tissue, as previously described (Denk and Horstmann, 2004).
Multi-electrode Array Experiments
A 3D multi-electrode array with 60 pyramidal platinum electrodes (Qwane Bioscience SA) was used to obtain extracellular recordings from neurons in slices, as previously described (Delattre et al., 2015; Rinaldi et al., 2008). Experimental data analysis was performed in Matlab (The MathWorks) with custom scripts. Extra-cellular spikes were detected when the recorded signal crossed a dynamic threshold.
Manipulating $[Ca^{2+}]_o$
Extracellular Ca^{2+} concentration ($[Ca^{2+}]_o$) was changed by bath perfusion with artificial extracellular fluid containing a modified $[Ca^{2+}]_o$. Bath changing times were minimized by employing a pipette to remove the recording chamber solution prior to changing the subsequent solution.

Reconstruction Process
Digital Neuron Morphologies
Following 3D reconstruction, the cut ends of neuronal morphologies were restored using a repair algorithm (Anwar et al., 2009). Neuronal arbors

were digitally unraveled to compensate for tortuosity caused by shrinkage, and neuron morphologies were cloned (see Supplemental Experimental Procedures).

Electrical Neuron Models

Multicompartmental conductance-based models of neurons were generated using up to 13 active ion channel types and a model of intracellular Ca^{2+} dynamics. Axon initial segments (AIS), somata, basal dendrites, and apical dendrites were separated. Interneurons contained only one dendritic region. Each region received a separate set of channels (see NMC portal, https://bbp.epfl.ch/nmc-portal; Ramaswamy et al., 2015). Of the axon, only the AIS was simulated. Each AIS was represented by two fixed-length sections, each with a length of 30 μm. AIS diameters were obtained from the reconstructed morphology used for model fitting. Action potentials detected in the AIS were sent to the postsynaptic synapses with a delay corresponding to the axonal length, assuming an axonal velocity of 0.3 m/s. Neuron models were fitted using a feature-based multi-objective optimization method, as previously described (Druckmann et al., 2007).

The Microcircuit Volume

Layer thicknesses and the diameter of the microcircuit were used to construct a virtual hexagonal prism (see main text). A virtual slice was generated from a 1 × 7 mosaic of microcircuits as a sheet (230.9 × 2800 μm). A meso-circuit was also generated. The meso-circuit consisted of a single microcircuit surrounded by additional microcircuits on all faces.

Cellular Composition

Cell density measurements and experimentally determined fractions of m- and me-types were used to generate the position of each cell in the volume of tissue, using E:I ratios to correct for sampling bias. Each cell was assigned the optimal morphology for its location in the volume (see Supplemental Experimental Procedures).

Synaptic Anatomy

Locations of synapses were derived using an algorithm described in the companion article (Reimann et al., 2015). The algorithm eliminates appositions that do not comply with the multi-synapse and plasticity reserve rules and ensures compatibility with observed biological bouton densities.

Synaptic Physiology

Excitatory synaptic transmission was modeled using both AMPA and NMDA receptor kinetics (Fuhrmann et al., 2002; Häusser and Roth, 1997; Markram et al., 1998; Ramaswamy et al., 2012; Tsodyks and Markram, 1997). Inhibitory synaptic transmission was modeled with a combination of $GABA_A$ and $GABA_B$ receptor kinetics (Gupta et al., 2000; Khazipov et al., 1995; De Koninck and Mody, 1997; Mott et al., 1999). Stochastic synaptic transmission was implemented as a two-state Markov model of dynamic synaptic release, a stochastic implementation of the Tsodyks-Markram dynamic synapse model (Fuhrmann et al., 2002; Tsodyks and Markram, 1997). Biological parameter ranges for the four model parameters were taken from experimental values for synaptic connections between specific m- and me-types or between larger categories of pre- and postsynaptic neurons (see Figure 9). Spontaneous miniature PSCs were modeled by implementing an independent Poisson process for each individual synapse that triggered release at rates (λ_{spont}) determined by the experimental data (Ling and Benardo, 1999; Simkus and Stricker, 2002).

Thalamic Innervation

Thalamic input was reconstructed using experimental data for ventro-posterior medial (VPM) axon bouton density profiles in rat barrel cortex (Meyer et al., 2010b), synapses per connection, and approximate numbers of incoming fibers. Synapse locations were determined using a variant of the connectome algorithm (Reimann et al., 2015; see Supplemental Experimental Procedures). Synapses were assigned to incoming fibers based on a Gaussian probability centered around each fiber.

Simulation

Microcircuit Simulation

The reconstructed microcircuit was simulated using the NEURON simulation package, augmented for execution on the supercomputer (Hines and Carnevale, 1997; Hines et al., 2008a, 2008b), together with additional custom tools to handle the setup and configuration of the microcircuit and the output of results.

In Silico Experiments

Depolarization was achieved by simulating current injection at the neuron soma. Currents were expressed as percent of first spike threshold for each neuron. Changes in $[Ca^{2+}]_o$ were simulated by changing the use parameter of synaptic transmission according to three curves for specific m-types (see Figure S15). Neuronal in silico knockout experiments were performed by hyperpolarizing the target population with somatic current injection (−100% threshold). Thalamic fiber stimulations were performed on circular clusters of minicolumns. The methods used to replicate previous in vivo experiments are described in the Supplemental Experimental Procedures.

Data Analysis

Anatomical and physiological data analysis were performed using a custom suite of Python-based tools operating on a Linux cluster (Supplemental Experimental Procedures). The same analysis as described in Kasthuri et al. (2015) was applied to compare results between a saturated EM reconstruction and the digital reconstruction that we generated (see Figure S20). PSPs were measured at the somata or dendrites of randomly selected pairs of neurons (30 trials). PSTHs were computed from all neurons in the circuit and were normalized by neuron number and time bin to express the average instantaneous firing rate. Mean spike-spike correlations were calculated as the histogram of intervals between all spike times of two different cells (bin size 1 ms). Evoked regenerative activity was defined as activity in which peak activity (PSTH) within 100 ms after stimulus of the outermost 20 minicolumns exceeded 30 Hz and 70% of the activity of the 20 central minicolumns in the 10 ms after stimulus. Spike rasters show spike events at the locations within the layers where they occurred (for clarity, only a fraction of spikes are plotted).

Supercomputing

Reconstruction and simulation workflows, such as neuron model optimization, circuit reconstruction, and network simulation, were executed on supercomputers. The systems used included an IBM Blue Gene/L (until 2009), a CADMOS 4-rack IBM Blue Gene/P (until 2013), a CADMOS 1-rack IBM Blue Gene/Q (until 2014), and the Blue Brain IV operated by the Swiss National Supercomputing Center (CSCS) on behalf of the Blue Brain Project, ranked the 100th most powerful supercomputing system (Top500, June 2015). Blue Brain IV includes a 4-rack IBM Blue Gene/Q, IBM Blue Gene Active Storage, and a 40-node Linux cluster for post-processing, analysis, and visualization, fully interconnected using Infiniband technology and a GPFS file system with 4.2 Petabyte raw storage (Schürmann et al., 2014).

Visualization

Large circuits and simulations in high resolution were visualized using a custom-developed tool, RTNeuron (Hernando et al., 2012). High-quality, static images of small neural circuits, individual neurons, and synaptic spines and boutons were created using Maya 3D animation software (Autodesk, San Rafael, California, USA).

Software Development

Data integration and post processing as well as reconstruction, simulation, analysis, and visualization of neuronal network models used >30 software applications, integrated into automated and semi-automated workflows. Development was supported by a comprehensive development environment based on best practices for version control (git), code review (gerrit), and continuous building, testing, packaging, and deployment (Jenkins).

SUPPLEMENTAL INFORMATION

Supplemental Information includes Supplemental Experimental Procedures, 20 figures, six tables, and three movies and can be found with this article online at http://dx.doi.org/10.1016/j.cell.2015.09.029.

AUTHOR CONTRIBUTIONS

H.M. conceived and led the study. F.S., S.L.H., I.S., and J.D. co-led the study. H.M. planned and supervised experiments, data integration, strategies and algorithms, model building, in silico experiments, and analysis. F.S. planned and supervised the development of algorithms, software and workflows, computing infrastructure, and technical integration. E.M., S.R., M.W.R., and S.L.H. drove and co-supervised the integration of the data, tools, models,

REFERENCES

Ali, A.B., Bannister, A.P., and Thomson, A.M. (2007). Robust correlations between action potential duration and the properties of synaptic connections in layer 4 interneurones in neocortical slices from juvenile rats and adult rat and cat. J. Physiol. *580*, 149–169.

Amitai, Y. (2001). Thalamocortical synaptic connections: efficacy, modulation, inhibition and plasticity. Rev. Neurosci. *12*, 159–173.

Amzica, F., Massimini, M., and Manfridi, A. (2002). Spatial buffering during slow and paroxysmal sleep oscillations in cortical networks of glial cells in vivo. J. Neurosci. *22*, 1042–1053.

Angulo, M.C., Rossier, J., and Audinat, E. (1999). Postsynaptic glutamate receptors and integrative properties of fast-spiking interneurons in the rat neocortex. J. Neurophysiol. *82*, 1295–1302.

Anwar, H., Riachi, I., Hill, S., Schurmann, F., and Markram, H. (2009). An approach to capturing neuron morphological diversity. In Computational Modeling Methods for Neuroscientists (The MIT Press), pp. 211–231.

Ascoli, G.A., Alonso-Nanclares, L., Anderson, S.A., Barrionuevo, G., Benavides-Piccione, R., Burkhalter, A., Buzsáki, G., Cauli, B., Defelipe, J., Fairén, A., et al.; Petilla Interneuron Nomenclature Group (2008). Petilla terminology: nomenclature of features of GABAergic interneurons of the cerebral cortex. Nat. Rev. Neurosci. *9*, 557–568.

Bannister, A.P., and Thomson, A.M. (2007). Dynamic properties of excitatory synaptic connections involving layer 4 pyramidal cells in adult rat and cat neocortex. Cereb. Cortex *17*, 2190–2203.

Beaulieu, C. (1993). Numerical data on neocortical neurons in adult rat, with special reference to the GABA population. Brain Res. *609*, 284–292.

Beaulieu, C., and Colonnier, M. (1983). The number of neurons in the different laminae of the binocular and monocular regions of area 17 in the cat, Canada. J. Comp. Neurol. *217*, 337–344.

Beggs, J.M., and Plenz, D. (2003). Neuronal avalanches in neocortical circuits. J. Neurosci. *23*, 11167–11177.

Beierlein, M., and Connors, B.W. (2002). Short-term dynamics of thalamocortical and intracortical synapses onto layer 6 neurons in neocortex. J. Neurophysiol. *88*, 1924–1932.

Beierlein, M., Gibson, J.R., and Connors, B.W. (2000). A network of electrically coupled interneurons drives synchronized inhibition in neocortex. Nat. Neurosci. *3*, 904–910.

Beierlein, M., Fall, C.P., Rinzel, J., and Yuste, R. (2002). Thalamocortical bursts trigger recurrent activity in neocortical networks: layer 4 as a frequency-dependent gate. J. Neurosci. *22*, 9885–9894.

Beierlein, M., Gibson, J.R., and Connors, B.W. (2003). Two dynamically distinct inhibitory networks in layer 4 of the neocortex. J. Neurophysiol. *90*, 2987–3000.

Berger, T., Larkum, M.E., and Lüscher, H.-R. (2001). High I(h) channel density in the distal apical dendrite of layer V pyramidal cells increases bidirectional attenuation of EPSPs. J. Neurophysiol. *85*, 855–868.

Blatow, M., Rozov, A., Katona, I., Hormuzdi, S.G., Meyer, A.H., Whittington, M.A., Caputi, A., and Monyer, H. (2003). A novel network of multipolar bursting interneurons generates theta frequency oscillations in neocortex. Neuron *38*, 805–817.

Borst, J.G.G. (2010). The low synaptic release probability in vivo. Trends Neurosci. *33*, 259–266.

Boyd, J., and Matsubara, J. (1991). Intrinsic connections in cat visual cortex: a combined anterograde and retrograde tracing study. Brain Res. *560*, 207–215.

Brunel, N. (2000). Dynamics of sparsely connected networks of excitatory and inhibitory spiking neurons. J. Comput. Neurosci. *8*, 183–208.

Bruno, R.M., and Sakmann, B. (2006). Cortex is driven by weak but synchronously active thalamocortical synapses. Science *312*, 1622–1627.

Callaway, E.M. (2008). Transneuronal circuit tracing with neurotropic viruses. Curr. Opin. Neurobiol. *18*, 617–623.

Carnevale, N.T., and Hines, M.L. (2006). The NEURON Book (New York, NY, USA: Cambridge University Press).

Cauli, B., Audinat, E., Lambolez, B., Angulo, M.C., Ropert, N., Tsuzuki, K., Hestrin, S., and Rossier, J. (1997). Molecular and physiological diversity of cortical nonpyramidal cells. J. Neurosci. *17*, 3894–3906.

Cauli, B., Porter, J.T., Tsuzuki, K., Lambolez, B., Rossier, J., Quenet, B., and Audinat, E. (2000). Classification of fusiform neocortical interneurons based on unsupervised clustering. Proc. Natl. Acad. Sci. USA 97, 6144–6149.

Celikel, T., Szostak, V.A., and Feldman, D.E. (2004). Modulation of spike timing by sensory deprivation during induction of cortical map plasticity. Nat. Neurosci. 7, 534–541.

Celio, M.R. (1986). Parvalbumin in most gamma-aminobutyric acid-containing neurons of the rat cerebral cortex. Science 231, 995–997.

Chen, N., Sugihara, H., and Sur, M. (2015). An acetylcholine-activated microcircuit drives temporal dynamics of cortical activity. Nat. Neurosci. 18, 892–902.

Cobb, S.R., Halasy, K., Vida, I., Nyíri, G., Tamás, G., Buhl, E.H., and Somogyi, P. (1997). Synaptic effects of identified interneurons innervating both interneurons and pyramidal cells in the rat hippocampus. Neuroscience 79, 629–648.

Condé, F., Lund, J.S., Jacobowitz, D.M., Baimbridge, K.G., and Lewis, D.A. (1994). Local circuit neurons immunoreactive for calretinin, calbindin D-28k or parvalbumin in monkey prefrontal cortex: distribution and morphology. J. Comp. Neurol. 341, 95–116.

Connors, B.W., and Gutnick, M.J. (1990). Intrinsic firing patterns of diverse neocortical neurons. Trends Neurosci. 13, 99–104.

Constantinople, C.M., and Bruno, R.M. (2011). Effects and mechanisms of wakefulness on local cortical networks. Neuron 69, 1061–1068.

Constantinople, C.M., and Bruno, R.M. (2013). Deep cortical layers are activated directly by thalamus. Science 340, 1591–1594.

Cragg, B.G. (1967). The density of synapses and neurones in the motor and visual areas of the cerebral cortex. J. Anat. 101, 639–654.

Crick, F.H. (1979). Thinking about the brain. Sci. Am. 241, 219–232.

Cunningham, M.O., Whittington, M.A., Bibbig, A., Roopun, A., LeBeau, F.E.N., Vogt, A., Monyer, H., Buhl, E.H., and Traub, R.D. (2004). A role for fast rhythmic bursting neurons in cortical gamma oscillations in vitro. Proc. Natl. Acad. Sci. USA 101, 7152–7157.

Datwani, A., Iwasato, T., Itohara, S., and Erzurumlu, R.S. (2002). NMDA receptor-dependent pattern transfer from afferents to postsynaptic cells and dendritic differentiation in the barrel cortex. Mol. Cell. Neurosci. 21, 477–492.

De Koninck, Y., and Mody, I. (1997). Endogenous GABA activates small-conductance K+ channels underlying slow IPSCs in rat hippocampal neurons. J. Neurophysiol. 77, 2202–2208.

DeFelipe, J. (1993). Neocortical neuronal diversity: chemical heterogeneity revealed by colocalization studies of classic neurotransmitters, neuropeptides, calcium-binding proteins, and cell surface molecules. Cereb. Cortex 3, 273–289.

DeFelipe, J., and Jones, E.G. (1988). Cajal on the Cerebral Cortex: An Annotated Translation of the Complete Writings (Oxford University Press).

DeFelipe, J., Alonso-Nanclares, L., and Arellano, J.I. (2002). Microstructure of the neocortex: comparative aspects. J. Neurocytol. 31, 299–316.

DeFelipe, J., López-Cruz, P.L., Benavides-Piccione, R., Bielza, C., Larrañaga, P., Anderson, S., Burkhalter, A., Cauli, B., Faírén, A., Feldmeyer, D., et al. (2013). New insights into the classification and nomenclature of cortical GABAergic interneurons. Nat. Rev. Neurosci. 14, 202–216.

Delattre, V., Keller, D., Perich, M., Markram, H., and Muller, E.B. (2015). Network-timing-dependent plasticity. Front. Cell. Neurosci. 9, 220.

Denk, W., and Horstmann, H. (2004). Serial block-face scanning electron microscopy to reconstruct three-dimensional tissue nanostructure. PLoS Biol. 2, e329.

Douglas, R.J., and Martin, K.A.C. (2004). Neuronal circuits of the neocortex. Annu. Rev. Neurosci. 27, 419–451.

Druckmann, S., Banitt, Y., Gidon, A., Schürmann, F., Markram, H., and Segev, I. (2007). A novel multiple objective optimization framework for constraining conductance-based neuron models by experimental data. Front. Neurosci. 1, 7–18.

Druckmann, S., Berger, T.K., Schürmann, F., Hill, S., Markram, H., and Segev, I. (2011). Effective stimuli for constructing reliable neuron models. PLoS Comput. Biol. 7, e1002133.

Druckmann, S., Hill, S., Schürmann, F., Markram, H., and Segev, I. (2013). A hierarchical structure of cortical interneuron electrical diversity revealed by automated statistical analysis. Cereb. Cortex 23, 2994–3006.

Dumitriu, D., Cossart, R., Huang, J., and Yuste, R. (2007). Correlation between axonal morphologies and synaptic input kinetics of interneurons from mouse visual cortex. Cereb. Cortex 17, 81–91.

Faírén, A., DeFelipe, J., and Regidor, J. (1984). Nonpyramidal neurons: general account. In Cerebral Cortex, Volume 1, Cellular Components of the Cerebral Cortex, A. Peters and E.G. Jones, eds. (Plenum Press), pp. 201–253.

Feldmeyer, D., Egger, V., Lubke, J., and Sakmann, B. (1999). Reliable synaptic connections between pairs of excitatory layer 4 neurones within a single 'barrel' of developing rat somatosensory cortex. J. Physiol. 521, 169–190.

Feldmeyer, D., Lübke, J., Silver, R.A., and Sakmann, B. (2002). Synaptic connections between layer 4 spiny neurone-layer 2/3 pyramidal cell pairs in juvenile rat barrel cortex: physiology and anatomy of interlaminar signalling within a cortical column. J. Physiol. 538, 803–822.

Feldmeyer, D., Lübke, J., and Sakmann, B. (2006). Efficacy and connectivity of intracolumnar pairs of layer 2/3 pyramidal cells in the barrel cortex of juvenile rats. J. Physiol. 575, 583–602.

Frick, A., Feldmeyer, D., and Sakmann, B. (2007). Postnatal development of synaptic transmission in local networks of L5A pyramidal neurons in rat somatosensory cortex. J. Physiol. 585, 103–116.

Frick, A., Feldmeyer, D., Helmstaedter, M., and Sakmann, B. (2008). Monosynaptic connections between pairs of L5A pyramidal neurons in columns of juvenile rat somatosensory cortex. Cereb. Cortex 18, 397–406.

Fuhrmann, G., Segev, I., Markram, H., and Tsodyks, M. (2002). Coding of temporal information by activity-dependent synapses. J. Neurophysiol. 87, 140–148.

Gentet, L.J., Avermann, M., Matyas, F., Staiger, J.F., and Petersen, C.C.H. (2010). Membrane potential dynamics of GABAergic neurons in the barrel cortex of behaving mice. Neuron 65, 422–435.

Gentet, L.J., Kremer, Y., Taniguchi, H., Huang, Z.J., Staiger, J.F., and Petersen, C.C.H. (2012). Unique functional properties of somatostatin-expressing GABAergic neurons in mouse barrel cortex. Nat. Neurosci. 15, 607–612.

Ghosh, A., and Shatz, C.J. (1993). A role for subplate neurons in the patterning of connections from thalamus to neocortex. Development 117, 1031–1047.

Gil, Z., Connors, B.W., and Amitai, Y. (1999). Efficacy of thalamocortical and intracortical synaptic connections: quanta, innervation, and reliability. Neuron 23, 385–397.

Glenn, L.L., Hada, J., Roy, J.P., Deschênes, M., and Steriade, M. (1982). Anterograde tracer and field potential analysis of the neocortical layer I projection from nucleus ventralis medialis of the thalamus in cat. Neuroscience 7, 1861–1877.

Gonchar, Y., and Burkhalter, A. (1997). Three distinct families of GABAergic neurons in rat visual cortex. Cereb. Cortex 7, 347–358.

Gonchar, Y., Wang, Q., Burkhalter, A., Gonchar, Y., Wang, Q., and Burkhalter, A. (2007). Multiple distinct subtypes of GABAergic neurons in mouse visual cortex identified by triple immunostaining. Front. Neuroanat. 1, 3.

Grange, P., Bohland, J.W., Okaty, B.W., Sugino, K., Bokil, H., Nelson, S.B., Ng, L., Hawrylycz, M., and Mitra, P.P. (2014). Cell-type-based model explaining coexpression patterns of genes in the brain. Proc. Natl. Acad. Sci. USA 111, 5397–5402.

Gupta, A., Wang, Y., and Markram, H. (2000). Organizing principles for a diversity of GABAergic interneurons and synapses in the neocortex. Science 287, 273–278.

Haider, B., Duque, A., Hasenstaub, A.R., and McCormick, D.A. (2006). Neocortical network activity in vivo is generated through a dynamic balance of excitation and inhibition. J. Neurosci. 26, 4535–4545.

Hallman, L.E., Schofield, B.R., and Lin, C.-S. (1988). Dendritic morphology and axon collaterals of corticotectal, corticopontine, and callosal neurons in layer V of primary visual cortex of the hooded rat. J. Comp. Neurol. 272, 149–160.

Harris, K.D., and Shepherd, G.M.G. (2015). The neocortical circuit: themes and variations. Nat. Neurosci. 18, 170–181.

Hasenstaub, A., Shu, Y., Haider, B., Kraushaar, U., Duque, A., and McCormick, D.A. (2005). Inhibitory postsynaptic potentials carry synchronized frequency information in active cortical networks. Neuron 47, 423–435.

Häusser, M., and Roth, A. (1997). Estimating the time course of the excitatory synaptic conductance in neocortical pyramidal cells using a novel voltage jump method. J. Neurosci. 17, 7606–7625.

Hay, E., Hill, S., Schürmann, F., Markram, H., and Segev, I. (2011). Models of neocortical layer 5b pyramidal cells capturing a wide range of dendritic and perisomatic active properties. PLoS Comput. Biol. 7, e1002107.

Heinemann, U., Lux, H.D., and Gutnick, M.J. (1977). Extracellular free calcium and potassium during paroxsmal activity in the cerebral cortex of the cat. Exp. Brain Res. 27, 237–243.

Hendry, S.H., Jones, E.G., and Emson, P.C. (1984). Morphology, distribution, and synaptic relations of somatostatin- and neuropeptide Y-immunoreactive neurons in rat and monkey neocortex. J. Neurosci. 4, 2497–2517.

Hendry, S.H.C., Jones, E.G., Emson, P.C., Lawson, D.E.M., Heizmann, C.W., and Streit, P. (1989). Two classes of cortical GABA neurons defined by differential calcium binding protein immunoreactivities. Exp. Brain Res. 76, 467–472.

Hernando, J., Schürmann, F., and Pastor, L. (2012). Towards real-time visualization of detailed neural tissue models: View frustum culling for parallel rendering. BioVis, 25–32.

Hestrin, S., and Armstrong, W.E. (1996). Morphology and physiology of cortical neurons in layer I. J. Neurosci. 16, 5290–5300.

Hevner, R.F., Shi, L., Justice, N., Hsueh, Y., Sheng, M., Smiga, S., Bulfone, A., Goffinet, A.M., Campagnoni, A.T., and Rubenstein, J.L.R. (2001). Tbr1 regulates differentiation of the preplate and layer 6. Neuron 29, 353–366.

Hill, S.L., Wang, Y., Riachi, I., Schürmann, F., and Markram, H. (2012). Statistical connectivity provides a sufficient foundation for specific functional connectivity in neocortical neural microcircuits. Proc. Natl. Acad. Sci. USA 109, E2885–E2894.

Hines, M.L., and Carnevale, N.T. (1997). The NEURON simulation environment. Neural Comput. 9, 1179–1209.

Hines, M.L., Markram, H., and Schürmann, F. (2008a). Fully implicit parallel simulation of single neurons. J. Comput. Neurosci. 25, 439–448.

Hines, M.L., Eichner, H., and Schürmann, F. (2008b). Neuron splitting in compute-bound parallel network simulations enables runtime scaling with twice as many processors. J. Comput. Neurosci. 25, 203–210.

Hines, M., Kumar, S., and Schürmann, F. (2011). Comparison of neuronal spike exchange methods on a Blue Gene/P supercomputer. Front. Comput. Neurosci. 5, 49.

Holmgren, C., Harkany, T., Svennenfors, B., and Zilberter, Y. (2003). Pyramidal cell communication within local networks in layer 2/3 of rat neocortex. J. Physiol. 551, 139–153.

Honey, C.J., Kötter, R., Breakspear, M., and Sporns, O. (2007). Network structure of cerebral cortex shapes functional connectivity on multiple time scales. Proc. Natl. Acad. Sci. USA 104, 10240–10245.

Horton, J.C., and Adams, D.L. (2005). The cortical column: a structure without a function. Philos. Trans. R. Soc. Lond. B. Biol. Sci. 360, 837–862.

Hughes, S.W., Cope, D.W., Blethyn, K.L., and Crunelli, V. (2002). Cellular mechanisms of the slow (<1 Hz) oscillation in thalamocortical neurons in vitro. Neuron 33, 947–958.

Jones, H.C., and Keep, R.F. (1988). Brain fluid calcium concentration and response to acute hypercalcaemia during development in the rat. J. Physiol. 402, 579–593.

Kapfer, C., Glickfeld, L.L., Atallah, B.V., and Scanziani, M. (2007). Supralinear increase of recurrent inhibition during sparse activity in the somatosensory cortex. Nat. Neurosci. 10, 743–753.

Karagiannis, A., Gallopin, T., Dávid, C., Battaglia, D., Geoffroy, H., Rossier, J., Hillman, E.M.C., Staiger, J.F., and Cauli, B. (2009). Classification of NPY-expressing neocortical interneurons. J. Neurosci. 29, 3642–3659.

Karube, F., Kubota, Y., and Kawaguchi, Y. (2004). Axon branching and synaptic bouton phenotypes in GABAergic nonpyramidal cell subtypes. J. Neurosci. 24, 2853–2865.

Kasper, E.M., Larkman, A.U., Lübke, J., and Blakemore, C. (1994). Pyramidal neurons in layer 5 of the rat visual cortex. II. Development of electrophysiological properties. J. Comp. Neurol. 339, 475–494.

Kasthuri, N., Hayworth, K.J., Berger, D.R., Schalek, R.L., Conchello, J.A., Knowles-Barley, S., Lee, D., Vázquez-Reina, A., Kaynig, V., Jones, T.R., et al. (2015). Saturated Reconstruction of a Volume of Neocortex. Cell 162, 648–661.

Kawaguchi, Y., and Kondo, S. (2002). Parvalbumin, somatostatin and cholecystokinin as chemical markers for specific GABAergic interneuron types in the rat frontal cortex. J. Neurocytol. 31, 277–287.

Kawaguchi, Y., and Kubota, Y. (1993). Correlation of physiological subgroupings of nonpyramidal cells with parvalbumin- and calbindinD28k-immunoreactive neurons in layer V of rat frontal cortex. J. Neurophysiol. 70, 387–396.

Kawaguchi, Y., and Kubota, Y. (1997). GABAergic cell subtypes and their synaptic connections in rat frontal cortex. Cereb. Cortex 7, 476–486.

Kawaguchi, Y., Karube, F., and Kubota, Y. (2006). Dendritic branch typing and spine expression patterns in cortical nonpyramidal cells. Cereb. Cortex 16, 696–711.

Keller, A., and Carlson, G.C. (1999). Neonatal whisker clipping alters intracortical, but not thalamocortical projections, in rat barrel cortex. J. Comp. Neurol. 412, 83–94.

Khazen, G., Hill, S.L., Schürmann, F., and Markram, H. (2012). Combinatorial expression rules of ion channel genes in juvenile rat (Rattus norvegicus) neocortical neurons. PLoS ONE 7, e34786.

Khazipov, R., Congar, P., and Ben-Ari, Y. (1995). Hippocampal CA1 lacunosum-moleculare interneurons: modulation of monosynaptic GABAergic IPSCs by presynaptic GABAB receptors. J. Neurophysiol. 74, 2126–2137.

Killackey, H.P., Gould, H.J., 3rd, Cusick, C.G., Pons, T.P., and Kaas, J.H. (1983). The relation of corpus callosum connections to architectonic fields and body surface maps in sensorimotor cortex of new and old world monkeys. J. Comp. Neurol. 219, 384–419.

Kisvárday, Z.F., Martin, K.A., Whitteridge, D., and Somogyi, P. (1985). Synaptic connections of intracellularly filled clutch cells: a type of small basket cell in the visual cortex of the cat. J. Comp. Neurol. 241, 111–137.

Klausberger, T., Magill, P.J., Márton, L.F., Roberts, J.D.B., Cobden, P.M., Buzsáki, G., and Somogyi, P. (2003). Brain-state- and cell-type-specific firing of hippocampal interneurons in vivo. Nature 421, 844–848.

Le Bé, J.-V., Silberberg, G., Wang, Y., and Markram, H. (2007). Morphological, electrophysiological, and synaptic properties of corticocallosal pyramidal cells in the neonatal rat neocortex. Cereb. Cortex 17, 2204–2213.

Krimer, L.S., Zaitsev, A.V., Czanner, G., Kröner, S., González-Burgos, G., Povysheva, N.V., Iyengar, S., Barrionuevo, G., and Lewis, D.A. (2005). Cluster analysis-based physiological classification and morphological properties of inhibitory neurons in layers 2-3 of monkey dorsolateral prefrontal cortex. J. Neurophysiol. 94, 3009–3022.

Larkman, A.U. (1991a). Dendritic morphology of pyramidal neurones of the visual cortex of the rat: I. Branching patterns. J. Comp. Neurol. 306, 307–319.

Larkman, A.U. (1991b). Dendritic morphology of pyramidal neurones of the visual cortex of the rat: III. Spine distributions. J. Comp. Neurol. 306, 332–343.

Larkum, M.E., Zhu, J.J., and Sakmann, B. (2001). Dendritic mechanisms underlying the coupling of the dendritic with the axonal action potential initiation zone of adult rat layer 5 pyramidal neurons. J. Physiol. 533, 447–466.
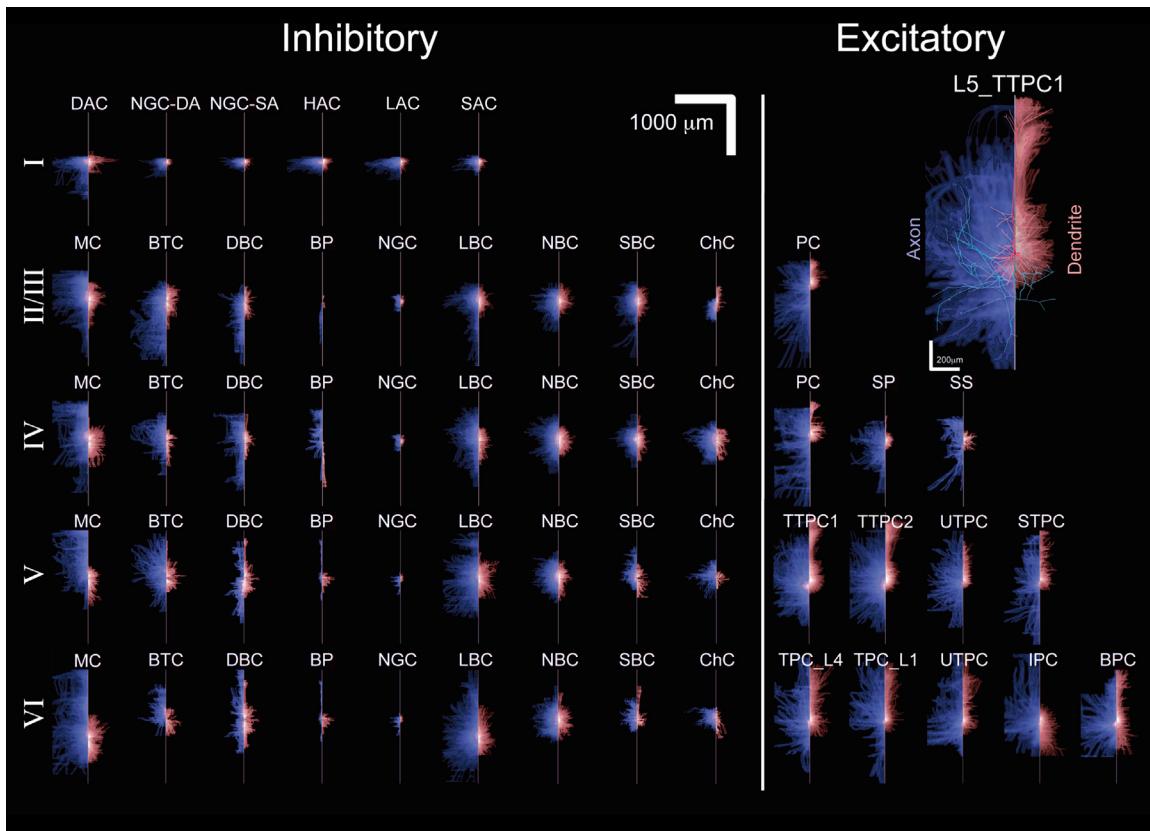
Lee, S.-H., and Dan, Y. (2012). Neuromodulation of brain states. Neuron *76*, 209–222.

Lefort, S., Tomm, C., Floyd Sarria, J.-C., and Petersen, C.C.H. (2009). The excitatory neuronal network of the C2 barrel column in mouse primary somatosensory cortex. Neuron *61*, 301–316.

Leinekugel, X., Khazipov, R., Cannon, R., Hirase, H., Ben-Ari, Y., and Buzsáki, G. (2002). Correlated bursts of activity in the neonatal hippocampus in vivo. Science *296*, 2049–2052.

Ling, D.S., and Benardo, L.S. (1999). Restrictions on inhibitory circuits contribute to limited recruitment of fast inhibition in rat neocortical pyramidal cells. J. Neurophysiol. *82*, 1793–1807.

Livingstone, M.S. (1996). Oscillatory firing and interneuronal correlations in squirrel monkey striate cortex. J. Neurophysiol. *75*, 2467–2485.

Lőrincz, M.L., Gunner, D., Bao, Y., Connelly, W.M., Isaac, J.T.R., Hughes, S.W., and Crunelli, V. (2015). A distinct class of slow (∼0.2-2 Hz) intrinsically bursting layer 5 pyramidal neurons determines UP/DOWN state dynamics in the neocortex. J. Neurosci. *35*, 5442–5458.

Luczak, A., Barthó, P., Marguet, S.L., Buzsáki, G., and Harris, K.D. (2007). Sequential structure of neocortical spontaneous activity in vivo. Proc. Natl. Acad. Sci. USA *104*, 347–352.

Maffei, A., Nelson, S.B., and Turrigiano, G.G. (2004). Selective reconfiguration of layer 4 visual cortical circuitry by visual deprivation. Nat. Neurosci. *7*, 1353–1359.

Mao, B.-Q., Hamzei-Sichani, F., Aronov, D., Froemke, R.C., and Yuste, R. (2001). Dynamics of spontaneous activity in neocortical slices. Neuron *32*, 883–898.

Markram, H. (2008). Fixing the location and dimensions of functional neocortical columns. HFSP J. *2*, 132–135.

Markram, H., Lübke, J., Frotscher, M., Roth, A., and Sakmann, B. (1997). Physiology and anatomy of synaptic connections between thick tufted pyramidal neurones in the developing rat neocortex. J. Physiol. *500*, 409–440.

Markram, H., Wang, Y., and Tsodyks, M. (1998). Differential signaling via the same axon of neocortical pyramidal neurons. Proc. Natl. Acad. Sci. USA *95*, 5323–5328.

Markram, H., Toledo-Rodriguez, M., Wang, Y., Gupta, A., Silberberg, G., and Wu, C. (2004). Interneurons of the neocortical inhibitory system. Nat. Rev. Neurosci. *5*, 793–807.

Mason, A., Nicoll, A., and Stratford, K. (1991). Synaptic transmission between individual pyramidal neurons of the rat visual cortex in vitro. J. Neurosci. *11*, 72–84.

Massimini, M., and Amzica, F. (2001). Extracellular calcium fluctuations and intracellular potentials in the cortex during the slow sleep oscillation. J. Neurophysiol. *85*, 1346–1350.

Mazurek, M.E., and Shadlen, M.N. (2002). Limits to the temporal fidelity of cortical spike rate signals. Nat. Neurosci. *5*, 463–471.

McCormick, D.A., Connors, B.W., Lighthall, J.W., and Prince, D.A. (1985). Comparative electrophysiology of pyramidal and sparsely spiny stellate neurons of the neocortex. J. Neurophysiol. *54*, 782–806.

McCormick, D.A., Shu, Y., Hasenstaub, A., Sanchez-Vives, M., Badoual, M., and Bal, T. (2003). Persistent cortical activity: mechanisms of generation and effects on neuronal excitability. Cereb. Cortex *13*, 1219–1231.

McGarry, L.M., Packer, A.M., Fino, E., Nikolenko, V., Sippy, T., and Yuste, R. (2010). Quantitative classification of somatostatin-positive neocortical interneurons identifies three interneuron subtypes. Front. Neural Circuits *4*, 12.

Mercer, A., West, D.C., Morris, O.T., Kirchhecker, S., Kerkhoff, J.E., and Thomson, A.M. (2005). Excitatory connections made by presynaptic cortico-cortical pyramidal cells in layer 6 of the neocortex. Cereb. Cortex *15*, 1485–1496.

Meyer, A.H., Katona, I., Blatow, M., Rozov, A., and Monyer, H. (2002). In vivo labeling of parvalbumin-positive interneurons and analysis of electrical coupling in identified neurons. J. Neurosci. *22*, 7055–7064.

Meyer, H.S., Wimmer, V.C., Oberlaender, M., de Kock, C.P.J., Sakmann, B., and Helmstaedter, M. (2010a). Number and laminar distribution of neurons in a thalamocortical projection column of rat vibrissal cortex. Cereb. Cortex *20*, 2277–2286.

Meyer, H.S., Wimmer, V.C., Hemberger, M., Bruno, R.M., de Kock, C.P., Frick, A., Sakmann, B., and Helmstaedter, M. (2010b). Cell type-specific thalamic innervation in a column of rat vibrissal cortex. Cereb. Cortex *20*, 2287–2303.

Meyer, H.S., Schwarz, D., Wimmer, V.C., Schmitt, A.C., Kerr, J.N.D., Sakmann, B., and Helmstaedter, M. (2011). Inhibitory interneurons in a cortical column form hot zones of inhibition in layers 2 and 5A. Proc. Natl. Acad. Sci. USA *108*, 16807–16812.

Micheva, K.D., and Smith, S.J. (2007). Array tomography: a new tool for imaging the molecular architecture and ultrastructure of neural circuits. Neuron *55*, 25–36.

Micheva, K.D., Busse, B., Weiler, N.C., O'Rourke, N., and Smith, S.J. (2010). Single-synapse analysis of a diverse synapse population: proteomic imaging methods and markers. Neuron *68*, 639–653.

Migliore, M., Cannia, C., Lytton, W.W., Markram, H., and Hines, M.L. (2006). Parallel network simulations with NEURON. J. Comput. Neurosci. *21*, 119–129.

Mott, D.D., Li, Q., Okazaki, M.M., Turner, D.A., and Lewis, D.V. (1999). GABAB-receptor-mediated currents in interneurons of the dentate-hilus border. J. Neurophysiol. *82*, 1438–1450.

Mountcastle, V.B. (1998). Perceptual neuroscience: The cerebral cortex (Harvard University Press).

Nelson, S. (2002). Cortical microcircuits: diverse or canonical? Neuron *36*, 19–27.

Nevian, T., Larkum, M.E., Polsky, A., and Schiller, J. (2007). Properties of basal dendrites of layer 5 pyramidal neurons: a direct patch-clamp recording study. Nat. Neurosci. *10*, 206–214.

O'Connor, D.H., Huber, D., and Svoboda, K. (2009). Reverse engineering the mouse brain. Nature *461*, 923–929.

Oberlaender, M., de Kock, C.P.J., Bruno, R.M., Ramirez, A., Meyer, H.S., Dercksen, V.J., Helmstaedter, M., and Sakmann, B. (2012). Cell type-specific three-dimensional structure of thalamocortical circuits in a column of rat vibrissal cortex. Cereb. Cortex *22*, 2375–2391.

Ohana, O., and Sakmann, B. (1998). Transmitter release modulation in nerve terminals of rat neocortical pyramidal cells by intracellular calcium buffers. J. Physiol. *513*, 135–148.

Okun, M., and Lampl, I. (2008). Instantaneous correlation of excitation and inhibition during ongoing and sensory-evoked activities. Nat. Neurosci. *11*, 535–537.

Okun, M., Steinmetz, N.A., Cossell, L., Iacaruso, M.F., Ko, H., Barthó, P., Moore, T., Hofer, S.B., Mrsic-Flogel, T.D., Carandini, M., and Harris, K.D. (2015). Diverse coupling of neurons to populations in sensory cortex. Nature *521*, 511–515.

Oláh, S., Komlósi, G., Szabadics, J., Varga, C., Tóth, E., Barzó, P., and Tamás, G. (2007). Output of neurogliaform cells to various neuron types in the human and rat cerebral cortex. Front. Neural Circuits *1*, 4.

Packer, A.M., and Yuste, R. (2011). Dense, unspecific connectivity of neocortical parvalbumin-positive interneurons: a canonical microcircuit for inhibition? J. Neurosci. *31*, 13260–13271.

Perin, R., Berger, T.K., and Markram, H. (2011). A synaptic organizing principle for cortical neuronal groups. Proc. Natl. Acad. Sci. USA *108*, 5419–5424.

Perrenoud, Q., Rossier, J., Geoffroy, H., Vitalis, T., and Gallopin, T. (2013). Diversity of GABAergic interneurons in layer VIa and VIb of mouse barrel cortex. Cereb. Cortex *23*, 423–441.

Peters, A. (1987). Number of Neurons and Synapses in Primary Visual Cortex. In Cerebral Cortex, E.G. Jones and A. Peters, eds. (Springer), pp. 267–294.

Peters, A., and Kaiserman-Abramof, I.R. (1970). The small pyramidal neuron of the rat cerebral cortex. The perikaryon, dendrites and spines. Am. J. Anat. *127*, 321–355.

Ramaswamy, S., and Markram, H. (2015). Anatomy and physiology of the thick-tufted layer 5 pyramidal neuron. Front. Cell. Neurosci. 9, 233.

Ramaswamy, S., Hill, S.L., King, J.G., Schürmann, F., Wang, Y., and Markram, H. (2012). Intrinsic morphological diversity of thick-tufted layer 5 pyramidal neurons ensures robust and invariant properties of in silico synaptic connections. J. Physiol. 590, 737–752.

Ramaswamy, S., Courcol, J.-D., Abdellah, M., Adaszewski, S., Antille, N., Arsever, S., Guy Antoine, A.K., Bilgili, A., Brukau, Y., Chalimourda, A., et al. (2015). The neocortical Microcircuit collaboration portal: A resource for rat somatosensory cortex. Front. Neural Circuits 9, 44.

Ramón y Cajal, S. (1909, 1911). Histologie du Systeme Nerveux de l'Homme et des Vertebres. L. Azoulay, trans. Maloine, Paris.

Reimann, M.W., Muller, E.B., Ramaswamy, S., and Markram, H. (2015). An algorithm to predict the connectome of neural microcircuits. Front. Comput. Neurosci. 9, 28.

Renart, A., de la Rocha, J., Bartho, P., Hollender, L., Parga, N., Reyes, A., and Harris, K.D. (2010). The asynchronous state in cortical circuits. Science 327, 587–590.

Reyes, A., and Sakmann, B. (1999). Developmental switch in the short-term modification of unitary EPSPs evoked in layer 2/3 and layer 5 pyramidal neurons of rat neocortex. J. Neurosci. 19, 3827–3835.

Reyes, A., Lujan, R., Rozov, A., Burnashev, N., Somogyi, P., and Sakmann, B. (1998). Target-cell-specific facilitation and depression in neocortical circuits. Nat. Neurosci. 1, 279–285.

Reyes-Puerta, V., Sun, J.-J., Kim, S., Kilb, W., and Luhmann, H.J. (2015). Laminar and Columnar Structure of Sensory-Evoked Multineuronal Spike Sequences in Adult Rat Barrel Cortex In Vivo. Cereb. Cortex 25, 2001–2021.

Rinaldi, T., Silberberg, G., and Markram, H. (2008). Hyperconnectivity of local neocortical microcircuitry induced by prenatal exposure to valproic acid. Cereb. Cortex 18, 763–770.

Romand, S., Wang, Y., Toledo-Rodriguez, M., and Markram, H. (2011). Morphological development of thick-tufted layer v pyramidal cells in the rat somatosensory cortex. Front. Neuroanat. 5, 5.

Rozov, A., Burnashev, N., Sakmann, B., and Neher, E. (2001). Transmitter release modulation by intracellular Ca^{2+} buffers in facilitating and depressing nerve terminals of pyramidal cells in layer 2/3 of the rat neocortex indicates a target cell-specific difference in presynaptic calcium dynamics. J. Physiol. 531, 807–826.

Rudy, B., Fishell, G., Lee, S., and Hjerling-Leffler, J. (2011). Three groups of interneurons account for nearly 100% of neocortical GABAergic neurons. Dev. Neurobiol. 71, 45–61.

Sakata, S., and Harris, K.D. (2009). Laminar structure of spontaneous and sensory-evoked population activity in auditory cortex. Neuron 64, 404–418.

Salinas, E., and Sejnowski, T.J. (2001). Correlated neuronal activity and the flow of neural information. Nat. Rev. Neurosci. 2, 539–550.

Sancesario, G., Pisani, A., D'Angelo, V., Calabresi, P., and Bernardi, G. (1998). Morphological and functional study of dwarf neurons in the rat striatum. Eur. J. Neurosci. 10, 3575–3583.

Sanchez-Vives, M.V., and McCormick, D.A. (2000). Cellular and network mechanisms of rhythmic recurrent activity in neocortex. Nat. Neurosci. 3, 1027–1034.

Santana, R., McGarry, L.M., Bielza, C., Larrañaga, P., and Yuste, R. (2013). Classification of neocortical interneurons using affinity propagation. Front. Neural Circuits 7, 185.

Sarid, L., Bruno, R., Sakmann, B., Segev, I., and Feldmeyer, D. (2007). Modeling a layer 4-to-layer 2/3 module of a single column in rat neocortex: interweaving in vitro and in vivo experimental observations. Proc. Natl. Acad. Sci. USA 104, 16353–16358.

Schroeder, C.E., and Foxe, J.J. (2002). The timing and laminar profile of converging inputs to multisensory areas of the macaque neocortex. Brain Res. Cogn. Brain Res. 14, 187–198.

Schürmann, F., Delalondre, F., Kumbhar, P.S., Biddiscombe, J., Gila, M., Tacchella, D., Curioni, A., Metzler, B., Morjan, P., Fenkes, J., et al. (2014). Rebasing I/O for Scientific Computing: Leveraging Storage Class Memory in an IBM BlueGene/Q Supercomputer (Leipzig, Germany: Springer International Publishing Switzerland), pp. 331–347.

Shu, Y., Hasenstaub, A., and McCormick, D.A. (2003). Turning on and off recurrent balanced cortical activity. Nature 423, 288–293.

Sigalas, C., Rigas, P., Tsakanikas, P., and Skaliora, I. (2015). High-Affinity Nicotinic Receptors Modulate Spontaneous Cortical Up States In Vitro. J. Neurosci. 35, 11196–11208.

Silberberg, G. (2008). Polysynaptic subcircuits in the neocortex: spatial and temporal diversity. Curr. Opin. Neurobiol. 18, 332–337.

Silberberg, G., and Markram, H. (2007). Disynaptic inhibition between neocortical pyramidal cells mediated by Martinotti cells. Neuron 53, 735–746.

Silberberg, G., Wu, C., and Markram, H. (2004). Synaptic dynamics control the timing of neuronal excitation in the activated neocortical microcircuit. J. Physiol. 556, 19–27.

Silva, L.R., Amitai, Y., and Connors, B.W. (1991). Intrinsic oscillations of neocortex generated by layer 5 pyramidal neurons. Science 251, 432–435.

Silver, R.A., Lubke, J., Sakmann, B., and Feldmeyer, D. (2003). High-probability uniquantal transmission at excitatory synapses in barrel cortex. Science 302, 1981–1984.

Simkus, C.R.L., and Stricker, C. (2002). Properties of mEPSCs recorded in layer II neurones of rat barrel cortex. J. Physiol. 545, 509–520.

Singer, W. (1993). Synchronization of cortical activity and its putative role in information processing and learning. Annu. Rev. Physiol. 55, 349–374.

Somogyi, P., Freund, T.F., and Cowey, A. (1982). The axo-axonic interneuron in the cerebral cortex of the rat, cat and monkey. Neuroscience 7, 2577–2607.

Somogyi, P., Tamás, G., Lujan, R., and Buhl, E.H. (1998). Salient features of synaptic organisation in the cerebral cortex. Brain Res. Brain Res. Rev. 26, 113–135.

Sporns, O., and Kötter, R. (2004). Motifs in brain networks. PLoS Biol. 2, e369.

Spruston, N. (2008). Pyramidal neurons: dendritic structure and synaptic integration. Nat. Rev. Neurosci. 9, 206–221.

Stepanyants, A., Martinez, L.M., Ferecskó, A.S., and Kisvárday, Z.F. (2009). The fractions of short- and long-range connections in the visual cortex. Proc. Natl. Acad. Sci. USA 106, 3555–3560.

Steriade, M., Nuñez, A., and Amzica, F. (1993). A novel slow (< 1 Hz) oscillation of neocortical neurons in vivo: depolarizing and hyperpolarizing components. J. Neurosci. 13, 3252–3265.

Svoboda, K., Denk, W., Kleinfeld, D., and Tank, D.W. (1997). In vivo dendritic calcium dynamics in neocortical pyramidal neurons. Nature 385, 161–165.

Szabadics, J., Varga, C., Molnár, G., Oláh, S., Barzó, P., and Tamás, G. (2006). Excitatory effect of GABAergic axo-axonic cells in cortical microcircuits. Science 311, 233–235.

Tamás, G., Somogyi, P., and Buhl, E.H. (1998). Differentially interconnected networks of GABAergic interneurons in the visual cortex of the cat. J. Neurosci. 18, 4255–4270.

Tan, A.Y.Y., Chen, Y., Scholl, B., Seidemann, E., and Priebe, N.J. (2014). Sensory stimulation shifts visual cortex from synchronous to asynchronous states. Nature 509, 226–229.

Thomson, A.M., and Bannister, A.P. (1998). Postsynaptic pyramidal target selection by descending layer III pyramidal axons: dual intracellular recordings and biocytin filling in slices of rat neocortex. Neuroscience 84, 669–683.

Thomson, A.M., and Deuchars, J. (1997). Synaptic interactions in neocortical local circuits: dual intracellular recordings in vitro. Cereb. Cortex 7, 510–522.

Thomson, A.M., and Lamy, C. (2007). Functional maps of neocortical local circuitry. Front. Neurosci 1, 19–42.

Thomson, A.M., Deuchars, J., and West, D.C. (1993). Large, deep layer pyramid-pyramid single axon EPSPs in slices of rat motor cortex display paired pulse and frequency-dependent depression, mediated presynaptically

and self-facilitation, mediated postsynaptically. J. Neurophysiol. *70*, 2354–2369.

Thomson, A.M., West, D.C., Hahn, J., and Deuchars, J. (1996). Single axon IPSPs elicited in pyramidal cells by three classes of interneurones in slices of rat neocortex. J. Physiol. *496*, 81–102.

Timofeev, I., Grenier, F., Bazhenov, M., Sejnowski, T.J., and Steriade, M. (2000). Origin of slow cortical oscillations in deafferented cortical slabs. Cereb. Cortex *10*, 1185–1199.

Toledo-Rodriguez, M., Blumenfeld, B., Wu, C., Luo, J., Attali, B., Goodman, P., and Markram, H. (2004). Correlation maps allow neuronal electrical properties to be predicted from single-cell gene expression profiles in rat neocortex. Cereb. Cortex *14*, 1310–1327.

Toledo-Rodriguez, M., Goodman, P., Illic, M., Wu, C., and Markram, H. (2005). Neuropeptide and calcium-binding protein gene expression profiles predict neuronal anatomical type in the juvenile rat. J. Physiol. *567*, 401–413.

Tsodyks, M.V., and Markram, H. (1997). The neural code between neocortical pyramidal neurons depends on neurotransmitter release probability. Proc. Natl. Acad. Sci. USA *94*, 719–723.

van Vreeswijk, C., and Sompolinsky, H. (1996). Chaos in neuronal networks with balanced excitatory and inhibitory activity. Science *274*, 1724–1726.

Wang, Z., and McCormick, D.A. (1993). Control of firing mode of corticotectal and corticopontine layer V burst-generating neurons by norepinephrine, acetylcholine, and 1S,3R-ACPD. J. Neurosci. *13*, 2199–2216.

Wang, Y., Gupta, A., Toledo-Rodriguez, M., Wu, C.Z., and Markram, H. (2002). Anatomical, physiological, molecular and circuit properties of nest basket cells in the developing somatosensory cortex. Cereb. Cortex *12*, 395–410.

Wang, Y., Toledo-Rodriguez, M., Gupta, A., Wu, C., Silberberg, G., Luo, J., and Markram, H. (2004). Anatomical, physiological and molecular properties of Martinotti cells in the somatosensory cortex of the juvenile rat. J. Physiol. *561*, 65–90.

Wang, Y., Markram, H., Goodman, P.H., Berger, T.K., Ma, J., and Goldman-Rakic, P.S. (2006). Heterogeneity in the pyramidal network of the medial prefrontal cortex. Nat. Neurosci. *9*, 534–542.

West, M.J., and Gundersen, H.J. (1990). Unbiased stereological estimation of the number of neurons in the human hippocampus. J. Comp. Neurol. *296*, 1–22.

Westerink, B.H.C., Hofsteede, H.M., Damsma, G., and de Vries, J.B. (1988). The significance of extracellular calcium for the release of dopamine, acetylcholine and amino acids in conscious rats, evaluated by brain microdialysis. Naunyn Schmiedebergs Arch. Pharmacol. *337*, 373–378.

Wickersham, I.R., Finke, S., Conzelmann, K.-K., and Callaway, E.M. (2007). Retrograde neuronal tracing with a deletion-mutant rabies virus. Nat. Methods *4*, 47–49.

Williams, S.R., and Mitchell, S.J. (2008). Direct measurement of somatic voltage clamp errors in central neurons. Nat. Neurosci. *11*, 790–798.

Williams, R.W., and Rakic, P. (1988). Three-dimensional counting: an accurate and direct method to estimate numbers of cells in sectioned material. J. Comp. Neurol. *278*, 344–352.

Wilson, N.R., Runyan, C.A., Wang, F.L., and Sur, M. (2012). Division and subtraction by distinct cortical inhibitory networks in vivo. Nature *488*, 343–348.

Wimmer, V.C., Bruno, R.M., de Kock, C.P.J., Kuner, T., and Sakmann, B. (2010). Dimensions of a projection column and architecture of VPM and POm axons in rat vibrissal cortex. Cereb. Cortex *20*, 2265–2276.

Yoshimura, Y., Kimura, F., and Tsumoto, T. (1999). Estimation of single channel conductance underlying synaptic transmission between pyramidal cells in the visual cortex. Neuroscience *88*, 347–352.

Yuste, R. (2005). Origin and classification of neocortical interneurons. Neuron *48*, 524–527.

Yuste, R., Tank, D.W., and Kleinfeld, D. (1997). Functional study of the rat cortical microcircuitry with voltage-sensitive dye imaging of neocortical slices. Cereb. Cortex *7*, 546–558.

Zagha, E., and McCormick, D.A. (2014). Neural control of brain state. Curr. Opin. Neurobiol. *29*, 178–186.

Zhu, J.J. (2000). Maturation of layer 5 neocortical pyramidal neurons: amplifying salient layer 1 and layer 4 inputs by Ca^{2+} action potentials in adult rat tuft dendrites. J. Physiol. *526*, 571–587.
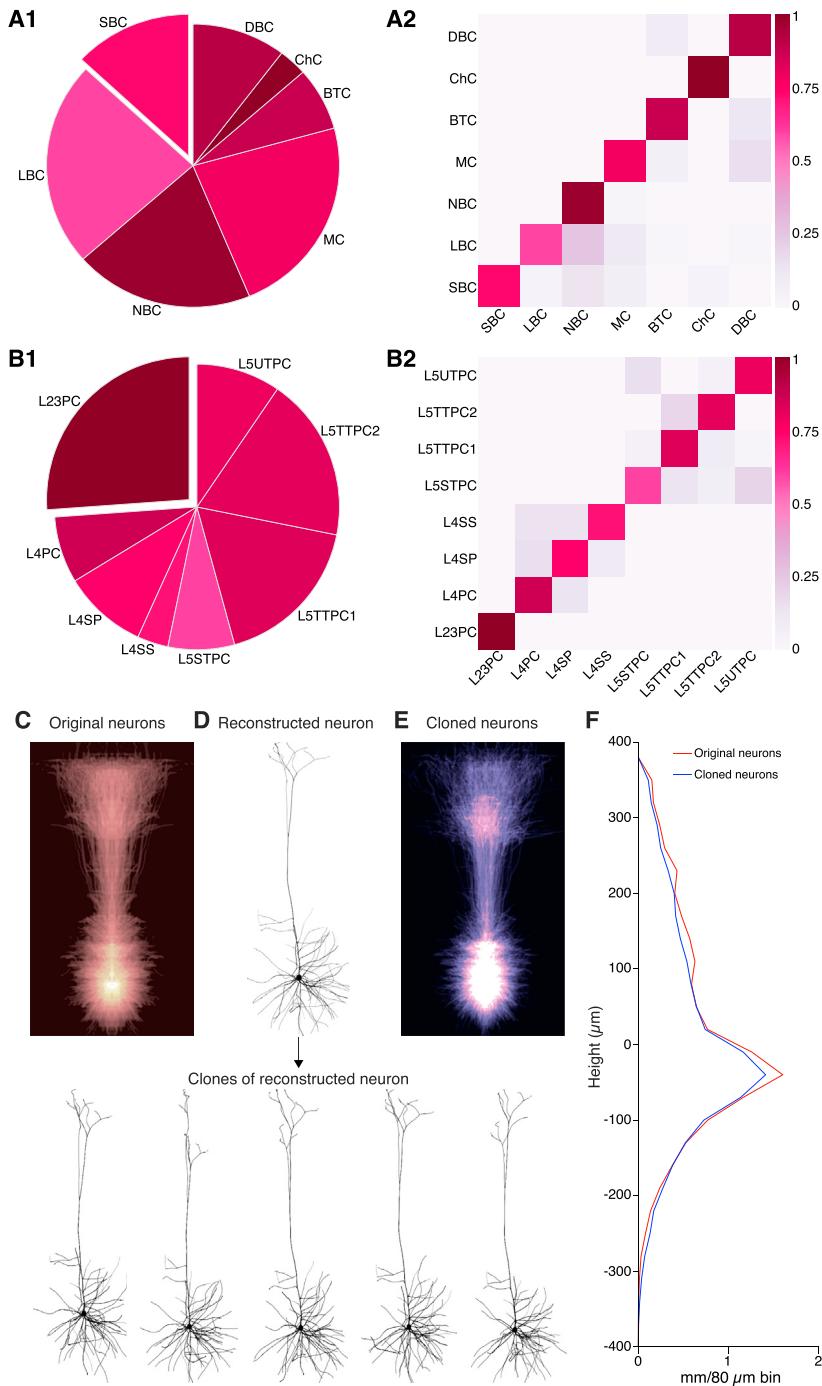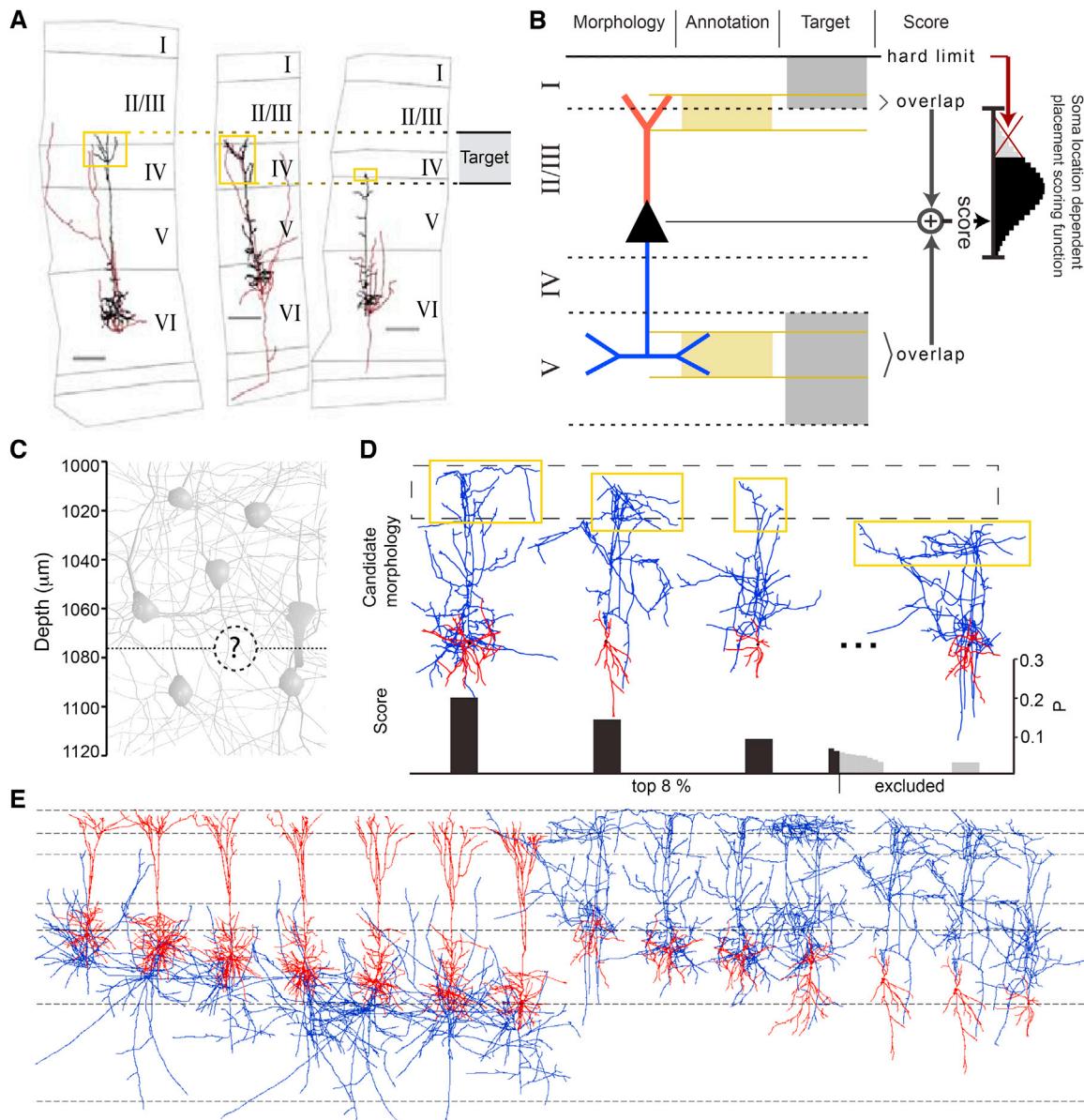
Figure S1. A Table of m-Type Arbor Densities, Related to Figure 2

2D projection of m-types, obtained by overlaying multiple reconstructed morphologies, aligning somata to a single point, and summing the fiber length per μm^3 (axon left, blue; dendrite right, red). Density plots for 55 known inhibitory and excitatory m-types arranged horizontally by layer. Inset, expanded L5TTPC with an exemplar reconstruction superimposed. Abbreviations as defined in Table 1.
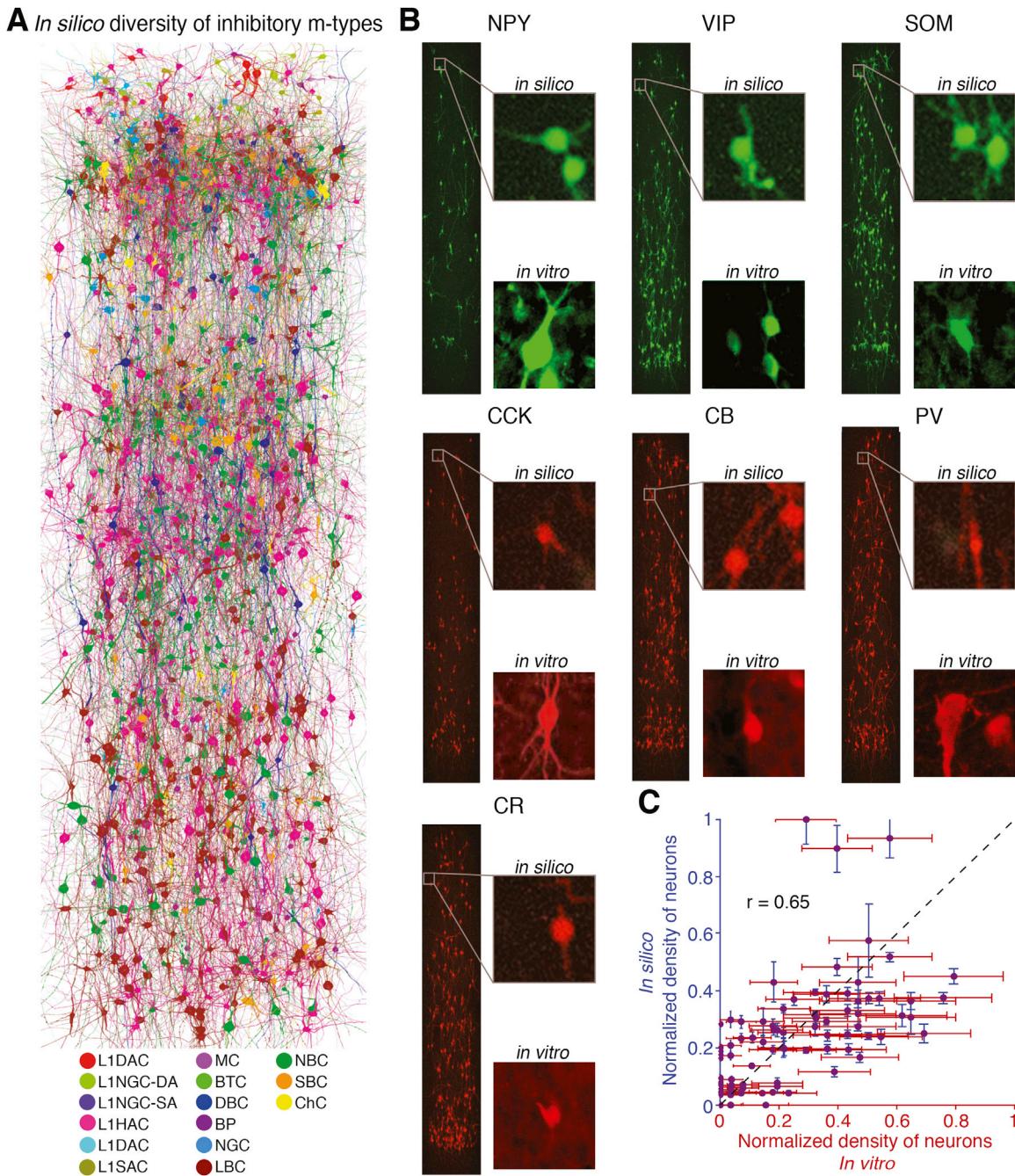
Figure S2. Objective Classification of m-Types and Cloning, Related to Figure 2

Summary of classification robustness for L2-6 interneurons (A1, A2) and L2-5 pyramidal cells (B1, B2). Left panels (A1, B1) show the relative sizes of the populations. Colors represent classification accuracy, which is quantified in the right hand panels. Classification accuracy is defined as the number of successfully classified cells over the total number of cells in a class for each m-type. (A2) Detailed results of hierarchical clustering for interneuron classes. The vertical axis shows expert assigned classes; the horizontal axis shows objectively assigned classes, using supervised hierarchical clustering with feature selection. (B2) Detailed results of supervised clustering with feature selection for pyramidal cell classes. The axes are the same as in panel (A2). (C) Fiber density image of all repaired L5TTPC as in Figure S1. (D) Upper reconstructed neuron was cloned by introducing variability in branch lengths and angles (see Experimental Procedures); 5 sample clones shown below. (E) As in C, for randomly selected L5TTPC clones. (F) Fiber density plot comparing mean fiber length of original versus cloned L5TTPCs at different heights grouped in 80 μm bins.
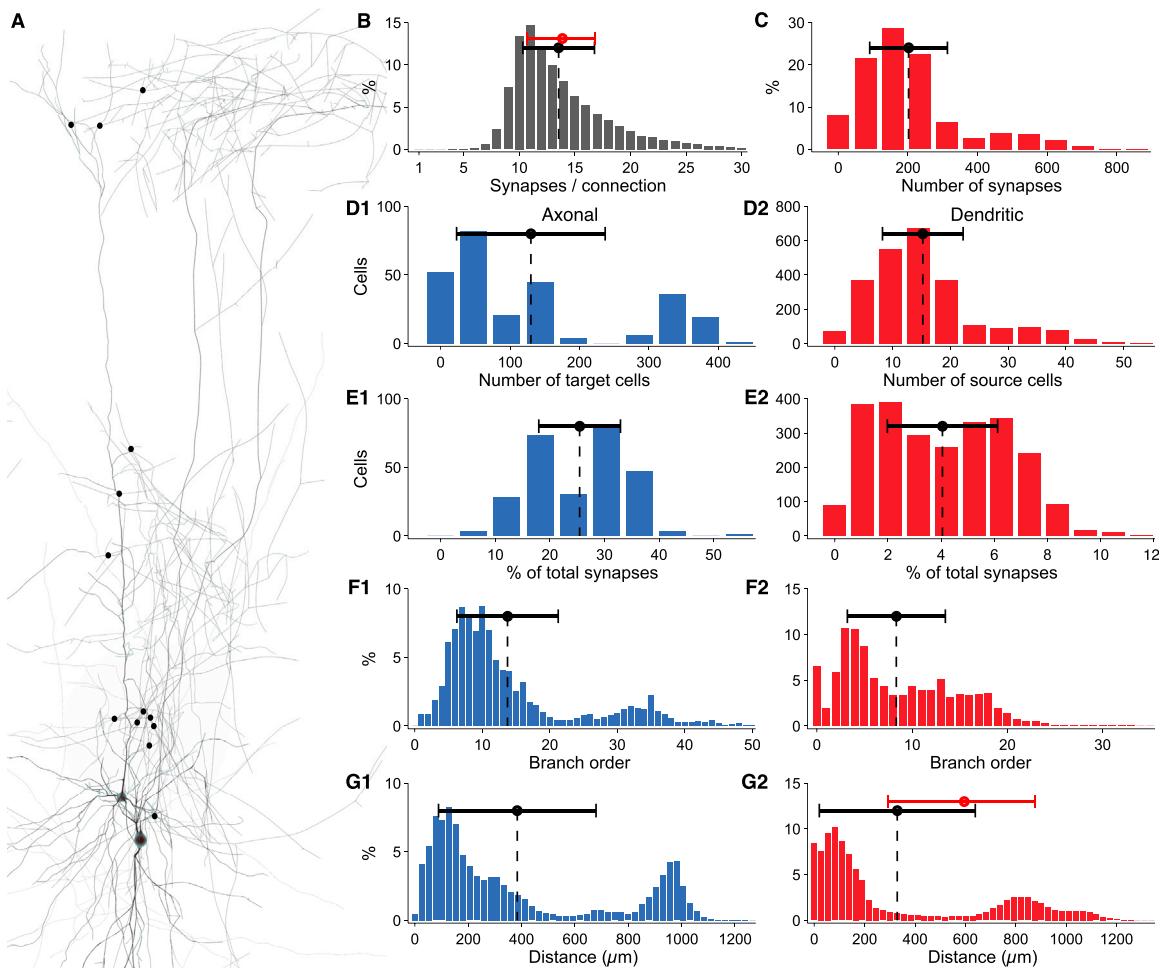
Figure S3. Reconstructing Inter-laminar Architecture, Related to Figure 3

(A) Constraining rules for placing morphologies of different m-types. (B) Morphology-placement scoring algorithm. *Placement* – placement of morphologies. *Annotation* – annotation of the extent of axonal and dendritic clusters. *Target* – determination of absolute target depth intervals. *Score* – calculation of overlap between annotated and target areas. (C) Determining soma and m-type positions. (D) Selecting morphologies. Scores are calculated for all morphologies for all m-type positions. Morphologies are ordered from left to right according to their descending scores for a given position. (E) Collage of L5TTPC1 (left) and L5MC (right) morphologies showing placement relative to layer boundaries.

A *In silico* diversity of inhibitory m-types

B NPY   VIP   SOM

in silico   *in silico*   *in silico*

in vitro   *in vitro*   *in vitro*

CCK   CB   PV

in silico   *in silico*   *in silico*

in vitro   *in vitro*   *in vitro*

CR   **C**

in silico

in vitro

Legend:
- L1DAC
- L1NGC-DA
- L1NGC-SA
- L1HAC
- L1DAC
- L1SAC
- MC
- BTC
- DBC
- BP
- NGC
- LBC
- NBC
- SBC
- ChC

(C) r = 0.65; axes: *In silico* Normalized density of neurons (y); Normalized density of neurons *In vitro* (x)

Figure S4. Validating Morphological Composition, Related to Figure 3

(A) Morphologically reconstructed microcircuit. Only inhibitory m-types are shown. (B) Tissue stainings. *In silico* and *in vitro* labeling of m-types for neuropeptides: Neuropeptide Y (NPY), Vasoactive intestinal polypeptide (VIP), Somatostatin (SOM), Cholecystokinin (CCK), and calcium binding proteins (Calbindin (CB), Parvalbumin (PV), and Calretinin (CR). (C) Neuron counts. The number of stained neurons per 100 μm bin from L1 to L6. Red: *in vitro* counts/bin, blue: *in silico* counts/bin (N = 100 bins; mean±SD). Dashed line has unit slope. Linear regression shows r = 0.65 (CR and CCK counts are excluded).
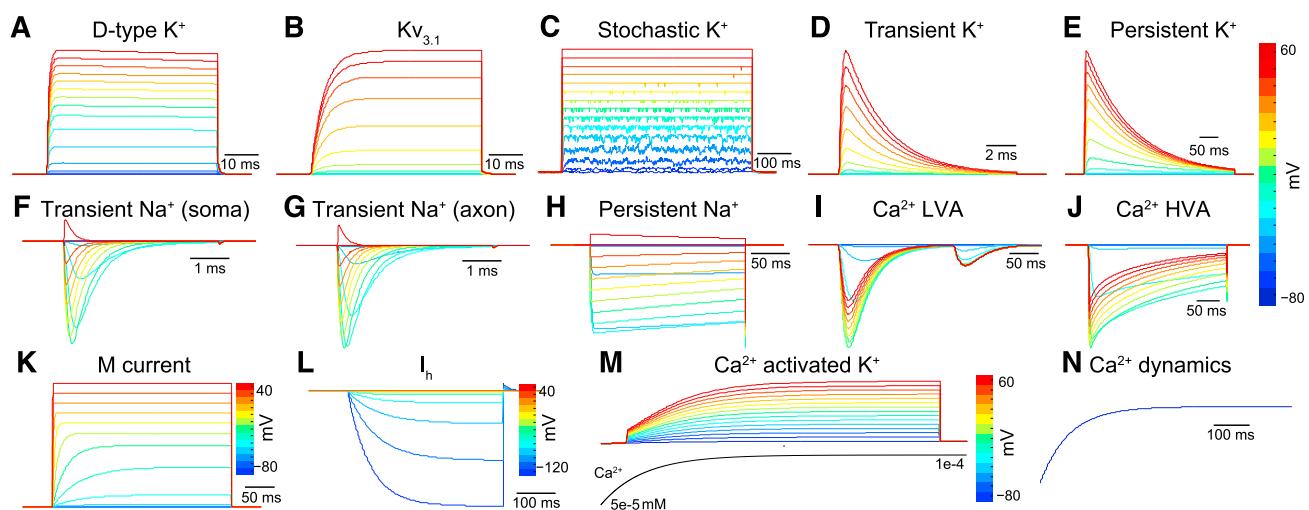
Figure S5. Predicting the Detailed Anatomical Properties of a Synaptic Pathway, Related to Figure 7

Predicted properties of the L5MC to L5TTPC pathway: (A) *In silico* L5MC to L5TTPC synaptic connection. Synaptic contacts are shown as black circles (B) Number of synapses per connection (black dashed line, predicted mean; black line, predicted SD; red line, experimental data, mean±SD). (C) Distribution of total number of synapses from L5MCs to L5TTPCs. (D1) Neuronal divergence, number of L5TTPCs targeted by single L5MCs. (D2) Neuronal convergence, number of L5MCs targeting single L5TTPCs. (E1) Synaptic divergence, fraction of all synapses formed by L5MCs that target L5TTPCs. (E2). Synaptic convergence, fraction of all synapses formed onto L5TTPCs from L5MCs. (F1) Axonal and (F2) dendritic innervation patterns in terms of branch order of synaptic contacts. (G1, G2) Same as F, in terms of geometrical distance of synaptic contacts.
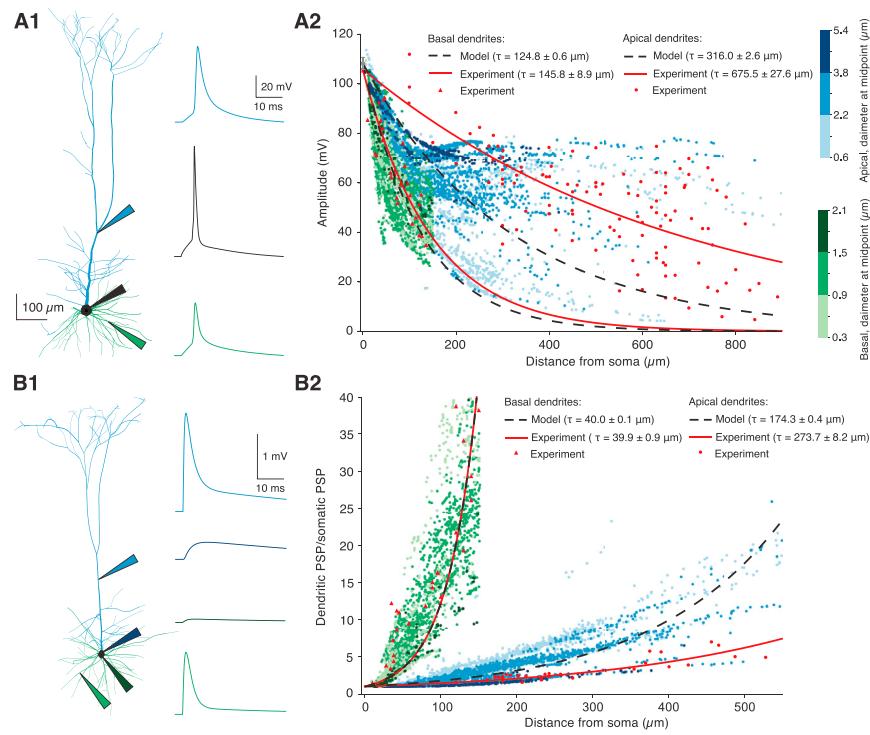
Figure S6. Synapse Counts and Balance by m-Type in the Reconstructed Microcircuit, Related to Figure 7

(A) Afferent synapses. Average number of afferent synapses per m-type (N = 35; mean±SD). Inset: Image of neurons placed in the 3D volume displaying a fraction of appositions converted into synapses. (B) E-I synapse ratios. Average ratio of excitatory and inhibitory synapses per m-type (N = 35; mean±SD). Inset: Image of excitatory (red) and inhibitory (blue) synapses. (C) Percentages of synapses in excitatory (red) and inhibitory (blue) connections in the microcircuit (layer 1 omitted). Arrow width and numbers indicate the percentage of total synapses formed by the pathway (omitted for pathways with <1% of synapses). The total percentage of plotted synapses is 98%; the remaining 2% originate in layer 1. Rectangle sizes are proportional to the sizes of the corresponding excitatory or inhibitory populations. (D) An exemplary L6UTPC with all afferent synapses highlighted. Different colors indicate different presynaptic m-types. (E) Comparing the density of excitatory synapses across the dendritic tree for 55 m-types in the reconstructed connectome (blue bars: mean±SD of neurons in a microcircuit) against biological data (red lines, data from: (Riccio and Matthews, 1985; Larkman, 1991b; Datwani, 2002; Bock et al., 2004; Mataga et al., 2004; Kawaguchi, 2006). The dashed line indicates the mean of the biological data, with the lower outliers excluded.
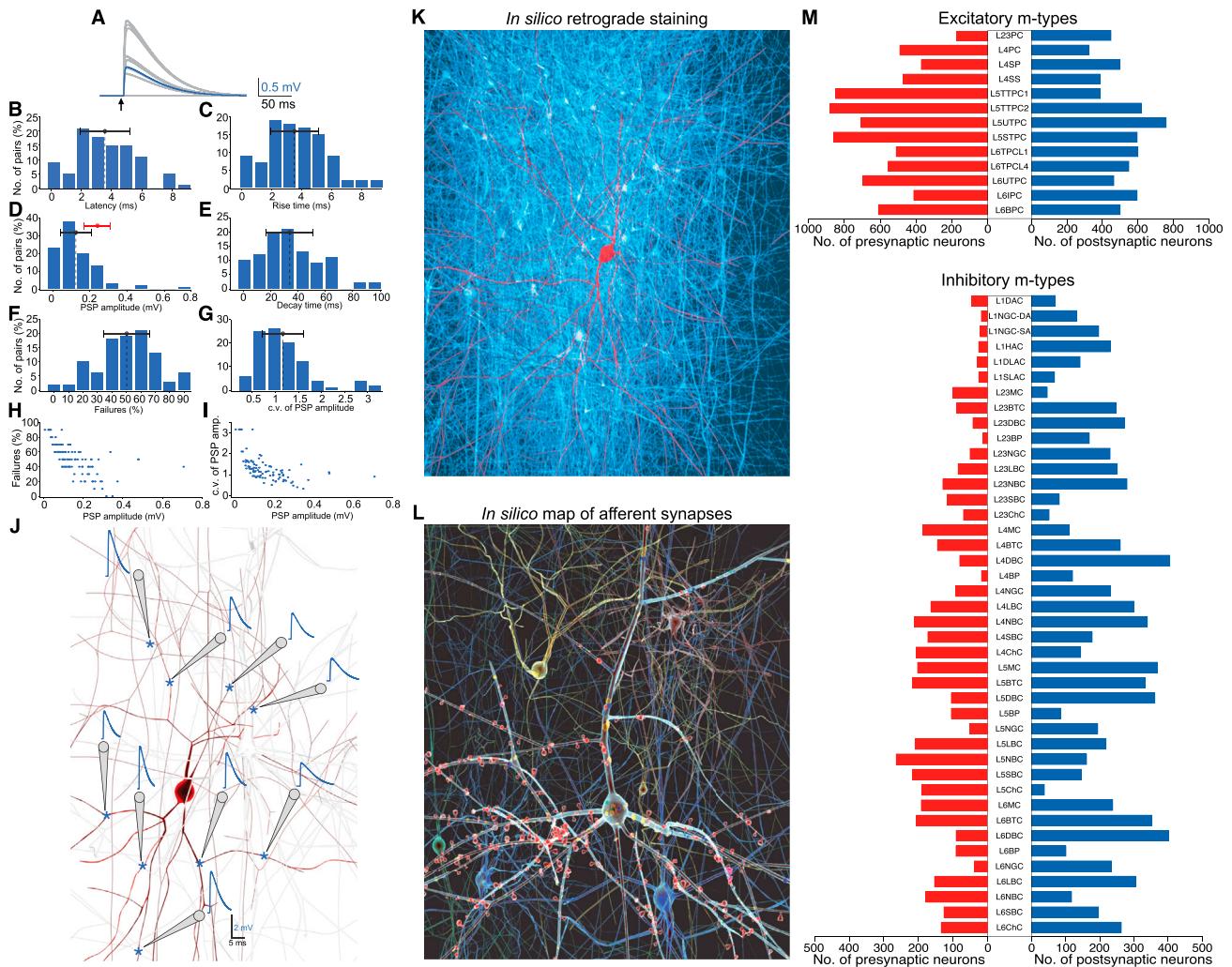
Figure S7. Modeling Ionic Mechanisms, Related to Figure 8
(A–N) Currents generated by voltage steps to model 13 Hodgkin-Huxley type ion channel classes, and one model of intracellular Ca^{2+} dynamics.
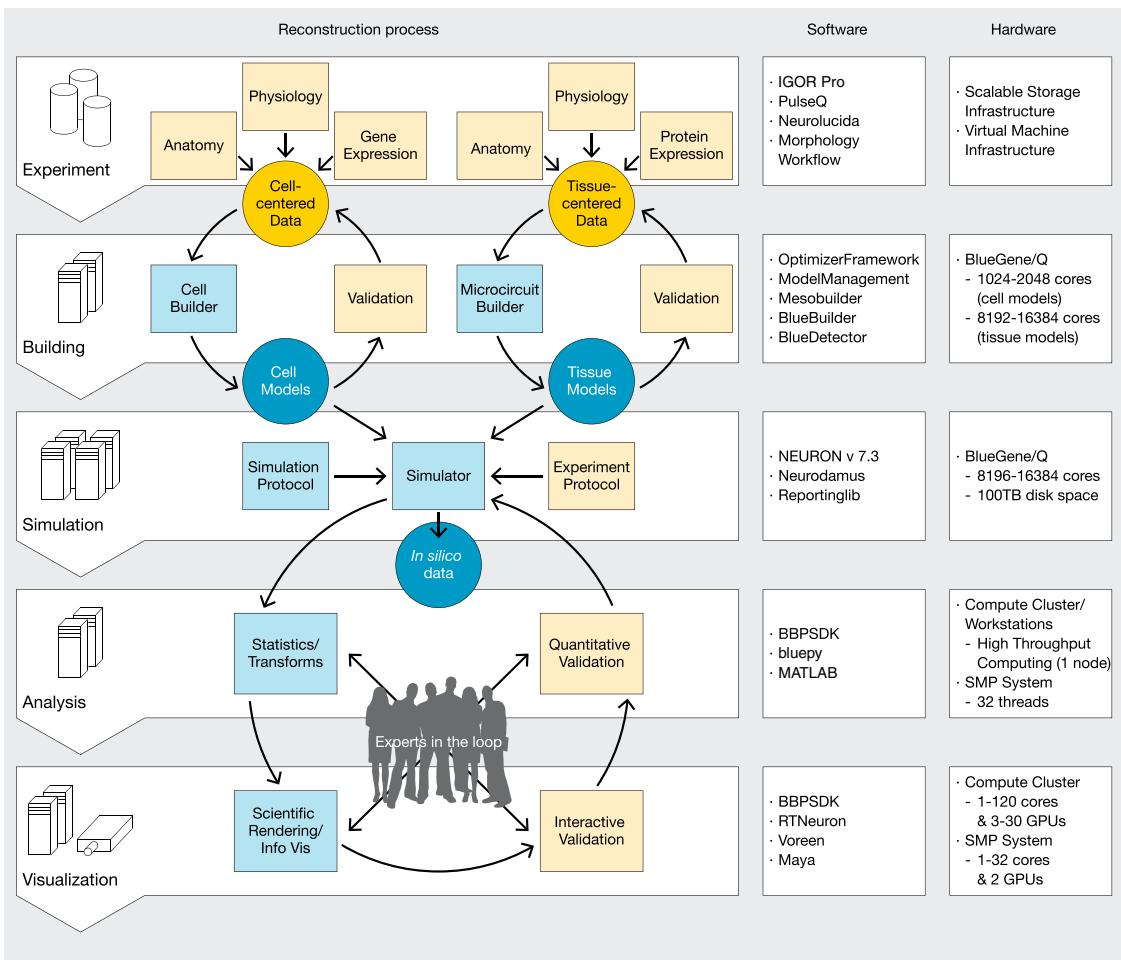
Figure S8. Validating Dendritic Properties of Neuron Models, Related to Figure 8

(A1) Simulation of back-propagating APs (bAP) evoked by somatic current pulse injections (5ms, 2nA) to a single L5TTPC (blue, apical dendrites; green, basal dendrites). Simultaneous recordings in the apical dendrite (blue voltage trace, ~300 μm from the soma), the soma (black) and basal dendrite (green, ~100 μm from the soma). (A2) Predicted bAP amplitude measured at different locations on apical (blue dots) or basal dendrites (green dots). Color bar indicates diameter of apical and basal dendrites at different distances from somata. Exponential fits shown as black dashed lines. Red dots, from Figure 8D of Larkum et al. (2001); red triangles from Figure 1g of Nevian et al. (2007). (B1) Simultaneous quadruple in silico recordings of evoked EPSPs induced by a transient change in synaptic conductance in distal apical (1.5 nS) and basal dendrites (0.2 nS) of a single L5TTPC (blue, apical dendrites; green, basal dendrites) mimicking previous recordings (apical, Figure 2B of Berger et al. (2001); basal, Figure 4C of Nevian et al. (2007)). Recording in distal apical dendrite (blue, ~270 μm from the soma), proximal apical dendrite (dark blue), distal basal dendrite (green, ~100 μm from the soma) and proximal basal dendrite (dark green). (B2) Predicted dendritic to somatic attenuation ratio for in silico EPSP amplitudes measured at different locations on apical (blue dots) and basal dendrites (green dots). Exponential fits shown as black dashed lines. Red dots, from Figure 3C of Berger et al. (2001). Red triangles, from Figure 2e of Nevian et al. (2007). Exponential fits used the Levenberg-Marquardt algorithm. In A2 and B2, in silico recordings from 500 randomly selected L5TTPCs with diameters larger than 0.5 μm; 10 recordings per neuron from apical and basal sections.
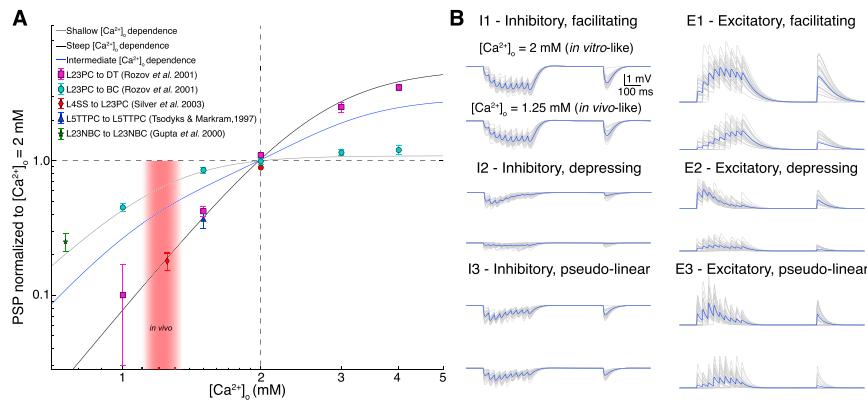
Figure S9. In Silico Synaptic Experiments, Related to Figure 10

(A) Average time course and amplitude of unitary EPSPs evoked in silico in a L5MC by a presynaptic L5TTPC. Black arrow, presynaptic AP; grey, 30 trials of individual postsynaptic responses; blue, mean of 30 trials. (B) Histogram of EPSP onset latency (N = 100 pairs, sampled at intersomatic distances ≤ 100 μm). Black dashed line, mean±SD. (C) Histogram of 20-80% EPSP rise time. (D) Histogram of EPSP amplitudes. Red line, mean±SD of experimental data. (E) Histogram of EPSP decay time constants. (F) Histogram of transmission failures. (G) Histogram of the coefficient of variation (c.v.; defined as SD/mean) of EPSP amplitudes. (H) Inverse relationship between the rate of transmission failures and EPSP amplitude. (I) Same as in H, but for c.v. of EPSP amplitudes. (J) Direct *in silico* dendritic patch recordings of single synaptic contacts (light grey, presynaptic L5_TTPC; red, postsynaptic L5MC; blue stars, synaptic contacts; dark grey, recording pipette; blue, average EPSP). (K) In silico retrograde staining. The presynaptic neurons of a L23BNC (red) were stained (blue). Only immediate neighboring presynaptic neurons are shown. (L) Afferent synapses. Predicted synapses on a single exemplar L23PC, colored according to presynaptic m-type (red excitatory; other, inhibitory). (M) Top: Number of pre- (red) and postsynaptic (blue) neurons for neurons of excitatory m-types (mean of neurons in a microcircuit). Bottom: Same, for inhibitory m-types.
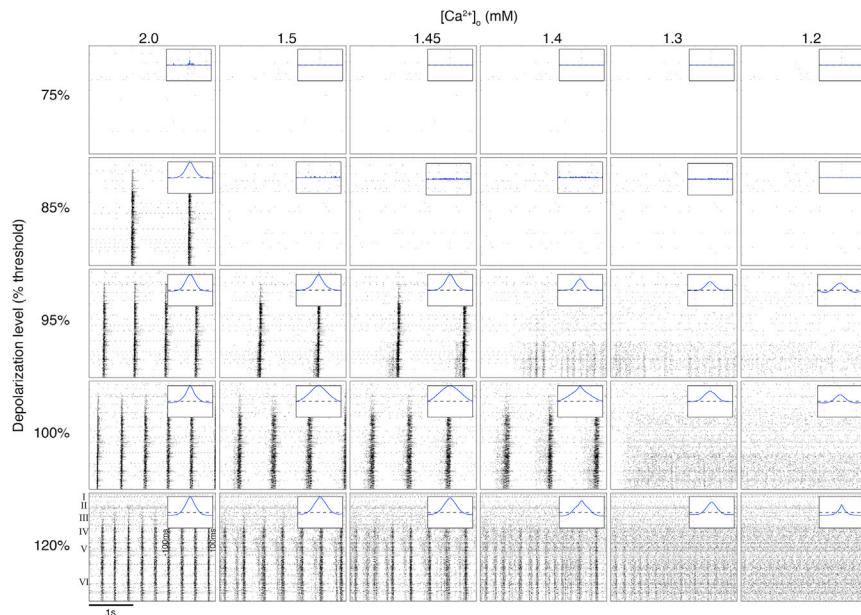
Figure S10. Computing Challenges, Related to Figure 11

Ecosystem of software components and workflows for the reconstruction of neural microcircuitry. Some components are executed on a supercomputer. Left: phases of the reconstruction process workflow; Right: software and hardware. Experiment: protocol standardization, metadata annotation, and curation workflows for consumption of experimental data. Building: Workflow for data-driven reconstruction of neuron, and tissue models. Simulation: *In silico* experimentation capabilities for reconstructed microcircuitry. Analysis and validation of reconstructed and simulated microcircuitry using common analysis environments. Visualization of simulated microcircuitry.
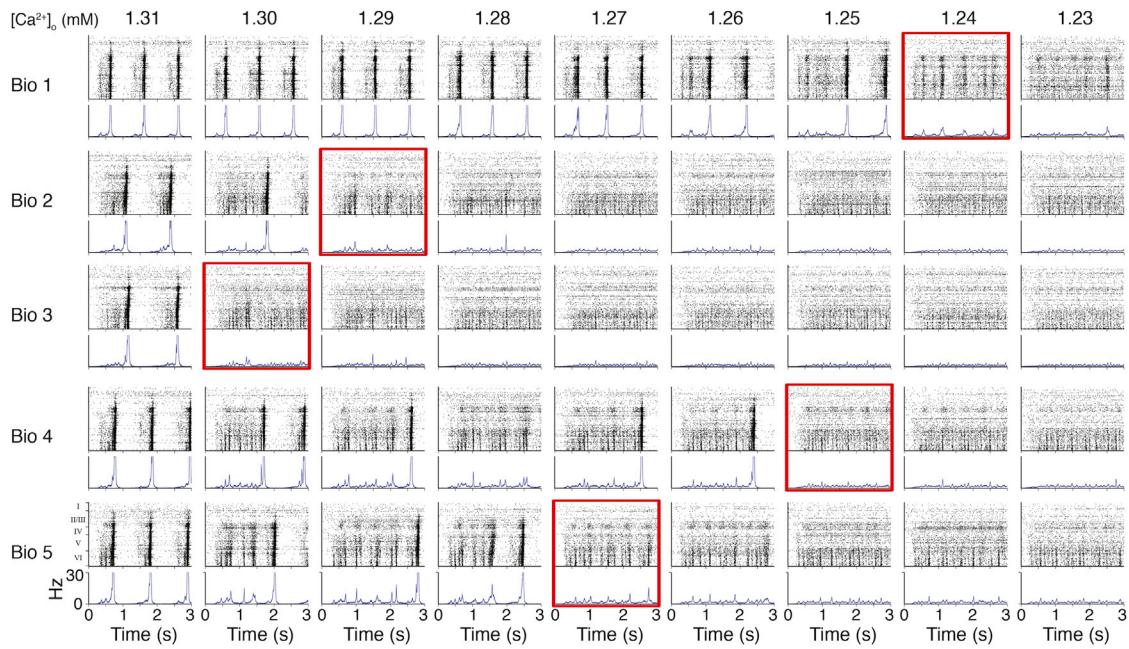
Figure S11. Ca²⁺ Sensitivity of Synaptic Physiology, Related to Figures 12 and 13

(A) Experimental data on the dependence between EPSP amplitudes and $[Ca^{2+}]_o$ are consistent with either a steep (black line) or shallow (grey line) dependence (adapted from Rozov et al. (2001)), fits are Hill isotherms; $K_{1/2}$=2.79 for steep, $K_{1/2}$=1.09 for shallow). Based on these sparse data, we assumed a steep Ca^{2+}-dependence for connections between PC-PC and PC-distal targeting cell types (DBC, BTC, MC, BP) and a shallow dependence between PC-proximal targeting cell types (LBCs, NBCs, SBCs, ChC). Pathways that had not been studied experimentally were assumed to have an intermediate level of dependence (blue line; average of steep and shallow). In vivo Ca^{2+} levels in the range 1.1-1.3mM are depicted in red (Borst, 2010). (B) Effect of changes in Ca^{2+} levels on synapse types. Synaptic responses in the presence of $[Ca^{2+}]$ = 2.0 mM (in vitro-like; upper traces) and 1.25 mM (in vivo-like; lower traces).
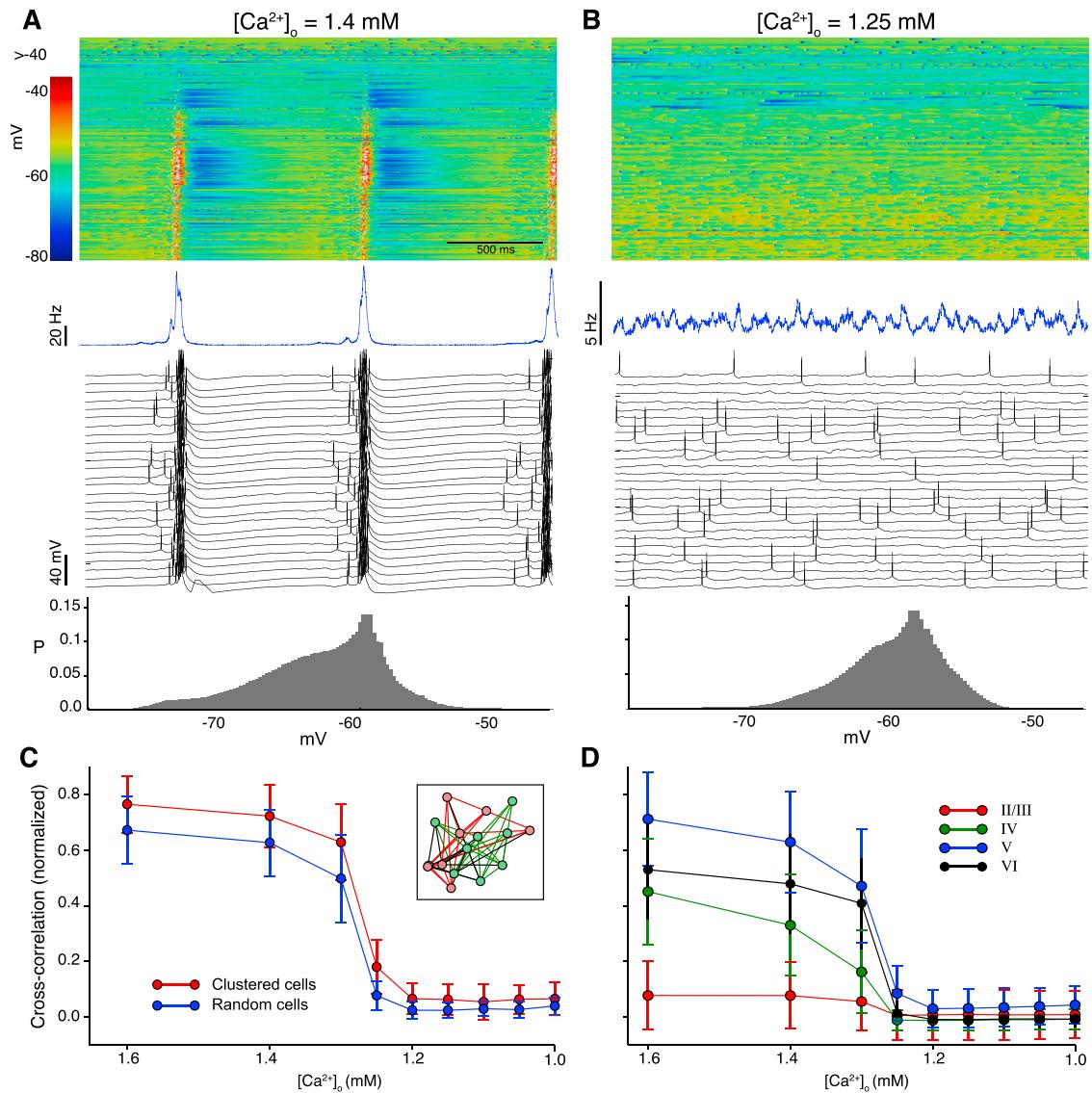
Figure S12. A Synchronous-Asynchronous Spectrum of Network States, Related to Figure 12

Systematic exploration of emergent network states, as assessed by spike raster plots, for a range of $[Ca^{2+}]_o$ (horizontal axis) and depolarization levels (vertical axis, see Experimental Procedures). $[Ca^{2+}]_o$ at typical in vitro levels (2.0 mM) and sufficient depolarization leads to synchronous network bursting. Lowering $[Ca^{2+}]_o$ towards in vivo levels ($\sim$1.0 mM) produces a transition to asynchronous firing. Spike-spike correlations (insets; each normalized) showing neurons remain functionally coupled in the asynchronous regime.
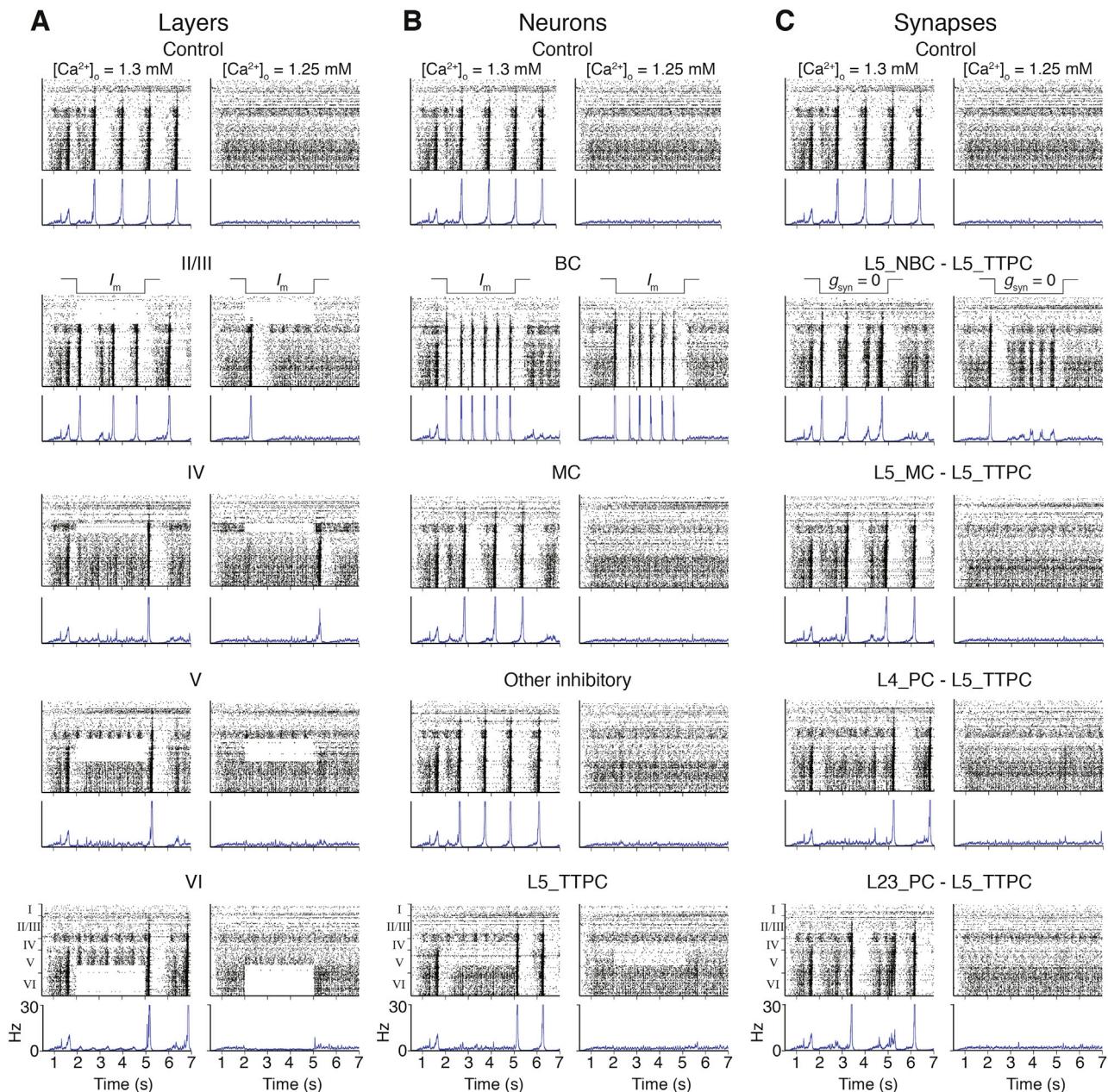
Figure S13. Biological Variability of the Synchronous-Asynchronous Transition, Related to Figure 12

Variability of the synchronous-asynchronous transition between instances of the microcircuit reconstructed using 5 biological datasets on neuron densities and layer heights in individual animals (vertical axis). Panels of raster plots (above) and PSTHs (below) of spontaneous activity are shown for a range of $[Ca^{2+}]_o$ (horizontal axis) for 100% depolarization. Red boxes indicate the level of $[Ca^{2+}]_o$ just below the transition to the synchronous regime.
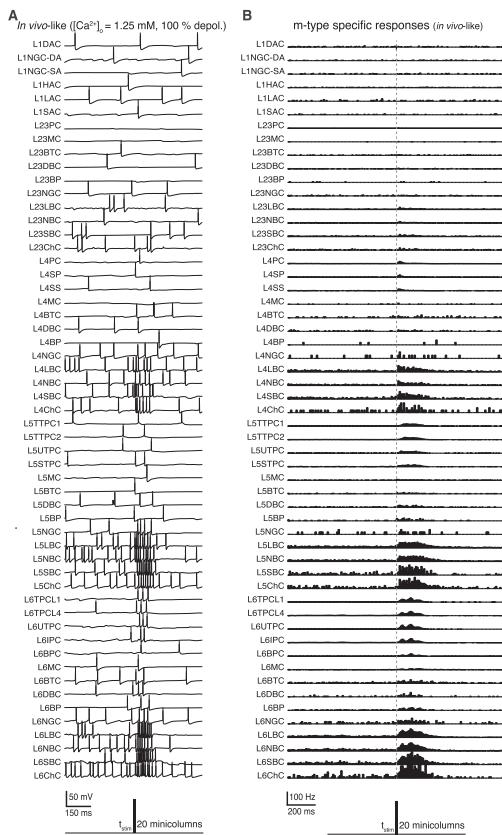
Figure S14. Synchrony of Synaptically Clustered Assemblies of Neurons, Related to Figure 12

(A) Spontaneous synchronous activity. Top to bottom: Voltage raster of a random selection of neurons across the 6 layers while the network was depolarized to 100% of spiking threshold (blue, hyperpolarized; red, depolarized; white, spike); PSTH of the activity; random selection of voltage traces of neurons across the 6 layers; the distribution of somatic membrane voltages. (B) Spontaneous asynchronous activity. Same as for A under lower $[Ca^{2+}]_o$. (C) Voltage cross-correlations for a range of $[Ca^{2+}]_o$. A set of 20 clusters having the highest number of common neighbors from a population of excitatory cells (inset; see Experimental Procedures). Voltage cross-correlation at dt = 0 (synchrony) for cell pairs in clusters (red), and for random pairs (blue; mean±SD). (D) Layer-dependent voltage cross-correlations. Voltage correlation at dt = 0 (synchrony) for cell pairs in clusters in different layers for a range of $[Ca^{2+}]_o$ (Red: L23PC; green: L4PC; blue: L5PC; black: L6PC, mean±SD).
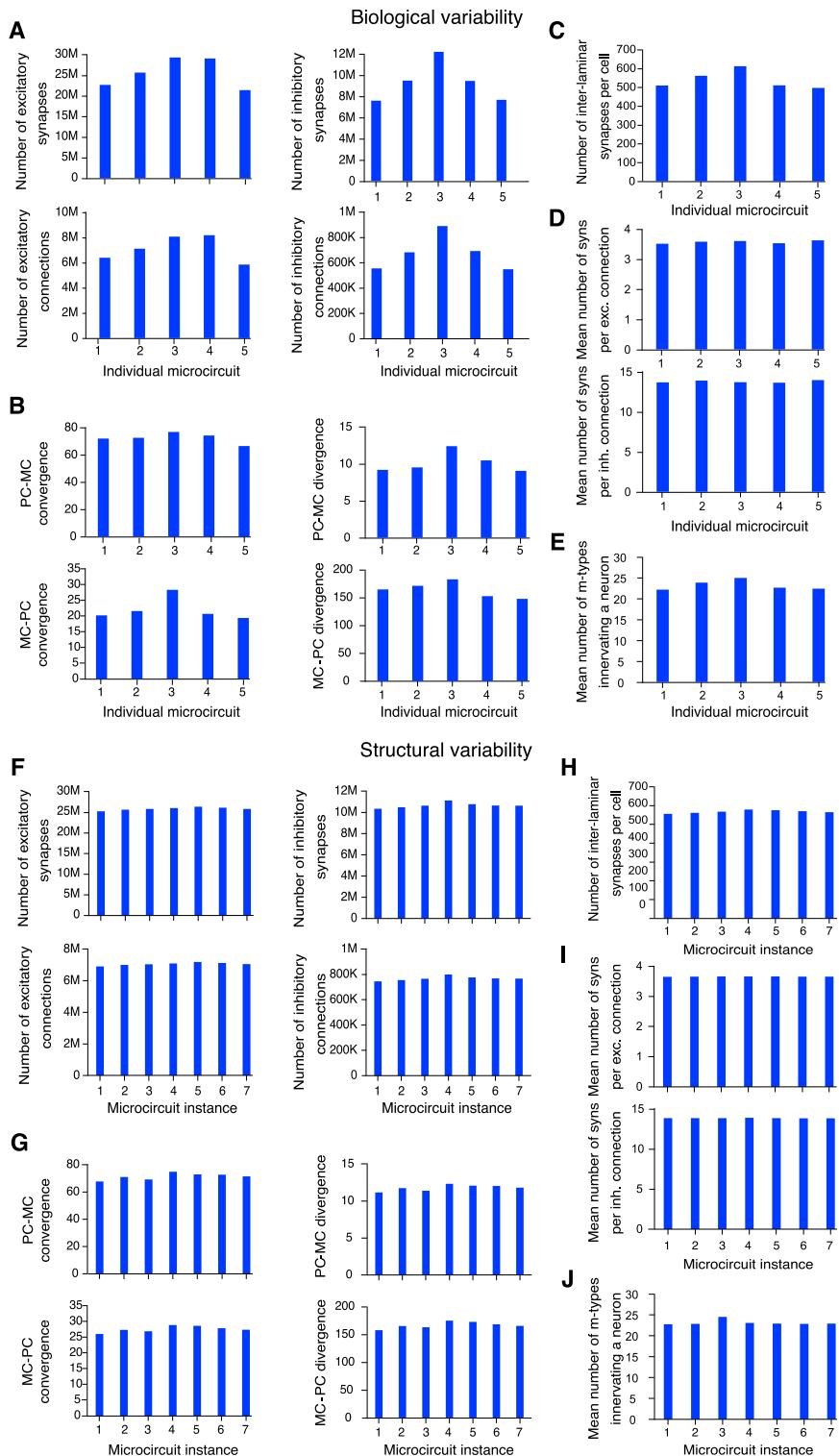
Figure S15. In Silico Blocking of Morphological Types, Synaptic Connections, and Layers, Related to Figure 12

Panels of raster plots (above) and PSTHs (below) of spontaneous activity just above (1.3 mM $[Ca^{2+}]_o$; left) and below (1.25 mM $[Ca^{2+}]_o$; right) the transition between the synchronous and asynchronous regimes. Upper panels show controls for A-C. (A) Blocking activity in all neurons in layers 2-6 (top to bottom) by hyperpolarization. (B) Blocking activity in selected sets of m-types by hyperpolarization. (C) Lesioning connections between specific pre- and postsynaptic m-types by transiently setting the conductances of all synapses between these m-types to zero. Onset and offset of blockade and lesion indicated below controls.
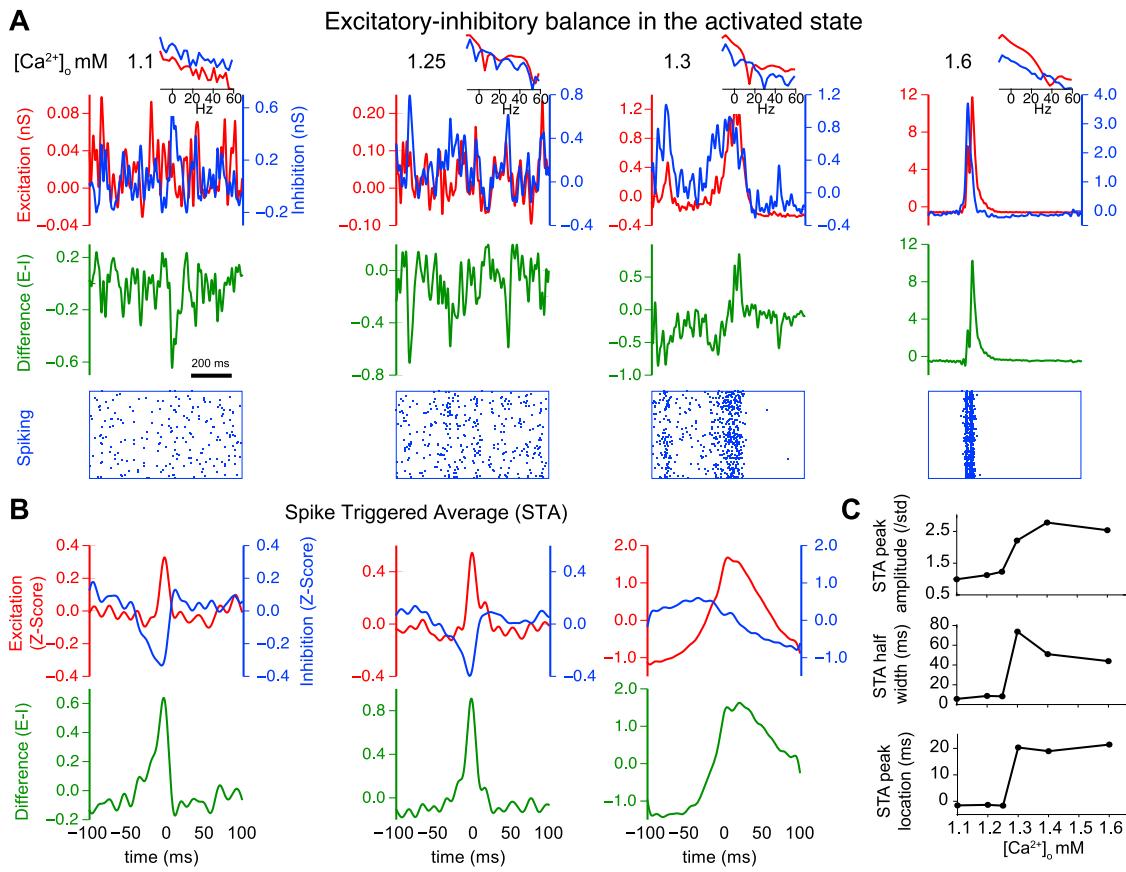
Figure S16. Evoked Activity, Related to Figure 14

Response of exemplary neurons from all 55 morphological types to a single pulse from 20 thalamic fibers. (A) Soma voltage traces under in-vivo-like conditions. (B) Spiking response as assessed by PSTHs.
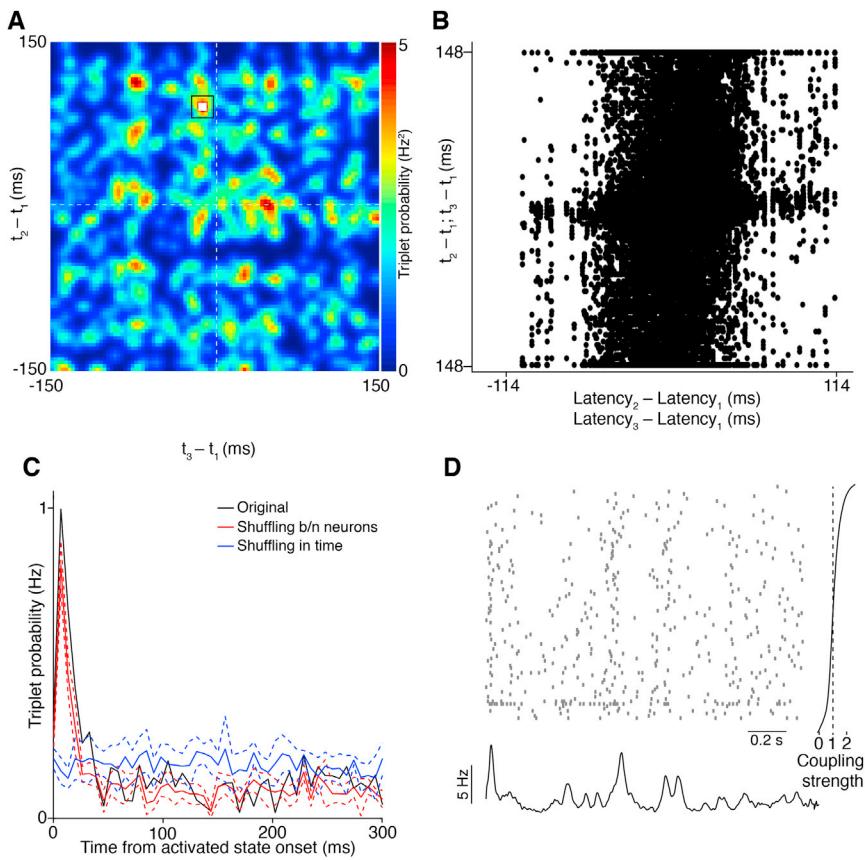
Figure S17. Biological and Statistical Variability of the Microcircuit, Related to Figure 16

Variability between instances of the microcircuit reconstructed using 5 biological datasets on neuron densities and layer heights in individual animals, as assessed by a number of emergent properties. (A) Numbers of synapses and connections. (B) Convergence and divergence in MC-PC connections. (C) Interlaminar innervation strength. (D) Synapses per connection. (E) Convergence of m-types. (F-J) As A-E, for the variability between seven statistical instances of the microcircuit, all reconstructed using the mean of the 5 biological datasets.
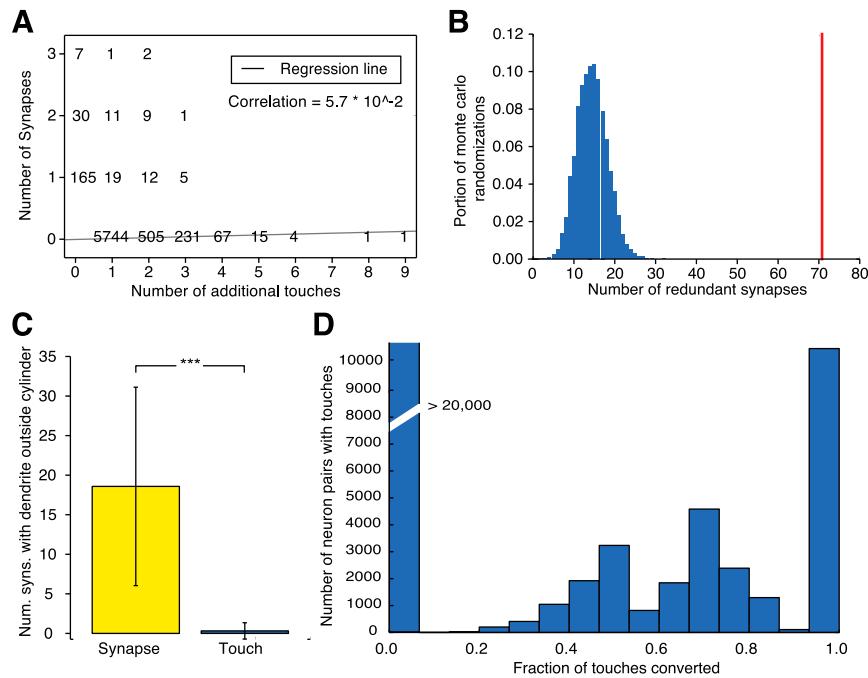
Figure S18. Excitatory-Inhibitory Balance in the Activated State, Related to Figure 17

(A) Top: Mean excitatory (red) and inhibitory (blue) conductance effective at the soma of 200 exemplary L6PCs at different points along the SA-spectrum (from left to right). Middle (green): Difference between effective excitation and inhibition. Bottom: Spiking activity of the population. (B) Top: Spike triggered average (STA) of excitation (red) and inhibition (blue) of L6PCs, normalized to a Z-Score; from left to right: different points along the SA-spectrum. Bottom (green): Difference between the excitatory and inhibitory STA. (C) From top to bottom: Amplitude, half width and location of the peak of E-I difference shown in B at different points of the SA-spectrum.

Figure S19. Degradation of Repeating Triplet Structure at Subthreshold Calcium Concentration and Examples of Soloists and Choristers, Related to Figure 18

(A) Count matrix for a representative neuron trio. Lowering extracellular calcium from 1.25 mM to 1.1 mM markedly increased isotropy of triplet structure probability distributions (cf. Figure 18A1). Count matrices for a majority of cell trios had no clearly distinguishable mode. (B) Correlation between neural latency differences and triplet structures. Correlation strength was severely attenuated with respect to Figure 18A2. (C) Precisely repeating triplet probability as a function of time from activated state onset. As in Figure 18A4, data was evaluated against two null hypotheses (common excitability model: red curve; independent Poisson model: blue curve). Dashed lines indicate standard deviations. (D) Top: Spike raster plots of exemplary neurons, sorted by their coupling coefficient from above two (top) to below zero (bottom). Bottom: Population firing rate during the same 2 second time window.

Figure S20. Higher Number of Synapses per Connection in Accordance with Recent Experimental Results, Related to Figure 7
(A) Histogram comparing the number of synapses formed by the same presynaptic neuron onto a randomly selected L6TPC against the number of additional touches from the same presynaptic neuron, i.e. the number of appositions that were not used for synapse placement. To emulate an electron microscopy (EM) experiment, only synapses and touches in a cylindrical volume around the apical dendrite of the L6TPC were considered. Pooled data shown for 50 L6TPCs. Black line shows linear regression. The correlation is weak (correlation coefficient: 0.05). (B) The L6TPCs received on average 71 redundant synapses inside the cylindrical volume defined around their apical dendrite (red line, 50 L6TPCs). Blue bars: in Monte Carlo randomizations that maintain the individual probabilities of placing a synapse at a touch for each presynaptic neuron and the total number of synapses in the volume, the redundant synapse count is significantly lower (blue bars, $p \ll 0.001$). (C) Number of additional synapses on a L6TPC outside the cylindrical volume, formed by neurons that form at least one synapse onto the L6TPC inside the volume (yellow bar) and by neurons that touch it inside the volume, but form no synapse (blue bar; mean±SD of 50 L6TPCs; $p \ll 0.001$, paired t-test). (D) Fraction of touches from the same presynaptic neuron to a L6_TPC converted to synapses. The bin at 0 contains 21,234 neuron pairs. Pooled data shown for 50 L6TPCs.

Reconstruction and Simulation

of Neocortical Microcircuitry

Henry Markram, Eilif Muller, Srikanth Ramaswamy, Michael W. Reimann, Marwan Abdellah, Carlos Aguado Sanchez, Anastasia Ailamaki, Lidia Alonso-Nanclares, Nicolas Antille, Selim Arsever, Guy Antoine Atenekeng Kahou, Thomas K. Berger, Ahmet Bilgili, Nenad Buncic, Athanassia Chalimourda, Giuseppe Chindemi, Jean-Denis Courcol, Fabien Delalondre, Vincent Delattre, Shaul Druckmann, Raphael Dumusc, James Dynes, Stefan Eilemann, Eyal Gal, Michael Emiel Gevaert, Jean-Pierre Ghobril, Albert Gidon, Joe W. Graham, Anirudh Gupta, Valentin Haenel, Etay Hay, Thomas Heinis, Juan B. Hernando, Michael Hines, Lida Kanari, Daniel Keller, John Kenyon, Georges Khazen, Yihwa Kim, James G. King, Zoltan Kisvarday, Pramod Kumbhar, Sébastien Lasserre, Jean-Vincent Le Bé, Bruno R.C. Magalhães, Angel Merchán-Pérez, Julie Meystre, Benjamin Roy Morrice, Jeffrey Muller, Alberto Muñoz-Céspedes, Shruti Muralidhar, Keerthan Muthurasa, Daniel Nachbaur, Taylor H. Newton, Max Nolte, Aleksandr Ovcharenko, Juan Palacios, Luis Pastor, Rodrigo Perin, Rajnish Ranjan, Imad Riachi, José-Rodrigo Rodríguez, Juan Luis Riquelme, Christian Rössert, Konstantinos Sfyrakis, Ying Shi, Julian C. Shillcock, Gilad Silberberg, Ricardo Silva, Farhan Tauheed, Martin Telefont, Maria Toledo-Rodriguez, Thomas Tränkler, Werner Van Geit, Jafet Villafranca Díaz, Richard Walker, Yun Wang, Stefano M. Zaninetta, Javier DeFelipe, Sean L. Hill, Idan Segev, and Felix Schürmann

Supplemental Information

Reconstruction and Simulation of Neocortical Microcircuitry

Henry Markram, Eilif Muller, Srikanth Ramaswamy, Michael W. Reimann, Marwan Abdellah, Carlos Aguado Sanchez, Anastasia Ailamaki, Lidia Alonso-Nanclares, Nicolas Antille, Selim Arsever, Guy Antoine Atenekeng Kahou, Thomas K. Berger, Ahmet Bilgili, Nenad Buncic, Athanassia Chalimourda, Giuseppe Chindemi, Jean-Denis Courcol, Fabien Delalondre, Vincent Delattre, Shaul Druckmann, Raphael Dumusc, James Dynes, Stefan Eilemann, Eyal Gal, Michael Emiel Gevaert, Jean-Pierre Ghobril, Albert Gidon, Joe W. Graham, Anirudh Gupta, Valentin Haenel, Etay Hay, Thomas Heinis, Juan B. Hernando, Michael Hines, Lida Kanari, Daniel Keller, John Kenyon, Georges Khazen, Yihwa Kim, James G. King, Zoltan Kisvarday, Pramod Kumbhar, Sébastien Lasserre, Jean-Vincent Le Bé Bruno R.C. Magalhães, Angel Merchán-Pérez, Julie Meystre, Benjamin Roy Morrice, Jeffrey Muller, Alberto Muñoz-Céspedes, Shruti Muralidhar, Keerthan Muthurasa, Daniel Nachbaur, Taylor H. Newton, Max Nolte, Aleksandr Ovcharenko, Juan Palacios, Luis Pastor, Rodrigo Perin, Rajnish Ranjan, Imad Riachi, José-Rodrigo Rodríguez, Juan Luis Riquelme, Christian Rössert, Konstantinos Sfyrakis, Ying Shi, Julian C. Shillcock, Gilad Silberberg, Ricardo Silva, Farhan Tauheed, Martin Telefont, Maria Toledo-Rodriguez, Thomas Tränkler, Werner Van Geit, Jafet Villafranca Díaz, Richard Walker, Yun Wang, Stefano M. Zaninetta, Javier DeFelipe, Sean L. Hill, Idan Segev, and Felix Schürmann.

Supplemental Experimental Procedures

MORPHOLOGICAL DIVERSITY

Reconstruction of morphologies

3D reconstructions of biocytin stained neuronal morphologies were obtained from whole-cell patch-clamp experiments on 300 µm thick brain slices from juvenile rat hind-limb somatosensory cortex, following experimental and post-processing procedures as previously described (Markram et al., 1997).

Neurons were chosen for 3D reconstruction that were high contrast, completely stained, and had few cut arbors. Reconstruction used the Neurolucida system (MicroBrightField Inc., USA) and a bright-field light microscope (Leica DMRB, Wetzlar, Germany) at a magnification of 100x (oil immersion objective, 1.4-0.7 NA) or of 60x (water immersion objective, 0.9 NA). The finest line traced at the 100x magnification with the Neurolucida program was 0.15 µm. The slice shrinkage due to staining procedure was approximately 25% in thickness (Z-axis) and approximately 10% anisotropically along the X- and Y-axes. Only the shrinkage of thickness was corrected at the time of reconstruction (X-Y shrinkage is corrected later by the unraveling step). Reconstruction resulted in a connected set of points traced from the morphology, each having a 3D (*x*, *y*, *z*) position and diameter.

Classification of morphologies

Following reconstruction, neuronal morphologies were classified into one of 55 different morphological types (m-types) based on the layer containing their somata, and their anatomical and electrical features (see Figure 2 for a complete listing of m-types) as described below.

Excitatory m-types in layers 2 to 6
Pyramidal cells (PC) in different cortical layers were mainly characterized by their apical dendrites, since their large axonal clusters were cut in the slice preparation. The classification of excitatory neurons in layers 2 to 6 was combined with quantitative analysis of 3D computer reconstructions of biocytin stained neurons. We attempted to correlate layer 6 PC m-types with their long-distance axonal projections by performing retrograde labeling experiments. The PC m-types defined here are consistent with previously reported subtypes that have distinct long-distance projections (Van Aerde and Feldmeyer, 2015; Marx and Feldmeyer, 2013; Mercer et al., 2005; Oberlaender et al., 2012; Zhang and Deschênes, 1997).

Layer 2/3 PCs: As reported previously (Feldmeyer, 2006; Holmgren et al., 2003), PCs in layer 2/3 were simply pooled together according to their location in the supragranular layer.

Layer 4 PCs: There were 3 excitatory m-types in layer 4 (Feldmeyer et al., 1999): 1) L4PC (tufted PC) had an apical dendrite with a small tuft that often did not extend to layer 1. 2) L4SP (untufted PC, or Star PC) had a slender apical dendrite without a tuft. 3) L4SS (Spiny Stellate cell) had an apical dendrite with one or few branches, having a radial length similar to basal dendrites. In comparison with the L4PC and L4SP m-types, L4SS had tortuous and thicker basal dendritic segments.

Layer 5 PCs: There were 4 PC m-types in layer 5 (Frick et al., 2007; Kasper et al., 1994; Markram et al., 1997; Romand et al., 2011): 1) L5TTPC1 (Thick-tufted PC 1) had a thick apical dendrite with a big tuft that bifurcated at the distal half of the apical dendrite. 2) L5TTPC2 (Thick-tufted PC 2) had a thick apical trunk that bifurcated at the proximal half of the apical dendrite into multiple apical dendrites that further bifurcated respectively forming a smaller tuft in layer I. 3) L5STPC (small tufted PC) had a thin apical dendrite with a small tuft. 4) L5UTPC (untufted PC) had a thin apical dendrite without a tuft. The L5TTPCs had bigger and more typical pyramidal-shaped somata compared to L5STPC and L5UTPC. While L5TTPC1 and L5TTPC2 were bigger neurons with basal dendritic clusters, L5STPC and the L5UTPC were smaller with similar basal dendritic clusters.

Layer 6 PCs: There were 5 PC m-types layer 6: 1) L6TPC (Tufted PC) had an apical dendrite with a tuft terminating in either layer 1 or 4. 2) L6UTPC (untufted PC) had an apical dendrite without a tuft. 3) L6IPC (Inverted PC) had large dendrites inverted towards the white matter with more branches than other basal dendrites. 4) L6BPC (Bipolar PC) had a typical apical dendrite towards the pia with or without a small tuft and a big inverted dendrite (towards the white matter) with more branches than other basal dendrites. According to retrograde labeling experiments, L6BPCs were similar to cortico-claustral PCs projecting to the ipsilateral claustrum; L6TPCs, L6UTPCs, and L6IPCs corresponded to cortico-cortical PCs projecting to the contralateral somatosensory cortex (also see (Kisvárday et al., 1990)).

Inhibitory m-types in layers 2 to 6

Interneurons were classified according to axonal and dendritic features, especially the characterized axonal morphological features, as published previously (Markram et al., 2004; Wang et al., 2002, 2004) . With the exception of layer 1, all other layers shared a similar set of m-types, with variations in the shape and size of dendritic and axonal clusters.

Large basket cell (LBC): LBCs had multipolar or bitufted dendrites, an axonal cluster characterized by straight and long axonal segments with low density of boutons, and long collaterals giving branches from both sides. Layer 2/3 LBCs commonly had descending axonal collaterals while those in deep layers 5 and 6 often had ascending axonal collaterals reaching layer 2/3 or even layer 1.

Nest basket cells (NBC): These cells correspond to Arcade or Willow cells, having multipolar or bitufted dendrites without long collaterals. NBCs in supragranular layers were in general smaller in size than those in infragranular layers.

Small basket cell (SBC): SBCs had multipolar or bitufted dendrites and axon collaterals with numerous curved or straight short axonal segments. The axon collaterals contained a high density of boutons and formed a dense local axonal cluster around the soma.

Chandelier cell (ChC): ChCs had multipolar or bitufted dendrites, and were distinguished by pre-terminal axon branches that form short vertical rows of boutons resembling candlesticks. These interneurons were also referred to as axo-axonic cells as they form synaptic contacts on the axon initial segment of target PCs (Somogyi et al., 1982).

Martinotti cells (MC): MCs had multipolar, bitufted, or bipolar dendrites, and were distinguished by ascending axons that commonly gave rise to two axonal arbors, one near the cell body and another in layer 1 except those in layer 6. Layer 6 MCs had a second axonal cluster formed below layer 1. The second axonal plexus of MCs were very dense (axonal tuft) or diffused. Axonal collaterals of MCs were characterized by spiny boutons while dendrites contained sparsely distributed spines that were uncommon for other interneuron types.

Double bouquet cell (DBC): DBCs had multipolar or bitufted dendrites, and were distinguished by a horse-tail like axon bundle. The axon bundle consisted of one to few long descending/ascending vertical axonal collaterals from which many short branches emerged, or by tightly intertwined bundles of long descending vertical collaterals (corresponding to horse-tail like neurons; (Somogyi and Cowey, 1981)). Layer 2/3 DBCs commonly had descending axonal collaterals while those in deeper layers 5 and 6 often had ascending axonal collaterals reaching layer 2/3 or even layer 1.

Bipolar cell (BP): BPs had bipolar dendrites that emerged from the two poles of a small vertical spindle like soma. A few BPs could have a third dendrite emerging from the middle of the soma. Their axonal clusters were narrow and vertically oriented.

Bitufted cell (BTC): BTCs had bitufted dendrites and were characterized by long axonal segments, typically forming a large translaminar or transcolumnar axonal cluster.

Neurogliaform cell (NGC): NGCs had multipolar dendrites and were characterized by very small and dense local axonal arborization around the soma, and short axonal segments bearing a high density of small boutons.

Inhibitory m-types in layer 1

Layer 1 contained six m-types - Neurogliaform Cells with dense (NGC-DA) and sparse local axonal arborization (NGC-SA), Horizontal Axon Cell (HAC), Descending Axon Cell (DAC); Large Axon Cell (LAC) and Small axon cell (SAC). Except NGCs, other m-types were specific only to layer 1. Cajal-Retzius cells were not included as they exist mainly in the embryonic stage before birth and are no longer present by post-natal day 11 (P11) in rodent neocortex (Hestrin and Armstrong, 1996)

Neurogliaform cells with dense axonal arbors (NGC-DA): NGC-DAs were very similar to the NGC cells reported in other cortical layers showing small compact axonal arborization (Kawaguchi and Kubota, 1997; Kisvárday et al., 1990; Szabadics et al., 2007). These neurons also typically displayed the shortest dendritic segments among all layer I neurons.

Neurogliaform cells with sparse axonal arbors (NGC-SA): Visually, NGC-SAs appeared as a sparser variation of NGC-DAs. They displayed similar axonal branching patterns in terms of segment length, tortuosity, and branch angles. However, NGC-SAs differ from NGC-DAs in that they displayed significantly smaller vertical arborizations with fewer and shorter axon collaterals. On the other hand, the dendritic arborization extended further horizontally with longer dendritic segments and smaller branching angles.

Horizontal axon cells (HAC): HACs were characterized by extensive horizontal axonal arborizations as compared to vertical extents, with long axonal segment lengths. Their horizontal/vertical extent ratio (often > 4 fold) was the highest among all other m-types in layer 1.

Descending axon cells (DAC): DACs were easily distinguished due to the presence of one to a few descending axon collaterals that reached layers 4, 5, and occasionally 6 (Hestrin and Armstrong, 1996). Their other striking distinguishing feature was the large horizontal (often > 1 mm) and vertical (often > 0.5 mm) extents of their axonal arborization, which was the largest of any m-type in layer 1.

Large axon cells (LAC): LACs appeared visually similar to the HACs. On closer inspection, however, the axonal segments were shorter and projected more radially compared with HACs. Particularly, many short branches emerged from long axonal collaterals. They displayed the longest total length of axon, the highest number of segments, and the highest maximum branch order among layer 1 m-types. The axonal collaterals of more than 50% of LACs were often seen to project vertically into layers 2 and 3. Their dendrites also displayed the highest segment number indicating frequent branching.

Small axon cells (SAC): SACs had the smallest axonal arborization reflected in the lowest total axonal lengths among layer 1 m-types. The axonal arbor also displayed the lowest number of axonal segments and the lowest maximum axonal branch order. The axons, however, had the largest axonal branch angles with straight axonal segments. About a third of SACs projected one or two axonal collaterals into layers 2 and 3.

Unraveling morphologies

The histological processing performed on brain slices results in tissue shrinkage, which leads to an increase in arbor tortuosity. This leads to a decrease in the overall reach of the neuron, while presumably maintaining a constant total arbor length (Jaeger, 2000). In order to correct for this increased tortuosity and reduction in overall reach, we developed an unraveling procedure to smoothen and extend the reach of arbors while maintaining their overall length. The unraveling process used a centered moving window algorithm for each arbor branch. Assuming a window size of N points, running on a branch of M points, the algorithm started on the first point of the branch to be unraveled (call this point's index p). The points in the window were fitted using principal component analysis (PCA) by a 3D direction vector, $\vec{D}_p$. The moving window ran on the tortuous neuron, computing the PCA direction vectors for each point. The algorithm then updated the position of each point sequentially to align them with the PCA direction. The coordinates of the point $p+1$ then became:

$$\begin{pmatrix} \hat{x}_{p+1} \\ \hat{y}_{p+1} \\ \hat{z}_{p+1} \end{pmatrix} = \begin{pmatrix} \hat{x}_p \\ \hat{y}_p \\ \hat{z}_p \end{pmatrix} + \|\vec{V}_p\| \times \frac{\vec{D}_p}{\|\vec{D}_p\|}$$

where

$$\vec{V}_p = \begin{pmatrix} x_{p+1} - x_p \\ y_{p+1} - y_p \\ z_{p+1} - z_p \end{pmatrix}$$

and (x, y, z) are the coordinates of the point before unraveling, ($\hat{x}, \hat{y}, \hat{z}$) are the coordinates after unraveling, and $\|\vec{V}_p\|$ is the distance to the previous point. The unraveling thus preserved the overall length of the arbors while decreasing the tortuosity (increasing the smoothness) and increasing the range of the neuron. At the boundaries (if $p < N/2$ or $p+N/2 > M$), the window was truncated to the points available. The window size could be adjusted to achieve a desired increase in the range of the neuron. We found empirically that using a window size ($N = 5$) resulted in a range increase of 10% on average, and this value was used for unraveling.

Repairing morphologies

Because neuronal morphologies were reconstructed from brain slices, some reconstructions were truncated at the slice edges. To restore the severed arbors we developed repair algorithms to mitigate the slicing artifacts. The repair process, described here briefly, was based on previously published methods (Anwar et al., 2009). The first step of this process was to determine if the morphology was actually truncated at the two cut-planes. Our coordinate system for reconstructing neurons defined the cut plane as XY (perpendicular to the Z-axis) and the origin as the center of the soma. Thus, the first step of cut-detection was to determine the maximum extent of arbors in the positive and negative Z directions. In order for a cut-plane to be detected, there must be a minimum number of terminal points within 30 μm of the maximum Z extents (five points by default, or the total number of terminal points divided by four if there are fewer than 20 terminal points). In the case of finding two cut-planes in this manner, we imposed an additional requirement of having a minimum span between maximum Z extents of 200 μm. If the span was less than this value, the side with the most terminal points

within the 30 µm range was considered the only cut side. Any terminal points further than 30 µm from the maximum Z extents were eliminated as cut points. Additionally, if any point along the arbor path from the soma to a terminal point was more distal in Z than the terminal point itself, this terminal point was eliminated as a cut point (i.e. the arbor loops back, or is re-entrant). This process resulted in reconstructed morphologies with a certain number of terminal points tagged as cut-points. These cut branches were then repaired using separate algorithms for dendrites and axons.

The dendrite repair process "regrows" cut dendrite branches in order to recover the portions severed during slicing (Anwar et al., 2009). This process was not intended to recover the original dendritic morphology, but rather recovered the overall morphology in a statistical manner, using the assumption of statistical symmetry. The dendrite repair process analyzed the properties of the intact dendrites of a single morphology and uses that data to stochastically generate "virtual" dendrites at its identified cut points. This process was developed on the basis of existing models (Ascoli and Krichmar, 2000; Ascoli et al., 2001; Burke et al., 1992; Donohue and Ascoli, 2008; Hillman, 1979; Pelt and Uylings, 2003). Our model utilized the behavior of uncut branches as a function of branch order and straight-line distance from the root. For basal dendrites the root was defined as the point where the dendrite emerges from the soma, for apical oblique dendrites the root was defined as the point where the dendrite emerges from the main apical trunk, and for apical tuft dendrites the root was defined as the point where the apical trunk begins forming the tuft. Probability density clouds for continuing, bifurcating, and terminating events were calculated in a series of spherical shells (Sholl, 1953) for each branch order. $P(E|O,S)$ was the probability of event E occurring, knowing that the branch is of order O and was in shell S. The event probabilities were calculated as

$$P(E|O,S) = \frac{N_{E,O,S}}{N_{O,S}}$$

where $N_{E,O,S}$ was the number of branches of order O undergoing event E in shell S and $N_{O,S}$ is the total number of branches of order O in shell S. At each cut point, the behavior of the branch was stochastically sampled utilizing the calculated event probabilities. If the branch is to continue, it was regrown up to the next spherical shell. If it was to bifurcate, a random number of points were added before the bifurcation, and the daughter branches were grown up to the next spherical shell, with the angle between the daughters randomly sampled from the daughter angle distribution of all bifurcations in the neuron. If the branch was to terminate, a random number of points were added and the branch terminated. The direction in which branches are re-grown was allowed to vary randomly from the current direction by 5 -10%.

The axonal repair process differed from dendrite repair in that it did not assume that the axonal arborization was symmetrical (Anwar et al., 2009). Neocortical axons are known to exhibit laminar preferences, with lateral extent dependent upon depth within the microcircuit (Larsen and Callaway, 2006). Thus, our axonal repair algorithm attempted to maintain the laminar structure. Due to the greater complexity of axonal arborization, instead of regrowing branches at cut points, the algorithm selected and pasted intact subtrees from the particular m-type. The first step was to create a pool of intact subtrees (those without any cut branches) from all reconstructed morphologies of a given m-type. For each axonal cut-point, the nearest intact tree became the target subtree. From the pool of intact subtrees, the one with the closest matching overall length was chosen and pasted onto the cut point.

Cloning morphologies

Morphological diversity is an important component of robust and invariant connectivity patterns (Ramaswamy et al., 2012). In order to increase morphological diversity, we performed several procedures on our population of reconstructed and repaired neurons.

Neurons reconstructed from brain slices lose all arbors outside of the cut planes, which is particularly problematic for m-types with extensive axonal arborizations. Even after our repair process, some of our neuronal morphologies exhibited impoverished axonal arborizations despite having excellent dendrite arborizations, or vice-versa. A mix-and-match procedure mitigated this problem by separating neurons at the axon, discarding poor dendrite and axonal reconstructions, and then recombining good dendrite and axonal reconstructions in all possible permutations, thus increasing utilization of reconstruction data and increasing the number of unique morphologies available for microcircuit building. We manually annotated the dendritic and axonal arborizations as acceptable or not and perform the procedure on all pyramidal cell m-types in layers 2-6 as well as on layer 4 spiny stellate neurons.

For placement of morphologies within the simulated neocortical column, a specific m-type was determined for each somatic location and then the morphology of that m-type which best fit the location was chosen, as described below. However, for some locations, especially near the layer boundaries, the best-fit morphology did not fit particularly well. This was assumed to be due to a combination of choice bias during the

experiments (experimenters looking for a specific cell type search near the middle of the layer) and variability in cortex height between different animals. To ameliorate this issue, the repaired morphologies were duplicated and scaled vertically (Y-axis) by ± 2.5% and ± 5.0%.

In order to further increase morphological diversity, a cloning algorithm was implemented. This algorithm took each morphology and injected noise into branch lengths and rotations, leaving the overall branching structure unchanged, but resulting in completely unique space-filling for each clone. For each branch in the current morphology, a random number was sampled from a Gaussian distribution of mean 0% and standard deviation 20%, and the branch's length was then scaled by this amount. At each bifurcation point, there were two subtrees, each of which were rotated by a degree sampled from a Gaussian distribution of mean 0° and standard deviation 10°. The rotation occurred around the vector determined by the point at the base of the subtree and the first principal component of all arbor lengths in the subtree. This generally resulted in unique cloned morphologies that maintained the general structure of the m-type (e.g. laminar structure). However, in L1HACs and Martinotti cells in all layers, this process resulted in a degradation of laminar structure, and thus cloning was not performed on these cells.

Some m-types occur very infrequently, resulting in small numbers of reconstructions for these types (e.g. neurogliaform cells, chandelier cells, and bipolar cells). As such, we allowed these cell types to be used in layers next to the layer in which they are found. Thus, L23NGCs could also be placed in layer 6, L6NGCs could be placed in layer 5, L5ChCs could be placed in layers 4 and 6, and L5BPs and L5DBCs could be placed in layer 6. Martinotti cells were also allowed to be placed in the layer above and below the layer in which they were found, with two exceptions: layer 1 did not contain Martinotti cells and layer 6 Martinotti cells were not allowed to be placed in layer 5.

Objective classification and validation of cloning

Following the unraveling, repair and cloning/scaling of the reconstructed morphologies, an objective classification was performed to ensure that the repaired cells and the clones belong to the same classes assigned by the expert classification. Of the original 55 m-types, 43 were objectively classified. The remaining classes (L23BP, L23NGC, L4BP, L4NGC, L4ChC, L5BP, L5NGC, L6BTC, L6ChC, L6DBC, L6NGC, L6BP) were not classified because too few biological reconstructions were available. The 583 repaired morphologies of 43 m-types were classified using the method of leave-one-out Linear Discriminant Analysis (Rao, 1948) provided by the open-source Python-based machine learning library Scikit-learn (Pedregosa et al., 2011).

The morphologies were divided into 9 superclasses in two steps. The first step distinguished the interneurons from the pyramidal cells depending on the absence or presence of an apical dendrite, and the second step categorized the cells of different layers, according to the expert layer assignment based on the layer containing their somata. An initial classification was performed with 105 anatomical features for pyramidal cells and 75 (apical features are not included) anatomical features for interneurons (see Table S4) that were extracted through NeuroM. The results of this classification showed 99% accuracy between the expert and the objective classification. However, randomization of classes within layers only reduced this accuracy to 97%, indicating over-fitting of the data. To reduce this problem, a second classification was performed using a subset of features. In order to select the most significant features for the anatomical classification of the cells a multi-objective optimization problem was designed to assign an importance score to each feature. The Pareto Front was extracted from the multi-objective optimization problem of minimizing within-group variance and maximizing between-group variance, with the constraint of the predefined 43 classes. The 15 most significant features were selected for each layer and type (Interneuron or Pyramidal cells). After the feature selection, the overall accuracy of the 43 m-types classification was around 70%, while the randomization of classes resulted in a significant decrease of the accuracy to around 40%. This shows that the expert-proposed features (see the section: Classification of morphologies) were also objectively significant.

In order to further improve the classification and minimize the effects of the sparsity of data in interneuron classes (layer 2-6), a hierarchical clustering approach was used for the group of interneurons. The local arborization of most interneurons results in similar morphometrics within their classes (BP, BTC, ChC, DBC, LBC, NBC, SBC, MC, NGC), independently of the position of their somata. This property, which is unique for interneurons, allowed the merging of interneuron classes of different layers into larger classes for classification purposes. Layer 1 interneurons were excluded from this process, because of their distinct morphologies, which cannot be integrated with the rest of the interneurons. The overall accuracy of supervised clustering with feature selection for Layer 1 interneurons is 68%. The described process increased the sample size and reduced the number of classes that could not be objectively classified to two (BP and NGC) because they still had less than 3 members. A subsequent application of hierarchical clustering, a technique commonly used in clustering problems with a large number of classes (here 7) and few members per class (here 7 to 50 members), resulted in a significant improvement of the overall classification accuracy for the interneurons (~

90%). The randomization of classes suggested terminating the hierarchical clustering at three final classes (DBC, ChC, BTC). The detailed results for the interneurons in Layers 2 to 6 are presented in Figure S2A1, A2.

The hierarchical clustering was not applied to the pyramidal cells for the following reasons. First, the pyramidal neurons are cells that commonly span larger areas and are not locally restricted to the layer of their somata. As a result, pyramidal cells of the same type with somata positions in different layers have significantly different morphologies. Second, the number of classes of pyramidal cells per layer (Layer 2/3: 1 class, Layer 4: 3 classes, Layer 5: 4 classes) and the sufficient number of members of each class did not indicate the need for hierarchical clustering. The overall accuracy of the pyramidal cells classification was around 88%. The detailed results of the classification of pyramidal cells Layer 2 to 5 are presented in Figure S2B1, B2. Layer 6 pyramidal cells are a special case, since 2 classes (IPC and BPC) can be identified by the number and the orientation of the apical trees with 100% accuracy, one class does not have sufficient members to participate in the objective classification (HPC) and the rest of the classes (TPCL1, TPCL4, UTPC) can be classified with ~60% accuracy. These results are not presented in Figure S2 since the used method is modified.

Once the performance of the classifier had been quantified, 9187 unique cloned-scaled morphologies were classified according to the described method to ensure that the cloning process did not modify the assigned cell classes. The mean score for the classification of the cloned morphologies was 81%, which is significantly similar to the accuracy of the repaired cells' classification. As a result of this objective classification, we concluded that the assignment of classes to the repaired and cloned cells agrees with the expert classification.

Morphological Structural Analysis

We generated a profile of the mean densities of arbors around the somata of all 55 m-types based on manually reconstructed and repaired morphologies in our database (N = 433), as shown in Figure S1. To generate the profile for a given morphology type we placed 10 copies of each relevant morphology at the same point in (virtual) space and rotated them between 0 and 360 degrees around the y-axis (perpendicular to the layer boundaries). Next, we converted the axons and dendrites into a point cloud by moving recursively from the soma to the tips of the arbors, placing a point in space every 1 μm. Each of these points represented 1 μm of arbor length centered at its location. The final result therefore represented density of arbor length, and not volume. The point clouds for dendrites and axons were converted into a volume separately by counting the number of axon/dendrite points that fall into a 1 μm cubic voxel. Finally, the volume was normalized to present the probability density of finding the center of a randomly picked 1 μm segment of arbor inside the voxel. To visualize the volumes, we calculated the sum along the z-axis (parallel to the layer boundaries) and mapped the densities to a color map. Axon density is shown in blue, dendrite density in red (see Figure S1).

Cell densities and layer boundaries

Slicing procedures

Layer boundaries and densities per layer were computed from light microscopic techniques on slices. P14 Wistar (Han) rats (N = 6) were anesthetized with pentobarbital (100 mg/kg) and transcardially perfused with 20 ml 0.1 M phosphate buffer followed by 100 ml of 4% paraformaldehyde (pH 7.4) prepared in the same buffer. The brains were post-fixed in the same solution for 24 h, and coronal sections were cut with a vibratome. All animals were handled in accordance with the guidelines for animal research set out in the European Community Directive 86/609/EEC and all the procedures were approved by the local ethics committee of the Spanish National Research Council (CSIC).

Immunohistochemistry

Free-floating sections were treated for 30 min with 1% H_2O_2 to deplete the endogenous peroxidase activity, and then non-specific binding was blocked for 1 h in PB with 0.25% Triton-X and 3% horse serum (Vector laboratories Inc., Burlingame, CA, USA). The sections were incubated overnight at 4°C with a mouse anti-neuron specific nuclear protein (NeuN, 1: 2000, Chemicon, Temecula, CA, USA), and they were then processed by the avidin-biotin method, using a biotinylated secondary antibody (1:200, Vector Laboratories, Burlingame, CA, USA) and the Vectastain ABC immunoperoxidase kit with 3,3'-diaminobenzidine tetrahydrochloride (DAB, Sigma-Aldrich, St Louis, MO, USA) as the chromogen. After staining, the sections were dehydrated, cleared with xylene and cover-slipped.

The specificity of the staining was controlled by processing selected sections after either replacing the primary antibody with preimmune horse serum, after omission of the secondary antibody, or after replacement of the secondary antibody with an inappropriate secondary antibody. No significant staining was detected under these control conditions.

To generate the figures, images were captured with a digital camera (Olympus DP70) attached to an Olympus BX51 light microscope (Olympus, Ballerup, Denmark), and Adobe Photoshop CS4 software (Adobe Systems, San Jose, CA, USA) was used to produce figure plates.

Estimation of layer boundaries and densities per layer in NeuN-stained sections

Neuronal density were estimated using optical dissectors (Bonthius et al., 2004; West and Gundersen, 1990), and with the aid of the Stereo Investigator software (StereoInvestigator 7.0, MicroBright Field Inc. Vermont, USA).

Optical dissectors were performed on every cortical layer (I, II, III, IV, Va, Vb, VI) from each animal. After randomly selecting a starting point, 5-6 sections (50 µm thick) were selected at equally spaced intervals in the same cortical area (HL somatosensory cortex (Paxinos and Watson, 1998)). Optical dissectors were made in an Olympus BX51 light microscope (Olympus, Ballerup, Denmark) with an oil immersion x100 objective, within a depth of 15 µm. To provide a systematic area offset, the movement of the stage was controlled through the Stereo Investigator software. A neuron was counted only if the nucleus was clearly identified in the height of the optical plane along the *z*-axis.

Correction for tissue shrinkage

To estimate the shrinkage in our samples, we measured the surface area and thickness of the vibratome sections with Stereo Investigator in three different experimental conditions: (1) before fixation, in fresh (unfixed) tissue; (2) after fixation (overnight at +4°C in 4% paraformaldehyde in 0.1M PB); (3) after processing for NeuN immunostaining. For fresh to fixed tissue, the surface area after fixation was divided by the value before fixation to obtain an area shrinkage factor of 0.929. The linear shrinkage factor for measurements in the plane of the section was therefore its square root, 0.964. From fixed tissue to NeuN-immunostained tissue, the surface area after processing was divided by the value before processing to obtain an area shrinkage factor of 0.83. The linear shrinkage factor for measurements in the plane of the section was therefore 0.91. The shrinkage factor in the z-axis was 0.47. Thus, the final values of the neuronal densities were corrected to obtain an estimation of the pre-processing values. Layer thicknesses were corrected by a factor of 0.964*0.91 to obtain an estimation of the pre-processing values.

Morphological composition

E/I ratios

A P14 Wistar (Han) rat was anesthetized with pentobarbital (150 mg/kg) and transcardially perfused with 50ml 0.1M phosphate buffer followed by 100ml of 4% paraformaldehyde (pH 7.4 in 0.1M phosphate buffer). The brain was post-fixed in the same solution for 2h, and 50 µm sagittal sections from right hemisphere were sliced with a vibratome (Leica, VT-1000-S), slices were placed into cryoprotectant (30% glycerol, 30% polyethylene glycol in distilled water) at -20°C until staining.

The non-specific binding sites of the free-floating sections were blocked for 2h in 0.1M PBS with 0.3% Triton X-100 and 1% bovine serum albumin. The sections were first incubated at 4°C for 20h first with a mouse anti-neuron specific nuclear protein 1:1000 (anti-NeuN, Chemicon, MAB377). They were then incubated with a rabbit anti-GABA (anti-GABA, Sigma-Aldrich Inc., A2052) 1:500, at room temperature for 1h followed by 24h at 4°C, with blocking steps in between (PBS-T with 3% normal goat serum). Revelation was done with a goat anti-mouse IgG Alexa488 (Alexa488, 1:1000, Molecular Probes, A11029) and with a donkey anti-rabbit Alexa568 (Alexa568, 1:200, Molecular Probes, A10042) in 0.1M PBS with 1% bovine serum albumin and 0.3% Triton X-100. DAPI was used as a nuclear counterstain (1:50'000, Sigma-Aldrich, D9542). After staining, the sections were mounted in aqueous anti-fading reagent (Dako, S3023) and cover-slipped. Negative control of staining was performed with secondary antibodies only. No significant staining was detected under this control condition.

Imaging was performed on a motorized confocal microscope (Zeiss LSM 700) with 40x magnification at 0.223 µm x 0.223 µm x 1 µm voxel size with 12-bit color depth. Stack depth was chosen to be 90 slices thick to account for possible errors in *z* alignment. A region of 640 µm x 2673 µm was imaged with 10% overlap - resulting in an image size of 2871 x 11990 x 90 voxel. Single stacks were stitched using the custom made Fiji "massive stitcher" plugin implemented by the BioImaging and Optics Platform of EPFL (http://biop.epfl.ch/).

The representative counting region was chosen to be 152.53 µm x 1800 µm x 53 µm in size inside the somatosensory area ranging from bottom of L6 to pia inside the hind-limb somatosensory cortex. Shrinkage correction was not necessary. Counting volume was re-sliced into horizontal plane to better assess nucleus position inside the slice. Counting was performed three times by independent experimenters using the Fiji cell counter plugin. All cells with matching criteria were counted. Upper and left bounding box borders were

defined as exclusion borders. Lower and right borders as inclusion borders. Cells with nuclei touching exclusion borders were not counted. Positions of counted cells were saved. Only double positive (NeuN/GABA; +/+) cells counted as inhibitory neurons. Layer boundaries were applied after counting. Volume rendering was performed with Imaris scientific visualization (Bitplane) and VTK (Kitware Inc., Visualization Toolkit).

All procedures were conducted in conformity with the Swiss Welfare Act and the Swiss National Institutional Guidelines on Animal Experimentation for the ethical use of animals. The Swiss Cantonal Veterinary Office approved the project, following its ethical review by the State Committee for Animal Experimentation.

Immunohistochemistry for Marker Visualization

Wistar rats (n=4 aged 14 days) were sacrificed by administering a lethal intraperitoneal injection of sodium pentobarbital (40 mg/kg), and they were then perfused intracardially with saline solution followed by 4% paraformaldehyde in 0.1 M phosphate buffer (PB), pH 7.4. All experiments were approved by the ethics committee of the Spanish National Research Council (CSIC) and performed in accordance with the guidelines established by the European Union regarding the use and care of laboratory animals (Directive 2010/63/EU). Brains were removed and postfixed by immersion in the same fixative for 7 h at 4ºC and then were cryo-protected in 30% sucrose solution in PB until they sank, frozen in dry ice and cut at 50 μm in the coronal plane with a sliding freezing microtome. The sections were pre-incubated for 1 h at room temperature in a stock solution containing 3% normal goat serum (Vector Laboratories, Burlingame, CA) in PB with Triton X-100 (0.25%) and then incubated for 48 h at 4 ºC in the same stock solution containing the following antibodies, alone or in combination: Mouse anti-CB (Swant 1:2000), mouse anti-PV (Swant 1:2000), mouse anti-CR (Swant 1:2000) rabbit anti-NPY (Peninsula, 1:2000), rabbit anti-Som (Peninsula, 1:2000), rabbit anti-CCK (Sigma 1:10000) and rabbit anti-VIP (Incstar 1:1000). Sections were then rinsed in PB and incubated in for 2 h at room temperature goat anti-rabbit and or goat anti-mouse coupled antibodies with Alexa 488 or Alexa 594 (1:1000; Molecular Probes, Eugene, OR). Sections were rinsed and stained with Dapi, to reveal borders between layers and cytoarchitectonical areas. The sections were then washed in PB, mounted in anti-fade mounting medium (Invitrogen/Molecular Probes, Eugene, OR) and studied confocal microscopy (Zeiss, 710). Controls were included in all the immunocytochemical procedures, either by replacing the primary antibodies with pre-immune goat serum in some sections, by omitting the secondary antibodies, or by replacing the secondary antibody with an inappropriate secondary antibody. No significant immunolabeling was detected under these control conditions. Additional quantitative staining was performed using a variation of a previously published protocol (Brionne et al., 2003).

Defining horizontal circuit dimensions

The horizontal dimensions of a microcircuit were estimated by evaluating the density of dendritic fiber at the center of the circuit, as cells are placed at successively farther distances from the center. In particular, we calculated the total length of morphological segments whose midpoint is contained inside a cylinder at the center of the circuit with a radius of 25 μm but spanning all layers. At first, we only considered dendritic segments of cells that had their soma within 25 μm horizontally of the center. We then increased that maximal distance in steps of 25 μm, each step increasing the total length in the center. We calculated the radius where 95% of the asymptotal maximal length is reached as 210 μm (linearly interpolated). Instead of a circle, we used a hexagon with identical area as the base of the microcircuit to facilitate tiling, while minimizing asymmetrical edge effects.

Soma positions

The horizontal and vertical extents yield a 3D microcircuit volume in the shape of a hexagonal prism that is 461.8 μm wide (at its widest point, side length 230.9 μm) and 2082 μm high (See Figure 3D), composed of 6 layers. This volume was then populated by assigning soma positions according to the derived layer-specific cell densities. The positions were distributed in mini-columnar arrangements using the Niederreiter space-filling algorithm (Niederreiter, 1988). Each mini-column contains around 100 neurons (depends on total numbers in circuit, which varies slightly across the different instantiations, Bio1-Bio5, BioM, according to their differing total numbers of neurons) and exactly 310 mini-columns per unitary microcircuit. Finally, each soma position was assigned an m-type according to the derived morphological composition and E-I fractions. Furthermore, each soma position was associated with a random rotation to be applied to the morphology.

Ensuring inter-laminar structure

The microcircuit contains morphologies of different sizes and shapes. Placing the soma of reconstructed morphologies in the layers they were found in during the reconstruction is insufficient to ensure a biologically correct placement. We found that there are more constraints on the morphologies than just the home layer of

the soma. For example, within a layer, a given morphology may be limited to only a small fraction of the available space, due to its axon or dendritic structure. We know for example, that the arbors of a cell cannot stretch further than the top of layer I. This means that the largest pyramidal cells of a given layer can only be placed at the bottom of that layer. Conversely, the dendrites of the smallest pyramidal cells originating from the top of layer II/III will be unable to reach layer I, if placed at the bottom of the layer.

Once a neuronal location was assigned an me-type, it was assigned a morphology from the database of morphologies provided by the morphology release process (unravel, repair, mix-and-match, scaling, cloning, substitution) according to a placement scoring algorithm designed to ensure adherence to known biological rules for laminar placement of morphological features (e.g. L1 targeting axon clusters of Martinotti axons, L4 targeting pyramidal dendrites).

A broad literature review was undertaken to identify described rules for the laminar targeting of morphological features, and individual repaired morphologies (prior to mix-and-match, scaling and cloning) were manually annotated for vertical intervals which should target specific layers. Annotations of parent intervals were carried over to mix-and-match, scaled, and cloned morphologies. For the latter, sections annotated in the parent were also annotated in the clone by correspondence of segments, and the clone was rejected if any extent of an annotated region was not within ± 60% of the parent region.

Scores were computed for each pool of m-types for bins of 10 μm along the vertical axis of the microcircuit. The score was computed as the generalized mean of the overlap of Gaussians between feature interval and target interval over all annotated rules for a given morphology. A given morphology was removed from consideration for placement if it penetrated the pia. For a given location, the candidate morphology was randomly chosen weighted by score from the pool of cells with the highest scores accounting for 8% of the total score of the m-type pool.

In the superficial layers 2 and 3, some m-types contained no exemplars that could be placed in upper regions of the layer without exiting the pia. In this case, the density of this m-type was redistributed to the sub-volume of the layer where exemplars were available to be placed.

MORPHO-ELECTRICAL DIVERSITY

Physiological recordings

Electrophysiology
The firing patterns of neurons, obtained from *in vitro* recordings in P14-16 rat somatosensory cortex, were expert-classified into one of 11 electrical types (e-type; cAC, bAC, cIR, bIR, cNAC, bNAC, dNAC, cSTUT, bSTUT, dSTUT, cAD; see Figure 4) based on their response to stimulus protocols as described below. The response properties recorded from several neurons (N = 143) were selected from our experimental database as the basis for the distributions of feature values used for electrical model optimization. The experimental procedures were published in previous studies (Toledo-Rodriguez et al., 2004).

Stimulus protocols
Neurons were stimulated with a set of previously described protocols (Le Bé et al., 2007; Wang et al., 2002, 2004). Only a subset of these stimuli was used to generate neuron models.

- **IDRest**: In the IDRest protocol the experimenter determines a hyperpolarizing offset current to keep the cell at -70 mV (before liquid junction potential correction) and applies this current during the entire protocol. After an initial period of 700 ms, a step current was applied for 2000 ms, and after the step, a final period of 300 ms is recorded. This protocol is repeated with different step currents normalized to the threshold current (i.e. the lowest current that generates one AP during the step). For this study, the current steps IDRest150, IDRest200 and IDRest250 (resp. 150%, 200% and 250% threshold) were used.
- **APWaveform:** The offset current is determined in the same way as in the IDRest protocol. To obtain a detailed profile of the action potential waveform, voltage is sampled with a period of 10 μs. After 5 ms, a step current is applied at typically 2 to 4 times the threshold step. Voltage is recorded for 50 ms, mostly generating a trace containing two to three high-resolution AP waveforms.
- **APThreshold**: The offset current is determined in the same way as in the IDRest protocol. A ramp current (from 0 pA to 4 times threshold) is injected for 2 seconds after an initial period of 100 ms

To create pyramidal cell models, only features extracted from voltage traces obtained during the IDRest protocol were calculated. For the interneuron models, APWaveform and APThreshold protocol traces were included.

Composition of e-types

The me-type fractions summarized in Figure 4C were assessed from statistics of assigned e-types from a pool of 511 m- and e-type classified inhibitory neurons. Since researchers are unable to target cells based on their electrical properties, the fractions are assumed to be unbiased. Excitatory m-types were uniformly classified as continuous adapting/accommodating (cAD). Since some m-types are infrequent, in some cases samples from different layers were pooled to have sufficient samples to assess the e-type fractions. Such pooling was done in a conservative manner, only when necessary, and only from neighboring layers if possible. For example, BTCs for layers 5 and 6 were pooled to assign the fractions in those layers. The pooling rules applied, in an m-type specific manner, are as follows: (A) L4 + L5 + L6, (B) L5 + L6, (C) L1 lumped (NGC + NGC-DA + NGA-SA), (D) L23 + L4 + L5 + L6. The application of these rules is summarized in Table S5.

RECONSTRUCTING MICROCIRCUIT CONNECTIVITY

Touch detection

After placing the morphologies in 3D space, the next step consisted of generating a structural circuit by detecting zones of geometric overlap called "touches". This step was performed by the custom developed BlueDetector software (Kozloski et al., 2008), which implemented the following workflow: 1) Reconstructed morphologies were loaded, translated and rotated according to the assigned soma positions and rotations (see Soma positions); 2) A division of the volumetric space into sub-volumes (called "slices") was calculated in such a way that every sub-volume held the same amount of data; 3) Morphology segments were evenly distributed over available cores, based on previous slicing; 4) An in-core touch detection algorithm was independently executed on each core (which holds a slice); 5) The detected touches were then sent back to the core that holds each full morphology of the previously sliced neurons; 6) Neurons touches were then filtered according to the biological rules (Riachi, 2010); 7) The resulting set of structural touches was written in parallel to disk. The execution of such a process for a microcircuit consisting of 219k neurons and around 7.0 billion structural touches ran on 8k cores of a CADMOS IBM BG/P or BG/Q supercomputer with an execution time of approximately 1.5 hours.

Touch filtering

For details of the filtering of touches or appositions to constrain synaptic connectivity to experimental data, see the companion paper (Reimann et al., 2015).

Estimation of external input

We estimated the fraction of external inputs into all layers (Figure S7E) by comparing the spine density emerging from connections within the microcircuit to biologically characterized densities. Spine densities in the reconstructed microcircuit were calculated as the density of excitatory synapses, thus assuming one excitatory synapse per spine. Densities were calculated on dendritic segments in the most central 50 µm of the microcircuit where axonal density was highest. They were then compared to m-type specific values from the literature, calculating the fraction of external input needed to reach full, biological density. Finally, fractions were averaged per layer.

NEURONAL PHYSIOLOGY

Neuron models

Multicompartmental, conductance-based models of neurons were obtained from reconstructed morphologies in P14 rat somatosensory cortex. Up to 13 active ion channels types and a model of intracellular Ca^{2+} dynamics were incorporated in neuron models. The compartments were separated into different regions: (1) axon initial segment (AIS), (2) soma, (3) basal dendrites and (4) apical dendrites. Interneurons contained only one dendritic region. Each region received a separate set of channels ((see NMC portal;(Ramaswamy et al., 2015)). The full axon was not simulated, but only the AIS. The AIS was represented by two fixed length sections with a 30 µm length, whose diameter was obtained from the reconstructed morphology used in the model fitting process.

Action potentials were detected in the AIS, and the information was transmitted with a delay to the dendritic locations of synaptic contacts on postsynaptic neurons (see Synaptic Physiology).

Compartment discretization
Reconstructed and repaired neuron morphologies (Anwar et al., 2009) were divided into isopotential compartments of a maximal length (20 µm). The average number of compartments in all neuron models was approximately 260.

Passive properties
Membrane capacitance (C_m) was set to 1 µF/cm^2 for the soma, AIS and dendrites. In pyramidal cells a value of 2 µF/cm^2 was used for the membrane capacitance in the basal and apical dendrites to correct for dendritic spine area. Axial resistance (R_a) was set to 100 Ω·cm for all compartments. For pyramidal cells the maximal conductance of the leak current was manually set to a value that created a resting potential, membrane time constant and input resistance in accordance with reported values (Le Bé et al., 2007; Stuart and Spruston, 1998). For interneurons, the leak reversal potential and the leak conductance were set as a free parameter in the optimization algorithm, within physiological bounds.

Conductance mechanisms
We included 13 key active ionic currents known to play a role in neocortical neurons, with kinetics obtained from published ion channel models or published experimental data (transient sodium (Colbert and Pan, 2002), persistent sodium (Magistretti and Alonso, 1999), transient potassium (Korngreen and Sakmann, 2000), persistent potassium (Korngreen and Sakmann, 2000), m-current (Adams et al., 1982), h-current (Kole et al., 2006), high voltage-activated calcium (Reuveni et al., 1993), low voltage-activated calcium (Avery and Johnston, 1996), Kv3.1 (Rettig et al., 1992), d-type potassium (Shu et al., 2007), stochastic potassium (Diba et al., 2006), SK calcium-activated potassium (Köhler et al., 1996)). The kinetics of ionic conductances that were characterized at room temperature (21 °C) were adjusted to the simulation temperature of 34°C using Q10 of 2.3. The kinetics obtained from experiments where the liquid junction potential was not corrected for were shifted by -10mV. The reversal potentials for Na$^+$, K$^+$ and Ih were set to 50, -85 and -45 mV respectively.

Ion currents were modeled using Hodgkin-Huxley formalism, so that for each ion current:

$$I = \bar{g} * m^x * h^y (V - E)$$

where $\bar{g}$ is the maximal conductance (or density); x and y are the number of gate activation and inactivation variables, respectively; E is the reversal potential of the given ion; and V is the membrane potential. Figure S8 describes the kinetics of each ion channel conductance mechanisms used in this study. To link the calcium channels to the calcium-activated potassium channels, an exponentially decaying intracellular calcium pool was included.

Reconstructing morpho-electrical behavior

Conductance distribution
For pyramidal cell models, all ion channel mechanisms were uniformly distributed in the soma, AIS, basal and apical dendrites, except Ih, which was exponentially distributed in apical dendrites (Kole et al., 2006). For the interneuron models, all ion channels were uniformly distributed in the soma, AIS and dendrites with the exception of Ih, which was exponentially distributed in dendrites. A complete description of all the channel distributions is provided in the Neocortical Microcircuit Collaboration (NMC) Portal - https://bbp.epfl.ch/nmc-portal (Ramaswamy et al., 2015).

Optimization of neuron models
A feature-based multi-objective optimization method as previously described (Druckmann et al., 2007) was used to fit the neuron models. In brief, feature-based error functions were designed to deal with the variability of experimental responses to identical stimuli. The free parameters in the optimization were primarily the density of ion channel conductances located in the soma, AIS and the dendrites (see NMC portal).

We developed an optimizer framework in C++ to integrate the NEURON simulation environment (Carnevale and Hines, 2006), optimization library PISA (Bleuler et al., 2003), and a feature extraction library. Among different implemented optimization algorithms (NSGA, NSGA-II, SPEA2, IBEA), we used the indicator-based evolutionary algorithm (IBEA). Cell model optimization converged faster and reliably found models with summed errors better than the previously reported modified NSGA algorithm (Druckmann et al., 2007). The evolutionary algorithm was run with a population size of typically 1024 individuals on 512 cores of a BlueGene/P system for 100-200 generations. After the optimization, the best solution was the individual in the

population with the smallest sum of its objective values. Every optimization was typically run with different random seeds. The best solution among different seeds was selected as the final electrical model.

We used a set of key electrical features (e-features) of target firing behavior at the soma and dendrites (see NMC portal). For every e-feature an absolute standard score Z_i was calculated:

$$Z_i = \frac{|f_i - \mu_i|}{\sigma_i}$$

with f_i the e-feature value measured from the output traces of the models, μ_i and σ_i the experimentally measured mean and standard deviation for the e-features in the respective cell types.

These Z-scores served to define the objectives O_j to be fitted by the evolutionary algorithm:

$$\boldsymbol{O_j} = \sum_{i=0}^{n_{O_j}} \boldsymbol{w_i \, Z_i}$$

with w_i weight factors, and n_{O_j} the number of e-features in objective O_j.

Every optimization was run with an exemplar morphology that corresponded to the target electrical firing type.

In total, 14 electrical models were created: Ten models corresponding to the inhibitory firing types (cAC, bAC, cIR, bIR, cNAC, bNAC, dNAC, cSTUT, bSTUT, dSTUT), and four models corresponding to excitatory firing types (one model each for PCs in layers 2/3 to 6, and one model for L4SS). This is required due to fact that the morphology of pyramidal cells found in different layers is markedly different.

Electrical models of pyramidal neurons were generated based on a set of experimental features identified from responses to "IDRest" stimuli (see (Hay et al., 2011)). The feature value set used for electrical models of pyramidal neurons across all layers was the same; only the morphology used during the optimization differed. The experimental mean and standard deviation for features measuring the mean frequency, adaptation, CV of the ISIs, doublet ISIs, time to the first spike, AP height / width, AHP depth / time were calculated for all these traces, and were used as target data. One feature also measured the height of the back-propagating action potential in the model at two different locations in the dendrites based on the literature (Larkum et al., 2001). Every objective seen by the optimization algorithm consisted of a combination of a selected set of features. The maximal conductance of the I_h channel and the reversal potential of the leak current were fixed to values based on previous studies (Kole et al., 2006).

Inhibitory cell models were based on the features extracted from responses to APWaveform, APThreshold IDRest150, IDRest200 and IDRest250 stimuli from the experimental data (see *Stimulus protocols*). Due to the large variability of firing types of the interneurons, and due to the computational cost of the optimizations, a different strategy was used for these models. First a set of four core e-types, namely cAC, bAC, cNAC and bNAC was selected, and full optimizations were run to generate models for these firing types. The maximal conductances of Ih and the leak current and the reversal potential of the leak current were part of the optimized parameters. For these interneuron models, every objective in the optimization algorithm corresponded with exactly one feature. Since all the cells of the same e-type were obtained from different m-types and pooled together, some of the resulting features had a large experimental standard deviation. Therefore, the experimental distributions of some features were manually restricted to yield tighter constraints for the optimization.

To generate models for delayed, stuttering and irregular spiking cells, an extra stochastic potassium channel was added to the soma and dendrites of the four core e-types, creating channel noise in the models (Diba et al., 2006). A new optimization was then run to find a value for the conductance of the channel, with the remaining parameters untouched. In this manner, cSTUT, bSTUT, dSTUT, cIR, bIR were derived from cNAC, bNAC, dNAC (see below), cAC, bAC respectively. The stochasticity of the channel was ensured by implementing a unique random number generator for each compartment in these electrical models. A different seed was assigned to every cell and compartment, and the long period of the random number generators avoided conflicts between the different seeds. In a similar way, dNAC was created from the cNAC model by adding a slowly inactivating D-type potassium channel (Shu et al., 2007). The conductance of this channel was optimized using the time to the first spike as a target feature.

Quality assurance of morpho-electrical models

After creating the 14 electrical models that were optimized for specific exemplar morphologies, these models were combined with all the relevant morphologies in our database to create a large set of morpho-electrical

(me) combinations. We ran a process called Model Management to ensure the quality of thus generalized me-combinations. First, the IDRest protocol was applied to every me-combination, and the features that were used during the optimization were calculated from the traces (for IR, STUT and delayed models these were combined with the feature values of the core e-type they were derived from). The repaired version of the exemplar morphology used during the optimization was a benchmark to accept or reject other me-combinations. Combinations were accepted if the Z-scores Z_i for all individual features f_i met the following criteria: $Z_i \leq \max(5, 5 \cdot Z_{i,\text{exemplar}})$ for pyramidal cells and $Z_i \leq 5 \cdot Z_{i,\text{exemplar}}$ for interneurons. To ensure sufficient numbers of interneuron combinations were retained, the scores of certain features were given a higher acceptance threshold.

Goodness-of-fit

Z-scores in Figure 8 were calculated based on experimental features, where values that were changed to improve the optimization algorithm were omitted. Pyramidal neuron models have higher Z-scores due to less variability in the experimental data as against inhibitory neurons, mainly because for interneurons data from more m-types was pooled together. For the Z-score calculation of L23 pyramidal cell models, additional traces specific to these cells from our experimental database were used.

SYNAPTIC PHYSIOLOGY

Modeling stochastic synaptic transmission

At each synaptic location identified by the algorithm to reconstruct microcircuit connectivity, we implemented a stochastic model of synaptic transmission based on previous work (Fuhrmann et al., 2002), but also including facilitation. The implemented two state Markov model is a stochastic model of dynamic synaptic release with an ensemble average response equal to that of the phenomenological Tsodyks-Markram dynamic synapse model (Tsodyks and Markram, 1997). The model further incorporates NMDA receptor (NMDAR) kinetics (Jahr and Stevens, 1990a, 1990b) where applicable. The underlying assumptions were derived from the classical quantal model of synaptic transmission, in which a synaptic connection is assumed to be composed of *N* independent release sites (Del Castillo and Katz, 1954); (Korn and Faber, 1991), each of which has a probability of release, *p,* and contributes a quanta *q* to the post-synaptic response. Release from any particular site is independent of release from all other sites (Fuhrmann et al., 2002). We assumed the number of release sites equals the number of synapses per connection (Ramaswamy et al., 2012).

The two state Markov model to simulate stochastic synaptic transmission has the following properties:

- There can be no consumption of synaptic resources when an event fails to release neurotransmitter - i.e. during failure of synaptic transmission
- After neurotransmitter release at any given release site, there can be no further release of at that site until it recovers.

The exact synapse models as implemented are included in the neuron model packages available for download on the NMC portal.

Parameterizing synaptic kinetics

Excitatory synaptic transmission was modeled with both AMPA and NMDA receptor kinetics. For AMPA receptor (AMPAR) kinetics, the rise ($\tau_{riseAMPA}$) and decay ($\tau_{decayAMPA}$) time constants were 0.2 ms and 1.74 ± 0.18 ms, respectively (Häusser and Roth, 1997). Pathway specific values for the parameter "utilization of synaptic efficacy" (U, analogous to the probability of neurotransmitter release) were unified from various experimental studies of synaptic transmission in juvenile rat somatosensory cortex (Le Bé et al., 2007; Brémaud et al., 2007; Feldmeyer, 2006; Koester and Johnston, 2005; Markram et al., 1997; Silver et al., 2003).For NMDAR kinetics, $\tau_{riseNMDA}$ and $\tau_{decayNMDA}$ were 0.29 ms and 43 ms, respectively (Sarid et al., 2007). The time constants are consistent with several previous in vitro studies (Feldmeyer, 2006; Flint et al., 1997; Monyer et al., 1994; Rinaldi et al., 2007). The concentration of Mg^{2+} was generally set to 1 mM (Jahr and Stevens, 1990b), but was set to 0.5mM where exceptionally specified. The reversal potential of AMPA and NMDA receptors was set to 0 mV. The axonal conduction delay for each synaptic contact was computed using the axonal path distance from the soma, and a AP conduction velocity of 300 μm/ms, based on experimental estimates (Stuart et al., 1997). Furthermore, experimentally measured ratios of NMDA and AMPA conductances were used in order to model their relative contribution to unitary the EPSC (Feldmeyer, 2006; Myme et al., 2003; Rinaldi et al., 2007; Silver et al., 2003; Wang and Gao, 2009). For pathways where specific

values are lacking, we used extrapolated conductance ratios of 0.8 ± 0.1 and 0.4 ± 0.1 for E-E and E-I connections, respectively (Wang and Gao, 2009).

Inhibitory synaptic transmission was modeled with a combination of GABA$_A$ and GABA$_B$ receptor kinetics. For GABA$_A$ receptor (GABA$_A$R) kinetics, the rise ($\tau_{riseGABAA}$) and decay ($\tau_{decayGABAa}$) time constants were 0.2 ms and 10.4 ± 6.1, 8.3 ± 2.2 or 6.44 ± 1.7 ms respectively, for the 3 specific inhibitory synapse types used (Gupta et al., 2000). Synapse-type-specific values for the parameter U (analogous to the probability of neurotransmitter release) were compiled from previous experimental studies (see Table S6). The reversal potentials for GABA$_A$ and GABA$_B$ were set to -80 mV and -93 mV respectively (Mott et al., 1999; Silberberg and Markram, 2007). Due to a lack of voltage-clamp experimental data on the synaptic kinetics of GABA$_B$Rs in neocortical connections, data from hippocampal connections was used (Khazipov et al., 1995; De Koninck and Mody, 1997; Mott et al., 1999; Rovira et al., 1990). For GABA$_B$ receptor (GABA$_B$R) kinetics, the rise ($\tau_{riseGABAB}$) and decay ($\tau_{decayGABAB}$) time constants were 3.5 ms and 260.9 ms respectively (Mott et al., 1999).

Synaptic conductances were determined by optimization of in silico paired recordings in the reconstructed microcircuit to match experimentally measured PSP amplitudes where available (see Table S2). For pathways where experimental data was not available, averages computed for E-E, E-I, I-E, and I-I connection types were assigned (see Table S6).

Reconstructing synaptic dynamics

Based on experimental data, synapse types (s-types) were separated into facilitating (E1 & I1), depressing (E2 & I2), and pseudo-linear (E3 & I3) types (Beierlein et al., 2003; Gupta et al., 2000; Reyes et al., 1998; Thomson et al., 1996; Wang et al., 2002, 2006); for a review see (Thomson and Lamy, 2007). We identified and used several constraining principles based on the current state of the art to map s-types associated with specific me-type to me-type pathways (Angulo et al., 1999; Bannister and Thomson, 2007; Blatow et al., 2003; Feldmeyer, 2006; Feldmeyer et al., 1999; Frick et al., 2007; Galarreta and Hestrin, 1998; Gupta et al., 2000; Holmgren et al., 2003; Kapfer et al., 2007; Maffei et al., 2004; Markram and Tsodyks, 1996; Markram et al., 1997, 1998; Mason et al., 1991; Mercer et al., 2005; Reyes et al., 1998; Rozov et al., 2001; Silberberg and Markram, 2007; Thomson and Bannister, 1998; Thomson and Lamy, 2007; Thomson et al., 1993; Wang et al., 1999, 2002, 2006). See Figure S9 for a summary of s-type assignment rules used.

Where directly available, experimental data were applied to relevant pathways, and where unavailable the constraining principles as previously identified were applied to produce a fully constrained map of synaptic dynamics for all possible me-type to me-type pathways. Unique dynamic synaptic parameters (U, D & F) for individual synapses were prescribed from a truncated Gaussian distribution with the SD parameter determined from experiments (Gupta et al., 2000; Silberberg and Markram, 2007; Wang et al., 2002, 2006).

Spontaneous synaptic release

Spontaneous miniature PSCs were modeled by implementing an independent Poisson process (of rate λ_{spont}) at each individual synapse to trigger release at low rates. The rates of spontaneous release for inhibitory and excitatory synapses were chosen to match experimental estimates(Ling and Benardo, 1999; Simkus and Stricker, 2002). The excitatory spontaneous rate was scaled up on a per layer basis to correct for missing extrinsic excitatory synapses. The resulting spontaneous release rates for unitary synapses were low enough (0.01Hz-0.6Hz) so as not to significantly depress individual synapse.

SIMULATION

Environment

The reconstructed microcircuit was simulated using the NEURON simulation package as the core computational engine (Hines and Carnevale, 1997). A collection of tools and templates, called Neurodamus, written in the HOC and NMODL programming languages (Hines and Carnevale, 2000) were employed to handle the setup and configuration of the microcircuit on the parallel machine architecture (Hines et al., 2008a). In addition, a reporting library written in C++ handled the parallel gathering of data and output to disk (Gropp et al., 1999). Simulations were configured in a configuration file to the main run script of Neurodamus, which specified the location of key data files, and assigned stimuli and reports to designated groups of cells, referred to as targets.

Simulation Configuration

A simulation was parameterized through a configuration file. Multiple sections in the file described an aspect of the simulation: general run parameters, stimuli, report generation, synapse and connection configurations. Key-Value pairs were used to apply settings within a given section. The initial section of the configuration provided user specified general settings for a simulation, including paths to various locations on disk such as the circuit and synapse files, the morphology files, the neuron models (electrical templates), and an output directory for generated reports. Other settings included the duration of a simulation, the time increment of the numerical solver, and the load-balancing mode. Stimulus sections were created for each stimulus to apply to a set of cells. Stimuli of various patterns were available to choose from: pulse, ramp, spike train, sine, random noise, etc. Depending on the stimulus pattern, additional settings were required. For example, a pulse stimulus required specification of a current amplitude (nA), a spike train required a frequency (Hz) and so on. All stimuli required a time delay and duration. Report sections were created to record a variable from a set of cells. Reports were configured to specify the variable in the NEURON simulation environment from which to record, for a starting time until some end time. In addition, the user could choose the file output format: ASCII, hdf5, or binary. Binary format was required when using multisplit load balancing in order to handle restructuring data that has been split across CPUs (Hines et al., 2008a). Connect sections were created to customize synapse creation. Users could designate two sets of cells, the source target and destination target, and any synapses from the source to the destination were configured as specified within the section.

Neurons were grouped together as a target. Two types of targets were used for regular simulations: cell and compartment targets. Cell targets were used more generally throughout simulation configuration. Members of a cell target were typically interpreted as whole cells for the purpose of connect sections. For stimuli and reports, members were interpreted as somata. Compartment targets provided a more specific addressing capacity in order to allow for dendritic or axonal locations of a cell to be included for stimulus and report usage.

Load-balancing and multisplit

When simulating the microcircuit on a massively parallel machine, it was important that the workload be distributed as evenly as possible to minimize idle CPUs. NEURON provides hooks to compute the computation load of a cell and determine the optimal way to separate that cell in multiple pieces assigned across multiple CPUs (Hines et al., 2008b). The initial microcircuit was instantiated by Neurodamus in a straightforward manner, which may not have very good load balancing. Calls were assessed by NEURON's load balancing algorithm and the optimal splitting strategy was written to disk. The microcircuit was then cleared from memory and Neurodamus recreated it using the now available load balancing information. During later stages of setup, checks were made to ensure that actions were executed for pieces on the local CPU and skipped when the piece exists on a remote CPU. The reporting library especially took care to handle the split cell case and managed the reorganization of data into the final output report file such that any cell's data appear all together within the report.

IN SILICO EXPERIMENTS

Bath manipulation simulations

In vivo and in vitro-like conditions were reconstructed in silico by modifying ionic concentrations in the extracellular bath medium. The extracellular Ca^{2+} concentration ($[Ca^{2+}]_o$) was manipulated by changing the utilization of synaptic efficacy parameter (U) in the stochastic synapse model (see section Synaptic Physiology). The reconstructed synaptic U parameters for standard in vitro bath conditions ($[Ca^{2+}]_o$ =2.0mM) were scaled as a function of $[Ca^{2+}]_o$ with pathway specific interpolating functions. The interpolating functions were determined from experimental data on changes in PSP amplitudes (relative to PSP at $[Ca^{2+}]_o$ =2.0mM) as a function of $[Ca^{2+}]_o$ by assuming all $[Ca^{2+}]_o$ induced changes where due to changes in U, and that U and PSP amplitude scalings have a linear relationship. As depicted in Figure S12, multiple data sources on such PSP scalings were collected from literature, and found to be consistent with one of two Hill isotherms reported previously (Rozov et al., 2001), either steep or shallow dependence. Parameterizations of $K_{1/2}$=2.79 for steep and $K_{1/2}$=1.09 for shallow are from previous reports (Rozov et al., 2001).

Specificities of $[Ca^{2+}]_o$ dependencies on connection type were implemented as follows: a) synapses between excitatory neurons, and between excitatory neurons and distal-targeting interneurons (DBC, BTC, MC, BP) in both directions have a steep calcium dependency; and b) synapses between excitatory and proximal-targeting PV+ interneurons (LBC, NBC, SBC, ChC) in both directions have a shallow calcium dependency (Figure S12A) (Gupta et al., 2000; Rozov et al., 2001; Silver et al., 2003; Tsodyks and Markram, 1997). Due to a lack of experimental data, synapses between inhibitory neurons, and between excitatory neurons and all other

inhibitory neurons are assumed to have level of dependency on $[Ca^{2+}]_o$ as the average of the two extremes (Figure S12A).

Depolarization in bath manipulation experiments (e.g. to mimic increased $[K^+]_o$ in vivo, tonic glutamate, or neuromodulators in the bath) was achieved by current injection at the neuron soma. Currents were expressed in terms of percentage of the minimum step current injection required for each cell to spike at least once (rheobase).

Bath manipulation experiments using multi-electrode array

To experimentally validate the observed transitions in the network state due to changes in $[Ca^{2+}]_o$, a multi-eletrode array was used to observe changes in synchronous network activity in brain slices while allowing rapid changes in bath composition. In accordance with the Swiss national and institutional guidelines, 300 µm thick sagittal brain slices were prepared from the somatosensory cortex of postnatal day 14 to 15 Wistar rats (N=2) of either sex in iced artificial cerebrospinal fluid (ACSF) containing (in mM) 125 NaCl, 2.5 KCl, 25 D-glucose, 25 NaHCO$_3$, 1.25 NaH$_2$PO$_4$, 2 CaCl$_2$, and 1 MgCl$_2$; all chemicals from Sigma-Aldrich, St. Louis, MO or Merck, Darmstadt, Germany) using a HR2 vibratome (Sigmann Elektronik, Heidelberg, Germany). The primary somatosensory cortex was manually dissected and isolated to obtain rectangular slices of 5 – 7 mm width and containing the neocortex in its entire height. Optimal slices, with apical cell dendrites running parallel to the slice surface, were selected for recordings. Slices were incubated at 22 ºC for 30 – 60 min until mounting in the recording chamber. Slices were mounted on a 3D-MEA with 60 pyramidal platinum electrodes (electrode basis: 40 µm × 40 µm, electrode height: 50 – 70 µm, electrode interspacing: 200 µm; Qwane Bioscience SA, Lausanne, Switzerland) after evaporation of a mounting solution of 0.14 mg/L nitrocellulose in an ethanol (99%) – methanol (1%) mixture. Experiments were conducted at room temperature (22°C).

We modified the concentration of potassium $[K^+]$, magnesium $[Mg^{2+}]$ and calcium $[Ca^{2+}]$ ions present in the extracellular solution to induce transitions in the network activity. We defined 3 different conditions corresponding to 3 sets of concentrations. Baseline solution: $[K^+]$ 2.5 mM; $[Mg^{2+}]$ 1.0 mM; $[Ca^{2+}]$ 2.0 mM; solution S1: High Potassium Low Calcium: $[K^+]$ 6.25 mM; $[Mg^{2+}]$ 0.5 mM; $[Ca^{2+}]$ 1.0 mM; and solution S2: High Potassium High Calcium: $[K^+]$ 6.25 mM; $[Mg^{2+}]$ 0.5 mM; $[Ca^{2+}]$ 2.0 mM. Bath changing times were minimized by employing a pipette to remove the recording chamber solution prior to changing the subsequent solution. We perfused the baseline solution for 5 minutes then recorded the network activity in the surface chamber for 90s; then, perfused solution S1 for 5 minutes recorded the network activity for 270s; and finally perfused solution S2 for 5 minutes recorded the network activity for 270s. Several experiments were undertaken to establish the transition time using this approach, and the 5 min interval between recording times was determined to be a minimal yet sufficient time to induce a transition to bursting (baseline->S2 or S1 ->S2).

We recorded activity in a total of 12 slices (3 slices per hemisphere per animal). Experimental data analysis was performed in Matlab (The MathWorks, Inc., Natick, MA, USA) with custom scripts. Extra-cellular spikes were detected when recorded signal crossed a dynamic threshold T:

$$T = \dot{x} - 5 * std(X)$$

X is the recorded data chunk over the whole recording duration whereas $\dot{x}$ is a local average of the recorded data (sliding window of 40 ms). We computed the inter burst interval (IBI) when slices were perfused with S2, and oscillations lasted for 30s or more. To avoid transitions in the network activity to affect this measure, the IBI was computed over period considered as regular (IBI below a threshold = avg(IBI) + 3 std(IBI)). Data are presented as the mean ± SEM. Paired Student's *t* tests were applied as statistical tests, and statistical significance was asserted for: [*]$p<0.05$; [**]$p<0.01$; [***]$p<0.001$.

Observations of oscillations for various solutions as follows. Baseline solution: 1/12 slices, 2 bursts (~20 Hz); S1: 2/12 slices, sparse bursting; S2: 9/12 slices, regular bursting with an IBI of 1.59 +/- 0.09 s (mean +/- SD) or 0.98 +/- 0.05 Hz.

Generating thalamic input

The hind-limb somatosensory cortex receives input from the ventro-posterolateral (VPL) nucleus of the thalamus (Kandel et al., 2000). As data for the VPL enervation pattern is scarce, we used published data from the ventral posterior medial (VPM) thalamic nucleus to generate a vertical density profile for external thalamic synaptic input (Meyer et al., 2010). In a number of successive steps, first the vertical depth profile was digitized and binned with a bin size of 25 µm. For each depth bin, we then found all morphological segments contained inside that bin (i.e. the midpoint of the segment was located inside the bin). We then continuously drew random segments from the pool and placed a synapse at their centers, until 2.6 times the biological density (oversampling) at that depth bin was reached. Synapses were then pruned using the multi-synapse rule step (see (Reimann et al., 2015)). Drawing was with replacement, i.e. a segment could be drawn more

than once. The probability of drawing a given segment was proportional to its length, i.e. longer segments will be drawn more often. The 2.6 oversampling factor was chosen to match thalamocortical synapses per connection onto L4 excitatory cells.

Dynamic synaptic parameters were drawn from distributions with means and standard deviations taken from the literature (Amitai, 2001; Gil et al., 1999).

Each external synapse was assigned a virtual presynaptic VPM cell, whose spike will activate it. To accurately capture the correlation between synaptic inputs, the mapping to virtual presynaptic cells was spatial according to minicolumns, i.e. synapses that were close together were likely to be innervated by the same virtual presynaptic cell. In particular, there was one virtual cell per minicolumn and the probability that a synapse was mapped to it was dependent on the distance to the center of the minicolumn:

$$P(S_{pre} = i) \propto e^{-\frac{|C_i - T_{pre}|}{2\sigma^2}},$$

where S_{pre} denotes the mapping of synapse S, T_{pre} its spatial location and C_i the location of the center of minicolumn i ; σ defined the degree of spatial mapping and was set to 25 µm.

Calculation of spike time correlations

The mean spike-spike correlations (Figure 17, S13) were calculated as the histogram of intervals between all spike times of two different cells (bin size 1 ms). The average was computed over 10 '000 randomly selected cell pairs.

Detection of structural assemblies

Structural assemblies (Figure S15) were detected based on the number of common neighbors between cell pairs, i.e. the number of neurons connected pre- or post-synaptically to both cells. We calculated the number for all N^2 potential pairs, where N is the number of neurons in the circuit. The numbers were converted into a distance measure between 0 and 1, setting the distance between pairs to 1 minus the cumulative probability of the number of common neighbors. The cumulative probability was calculated once based on the number of common neighbors of all pairs involving one cell of the pair, then based on the other cell and finally the root mean square was used:

$$D(i,j) = 1 - \sqrt{\frac{C_i\left(N(i,j)\right)^2 + C_j\left(N(i,j)\right)^2}{2}},$$

where *N(i,j)* refers to the number of common neighbors between *i* and *j* and C_x to the cumulative probability function based on the number of common neighbors of *x* with any cell.

Assemblies were then detected by creating a hierarchical cluster tree based on the distance matrix using Matlab (The MathWorks, Inc., Natick, MA, USA).

Calculation of voltage correlations

Voltage correlation was computed by convolving the two voltage traces with their means subtracted.

REPRODUCTION OF *IN VIVO* EXPERIMENTS

Emergence

We performed a series of simulations on monotonically increasing circuit sizes (50, 100, 200, 300, 400 and 1000 minicolumns per microcircuit, $[Ca^{2+}]_o = 1.25$ mM, 100% depolarization), resulting in a collection of six 20 second recordings of spontaneous *in silico* activity. Subsequently, each microcircuit's minicolumns were sorted into spatially coherent clusters comprising an average of ten minicolumns using a k-means clustering algorithm. The result was that the six circuits were grouped into 5, 10, 20, 30, 40 and 100 clusters of 10 minicolumns, respectively. Finally, we computed the population-level firing rate PSTH for each cluster in each circuit using a time bin of 5 ms (Figures 20E,F) or 20ms (Figures 20C,D). Spatial profile plots were obtained by interpolation of the estimated PSTH for a given time slice assigned to the locations of the minicolumns using the 'cubic' method of scipy.interpolate.griddata. Pairwise cross-correlation coefficients between the PSTHs were computed for each possible combination of two clusters.

Temporally sequential structure during spontaneous activity of L5 neurons

To construct an in silico approximation of an in vivo UP state, the inner 20 minicolumns of the reconstructed microcircuit were stimulated by activating the afferent VPM fibers innervating these minicolumns. The stimulus was delivered 1500 ms after the commencement of each trial to ensure that the circuit dynamics had achieved a steady-state prior to stimulation. Neural responses were recorded for 500 ms following application of the stimulus. The data contained in Fig. 18A were obtained by repeating the stimulus protocol described above 25 times, and concatenating the spike trains generated by each neuron during each trial. Thus, we obtained a dataset consisting of 25 activated (UP state-like) states, each lasting 500 ms (though the time course of neural activity throughout this period was typically much shorter, on the order of 250 ms), preceded by 1500 ms of spontaneous activity.

In line with Luczak *et al.* (Luczak et al., 2007), we restricted our analysis to a randomly selected pool of 50 neurons in L5, whose average firing rate was greater than 3 Hz throughout the course of each trial. 19,600 cell trios were constructed from this pool by considering all distinct combinations of 3 neurons. The collection of triplets associated with a given trio was obtained by sequentially iterating over each spike in the raster of the trio's first cell, and calculating the time differences between the occurrence of that spike and the occurrences of all spikes in the rasters of the remaining two neurons (see Fig. 18A). Next, for each trio, we computed a count matrix of triplet structures (see Fig. 18A1), comprising a normalized 2D histogram of the trio's triplets binned at 3.2 ms, which we subsequently smoothed with a 10 ms Gaussian kernel. From each trio's count matrix, we extracted the precisely repeating triplets, defined as those triplets occurring within +/- 10 ms of the mode. Furthermore, to produce Fig. 18A2, we calculated each neuron's average latency, which we defined as the center of mass of a given cell's activated state-triggered PETH (smoothed by a 10 ms Gaussian kernel) within a 250 ms time window. Finally, we compared the results of our analysis against two competing null hypotheses (see Fig. 18A3). In the first, an independent Poisson model, we randomly permuted the spike times of each cell's spike train (thereby preserving the overall firing rate of each cell), and calculated the average probability of observing a precisely repeating triplet as a function of time from the onset of an activated state. To this end, we constructed a normalized histogram (binned at 3.2 ms) of the temporal occurrence of precisely repeating triplets produced by all trios. In the second, a "common excitability" model of triplet activity, we randomly exchanged spikes between the rasters of all 50 neurons, thereby preserving both the average firing rate of each cell and the exact spike times contained in the pooled set of raster data, and computed the average probability of observing precisely repeating triplets as described above.

Neuronal Responses to Single Whisker Deflection

In each trial, the 60 VPM fibers closest to the center of the microcircuit were stimulated with synchronous action potentials. There were 200 trials with different simulation seeds. Only the stimulated column was simulated.

Neurons for the scatter plot were randomly selected reflecting the statistics used in the in vivo study by Reyes-Puerta *et al.* (see Fig 3B in (Reyes-Puerta et al., 2015)). The overall neuron counts that were chosen in silico were: 2630 excitatory neurons (2080 in L5, 360 in L4, 100 in L3, and 90 in L2), 550 inhibitory neurons (370 in L5, 50 in L4, 20 in L3, 10 in L2). NR cells were defined as those that either did not pass the significance test ($p > 5$) or did not fire at all.

VISUALIZATION

Mesh Generation

In order to generate the meshes used in the visualization, we used the Visualization Tool Kit, an open-source software package for 3D computer graphics. The mesh generator built upon our previous technique (Lasserre, 2012). Morphology files were read in and a kernel of the appropriate radius was extruded along the morphology. At branch points, new holes were opened in the mesh and joined with the child processes. Processes were connected to a spherical soma kernel and smoothing performed. The final product was a watertight, manifold mesh suitable for simulation with subcellular simulators such as MCell as well as visualization using RTNeuron. The mesh generation step could export in a variety of formats, including ply, obj, vtk and internal formats that include information about the identity of the subcellular components and their mapping to the neuronal morphologies.

RT Neuron

Some of the high resolution images and the simulation playback movies were rendered with RTNeuron (Hernando et al., 2008, 2012). RTNeuron is a C++ rendering engine with a Python wrapping based on

OpenSceneGraph and Equalizer (for parallel rendering) (Eilemann et al., 2009), usable as either a standalone application or a Python module. It was developed in house as the result of a long-term collaboration between the BBP and the Cajal Blue Brain project. Apart from being a tool for generating presentation media, RTNeuron also allowed the interactive visualization of the structural information and the simulation results of large cortical circuits (~10K cells). These capabilities were used for debugging the model building process as well as the simulation. The interactive capabilities were used to design the color maps used to map simulation variables onto the mesh model of each cell membrane. RTNeuron implemented a fast algorithm for rendering transparent geometry that was used to generate the images showing simulation data. RTNeuron read the file formats produced by other applications from the tool chain using an object-oriented library developed for that purpose, the BBP-SDK. Apart from interactive visualization, it can write images in all file formats supported by OpenSceneGraph for monoscopic and stereoscopic visualization.

Maya

For some visualizations, we used Maya® 3D animation software (Autodesk, San Rafael, California, USA). As Maya is limited in the number of meshes it can handle, it was mainly used for creating high quality static images of small neural circuits. We built an automated workflow on top of Maya and the mesh generation software to visualize individual neurons color-coded according to their morphology types or layers that could also show the distribution of the excitatory and inhibitory synapses color-coded according to the morphology type of their pre-synaptic partners.

The neuron meshes were exported in Wavefront object format from the mesh generation stage and read on the fly into Maya. We mapped a shader onto the mesh in order to give the appearance of texturing seen in electron micrograph images. Color, glow, transparency were also altered according to the visualization scenario. In images displaying synapses and spines, the positions were assigned according to an input list, generated from the circuit. In images involving multiple neurons, the neuron meshes were rotated and translated according to their position in the circuit.

Rendering was performed on a cluster of 12 Intel Xeon X5690 cores, running at 3.47 GHz. Rendering time per frame on one node ranged from 10 seconds. Frames were integrated and post-processed using Adobe Aftereffects (Adobe Systems, San Jose, California, USA).

Volume Rendering

Some microcircuit images were generated using volume rendering. We chose this method because volumetric effects such as slicing, segmenting, volumetric noise and transparency were needed to simulate the sample images taken from laboratory microscopes. The volume rendering equations were evaluated using volume ray casting (Levoy, 1990), which calculates the absorption incurred by rays cast from the eye of the observer.

There were two stages in volume rendering: rasterization and rendering. In the first stage, meshes were rasterized into regular grids and then placed in the circuit volume. This resulted in a large regular grid data containing the density values of the rasterized meshes in each cell. The tools employed in this stage included C++ libraries and python scripts. One could set the branch order for visualizing different number of branching depths of the cell processes, the inclusion of soma, dendrites, axons, as well as shell rendering for just visualizing the iso-surface of the neuron mesh.

In the rendering stage, the engines employed were the Python-based Mayavi (Ramachandran and Varoquaux, 2011) library for easy python scripting and the Voreen tool (Meyer-Spradow et al., 2009) for easy GUI-based modifications to the rendering. The coloring and transparency of the images are evaluated through modifying the transfer functions of the rendering equation in volume ray casting.

The stained sample images taken from laboratory microscopes exhibited staining noise. This noise was mimicked computationally using the Perlin noise generator (Perlin) integrated into the Voreen tool with the Libnoise library (available from Sourceforge). The cells in these images also had noise on the soma surface, which was simulated using uniformly distributed noise in the volume multiplied by the intensities in the non-empty grid cells.

In silico Fluorescence Microscopy

A novel method was developed to visualize the fluorescent tissue models (Abdellah et al., 2015) using the spectral characteristics of fluorescent dyes including their emission and excitation spectra, quantum yield and their concentration in the tissue. This method uses physically-based volume rendering to simulate the light interaction with the fluorescent-labeled brain structures relying on the optical properties of the tissue and the fluorescent dyes. The generated renderings can accurately reflect the optical sections created from fluorescence microscopy.

Connectivity diagrams

The ribbon plot in Figure 7C was generated using Circos software (Krzywinski et al., 2009).

SOFTWARE INTEGRATION AND COMPUTING INFRASTRUCTURE

Development process and continuous integration

Data integration and post processing as well as building, simulation, analysis and visualization of neuronal network models relied on developing and integrating more than 30 software applications in complex workflows. The efficient development of such a large set of applications, by dozens of contributors, required putting together a comprehensive development environment. All major software tools are registered with a common versioning system (Git) and all modifications are traced. For the major software applications, online code review via Gerrit is implemented as well as continuous building, testing, packaging and deployment using Jenkins. The software is released on various machines and architectures and GNU modules are used to expose the installed software to the end user.

Workflows and Provenance

A significant aspect of reproducibility is the tracking of the input and output artifacts in each step in the circuit building, simulation, and analysis workflow. To this end, we constructed a collaboration portal, which provides a) functionality to register artifacts and process execution manually or automatically upon workflow execution b) a forum to view and discuss the results of simulations c) functionality to do comparative analysis of different simulations. Workflows are collections of standardized conversion, analysis and validation tasks using a custom Python-based Task component framework. The Task component framework allows the wrapping of any type of code into a source-controlled component, which automatically tracks provenance of artifacts during execution. This is accomplished by leveraging the OPM provenance model as implemented by the Karma Provenance Server (http://d2i.indiana.edu/provenance_karma).

Storage for Experimental Data

Experimental data is stored on a scalable unified storage resource delivered by a NetApp FAS3240 cluster. A unified storage architecture allows the consolidation of diverse workloads and helps maximizing the efficiency. It also allows us to support multiple network configurations and protocols. Experimental data is internally accessible via native NFS and CIFS protocols, and federated externally via iRODS system. The Integrated Rule-Oriented Data System (iRODS) is an open-source data management software in use at research organizations and government agencies worldwide. It functions independently of storage resources and abstracts data control away from storage devices and device location.

Analysis and Visualization Cluster

Computation for processing of experimental data, models or for interactive visualization sessions is provided by a fully model-managed cluster (Intel 188-cores, 39 x nVidia GTX580) with SLURM reservation system and scheduler. The model-based approach helps to manage the cluster throughout its lifecycle, from provisioning and configuration to orchestration and reporting, by enforcing a standard operating environment and thus eliminating configuration drifts.

Supercomputing

For more compute intensive workflow steps, such as cell building, circuit building, network simulation the study relied on supercomputers. Amongst the systems used were the CADMOS 4-rack IBM Blue Gene/P (until February 2013), CADMOS 1-rack IBM Blue Gene/Q (March 2013 until March 2014). The CADMOS infrastructure was interconnected with the Analysis and Visualization Cluster by using a common shared GPFS file system where data exchange between the two machines is supported by 2x10 Gib/s Ethernet links.

Building on the CADMOS-EPFL hardware integration experience, a tighter design resulted in the construction of Blue Brain IV, 100th most powerful supercomputing system (Top500, June 2015), which is operated by the Swiss National Supercomputing Center (CSCS) for the Blue Brain Project. It includes a 4-rack IBM Blue Gene/Q, IBM Blue Gene Active Storage, and a 40-node Intel cluster fully interconnected using Infiniband technology and a GPFS file system with 4.2 Petabyte raw storage (Schürmann et al., 2014).

REFERENCES

Abdellah, M., Bilgili, A., Eilemann, S., Markram, H., and Schürmann, F. (2015). A Computational Model of Light-Sheet Fluorescence Microscopy using Physically-based Rendering. In Proc. Eurographics - Posters, (Eurographics Association),.

Adams, P.R., Brown, D.A., and Constanti, A. (1982). M-Currents and Other Potassium Currents in Bullfrog Sympathetic Neurones. J. Physiol. *330*, 537–572.

Van Aerde, K.I., and Feldmeyer, D. (2015). Morphological and Physiological Characterization of Pyramidal Neuron Subtypes in Rat Medial Prefrontal Cortex. Cereb. Cortex *25*, 788–805.

Amitai, Y. (2001). Thalamocortical synaptic connections: efficacy, modulation, inhibition and plasticity. Rev. Neurosci. *12*, 159–173.

Angulo, M.C., Rossier, J., and Audinat, E. (1999). Postsynaptic Glutamate Receptors and Integrative Properties of Fast-Spiking Interneurons in the Rat Neocortex. J. Neurophysiol. *82*, 1295–1302.

Anwar, H., Riachi, I., Hill, S., Schurmann, F., and Markram, H. (2009). An approach to capturing neuron morphological diversity. In Computational Modeling Methods for Neuroscientists, (The MIT Press), pp. 211–231.

Ascoli, G.A., and Krichmar, J.L. (2000). L-neuron: A modeling tool for the efficient generation and parsimonious description of dendritic morphology. Neurocomputing *32–33*, 1003–1011.

Ascoli, G.A., Krichmar, J.L., Scorcioni, R., Nasuto, S.J., Senft, S.L., and Krichmar, G.L. (2001). Computer generation and quantitative morphometric analysis of virtual neurons. Anat. Embryol. (Berl.) *204*, 283–301.

Avery, R.B., and Johnston, D. (1996). Multiple Channel Types Contribute to the Low-Voltage-Activated Calcium Current in Hippocampal CA3 Pyramidal Neurons. J. Neurosci. *16*, 5567–5582.

Bannister, A.P., and Thomson, A.M. (2007). Dynamic properties of excitatory synaptic connections involving layer 4 pyramidal cells in adult rat and cat neocortex. Cereb. Cortex *17*, 2190–2203.

Beierlein, M., Gibson, J.R., and Connors, B.W. (2003). Two Dynamically Distinct Inhibitory Networks in Layer 4 of the Neocortex. J. Neurophysiol. *90*, 2987–3000.

Le Bé, J.-V., Silberberg, G., Wang, Y., and Markram, H. (2007). Morphological, Electrophysiological, and Synaptic Properties of Corticocallosal Pyramidal Cells in the Neonatal Rat Neocortex. Cereb. Cortex *17*, 2204–2213.

Blatow, M., Rozov, A., Katona, I., Hormuzdi, S.G., Meyer, A.H., Whittington, M.A., Caputi, A., and Monyer, H. (2003). A novel network of multipolar bursting interneurons generates theta frequency oscillations in neocortex. Neuron *38*, 805–817.

Bleuler, S., Laumanns, M., Thiele, L., and Zitzler, E. (2003). PISA — A Platform and Programming Language Independent Interface for Search Algorithms. In Evolutionary Multi-Criterion Optimization, C. Fonseca, P. Fleming, E. Zitzler, L. Thiele, and K. Deb, eds. (Springer Berlin / Heidelberg), pp. 1–1.

Bonthius, D.J., McKim, R., Koele, L., Harb, H., Karacay, B., Mahoney, J., and Pantazis, N.J. (2004). Use of frozen sections to determine neuronal number in the murine hippocampus and neocortex using the optical disector and optical fractionator. Brain Res. Protoc. *14*, 45–57.

Brémaud, A., West, D.C., and Thomson, A.M. (2007). Binomial Parameters Differ Across Neocortical Layers and with Different Classes of Connections in Adult Rat and Cat Neocortex. 14134–14139.

Brionne, T.C., Tesseur, I., Masliah, E., and Wyss-Coray, T. (2003). Loss of TGF-beta 1 leads to increased neuronal cell death and microgliosis in mouse brain. Neuron *40*, 1133–1145.

Burke, R.E., Marks, W.B., and Ulfhake, B. (1992). A parsimonious description of motoneuron dendritic morphology using computer simulation. J. Neurosci. *12*, 2403–2416.

Carnevale, N.T., and Hines, M.L. (2006). The NEURON Book (New York, NY, USA: Cambridge University Press).

Del Castillo, J., and Katz, B. (1954). Quantal components of the end-plate potential. J. Physiol. *124*, 560–573.

Colbert, C.M., and Pan, E. (2002). Ion channel properties underlying axonal action potential initiation in pyramidal neurons. Nat. Neurosci. *5*, 533–538.

Diba, K., Koch, C., and Segev, I. (2006). Spike propagation in dendrites with stochastic ion channels. J. Comput. Neurosci. *20*, 77–84.

Donohue, D.E., and Ascoli, G.A. (2008). A Comparative Computer Simulation of Dendritic Morphology. PLoS Comput Biol *4*, e1000089.

Druckmann, S., Banitt, Y., Gidon, A., Schürmann, F., Markram, H., and Segev, I. (2007). A Novel Multiple Objective Optimization Framework for Constraining Conductance-Based Neuron Models by Experimental Data. Front. Neurosci. *1*, 7–18.

Eilemann, S., Makhinya, M., and Pajarola (2009). Equalizer: A scalable parallel rendering framework. IEEE Trans. Vis. Comput. Graph. *15*, 436–452.

Feldmeyer, D. (2006). Efficacy and connectivity of intracolumnar pairs of layer 2/3 pyramidal cells in the barrel cortex of juvenile rats. J. Physiol. *575*, 583–602.

Feldmeyer, D., Egger, V., Lübke, J., and Sakmann, B. (1999). Reliable synaptic connections between pairs of excitatory layer 4 neurones within a single "barrel" of developing rat somatosensory cortex. J. Physiol. *521*, 169–190.

Flint, A.C., Maisch, U.S., Weishaupt, J.H., Kriegstein, A.R., and Monyer, H. (1997). NR2A subunit expression shortens NMDA receptor synaptic currents in developing neocortex. J. Neurosci. *17*, 2469–2476.

Frick, A., Feldmeyer, D., and Sakmann, B. (2007). Postnatal development of synaptic transmission in local networks of L5A pyramidal neurons in rat somatosensory cortex. J. Physiol. *585*, 103–116.

Fuhrmann, G., Segev, I., Markram, H., and Tsodyks, M. (2002). Coding of temporal information by activity-dependent synapses. J Neurophysiol *87*, 140–148.

Galarreta, M., and Hestrin, S. (1998). Frequency-dependent synaptic depression and the balance of excitation and inhibition in the neocortex. Nat. Neurosci. *1*, 587–594.

Gil, Z., Connors, B.W., and Amitai, Y. (1999). Efficacy of Thalamocortical and Intracortical Synaptic Connections: Quanta, Innervation, and Reliability. Neuron *23*, 385–397.

Gropp, W., Lusk, E., and Skjellum, A. (1999). Using MPI, 2nd Edition: Portable Parallel Programming with the Message Passing Interface (MIT Press).

Gupta, A., Wang, Y., and Markram, H. (2000). Organizing Principles for a Diversity of GABAergic Interneurons and Synapses in the Neocortex. Science *287*, 273–278.

Häusser, M., and Roth, A. (1997). Estimating the time course of the excitatory synaptic conductance in neocortical pyramidal cells using a novel voltage jump method. J. Neurosci. *17*, 7606–7625.

Hay, E., Hill, S., Schürmann, F., Markram, H., and Segev, I. (2011). Models of Neocortical Layer 5b Pyramidal Cells Capturing a Wide Range of Dendritic and Perisomatic Active Properties. PLoS Comput Biol *7*, e1002107.

Hernando, J., Schürmann, F., Markram, H., and de Miguel, P. (2008). RTNeuron, an Application for Interactive Visualization of Detailed Cortical Column Simulations. XIX Jorn. Paralelismo.

Hernando, J., Schürmann, F., and Pastor, L. (2012). Towards real-time visualization of detailed neural tissue models: view frustum culling for parallel rendering. Proc. 2nd IEEE Symp. Biol. Data Vis. *in press.*

Hestrin, S., and Armstrong, W.E. (1996). Morphology and physiology of cortical neurons in layer I. J. Neurosci.*16*, 5290–5300.

Hillman, D.E. (1979). Neuronal shape parameters and substructures as a basis of neuronal form. In The Neurosciences, 4th Study Program, F. Schmitt, ed. (Cambridge: MIT Press), pp. 477–498.

Hines, M.L., and Carnevale, N.T. (1997). The NEURON Simulation Environment. Neural Comput. *9*, 1179–1209.

Hines, M.L., and Carnevale, N.T. (2000). Expanding NEURON's Repertoire of Mechanisms with NMODL. Neural Comput. *12*, 995–1007.

Hines, M., Markram, H., and Schürmann, F. (2008a). Fully implicit parallel simulation of single neurons. J. Comput. Neurosci. *25*, 439–448.

Hines, M., Eichner, H., and Schürmann, F. (2008b). Neuron splitting in compute-bound parallel network simulations enables runtime scaling with twice as many processors. J. Comput. Neurosci. *25*, 203–210.

Holmgren, C., Harkany, T., Svennenfors, B., and Zilberter, Y. (2003). Pyramidal cell communication within local networks in layer 2/3 of rat neocortex. J. Physiol. *551*, 139–153.

Jaeger, D. (2000). Accurate reconstruction of neuronal morphology. In Computational Neuroscience: Realistic Modeling for Experimentalists, E. De Schutter, ed. (Boca Raton, Florida: CRC Press), pp. 159–178.

Jahr, C.E., and Stevens, C.F. (1990a). Voltage dependence of NMDA-activated macroscopic conductances predicted by single-channel kinetics. J. Neurosci. *10*, 3178–3182.

Jahr, C.E., and Stevens, C.F. (1990b). A quantitative description of NMDA receptor-channel kinetic behavior. J. Neurosci. *10*, 1830–1837.

Kandel, E., Schwartz, J., and Jessell, T. (2000). Principles of Neural Science (McGraw-Hill Medical).

Kapfer, C., Glickfeld, L.L., Atallah, B.V., and Scanziani, M. (2007). Supralinear increase of recurrent inhibition during sparse activity in the somatosensory cortex. Nat. Neurosci. *10*, 743–753.

Kasper, E.M., Larkman, A.U., Lübke, J., and Blakemore, C. (1994). Pyramidal neurons in layer 5 of the rat visual cortex. II. Development of electrophysiological properties. J. Comp. Neurol. *339*, 475–494.

Kawaguchi, Y., and Kubota, Y. (1997). GABAergic cell subtypes and their synaptic connections in rat frontal cortex. Cereb. Cortex *7*, 476–486.

Khazipov, R., Congar, P., and Ben-Ari, Y. (1995). Hippocampal CA1 lacunosum-moleculare interneurons: modulation of monosynaptic GABAergic IPSCs by presynaptic GABAB receptors. J. Neurophysiol. *74*, 2126–2137.

Kisvárday, Z.F., Gulyas, A., Beroukas, D., North, J.B., Chubb, I.W., and Somogyi, P. (1990). Synapses, axonal and dendritic patterns of GABA-immunoreactive neurons in human cerebral cortex. Brain J. Neurol. *113 (Pt 3)*, 793–812.

Koester, H.J., and Johnston, D. (2005). Target Cell-Dependent Normalization of Transmitter Release at Neocortical Synapses. Science *308*, 863–866.

Köhler, M., Hirschberg, B., Bond, C.T., Kinzie, J.M., Marrion, N.V., Maylie, J., and Adelman, J.P. (1996). Small-Conductance, Calcium-Activated Potassium Channels from Mammalian Brain. Science *273*, 1709–1714.

Kole, M.H.P., Hallermann, S., and Stuart, G.J. (2006). Single Ih Channels in Pyramidal Neuron Dendrites: Properties, Distribution, and Impact on Action Potential Output. J. Neurosci. *26*, 1677–1687.

De Koninck, Y., and Mody, I. (1997). Endogenous GABA Activates Small-Conductance K+ Channels Underlying Slow IPSCs in Rat Hippocampal Neurons. J. Neurophysiol. *77*, 2202–2208.

Korn, H., and Faber, D.S. (1991). Quantal analysis and synaptic efficacy in the CNS. Trends Neurosci. *14*, 439–445.

Korngreen, A., and Sakmann, B. (2000). Voltage-gated K+ channels in layer 5 neocortical pyramidal neurones from young rats: subtypes and gradients. J. Physiol. *525*, 621–639.

Kozloski, J., Sfyrakis, K., Hill, S., Schürmann, F., Peck, C., and Markram, H. (2008). Identifying, tabulating, and analyzing contacts between branched neuron morphologies. IBM J Res Dev *52*, 43–55.

Krzywinski, M., Schein, J., Birol, I., Connors, J., Gascoyne, R., Horsman, D., Jones, S.J., and Marra, M.A. (2009). Circos: An information aesthetic for comparative genomics. Genome Res. *19*, 1639–1645.

Larkum, M.E., Zhu, J.J., and Sakmann, B. (2001). Dendritic Mechanisms Underlying the Coupling of the Dendritic with the Axonal Action Potential Initiation Zone of Adult Rat Layer 5 Pyramidal Neurons. J. Physiol. *533*, 447–466.

Larsen, D.D., and Callaway, E.M. (2006). Development of layer-specific axonal arborizations in mouse primary somatosensory cortex. J. Comp. Neurol. *494*, 398–414.

Lasserre, S. (2012). A neuron membrane mesh representation for visualization of electrophysiological simulations. IEEE Trans Vis Comput Graph *18*, 214–227.

Levoy, M. (1990). Efficient Ray Tracing of Volume Data. ACM Trans. Graph. *9*, 245–261.

Ling, D.S., and Benardo, L.S. (1999). Restrictions on inhibitory circuits contribute to limited recruitment of fast inhibition in rat neocortical pyramidal cells. J. Neurophysiol. *82*, 1793–1807.

Luczak, A., Barthó, P., Marguet, S.L., Buzsáki, G., and Harris, K.D. (2007). Sequential structure of neocortical spontaneous activity in vivo. Proc. Natl. Acad. Sci. *104*, 347–352.

Maffei, A., Nelson, S.B., and Turrigiano, G.G. (2004). Selective reconfiguration of layer 4 visual cortical circuitry by visual deprivation. Nat. Neurosci. *7*, 1353–1359.

Magistretti, J., and Alonso, A. (1999). Biophysical Properties and Slow Voltage-Dependent Inactivation of a Sustained Sodium Current in Entorhinal Cortex Layer-II Principal Neurons A Whole-Cell and Single-Channel Study. J. Gen. Physiol. *114*, 491–509.

Markram, H., and Tsodyks, M. (1996). Redistribution of synaptic efficacy between neocortical pyramidal neurons. Nature *382*, 807–810.

Markram, H., Lubke, J., Frotscher, M., Roth, A., and Sakmann, B. (1997). Physiology and anatomy of synaptic connections between thick tufted pyramidal neurones in the developing rat neocortex. J. Physiol. *500*, 409–440.

Markram, H., Wang, Y., and Tsodyks, M. (1998). Differential Signaling Via the Same Axon of Neocortical Pyramidal Neurons. Proc. Natl. Acad. Sci. *95*, 5323–5328.

Markram, H., Toledo-Rodriguez, M., Wang, Y., Gupta, A., Silberberg, G., and Wu, C. (2004). Interneurons of the neocortical inhibitory system. Nat. Rev. Neurosci. *5*, 793–807.

Marx, M., and Feldmeyer, D. (2013). Morphology and Physiology of Excitatory Neurons in Layer 6b of the Somatosensory Rat Barrel Cortex. Cereb. Cortex *23*, 2803–2817.

Mason, A., Nicoll, A., and Stratford, K. (1991). Synaptic transmission between individual pyramidal neurons of the rat visual cortex in vitro. J. Neurosci. *11*, 72–84.

Mercer, A., West, D.C., Morris, O.T., Kirchhecker, S., Kerkhoff, J.E., and Thomson, A.M. (2005). Excitatory Connections Made by Presynaptic Cortico-Cortical Pyramidal Cells in Layer 6 of the Neocortex. Cereb. Cortex *15*, 1485–1496.

Meyer, H.S., Wimmer, V.C., Hemberger, M., Bruno, R.M., Kock, D., P.j, C., Frick, A., Sakmann, B., and Helmstaedter, M. (2010). Cell Type–Specific Thalamic Innervation in a Column of Rat Vibrissal Cortex. Cereb. Cortex *20*, 2287–2303.

Meyer-Spradow, J., Ropinski, T., Mensmann, J., and Hinrichs, K. (2009). Voreen: A Rapid-Prototyping Environment for Ray-Casting-Based Volume Visualizations. IEEE Comput. Graph. Appl. *29*, 6–13.

Monyer, H., Burnashev, N., Laurie, D.J., Sakmann, B., and Seeburg, P.H. (1994). Developmental and regional expression in the rat brain and functional properties of four NMDA receptors. Neuron *12*, 529–540.

Mott, D.D., Li, Q., Okazaki, M.M., Turner, D.A., and Lewis, D.V. (1999). GABAB-Receptor–Mediated Currents in Interneurons of the Dentate-Hilus Border. J. Neurophysiol. *82*, 1438–1450.

Myme, C.I.O., Sugino, K., Turrigiano, G.G., and Nelson, S.B. (2003). The NMDA-to-AMPA Ratio at Synapses Onto Layer 2/3 Pyramidal Neurons Is Conserved Across Prefrontal and Visual Cortices. J. Neurophysiol. *90*, 771–779.

Niederreiter, H. (1988). Low-discrepancy and low-dispersion sequences. J. Number Theory *30*, 51–70.

Oberlaender, M., Kock, C.P.J. de, Bruno, R.M., Ramirez, A., Meyer, H.S., Dercksen, V.J., Helmstaedter, M., and Sakmann, B. (2012). Cell Type–Specific Three-Dimensional Structure of Thalamocortical Circuits in a Column of Rat Vibrissal Cortex. Cereb. Cortex *22*, 2375–2391.

Paxinos, G., and Watson, C. (1998). The rat brain in stereotaxic coordinates (San Diego: Academic Press).

Pedregosa, F., Varoquaux, G., Gramfort, A., Michel, V., Thirion, B., Grisel, O., Blondel, M., Prettenhofer, P., Weiss, R., Dubourg, V., et al. (2011). Scikit-learn: Machine Learning in Python. J. Mach. Learn. Res. *12*, 2825–2830.

Pelt, J.V., and Uylings, H.B.M. (2003). Growth Functions in Dendritic Outgrowth. Brain Mind *4*, 51–65.

Perlin, K. An Image Synthesizer. Comput. Graph. Mag. *19*.

Ramachandran, P., and Varoquaux, G. (2011). Mayavi: 3D Visualization of Scientific Data. IEEE Comput. Sci. Eng. *13*, 40–51.

Ramaswamy, S., Hill, S.L., King, J.G., Schürmann, F., Wang, Y., and Markram, H. (2012). Intrinsic Morphological Diversity of Thick-Tufted Layer 5 Pyramidal Neurons Ensures Robust and Invariant Properties of in Silico Synaptic Connections. J. Physiol. *590*, 737–752.

Ramaswamy, S., Courcol, J.-D., Abdellah, M., Adaszewski, S., Antille, N., Arsever, S., Guy Antoine, A.K., Bilgili, A., Brukau, Y., Chalimourda, A., et al. (2015). The Neocortical Microcircuit Collaboration Portal: A Resource for Rat Somatosensory Cortex. Front. Neural Circuits *9*, 44. doi: 10.3389/fncir.2015.00044

Rao, C.R. (1948). The Utilization of Multiple Measurements in Problems of Biological Classification. J R. Stat. Soc Ser B *10*, 159–203.

Rao, C.R. The Utilization of Multiple Measurements in Problems of Biological Classification. J. R. Stat. Soc. Ser. B Methodol. *10*, 159–203.

Reimann, M.W., Muller, E.B., Ramaswamy, S., and Markram, H. (2015). An Algorithm to Predict the Connectome of Neural Microcircuits. *Front. Comput. Neurosci. 9*, 28. doi: 10.3389/fncom.2015.00120

Rettig, J., Wunder, F., Stocker, M., Lichtinghagen, R., Mastiaux, F., Beckh, S., Kues, W., Pedarzani, P., Schröter, K.H., and Ruppersberg, J.P. (1992). Characterization of a Shaw-related potassium channel family in rat brain. EMBO J. *11*, 2473–2486.

Reuveni, I., Friedman, A., Amitai, Y., and Gutnick, M.J. (1993). Stepwise Repolarization from Ca2+ Plateaus in Neocortical Pyramidal Cells: Evidence for Nonhomogeneous Distribution of HVA Ca2+ Channels in Dendrites. J. Neurosci. *13*, 4609–4621.

Reyes, A., Lujan, R., Rozov, A., Burnashev, N., Somogyi, P., and Sakmann, B. (1998). Target-cell-specific facilitation and depression in neocortical circuits. Nat. Neurosci. *1*, 279–285.

Reyes-Puerta, V., Sun, J.-J., Kim, S., Kilb, W., and Luhmann, H.J. (2015). Laminar and Columnar Structure of Sensory-Evoked Multineuronal Spike Sequences in Adult Rat Barrel Cortex In Vivo. Cereb. Cortex *25*, 2001–2021.

Riachi, I. (2010). Emergent connectivity principles in the neocortical column. EPFL Lausanne.

Rinaldi, T., Kulangara, K., Antoniello, K., and Markram, H. (2007). Elevated NMDA receptor levels and enhanced postsynaptic long-term potentiation induced by prenatal exposure to valproic acid. Proc. Natl. Acad. Sci. U. S. A. *104*, 13501–13506.

Romand, S., Wang, Y., Toledo-Rodriguez, M., and Markram, H. (2011). Morphological development of thick-tufted layer v pyramidal cells in the rat somatosensory cortex. Front. Neuroanat. *5*, 5.

Rovira, C., Gho, M., and Ben-Ari, Y. (1990). Block of GABAb-activated K+ conductance by kainate and quisqualate in rat CA3 hippocampal pyramidal neurones. Pflüg. Arch. Eur. J. Physiol. *415*, 471–478.

Rozov, A., Burnashev, N., Sakmann, B., and Neher, E. (2001). Transmitter release modulation by intracellular Ca2+ buffers in facilitating and depressing nerve terminals of pyramidal cells in layer 2/3 of the rat neocortex indicates a target cell-specific difference in presynaptic calcium dynamics. J. Physiol. *531*, 807–826.

Sarid, L., Bruno, R., Sakmann, B., Segev, I., and Feldmeyer, D. (2007). Modeling a Layer 4-to-Layer 2/3 Module of a Single Column in Rat Neocortex: Interweaving in Vitro and in Vivo Experimental Observations. Proc. Natl. Acad. Sci. *104*, 16353–16358.

Sholl, D.A. (1953). Dendritic organization in the neurons of the visual and motor cortices of the cat. J. Anat. *87*, 387–406.1.

Shu, Y., Yu, Y., Yang, J., and McCormick, D.A. (2007). Selective Control of Cortical Axonal Spikes by a Slowly Inactivating K+ Current. Proc. Natl. Acad. Sci. *104*, 11453–11458.

Silberberg, G., and Markram, H. (2007). Disynaptic inhibition between neocortical pyramidal cells mediated by Martinotti cells. Neuron *53*, 735–746.

Silver, R.A., Lubke, J., Sakmann, B., and Feldmeyer, D. (2003). High-Probability Uniquantal Transmission at Excitatory Synapses in Barrel Cortex. Science *302*, 1981–1984.

Simkus, C.R.L., and Stricker, C. (2002). Properties of mEPSCs recorded in layer II neurones of rat barrel cortex. J. Physiol. *545*, 509–520.

Somogyi, P., and Cowey, A. (1981). Combined golgi and electron microscopic study on the synapses formed by double bouquet cells in the visual cortex of the cat and monkey. J. Comp. Neurol. *195*, 547–566.

Somogyi, P., Freund, T.F., and Cowey, A. (1982). The axo-axonic interneuron in the cerebral cortex of the rat, cat and monkey. Neuroscience *7*, 2577–2607.

Stuart, G., and Spruston, N. (1998). Determinants of Voltage Attenuation in Neocortical Pyramidal Neuron Dendrites. J. Neurosci. *18*, 3501–3510.

Stuart, G., Schiller, J., and Sakmann, B. (1997). Action potential initiation and propagation in rat neocortical pyramidal neurons. J. Physiol. *505 (Pt 3)*, 617–632.

Szabadics, J., Tamás, G., and Soltesz, I. (2007). Different transmitter transients underlie presynaptic cell type specificity of GABAA,slow and GABAA,fast. Proc. Natl. Acad. Sci. U. S. A. *104*, 14831–14836.

Thomson, A.., and Bannister, A.. (1998). Postsynaptic pyramidal target selection by descending layer III pyramidal axons: dual intracellular recordings and biocytin filling in slices of rat neocortex. Neuroscience *84*, 669–683.

Thomson, A.M., and Lamy, C. (2007). Functional Maps of Neocortical Local Circuitry. Front. Neurosci. *1*, 19–42.

Thomson, A.M., Deuchars, J., and West, D.C. (1993). Large, deep layer pyramid-pyramid single axon EPSPs in slices of rat motor cortex display paired pulse and frequency-dependent depression, mediated presynaptically and self-facilitation, mediated postsynaptically. J. Neurophysiol. *70*, 2354–2369.

Thomson, A.M., West, D.C., Hahn, J., and Deuchars, J. (1996). Single axon IPSPs elicited in pyramidal cells by three classes of interneurones in slices of rat neocortex. J. Physiol. *496*, 81–102.

Toledo-Rodriguez, M., Blumenfeld, B., Wu, C., Luo, J., Attali, B., Goodman, P., and Markram, H. (2004). Correlation maps allow neuronal electrical properties to be predicted from single-cell gene expression profiles in rat neocortex. Cereb. Cortex *14*, 1310–1327.

Tsodyks, M., and Markram, H. (1997). The neural code between neocortical pyramidal neurons depends on neurotransmitter release probability. Proc Natl Acad Sci USA *94*, 5495.

Wang, H.-X., and Gao, W.-J. (2009). Cell type-specific development of NMDA receptors in the interneurons of rat prefrontal cortex. Neuropsychopharmacol. *34*, 2028–2040.

Wang, Y., Gupta, A., and Markram, H. (1999). Anatomical and functional differentiation of glutamatergic synaptic innervation in the neocortex. J. Physiol. Paris *93*, 305–317.

Wang, Y., Gupta, A., Toledo-Rodriguez, M., Wu, C.Z., and Markram, H. (2002). Anatomical, Physiological, Molecular and Circuit Properties of Nest Basket Cells in the Developing Somatosensory Cortex. 395–410.

Wang, Y., Toledo-Rodriguez, M., Gupta, A., Wu, C., Silberberg, G., Luo, J., and Markram, H. (2004). Anatomical, physiological and molecular properties of Martinotti cells in the somatosensory cortex of the juvenile rat. J. Physiol. *561*, 65–90.

Wang, Y., Markram, H., Goodman, P.H., Berger, T.K., Ma, J., and Goldman-Rakic, P.S. (2006). Heterogeneity in the pyramidal network of the medial prefrontal cortex. Nat. Neurosci. *9*, 534–542.

West, M.J., and Gundersen, H.J. (1990). Unbiased stereological estimation of the number of neurons in the human hippocampus. J. Comp. Neurol. *296*, 1–22.

Zhang, Z.W., and Deschênes, M. (1997). Intracortical axonal projections of lamina VI cells of the primary somatosensory cortex in the rat: a single-cell labeling study. J. Neurosci. *17*, 6365–6379.

Author Contributions

H.M. conceived and led the study. F.S., S.L.H., I.S., J.DF. co-led the study. H.M. planned & supervised experiments, data integration, strategies and algorithms, model building, *in silico* experiments and analysis. F.S. planned & supervised the development of algorithms, software & workflows, computing infrastructure and technical integration. E.M., S.R., M.W.R., and S.L.H. drove & co-supervised the integration of the data, tools, models, simulations, and analyses.

Manuscript

H.M., S.R., E.M., and M.W.R. wrote the manuscript.

I.S., D.K., and R.W. contributed to the writing of the manuscript.

S.R., E.M., M.W.R., and H.M. generated the figures.

D.K., W.V.G., N.A., M.A., A.B., F.D., F.S., A.C., J-P.G., M.T., L.K., Y.K., R.R., C.A.R., G.C., T.H.N., M.N., E.G., J.V.D., R.D., and M.T-R. contributed to the generation of figures.

S.R. compiled and integrated all the references.

All authors provided input to the manuscript.

Data Integration

E.M., S.L.H., F.S., and M.T. co-supervised and performed data integration.

S.R. integrated synaptic data from the literature, and lead the literature consistency assessment.

Modeling

E.M., S.L.H., I.S., and F.S. co-supervised model building and analysis.

I.S., W.V.G., S.D., E.H., R.R., S.R., A.Gi., C.A.R. performed modeling of channels and cells.

E.M., S.L.H. performed modeling of cells & circuits, in silico experiments & analysis.

M.T., G.K., D.K., E.M., Y.W., F.S. performed neuronal composition modeling.

S.R., E.M., and M.W.R. performed modeling of synapses.

S.R. performed modeling of synaptic pathways.

M.W.R., S.R. and E.M. devised and implemented algorithms for modeling thalamo-cortical projections.

E.M., S.R., M.W.R., and D.K. conceived, supervised and E.M. performed network level simulations for the synchrony-asynchrony spectrum.

E.M., M.W.R., S.R., W.V.G., J.G.K, G.C., T.H.N., and M.N. conceived and performed *in silico* experiments.

E.M., M.W.R., S.R., A.C., R.P. performed circuit analyses.

J.C.S., J.G. co-supervised and J.G., G.A., L.K. co-developed algorithms and validations for cloning and morphology classification.

Software Development

J.G.K., R.R., W.V.G., K.M., M.T., G.K., R.P. co-developed software & workflows for data acquisition, databasing, and/or data integration.

J.C.S., J.G. co-supervised morphology data integration and J.G., I.R., J.K., D.K., G.A., A.K., L.K., Y.K., and E.M. co-developed algorithms, software & workflows for cell morphologies.

W.V.G., S.D., E.H., R.R., J.G.K., A.Gi. co-developed algorithms, software & workflows for cell building.

E.M., S.L.H., F.D. co-supervised and E.M., J.G.K., M.W.R., S.R., I.R., M.T., G.K., B.R.C.M., N.V.H., P.K., J.D., M.E.G., J.L.R., K.S. co-developed algorithms, software & workflows for circuit building.

M.W.R. developed the connectome algorithm.

S.R., J.G.K., E.M., and M.W.R. developed algorithms, software & workflows for synaptic pathways.

F.D. co-supervised and M.H., J.G.K, R.R., M.W.R., W.V.G., E.M., F.D., A.Gi., A.O. co- developed algorithms, software and workflows for simulation.

J.Mu. co-supervised and J.Mu., J-D.C., S.M.Z., M.T., S.A. co-developed software & workflows for the portal.

E.M., S.L.H., F.D. co-supervised and J.B.H., S.L., T.T., E.M., J.K., I.R., M.W.R., S.R., R.R., M.T., F.D., D.N., N.V.H., J.D., M.E.G., J.L.R., J.P. co-developed algorithms, software & workflows for analysis.

S.E. and L.P. co-supervised and J.B.H., S.L., T.T., M.A., A.B., S.E., D.N., M.W.R., D.K., J.V., R.D. co-developed algorithms, software & workflows for visualization.

A.A. supervised, T.H. co-supervised, and F.T., T.H., B.R.C.M., S.E. co-developed algorithms, software and workflows for spatial indexing.

Visualizations

S.E. co-supervised and M.A., A.B., J.B.H., M.T., M.W.R., S.R., N.A., J.V.D., R.D., and E.M. generated scientific visualizations and movies.

Computing Infrastructure

F.D. and N.B. co-supervised and F.D., N.B., C.A., R.S., B.R.M., planned, implemented, and operated general and high performance computing infrastructure.

Experiments

Y.W., Z.K. co-supervised cell reconstructions. Y.W., T.K.B., and H.M. performed classifications, J.Me., Y.S. coordinated and performed reconstructions and organized morphology data.

T.K.B., S.M., R.P., V.D., G.S., J.V.-LB., A.Gu. performed single and multi-cell electrophysiology experiments.

V.D. performed and analyzed multi-electrode array experiments.

M.T-R. performed single cell electrophysiology, eCode, and gene expression experiments.

J-P.G. and J.Me. performed immunohistochemistry experiments.

J.Me. organized data.

J.DF. supervised and L.A-N., A. M-P., A.M., and J.-R.R. performed experiments and analysis on synapse/cell densities, volume fractions, and somatic innervation patterns.

R.R. performed ion channel experiments.

Additional Supplementary Tables

Table S4. Complete List of Features Used in the Classification of Morphologies, Related to Figure 2.

Bifurcation Mean Branch Length (all neurites)	Bifurcation Mean Branch Length (apical dendrites)	First Moment in z axis (axon)
Mean Density (all neurites)	Mean Trunk Diameter (apical dendrites)	Second Moment in x axis (axon)
Horizontal-Vertical ratio (all neurites)	First Moment in x axis (apical dendrites)	Second Moment in y axis (axon)
Mean Horizontal Range (all neurites)	First Moment in y axis (apical dendrites)	Second Moment in z axis (axon)
Maximum Branch Order (all neurites)	First Moment in z axis (apical dendrites)	Number of Neurites (axon)
Maximum Degree (all neurites)	Second Moment in x axis (apical dendrites)	Number of Fragments (axon)
Maximum Path Length (all neurites)	Second Moment in y axis (apical dendrites)	Mean Termination Branch Length (axon)
Maximum Radial Distance (all neurites)	Second Moment in z axis (apical dendrites)	Min Termination Path Distance (axon)
Mean Trunk Diameter (all neurites)	Number of Neurites (apical dendrites)	Mean Tortuosity (axon)
First Moment in x axis (all neurites)	Number of Fragments (apical dendrites)	Number of Branches (axon)
First Moment in y axis (all neurites)	Distance of Apical Point To Soma (apical dendrites)	Total Length (axon)
First Moment in z axis (all neurites)	Mean Termination Branch Length (apical dendrites)	Total Surface Area (axon)
Second Moment in x axis (all neurites)	Min Termination Path Distance (apical dendrites)	Total Volume (axon)
Second Moment in y axis (all neurites)	Mean Tortuosity (apical dendrites)	Bifurcation Mean Branch Length (basal dendrites)
Second Moment in z axis (all neurites)	Number of Branches (apical dendrites)	Mean Density (basal dendrites)
Number of Neurites (all neurites)	Total Length (apical dendrites)	Horizontal-Vertical ratio (basal dendrites)
Number of Fragments (all neurites)	Total Surface Area (apical dendrites)	Mean Horizontal Range (basal dendrites)
Mean Termination Branch Length (all neurites)	Horizontal length of Apical Tuft (apical dendrites)	Maximum Branch Order (basal dendrites)
Min Termination Path Distance (all neurites)	Vertical length of Apical Tuft (apical dendrites)	Maximum Degree (basal dendrites)
Mean Tortuosity (all neurites)	Depth of Apical Tuft (apical dendrites)	Maximum Path Length (basal dendrites)
Number of Branches (all neurites)	Total Volume (apical dendrites)	Maximum Radial Distance (basal dendrites)
Total Length (all neurites)	Mean Vertical Range (apical dendrites)	Mean Trunk Diameter (basal dendrites)
Total Surface Area (all neurites)	Bifurcation Mean Branch Length (axon)	First Moment in x axis (basal dendrites)
Total Volume (all neurites)	Mean Density (axon)	First Moment in y axis (basal dendrites)
Mean Vertical Range (all neurites)	Horizontal-Vertical ratio (axon)	First Moment in z axis (basal dendrites)
Bifurcation Mean Branch Length (apical dendrites)	Mean Horizontal Range (axon)	Second Moment in x axis (basal dendrites)
Mean Density (apical dendrites)	Maximum Branch Order (axon)	Second Moment in y axis (basal dendrites)
Horizontal-Vertical ratio (apical dendrites)	Maximum Degree (axon)	Second Moment in z axis (basal dendrites)
Mean Horizontal Range (apical dendrites)	Maximum Path Length (axon)	Number of Neurites (basal dendrites)
Maximum Branch Order (apical dendrites)	Maximum Radial Distance (axon)	Number of Fragments (basal dendrites)
Maximum Degree (apical dendrites)	Mean Trunk Diameter (axon)	Mean Termination Branch Length (basal dendrites)
Maximum Path Length (apical dendrites)	First Moment in x axis (axon)	Min Termination Path Distance (basal dendrites)
Maximum Radial Distance (apical dendrites)	First Moment in y axis (axon)	Mean Tortuosity (basal dendrites)
Number of Branches (basal dendrites)	Total Surface Area (basal dendrites)	Mean Vertical Range (basal dendrites)
Total Length (basal dendrites)	Total Volume (basal dendrites)	Soma Cross Section Area

Table S5. Rules for m-type Specific Pooling for e-types across Layers, Related to Figures 2 and 4.
The pooling rules applied, in an m-type specific manner, are as follows: (A) L4 + L5 + L6, (B) L5 + L6, (C) L1 lumped (NGC + NGC-DA + NGA-SA), (D) L23 + L4 + L5 + L6. See Supplementary Experimental Procedures: Composition of e-types.

	BP	BTC	ChC	DBC	LBC	MC	NBC	NGC	SBC
L2/3	D		D					C	D
L4	D		D	A				C	D
L5	D	B	D	A			B	C	D
L6	D	B	D	A			B	C	D

Table S6. Prescribed Parameters for Synaptic Transmission, Related to Figures 9 and 10.

Excitatory-excitatory connections

Connection type	Synapse type	Kinetic parameters (mean ± SD)			Dynamic parameters (mean ± SD)		
		g_{syn} (ns)	τ_{rise} (ms)	τ_{decay} (ms)	U	D (ms)	F (ms)
L23PC-L23PC	Excitatory, depressing (E2)	0.68± 0.46	0.2 ± 0.1	1.7 ± 0.14	0.46 ± 0.26	671 ± 17	17 ± 5
L4Exc-L4Exc	Excitatory, depressing (E2)	0.68 ± 0.45	0.2 ± 0.1	1.7 ± 0.14	0.86 ± 0.09	671 ± 17	17 ± 5
L4SS-L23PC	Excitatory, depressing (E2)	0.19 ± 0.12	0.2 ± 0.1	1.7 ± 0.14	0.79 ± 0.04	671 ± 17	17 ± 5
L5TTPC - L5TTPC	Excitatory, depressing (E2)	1.5 ± 1.05	0.2 ± 0.1	1.7 ± 0.14	0.5 ± 0.02	671 ± 17	17 ± 5
L5STPC - L5STPC	Excitatory, depressing (E2)	0.8 ± 0.53	0.2 ± 0.1	1.7 ± 0.14	0.39 ± 0.03	671 ± 17	17 ± 5
All other E - E connections	Excitatory, depressing (E2)	0.72 ± 0.5	0.2 ± 0.1	1.7 ± 0.14	0.5 ± 0.02	671 ± 17	17 ± 5

Excitatory-inhibitory connections

Connection type	Synapse type	Kinetic parameters (mean ± SD)			Dynamic parameters (mean ± SD)		
		g_{syn} (ns)	τ_{rise} (ms)	τ_{decay} (ms)	U	D (ms)	F (ms)
L5TTPC-L5MC	Excitatory, facilitating (E1)	0.11 ± 0.08	0.2 ± 0.1	1.7 ± 0.14	0.09 ± 0.12	138 ± 211	670 ± 830
L5PC - L5BC/ L5ChC	Excitatory, depressing (E2)	0.72 ± 0.5	0.2 ± 0.1	1.7 ± 0.14	0.72 ± 0.12	227 ± 70	13 ± 24
All other E - I connections	Excitatory, depressing (E2)	0.43 ± 0.28	0.2 ± 0.1	1.7 ± 0.14	0.5 ± 0.02	671 ± 17	17 ± 5

Inhibitory-excitatory connections

Connection type	Synapse type	Kinetic parameters (mean ± SD)			Dynamic parameters (mean ± SD)		
		g_{syn} (ns)	τ_{rise} (ms)	τ_{decay} (ms)	U	D (ms)	F (ms)
L5MC-L5TTPC	Inhibitory, depressing (I2)	0.75 ± 0.32	0.2 ± 0.1	8.3 ± 2.2	0.3 ± 0.08	1250 ± 520	2 ± 4
L23(NBC, LBC)/L23ChC - L23PC	Inhibitory, depressing (I2)	0.91 ± 0.61	0.2 ± 0.1	8.3 ± 2.2	0.14 ± 0.05	875 ± 285	22 ± 5
All other I - E connections	Inhibitory, depressing (I2)	0.83 ± 0.2	0.2 ± 0.1	8.3 ± 2.2	0.25 ± 0.13	706 ± 405	21 ± 9

Inhibitory-inhibitory connections

Connection type	Synapse type	Kinetic parameters (mean ± SD)			Dynamic parameters (mean ± SD)		
		g_{syn} (ns)	τ_{rise} (ms)	τ_{decay} (ms)	U	D (ms)	F (ms)
All I - I connections	Inhibitory, depressing (I2)	0.83 ± 0.55	0.2 ± 0.1	8.3 ± 2.2	0.25 ± 0.13	706 ± 405	21 ± 9